Universidade Estadual Paulista (UNESP)

Instituto de Química

Departamento de Química Analítica

Relatório Científico de Pós-Doutorado

Sensores eletroquímicos baseados em eletrodos impressos modificados com nanoporos metálicos e monitorados por rede sem fio para determinação de flavonóides nos resíduos da indústria cítrica

Processo FAPESP n° 2018/12131-6

Período: 01 de fevereiro de 2019 - 31 de janeiro de 2021

Maísa Azevedo Beluomini
Pós-doutoranda

Profa. Dra. Maria Valnice Boldrin
Supervisora

Araraquara, outubro de 2020.

Sumário

1. Resumo do projeto proposto

A água residual da indústria cítrica é considerada um agente de alto poder poluente devido a sua rica composição orgânica. Por outro lado, o controle de modo rápido e eficiente destes compostos nos processos industriais é de alta relevância para a avaliação do reaproveitamento da biomassa, para fins mais econômicos, estratégicos e ambientalmente amigáveis. Neste contexto, os sensores eletroquímicos baseados em eletrodos impressos podem ser uma alternativa com respostas confiáveis, rápidas, de fácil manuseio e de baixo custo, pois permitem o desenvolvimento de métodos mais robustos, com elevado desempenho, portabilidade e superfícies livres de contaminantes. Assim, este projeto tem como objetivo desenvolver sensores eletroquímicos baseados em eletrodos impressos modificados com materiais metálicos nanoporosos para determinação dos flavonóides hesperidina, narirutina, sinensitina e naringenina. A oxidação destes analitos sobre os sensores de elevada condutividade elétrica e atividade eletrocatalítica proporcionará alta sensibilidade e seletividade na detecção desses flavonóides em resíduos da indústria cítrica. Além disso, pretende-se combinar a portabilidade desses sensores com a comunicação sem fio, através do desenvolvimento de plataformas que permitirá coletar, processar e enviar os dados via wi-fi para um smartphone/laptop, visando a aplicação em campo e em tempo real, através de dispositivos inteligentes, com baixo consumo de energia e robustos.

2. Realizações no período

Durante todo o desenvolvimento do projeto de pesquisa, uma extensa revisão bibliográfica sobre a preparação de eletrodos nanoporosos aplicados a sensores eletroquímicos e o comportamento eletroquímico dos flavonoides foi realizada. A primeira etapa do desenvolvimento deste projeto refere-se ao conhecimento de quais flavonoides compõe a amostra de água amarela. Com isso, a amostra foi coletada na indústria Citrosuco, em Matão-SP, e análises cromatográficas foram realizadas. A segunda etapa envolve o desenvolvimento dos eletrodos impressos (SPE) modificados com nanoporos metálicos, em que o método de corrosão eletroquímica seletiva e o baseado no modelo de bolhas dinâmicas de hidrogênio, foram explorados na construção de nanoestruturas tridimensionais nanoporosas. Como a literatura não reporta até momento estudos sobre o comportamento eletroquímico da molécula de narirutina, ou métodos eletroquímicos para sua determinação, o eletrodo impresso modificado com nanoporos de níquel tridimensionais (3DnpNi/SPE) foi desenvolvido, caracterizado por MEV, EDS, EIS e XPS e empregado no estudo do comportamento eletroquímico da molécula. Devido ao bom desempenho analítico, boa sensibilidade e baixo limite de detecção, o 3DnpNi/SPE foi aplicado na determinação da molécula em amostra de água amarela, resultando no artigo “Synthesis of three-dimensional nanoporous

nickel based on dynamic hydrogen bubble template used for electrochemical detection of narirutin in citrus wastewater" submetido para revista *Electrochimica Acta* - EA20-04756 (anexado no item 9 deste relatório). O 3DnpNi/SPE também foi utilizado no estudo do comportamento eletroquímico da hesperidina e aplicado na determinação da molécula. O segundo eletrodo impresso foi modificado com nanoporos de platina (3DnpPt), pelo método de corrosão eletroquímica seletiva. O elevado fator de rugosidade da superfície assegurou um aumento na atividade eletrocatalítica para a oxidação dos flavonoides. Outro eletrodo que deverá ser desenvolvido na próxima etapa do trabalho, será modificado com nanoporos de prata, e tem como objetivo explorar a resposta catódica dos flavonoides.

Juntamente com a construção dos eletrodos, também está sendo desenvolvido em colaboração com o Prof. Dr. Eduardo Paciência Godoy, do Instituto de Ciências e Tecnologia da UNESP campus Sorocaba, um sistema que permitirá a comunicação sem fio entre o sinal fornecido pelos eletrodos na oxidação/redução dos flavonoides e um software, para análises em campo e em tempo real. Os testes realizados no circuito desenvolvido apresentaram resultados promissores, empregando o ESP32 como placa de aquisição e transmissão de dados sem fio. Infelizmente, estes estudos foram interrompidos em março devido ao fechamento da universidade causado pela pandemia do novo coronavírus, dificultando o andamento das atividades. Portanto, a renovação da bolsa de pós-doutorado nós dará a oportunidade de continuar estes estudos, como consta na carta de apoio à renovação do Prof. Dr. Eduardo, anexada em "outros documentos".

Além disso, estabelecemos colaboração com o Prof. Dr. Frank Marken da University of Bath, no Reino Unido, durante a participação da Dra. Maísa na escola de eletroquímica de Bath (Bath Electrochemical Winter School), em janeiro de 2020. O Prof. Dr. Frank desenvolve uma das principais pesquisas no campo de sensores eletroquímicos baseados no sistema "feedback redox", através de um "small gap". O grupo do Prof. Frank é um dos poucos grupos de pesquisa no mundo que trabalham com este tipo de dispositivo, e esta parceria representa uma grande oportunidade para desenvolver sensores tecnológicos para detecção eletroquímica em nanoescala. O projeto BEPE intitulado "Benchtop fabrication of microgap sensor based on carbon nanomaterials for selective detection of flavonoids" foi submetido para a FAPESP (processo #2020/01822-8) em fevereiro de 2020, porém foi cancelado devido às incertezas causadas pela pandemia de COVID-19. Com isso, esperamos que a renovação da bolsa nos permita solicitar novamente a bolsa BEPE, para ter a oportunidade de realizar o estágio de pesquisa no exterior, que muito contribuirá para o desenvolvimento deste projeto e para a formação acadêmico-científica da bolsista. Além disso, o Prof. Dr. Frank também demostrou seu apoio a renovação da bolsa, como pode ser verificado na carta que está anexada em "outros documentos".

Durante a execução deste projeto de pesquisa, além da participação na escola de eletroquímica de Bath, a Dra. Maísa também participou do XXII Simpósio Brasileiro de Eletroquímica e Eletroanalítica e do III Workshop INCT DATREM, do qual este projeto está vinculado, e que foi premiado como melhor pôster na área de Sensores. Também não podemos deixar de mencionar os trabalhos que foram publicados e submetidos por meio das colaborações científicas da pós-doutoranda e que constam nos itens 7 e 9 deste relatório.

3. Resultados e Discussão

Devido a restrição ao número de páginas, que deve conter no máximo 17 páginas até o item 5, segundo consta na nova norma sobre o formato dos Relatórios Científicos, (https://fapesp.br/14453/formato-para-os-relatorios-cientificos-anuais-e-final-bolsas-no-pais), todas as tabelas, figuras e esquemas constam no Apêndice I.

3.1. Estudos Cromatográficos

A quantidade de flavonoides presentes no resíduo de água amarela foi avaliada primeiramente por cromatográfica liquida de alta eficiência com detecção por arranjo de diodos (CLAE-DAD). As análises foram realizadas em um espectrofotômetro Shimadzu UV-1800 com metodologia semelhante à descrita por Barfi et al., [1]. A coluna cromatográfica utilizada foi C18 à temperatura de 35 ° C e fluxo de 1 ml min^{-1}. O comprimento de onda foi mantido em 280 nm. A fase móvel foi água e acetonitrila contendo 0,1% de ácido fórmico (ACN + 0,1 % AF).

As flavanonas glicosídicas mais abundantes nos resíduos da indústria cítrica brasileira são a hesperdina, naringina, narirutina e naringenina [2,3]. Assim, os padrões analíticos de cada uma dessas moléculas foram preparados a partir de uma solução estoque de 0.01 mol L^{-1} e diluídos em etanol para a concentração de $5,0 \times 10^{-5}$ mol L^{-1}, e uma alíquota de 5,0 μL foi injetado para eluição na coluna (gradiente apresentado na Tabela A1). O cromatograma dos padrões é mostrado na Fig. A1. Os tempos de retenção para narirutina, hesperidina, naringina e naringenina foram 4,63; 5,05; 5,47 e 10.92 min, respectivamente. A identificação cromatográfica dos flavonóides na amostra de água amarela foi realizada através da comparação dos tempos de retenção de cada molécula. Assim, 5,0 μL de amostra filtrada foi injetada diretamente no sistema e o cromatograma é mostrado na Fig. A2. Apenas os picos de (1) narirutina e (2) hesperidina foram observados. Com isso, uma curva analítica na faixa de $5,0 \times 10^{-6}$ mol L^{-1} a $1,0 \times 10^{-4}$ mol L^{-1} (Fig. A3) foi construída para obter a concentração desses flavonoides na amostra. Através das áreas dos picos obtidos, a quantidade de narirutina e hesperidina foram determinadas como mostra a Tabela A2. O valor encontrado foi $(8,5 \pm 0,25) \times 10^{-5}$ mol L^{-1} de narirutina e $1,7 \pm 0,11 \times 10^{-4}$ mol L^{-1} de hesperidina.

Com isso, o desenvolvimento dos eletrodos modificados com nanoporos metálicos foi focado para a determinação de narirutina e hesperidina.

3.2. Eletrossíntese e caracterização do 3DnpNi/SPE

Os estudos eletroquímicos foram realizados em um potenciostato Autolab PGSTAT30 acoplado a um microcomputador utilizando o software de controle Nova 1.11 Os eletrodos impressos (SPE) foram adquiridos da DropSens (código: DRP - C11L).

A eletrossíntese do eletrodo impresso modificado com nanoporos de níquel tridimensionais (3DnpNi/SPE) está detalhadamente explicada no artigo anexado no item 9, intitulado: "Synthesis of three-dimensional nanoporous nickel based on dynamic hydrogen bubble template used for electrochemical detection of narirutin in citrus wastewater*"*. Resumidamente, a eletrodeposição do níquel nanoporoso no SPE foi realizada em densidade de corrente constante em uma solução contendo 0,01 mol L^{-1} de $NiCl_2$, 0,1 mol L^{-1} de NaCl e 0,2 mol L^{-1} de NH_4Cl. Este método, conhecido como modelo dinâmico de geração de bolhas de hidrogênio (do inglês *dynamic hydrogen bubble template*, ou DHBT) foi escolhido ao invés do método de corrosão eletroquímica seletiva, pois produziu poros de níquel livre de contaminação.

No método DHBT, a redução dos íons níquel e a reação de evolução do hidrogênio acontecem simultaneamente. Os parâmetros que afetam a formação dos nanoporos são: fonte e concentração de H^+ presente na solução de eletrodeposição, densidade de corrente aplicada, substrato e sal metálico utilizado. Para obter nanoporos de níquel em uma única etapa, a escolha do eletrólito suporte é fundamental devido a sua forte influência na morfologia e nas propriedades dos poros. Assim, o NH_4Cl foi escolhido como um dos eletrólitos, pois sua presença além de aumentar a taxa de evolução de H^+, melhora a resistência mecânica do material. Além disso, a presença de NaCl contribui para a formação de $NiCl^+$, evitando a formação de $Ni(OH)_2$ e mantendo o níquel livre para a eletrodeposição [4,5]. Durante o estudo foi observado que a densidade de bolhas de hidrogênio aumentou com a densidade de corrente aplicada, produzindo microbolhas de hidrogênio na superfície do SPE. A densidade de corrente foi então estudada na faixa de 0,08 a 0,6 A cm^{-2}, durante 20 s. As imagens de FEG-SEM da superfície do SPE para cada condição são mostradas na Fig. A4. A Fig. A4A mostra o SPE sem modificação, a Fig. A4B para eletrodeposição de níquel realizada com aplicação de 0,08 A cm^{-2}, a Fig. A4C com 0,2 A cm^{-2}, a Fig. A4D com 0,6 A cm^{-2} e a Fig. A4E com 0,8 A cm^{-2}. Devido à rápida mudança da camada de difusão com o tempo, maiores densidades de corrente produziram poros com melhor morfologia. Por outro lado, densidades de corrente muito elevadas podem gerar grandes bolhas de hidrogênio, e a coalescência entre elas pode levar a formação de grandes poros, com baixa resistência

mecânica, como pode ser observado na Fig.A 4E. Assim, a densidade de corrente escolhida foi de 0,6 A cm^{-2}, em que os poros foram distribuídos homogeneamente na superfície do eletrodo, com diâmetros entre 70 - 120 nm. A Fig. A4F mostra a EDS relacionada à imagem D, que confirma a presença de Ni. A avaliação do fator de rugosidade superficial (R*f*) dos nanoporos de Ni, foi realizada por meio de CV em solução de 0,1 mol L^{-1} NaOH na faixa de 0,2 a 0,7 V, υ = 50 mV s^{-1}, como mostra a Fig. A5A. O aumento da rugosidade do 3DnpNi/SPE foi observado até o tempo de eletrodeposição de 40 s, com R*f* de 4,8 (quatro vezes maior em relação ao tempo de 10 s). Após esse tempo foi observada uma diminuição da rugosidade (Fig.A5B), que é atribuída à coalescência das bolhas de hidrogênio [6]. Assim, para a formação do 3DnpNi/SPE, as melhores condições foram a aplicação de densidade de corrente de 0,6 A cm^{-2} durante 40 s. A FEG-SEM desta condição ideal é mostrada na Fig.A6.

O EIS foi utilizado para a caracterização eletroquímica do 3DnpNi/SPE. A resistência de transferência de carga (Rct) foi examinada usando uma solução de $5{,}0 \times 10^{-3}$ mol L^{-1} $[Fe(CN)_6]^{3-/4-}$ em 0,1 mol L^{-1} KCl, no potencial de 0,2V. Analisando o diagrama de Nyquist da Fig. A7, é possível observar um semicírculo para a SPE (curva a) com Rct de 2,3 KΩ. Quando para o SPE foi modificado com 3DnpNi (curva b), o valor Rct foi notavelmente menor, 39 Ω. Esses resultados mostram que a modificação facilitou a transferência de elétrons entre a sonda redox e a superfície do eletrodo.

A composição química da superfície do 3DnpNi/SPE foi caracterizada por XPS, a fim de estudar o nível de oxidação, bem como a natureza das ligações químicas (Fig.A8). A análise dos componentes relacionais ao carbono, oxigênio e níquel mostram as principais ligações envolvidas na modificação e estão detalhadamente descritas no artigo “Synthesis of three-dimensional nanoporous nickel based on dynamic hydrogen bubble template used for electrochemical detection of narirutin in citrus wastewater”.

3.2.1. Comportamento eletroquímico da narirutina em SPE e em 3DnpNi/SPE.

Uma vez que a literatura não reporta estudos sobre o mecanismo de oxidação eletroquímica da narirutina, nem o desenvolvimento de um método eletroquímico para sua determinação, este projeto explorou mais profundamente este tópico.

A Fig.A9 mostra a resposta voltamétrica em SPE (curva a) e em 3DnpNi/SPE (curva b), para $1{,}0 \times 10^{-5}$ mol L^{-1} de narirutina em solução tampão de citrato pH 4,0. É possível observar um pico anódico no potencial de 0,64 V. Analisando a varredura reversa, nenhum pico foi visualizado, sugerindo que o processo de oxidação da narirutina é irreversível. Em comparação com o SPE, o 3DnpNi/SPE apresentou um pico de corrente 2,2 vezes maior, comprovando que a maior

porosidade da superfície aumentou a atividade eletrocatalítica da narirutina. A influência do pH foi investigada na faixa de 2,6 a 5,6 utilizando 0,1 mol L^{-1} de solução tampão citrato. A concentração de narirutina foi de $1,0 \times 10^{-5}$ mol L^{-1} e os CVs da Fig.A10 mostra que a corrente de pico com melhor definição foi obtida em pH 4,0. Além disso, os picos deslocaram negativamente com o aumento do pH, indicando que a oxidação da narirutina é acompanhada pela transferência de prótons. A relação linear obtida entre o potencial de oxidação da narirutina e o pH da solução tampão citrato, E (V) = - 0,0501pH + 0,86, apresentou boa concordância com o valor teórico de -0,059 V/pH, a 25˚C, da equação de Nernst. Assim, o número elétrons envolvidos na oxidação da narirutina é acompanhado por um número igual de prótons. A influência da velocidade de varredura (υ) na eletrooxidação de $1,0 \times 10^{-5}$ mol L^{-1} de narirutina em 3DnpNi/SPE, foi investigada entre 20 e 500 mV s^{-1}. A Fig.A11A mostra uma boa relação linear entre o logaritmo de I (A) e o logaritmo de υ, indicando que a oxidação da narirutina é controlada por um processo misto de difusão-adsorção no 3DnpNi/SPE. Este resultado está de acordo com o encontrado para flavonóides semelhantes [7,8]. Além disso, o potencial de pico *E versus* log υ, Fig.A11B, também mostrou que o valor *E* deslocou para valores mais positivos com o aumento da velocidade de varredura, comprovando a irreversibilidade da reação eletródica [9]. A partir da relação entre *E* e log υ, $E = 0,105 \log\upsilon + 0,760$, R = 0,997 (Fig.A11B), foi possível calcular o valor de αn, expressa pela equação de Laviron [10], o valor encontrado foi de 0,56. Em geral, considera-se o valor teórico de $\alpha = 0,50$ para processos irreversíveis, segundo Bard e Faulkner [11]. Portanto, o valor de *n* pode ser estimado em 1, indicando que um elétron está envolvido no processo de oxidação da narirutina. Além disso, valor E^0 foi determinando em 0,66 V, a partir da relação *E vs.* υ (Fig.A11C), e o valor de k_0 foi calculado em $1,0 \times 10^{-3}$ cm s^{-1}, a 25˚C, a partir da equação de Laviron. A técnica de cronocoulometria foi utilizada para a investigar a capacidade de adsorção (Γ^*) e obtenção do coeficiente de difusão (D) da narirutina em 3DnpNi/SPE. Os experimentos foram no potencial de 0,63 V na presença e na ausência de $1,0 \times 10^{-5}$ mol L^{-1} de narirutina. As curvas de carga (Q) versus $t^{1/2}$ são mostradas na Fig.A12. A curva a_0 foi obtida somente em eletrólito suporte e a curva a_1 em solução contendo narirutina. As equações lineares das curvas a_0 e a_1 foram Q (10^{-6} C) = 5,49 $t^{1/2}$ - 2,64 (R = 0,999) e Q (10^{-6} C) = 22,8 $t^{1/2}$ - 1,28, respectivamente. É possível observar que a inclinação e o intercepto das duas retas foram diferentes, confirmando que processo de oxidação da narirutina é controlado por um processo misto. A partir da equação de Anson [12], o valor de Q_{ads} foi obtido a partir da diferença entre os dois interceptos das curvas de a_0 e a_1. Assim, o valor de Γ^* foi de $1,1 \times 10^{-10}$ mol cm^{-2}. Além disso, a partir da inclinação da curva a_1, D foi de $2,8 \times 10^{-8}$ cm^2 s^{-1}.

De acordo com a literatura, os grupos fenólicos do anel B dos flavonóides são considerados a parte eletroativa da molécula [13,14]. O processo de oxidação envolveu 1 elétron e 1 próton em uma única etapa irreversível, com a formação do radical fenoxila (pico observado), que foi adsorvido na superfície do eletrodo devido à reação irreversível (dimerização) [15,16]. Comportamentos análogos foram relatados para compostos estruturalmente semelhantes [17–19]. Com base nesses resultados, o mecanismo proposto para a oxidação eletroquímica da narirutina é mostrado no esquema A1.

3.2.2. Comportamento eletroquímico da hesperidina em SPE e em 3DnpNi/SPE

A Fig.A13A exibe os CVs de $1,0 \times 10^{-4}$ mol L^{-1} de hesperidina em SPE e em 3DnpNi/SPE em solução de 0,1 mol L^{-1} tampão citrato (pH 4,0). Analisando os CVs é possível observar que uma resposta eletroquímica pouco intensa da hesperidina em SPE (curva a). Depois que o SPE foi modificado com3DnpNi (curva b), a corrente foi aumentada, o que pode ser atribuído às boas características do 3DnpNi, principalmente quanto a maior rugosidade da superfície. A Fig.A13B mostra o comportamento redox da hesperidina no eletrodo modificado. Podemos observar que na primeira varredura um pico anódico P_1 ocorreu no potencial de 0,42 V e o pico P_2, no potencial de 0,97 V, ocorreu na varredura reversa. No segundo ciclo, um novo pico anódico, P_3, apareceu em 0,70 V e a intensidade do P_1 diminui. Na varredura reversa, o P_2 praticamente não sofreu nenhuma mudança. A partir desta observação e com base nos dados reportados na literatura [8,20] o P_1 é um pico anódico irreversível e P_2/P_3 é um par de picos redox, cujo grupo ativo é o resultado do produto da oxidação de P_1.

O efeito do pH na eletrooxidação da hesperidina ($1,0 \times 10^{-4}$ mol L^{-1}) foi realizada por CV em diferentes soluções de pH como eletrólito suporte, incluindo tampão fosfato e tampão citrato, 0,1 mol L^{-1}, de 3,6 a 7,0. Cada varredura foi realizada 2 vezes, sendo P_1 obtido no primeiro ciclo e P_2 e P_3 obtidos no segundo ciclo. Todos os três picos mudaram para potenciais mais negativos com o aumento do pH, indicando que a reação redox da hesperidina envolve a transferência de prótons. Os cálculos foram realizados baseados nos mostrados para a molécula de narirutina, com algumas ressalvadas. O valor de E variou linearmente com o pH (Fig.A14) para cada um dos picos estudados, conforme segue as equações lineares: EP_1 (V) = - 0,039 pH + 0,85 (curva a), EP_2 (V) = - 0,058 pH + 0,65 (curva b) e EP_3 (V) = - 0,057 pH + 0,67 (curva c). A inclinação da regressão linear de 0,039 para o P_1 indica que o processo envolve prótons e elétrons na proporção de 1:2. A inclinação de P_2 e P_3, por unidade de pH, estão próximos do valor teórico de -0,059 V/pH, indicando que a reação P_2/P_3 envolve um número igual de prótons e elétrons. A influência da velocidade de varredura na resposta eletroquímica da hesperidina ($5,0 \times 10^{-5}$ mol L^{-1}) foi estudada

na faixa de 10 – 500 mV s^{-1}. Cada varredura foi realizada duas vezes e os dados do P_1 foram obtidos na primeira varredura (Fig.A15A), enquanto para os picos P_2/P_3 foram obtidos na segunda varredura, Fig.A15B. Foi observado que com o aumento da velocidade de varredura, os picos P_1 e P_3 deslocaram para potenciais mais positivos, enquanto o pico P_2 deslocou negativamente. A relação linear entre log I e o log υ para P_1 ($\log P_1$ (μA) = 0.93 log (V s^{-1}) + 1,01), indica que P_1 foi controlado por adsorção e difusão (Fig.A15C). Além disso, os valores de EP_1 e log υ exibiram uma boa relação linear, dada por EP_1 = 0.082 logυ + 0.57 (Fig.A15D). Assim, baseado na teoria de Laviron[21] e no *slope* de EP_1 *versus* log υ (Fig.A15E), o valor de n foi de 2, assumindo α = 0.5. Como isso, 2 elétrons estão envolvidos na reação de oxidação de P_1. Como o processo de oxidação envolve prótons e elétrons na proporção de 1:2, o número de prótons envolvida na reação de P_1 foi de 1. Além disso, o valor do potencial padrão foi de 0,45, de acordo com o gráfico EP_1 *versus* V (EP_1 = 0,24 υ + 0,45), obtido quando υ = 0 (Fig.A15F). Assim, o valor da constante k_0 foi de 1,34 × 10^{-4} s^{-1}. Para os picos P_2 e P_3, a corrente de pico e a velocidade de varredura exibiu uma boa relação (Fig.A15G), e a equação de regressão linear foi de I_{p2} = 5.9 υ + 0.17 e I_{p3} = 9.8 υ + 0,018, sugerindo que a reação eletródica de P_2 e P_3 é um reação controlada pela adsorção. Além disso, com o aumento da velocidade de varredura, o deslocamento do pico P_2 para regiões mais negativas e P_3 para regiões mais positivas, indicando que o processo redox P_2/P_3 é quase-reversível. A partir da relação linear entre o potencial redox (EP_2 e EP_3) e o log υ, dada por EP_2 = -0,078 log υ + 0,034 e EP_3 = 0,058 log υ + 0,25, é possível calcular os valores de *n* e α, a partir da equação de Laviron. Assim, o slope de EP_2 *versus* log υ e EP_3 *versus* log υ pode ser expresso como: 2,3RT/(1-α)nF e 2,3RT/nα. Com isso, os valores de α e n foram de 0,43 e 1,8, respectivamente. O valor de k_0 foi calculado a partir da expressão $\log k_o$ = αlog(1- α) + (1- α)log α -log(RT/nFυ) – α(1-α)[nFΔEp/2,3RT] [8]. O valor k_0 foi de 2,45 × 10^{-3} s^{-1}. Assim, o processo redox de P_2/P_3 envolveu 2 e^- e 2 prótons. O resultado desses estudos foram similares ao observado por Wu et el., [8] e Compton et al., [20] e consistentes com o mecanismo $EC_{irrev}E$, como mostra o esquema 2. O primeiro pico é característico da oxidação eletroquímica irreversível da unidade guaiacol da molécula de hesperidina, com a formação do par *o*-benzoquinona/catecol quase reversível.

O estudo cronocoulométrico foi realizado para obter a capacidade de adsorção (Γ) da molécula na superfície do eletrodo. As curvas dos picos P_1, P_2 e P_3 são mostradas na Fig.A16 e as equações lineares foram: Q_1 (10^{-6} C) = 15,6 $t^{1/2}$ + 25,7, Q_2 (10^{-6} C) = -14,83 $t^{1/2}$ – 39,9 e Q_3 (10^{-6} C) = -0.52 $t^{1/2}$ – 0,92. Na ausência de hesperidina a equação linear foi Q (10^{-6} C) = 1,6 $t^{1/2}$ + 3,7. Como a inclinação e o intercepto das equações foram diferentes, o processo de oxidação da hesperidina foi controlada por adsorção acompanhada de difusão. O valor da Γ para P_1 foi 9,2 × 10^{-10} mol cm^{-2}. A partir do pico P_1, o valor de D_o foi calculado em 1,0 × 10^{-8} cm^2 s^{-1}. As curvas

Q *versus* $t^{1/2}$ para os demais picos foram quase paralelas, evidenciando o processo de adsorção. Os valores da Γ para o par P_2/P_3 foram de $1,5 \times 10^{-9}$ mol cm^{-2} e $1,3\times 10^{-10}$ mol cm^{-2}, respectivamente.

3.3. Desempenho analítico para 3DnpNi/SPE

3.3.1. Curva de calibração, repetibilidade, estabilidade, seletividade e aplicabilidade do 3DnpNi/SPE para determinação de narirutina em amostra.

A técnica de DPV foi usada para avaliar o desempenho analítico e a viabilidade prática do 3DnpNi/SPE na determinação de narirutina e está detalhadamente descrita no artigo [1] do item 9

Os voltamogramas para a narirutina foram estudados na faixa de concentração de $1,0 \times 10^{-7}$ mol L^{-1} a $1,0 \times 10^{-5}$ mol L^{-1} e são mostrados na Fig.A17A. A variação da corrente de pico em relação à concentração de narirutina é mostrada na Fig.A17B. A equação de regressão linear foi de I (A) = 0,31 x + $1,1 \times 10^{-6}$, R = 0,999 e as figuras de mérito foram de $3,9 \times 10^{-8}$ mol L^{-1} para o LOD e $1,3 \times 10^{-7}$ mol L^{-1} para o LOQ, com sensibilidade analítica de 0,31 A L mol^{-1} (n = 3). Além disso, como este trabalho relata o primeiro método eletroanalítico para determinação de narirutina, a comparação do método proposto com outros métodos analíticos descritos na literatura é listada na Tabela A3. Ao analisar a tabela, é possível observar que o presente trabalho proporcionou um excelente desempenho analítico, com LOD significativamente inferior à maioria dos trabalhos encontrados na literatura, com exceção dos trabalhos de Cho et al., [22], Seo et al., [23] e Zhao et al., [24]. Porém, em comparação aos métodos cromatográficos é importante observar que o eletrodo proposto, apresenta um menor custo, não requer grandes volumes de solventes, preparo de fase móvel ou longos tempos de análises. A repetibilidade inter-eletrodos (n = 5) foi investigada por CV utilizando a concentração de $5,0 \times 10^{-6}$ mol L^{-1} de narirutina em 0,1 mol L^{-1} de solução tampão de citrato (pH 4,0). A corrente de oxidação média foi de 2,2 µA com RSD de 5,9 %. Além disso, o 3DnpNi/SPE foi armazenado por 10 dias em contato com o ar à temperatura ambiente (25 °C) e a resposta permaneceu 94,2 % do seu valor de inicial.

Para avaliar a seletividade do 3DnpNi/SPE na determinação da narirutina, foram investigados os efeitos de alguns flavonóides, como naringenina e hesperidina, além da glicose e frutose (Fig.A18). Os sinais de corrente obtidos por DPV em $1,0 \times 10^{-6}$ mol L^{-1} de narirutina em solução tampão de citrato 0,1 mol L^{-1} (pH 4,0) foram comparados na ausência e na presença da molécula interferente (na concentração de $1,0 \times 10^{-5}$ mol L^{-1}). A espécie adicionada foi considerada interferente se o valor da corrente causar um erro relativo ≤ ± 5,0 % (limite de tolerância) na resposta da narirutina. Os resultados mostraram uma porcentagem de erro relativo de - 4,7 %, - 3,8 %, 3,2 % e 2,9 % na corrente de pico para análises contendo hesperidina, naringenina, glicose e frutose, respectivamente. Assim, o 3DnpNi/SPE apresentou boa seletividade para a molécula.

A aplicabilidade do 3DnpNi/SPE na determinação da narirutina em amostra de água amarela foi examinada usando DPV. A amostra foi coletada na empresa CITROSUCO®, na cidade de Matão-SP. As amostras foram centrifugadas a 4000 rpm por 20 min para remover as partículas sólidas. O sobrenadante foi coletado e filtrado em filtros com porosidade de 0,47 e 0,22 µm e congelado até o uso. A amostra foi diluída 20 vezes em eletrólito e utilizada para detecção de narirutina. O método de adição de padrão foi adotado para determinar a concentração da molécula na amostra e os resultados são apresentados na Tabela A4. As amostras foram enriquecidas e a relação linear entre a corrente e a concentração foi $I(\mu A) = 0{,}56\ C_{narirutina} + 2{,}3 \times 10^{-6}$ (Fig.A19) Assim, a concentração encontrada de narirutina na água amarela foi de $8{,}3 \pm 0{,}39 \times 10^{-5}$ mol L^{-1} (n = 3). As porcentagens de recuperação são mostradas na Tabela A4 e os resultados variaram de 97,1 % a 100,9 %, com RSD menor que 7,0 %, mostrando que o método analítico desenvolvido pode ser considerado adequado para a detecção de narirutina. Como a quantidade encontrada de narirutina por HPLC foi $8{,}6 \pm 0{,}25 \times 10^{-5}$ mol L^{-1}, o RSD entre as duas técnicas foi de 0,16 %. Esse resultado monstra boa concordância entre os métodos, indicando a confiabilidade do 3DnpNi/SPE para a determinação de narirutina em água amarela.

3.3.2. Curva de calibração, repetibilidade, estabilidade, seletividade e aplicabilidade do 3DnpNi/SPE para determinação de hesperidina em amostra.

Para obtenção da curva analítica o par redox P_2/P_3 foi avaliado por SWV na faixa de -0,05 a 0,2 V, frequência de 20 Hz, amplitude e incremento de potencial de 25 mV. O par redox foi escolhido uma vez que o pico P_1 é irreversível (menor contribuição para técnica de SWV). Duas faixas lineares foram obtidas, entre $5{,}0 \times 10^{-8}$ mol L^{-1} – $1{,}0 \times 10^{-6}$ mol L^{-1} e entre $1{,}0 \times 10^{-6}$ mol L^{-1} – $1{,}0 \times 10^{-5}$ mol L^{-1}, conforme mostra a Fig.A20. O LOD foi de $8{,}3 \times 10^{-9}$ mol L^{-1} e o LOQ de $2{,}8 \times 10^{-8}$ mol L^{-1}. A corrente de oxidação média (n = 3) para P_1 foi de 2,5 µA com RSD de 9,1 %, para P_2 foi de 0,51 µA com RSD de 6,8% e para P_3 de 0,68 µA com RSD de 4,6 %. Além disso, um mesmo eletrodo foi utilizado para detecção do par redox P_2/P_3 por SWV e em seguida armazenado por 10 dias em contato com o ar à temperatura ambiente (25 °C). Após esse período o RSD foi de apenas 7,1 %, mostrando excelente estabilidade. A seletividade do eletrodo foi avaliada por cronoamperometria, no potencial de 0.075 V após um pré-tratamento de 50 s no potencial de 0,35 V. Como podemos observar na Fig.A21, no tempo de 20 s foi realizada a adição de $1{,}0 \times 10^{-5}$ mol L^{-1} de hesperidina, produzindo uma corrente de 2,2 µA. No tempo de 50 s foi adicionada $1{,}0 \times 10^{-5}$ mol L^{-1} de narirutina e naringenina e no tempo de 80 s a adição de $1{,}0 \times 10^{-5}$ mol L^{-1} frutose e glicose. A corrente gerada pelas moléculas foi insignificante perto da produzida pela hesperidina, indicando que o método desenvolvido possuí excelente seletividade.

A determinação de hesperidina em amostra de água amarela foi realizada por adição padrão. Os resultados são apresentados na Tabela A5. As amostras foram enriquecidas com concentrações conhecidas de hesperidina na faixa de $1,0 \times 10^{-6}$ mol L^{-1} a $1,0 \times 10^{-5}$ mol L^{-1}. A equação de regressão linear média foi I (μA) = $2,8 \times 10^{-5}$ $C_{hesperidina}$ + 1,9. Após a construção da curva de adição padrão, por extrapolação da reta até o eixo das abscissas, levando em consideração as diluições, a concentração de hesperidina encontrada na água amarela foi de $15,4 \pm 2,19 \times 10^{-5}$ mol L^{-1} (n = 3). As porcentagens de recuperação variaram de 96 % a 111 %, com RSD menor que 11 %, indicando que o método analítico é preciso para a detecção da molécula. Em comparação com a concentração de hesperidina determinada por HPLC, o RSD foi de 0,15 %, mostrando boa concordância entre as técnicas e confiabilidade do 3DnpNi/SPE para a determinação de hesperidina em água amarela.

3.4. Eletrossíntese e caracterização do 3DnpPt/SPE

Outro eletrodo nanoporoso que está sendo desenvolvido, utiliza o método de corrosão eletroquímica seletiva a partir da eletrodeposição da liga de Pt-Cu na superfície do SPE. A platina nanoporosa foi obtida a partir de sucessivos CVs em solução contendo $5,0 \times 10^{-3}$ mol L^{-1} de H_2PtCl_6 e $1,0 \times 10^{-3}$ mol L^{-1} de $CuSO_4$ em 0,5 mol L^{-1} H_2SO_4, na faixa de potencial de 1,2 a -0,6 V, υ = 100 mV s^{-1}. A cada ciclo, uma camada da liga de Pt-Cu foi eletrodepositada na superfície do SPE durante a varredura catódica, enquanto que na varredura anôdica ocorreu a dissolução do Cu e formação de Pt nanoporoso. Os CVs da Fig A22A mostram a resposta para do SPE para uma solução de $5,0 \times 10^{-3}$ mol L^{-1} de $CuSO_4$ (curva preta), H_2PtCl_6 (curva azul) e para $CuSO_4 + H_2PtCl_6$ (curva vermelha). Para a curva de Cu, o pico em ~ - 0,18 V representa a oxidação do Cu e em ~0,4 V a redução. As curvas para Pt mostram curvas CV características do metal. Os picos na região entre -0,1 e 0,1 V pode ser atribuído à adsorção e dessorção de hidrogênio. Quando os potenciais são maiores que 0,3 V, ocorre a oxidação da Pt e na varredura reversa ocorre a redução do seu óxido (~ 0.2 V). Na Fig.A22B, o CV da eletrodeposição da liga Pt-Cu mostra um pico de corrente redutiva na varredura catódica (Pb) que é atribuído à co-deposição da liga. O pico observado na varredura anódica (Pa) é reflexo da dissolução do cobre, menos nobre da liga. À medida que o número de ciclos aumenta, a área dos picos (a) e (b) também aumenta indicando o crescimento dos poros de platina no SPE. Assim, a influência no número de ciclos na formação do 3DnpPt/SPE foi estudada na faixa 5 a 30, por estar diretamente correlacionados à rugosidade da superfície. Após a eletrodeposição, os eletrodos foram submetidos a sucessivos CVs em 0,5 mol L^{-1} H_2SO_4 na faixa de potencial de −0,25 a 1,4 V, 100 mV s^{-1}, até estabilização da corrente. A carga (μC) associada à área do pico de redução do óxido de platina, foi dividida por um fator de

conversão de 420 μC cm^{-2}. A área eletroquímica foi dividida pela área geométrica, resultando no R*f* da superfície. O R*f* variou entre 33 a 120 (Fig.A22C), sendo o valor de 120 obtido durante a aplicação de 15 ciclos, e o escolhido como ótimo para a construção do eletrodo.

As análises de MEV, Fig.A23A e A23B, mostra a morfologia da superfície do SPE porosa, em que aglomerados de partículas de Pt de tamanho nanométrico foram eletrodepositadas por CV. Os espaços entre os aglomerados nanométricos de Pt, possivelmente refere aos íons Cu que foram dissolvidos da estrutura, levando a formação de lacunas abertas e nanoporosas. A Fig.A23C mostra o respectivo EDS, confirmando a presença de grandes quantidades de Pt em comparação ao Cu, ainda remanescente na estrutura. A caracterização eletroquímica foi realizada por EIS na faixa de frequência de 0,10 Hz a 100 kHz, para monitorar a resistência de transferência de elétrons na interface do 3DnpPt/SPE. A Fig.A24 mostra que o gráfico de Nyquist para SPE apresenta um semi-circulo com um Rct de 2,4 kΩ. Após a modificação da superfície com 3DnpPt, o Rct diminui aproximadamente 2,6 vezes, caindo para o valor de 924 Ω. Esses resultados mostram que o material nanoporoso atuou como um excelente mediador no processo de transferência de elétrons. Outras caracterizações estão sendo realizadas na superfície, como o XPS.

3.4.1. Comportamento eletroquímico da hesperidina e da narirutina em 3DnpPt/SPE

Após a otimização na construção do 3DnpPt/SPE, o estudo do comportamento eletroquímica da hesperidina e da narirutina ($5,0 \times 10^{-5}$ mol L^{-1}) em solução de 0,1 mol L^{-1} tampão citrato (pH 4,0) foi realizado por CV, como mostra a Fig.A25. Para o 3DnpPt/SPE, a primeira etapa da eletrooxidação da hesperidina ocorreu no potencial ~ 0,93 V, com uma corrente de oxidação média de 5,2 μA (n = 3), referente a troca de dois elétrons durante a oxidação dos grupos hidroxila no anel mais eletroativo. Em relação ao 3DnpNi/SPE o eletrodo nanoporoso de Pt apresentou maior corrente de oxidação, porém houve um deslocamento do potencial para a região mais positiva, mostrando que a molécula foi oxidada mais dificilmente. Com isso, a constante de velocidade heterogênea da hesperidina no 3DnpPt/SPE deverá ser avaliada. Além disso, atividade do produto de oxidação da hesperidina ainda não está muito clara e deverá ser estudada mais detalhadamente. Para a molécula da narirutina, o potencial de oxidação foi de 0,36 V, com uma corrente média de 5,9 μA (n=3), que em comparação ao 3DnpNi/SPE, houve um pequeno deslocamento para a região catódica, mostrando que a oxidação da molécula foi ligeiramente facilitada. A partir desses dados e com a conclusão dos estudos do comportamento eletroquímico das moléculas no 3DnpPt/SPE, será possível avaliar a melhor forma de determinar narirutina e hesperidina, empregando técnicas voltamétricas e amperométricas, ainda não exploradas. Além disso, a construção da curva analítica, a avaliação das figuras de mérito, os estudos de

repetibilidade, estabilidade e aplicação em amostra, também deverão ser realizados. A comparação entre a performance analítica dos eletrodos desenvolvidos será avaliada.

3.5. Construção do dispositivo sem fio para determinação em campo dos flavonoides.

Está parte do projeto está sendo realizada em colaboração com o Prof. Dr. Eduardo Paciência Godoy, do Instituto de Ciências e Tecnologia, campus Sorocaba. O sistema que será utilizado para uma comunicação sem fio entre o sinal fornecido pelos eletrodos impressos modificados na oxidação dos flavonoides e o dispositivo sem fio, está sendo baseado em uma placa ESP32, para aquisição e envio de dados para um computador ou outro dispositivo que faça a interface com o usuário, de maneira a apresentar as curvas características de cada um dos flavonoides analisados. Uma vez que a corrente drenada pelo eletrodo é, na maioria das vezes, da escala de microampère (uA), foi necessário a elaboração de um circuito para tratamento e amplificação do sinal antes do mesmo ser enviado para placa de aquisição. Em todos os testes, a corrente obtida foi comparada com a gerada por uma solução de $5{,}0 \times 10^{-3}$ mol L^{-1} de $K_3[Fe(CN)_6)$ em 0,1 mol L^{-1} de KCl, obtida pelo equipamento Autolab PGSTAT30 e registrados pelo software Nova 2.0. Assim, foi montado um circuito de amplificação utilizando amplificadores operacionais, pois além de serem circuitos relativamente simples, são eficazes e de baixo custo. O circuito foi composto por três amplicadores operacionais em cascata utilizando o software *Multisim* da National Instruments, de modo a conseguir uma melhor regulagem no fator de ganho da amplificação. Todas as simulações apresentaram resultados próximo do esperado, porém o modelo de amplificador operacional não foi encontrado comercialmente. Assim, foi realizada uma busca por amplificadores e dentre os encontrados comercialmente, o modelo LM741 atendeu as especificações, além de ser um modelo de baixo custo e facilmente encontrado no mercado. Com isso, foi montado um novo circuito, como apresentado na Fig A26. Com a realização dos testes foi observado que o circuito entregou resultados muito próximos dos almejados, porém alguns problemas foram encontrados na parte de alimentação do amplificador operacional, uma vez que o objetivo do projeto é ter apenas uma fonte simples de energia, provavelmente algum tipo de bateria. Desta forma, foi iniciado uma procura por circuitos que geram uma tensão simétrica a partir de uma fonte de tensão simples. Após simulações necessárias, o amplificador operacional foi substituído pelo LM741. O circuito é mostrado na Fig.A27. A montagem dos circuitos em laboratório foi realizada em um *protoboard*, testando etapa por etapa a fim de mitigar possíveis erros. Após isso, os primeiros testes de funcionalidade foram realizados. Os três circuitos integrados, (CI's) LM741, foram conectados entre si em forma de cascata, cada CI possui apenas um amplificador operacional interno e três resistores, as demais conexões nas extremidades foram entradas, saídas e alimentação. As saídas

de tensão simétrica foram conectadas na alimentação dos amplificadores operacionais do circuito de amplificação, como mostra a Fig.A28. O circuito funcionou de forma muito próxima ao esperado, sendo alimentado com uma única fonte de tensão, com amplitude de 5,0 V. Assim, foi iniciado os testes utilizando o sinal de corrente do eletrodo impresso como corrente de entrada do circuito de amplificação. O eletrodo de trabalho forneceu a corrente que entrará no circuito para ser amplificada e, nos eletrodos auxiliar (CE) e de referência (RE), uma tensão fixa é recebida, que terá seu valor definido de acordo com a substância que será analisada. Através da conexão do eletrodo no circuito, os testes foram realizados utilizando o sinal fornecido por 50 µL da solução de ferricianato gotejada na superfície do eletrodo. Assim, o funcionamento do circuito foi monitorado por uma interface gráfica montada no software *LabView* da *National Instruments*. No software foi possível visualizar em tempo real o sinal proveniente do eletrodo, devido a conexão entre a saída amplificada do circuito e a entrada analógica da placa de aquisição ligada a um computador. As curvas de corrente *vs* tempo fornecidas pelo sistema foram comparadas com as do equipamento comercial Autolab PGSTAT30, obtendo resultados muito similares, porém alguns pequenos ajustes ainda deverão ser realizados no ganho de amplificação. A próxima etapa a ser realizada será empregar a ESP32 como placa de aquisição e transmissão de dados sem fio. Esses dados serão enviados para um dispositivo de visualização gráfica, podendo ser laptop, celular ou tablet. Também será realizado o desenvolvimento de um firmware para recebimento e controle dos dados, de preferência usando a plataforma de programação simples e gratuita. Após a construção do hardware, firmware e aplicativos, o minipotenciostato deverá ser calibrado.Os resultados deverão ser similares ao potenciostato comercial.

3.6. Conclusão

Neste relatório, 3DnpNi/SPE e 3DnpPt/SPE foram preparados utilizando diferentes abordagens de modificação (DHBT e corrosão eletroquímica seletiva), visando a construção rápida, fácil e eficiente de nanoporos de níquel e platina na superfície do SPE, para a determinação de flavonoides presentes na água amarela. Em comparação com o SPE, os eletrodos modificados com nanoporos apresentaram significante aumento na corrente de resposta, principalmente devido sua elevada área superficial e boa condutividade elétrica. Além disso, foi investigado o comportamento eletroquímico da narirutina e da hesperidina e o mecanismo envolvido na oxidação da narirutina foi proposto pela primeira vez. A boa performance eletrocatalítica e analítica do 3DnpNi/SPE mostrou que o eletrodo é eficaz, seletivo, sensível e confiável para a determinação de narirutina e hesperidina em amostras de água amarela. Os resultados obtidos com a aplicação do 3DnpNi/SPE na análise dos flavonoides em água amarela, foram comparados com

os obtidos pela técnica de HPLC e foi encontrada uma excelente concordância entre as duas técnicas. Além disso, o desenvolvimento do dispositivo portátil para a análise em campo e em tempo real está sendo realizado e apresenta resultados promissores.

4. Descrever como o Plano de Gestão de Dados está sendo seguido e eventuais modificações

Este item é aplicável somente para bolsas solicitadas a partir de 01/09/2020.

5. Plano de atividades para o próximo período

Acreditamos que o desenvolvimento da metodologia analítica para 3DnpPt/SPE e a construção, caracterização e aplicação do 3DnpAg/SPE poderá ser realizada rapidamente, considerando a experiência adquirida na fabricação desses eletrodos. Também deverá ser realizada a comparação entre os eletrodos desenvolvidos em relação a performance eletroquímica e analítica dos flavonoides. Além disso, nosso maior foco será avançar no desenvolvimento do dispositivo portátil para aplicação dos eletrodos na análise em campo e em tempo real dos flavonóides. Também pretendemos consolidar nossa parceria com o Prof. Dr. Frank Marken, da University of Bath, através da solicitação da bolsa BEPE que foi cancelada devido a pandemia. Assim, planejamos iniciar a pesquisa na Inglaterra em julho de 2021, mas a solicitação da BEPE à FAPESP será feita o mais breve possível. Desta forma, temos certeza de que a extensão da bolsa de pós-doutorado é necessária para que o projeto tenha sucesso completo.

ATIVIDADES A SEREM DESEMPENHADAS	**TRIMESTRE**			
	1°	**2°**	**3°**	**4°**
Desenvolvimento do método analítico utilizando o 3DnpPt/SPE.	■			
Modificação dos SPEs com nanoporos de Ag.	■			
Caracterização morfológica, química e eletroquímica da superfície do 3DnpAg/SPE.	■	■		
Desenvolvimento da metodologia analítica utilizando o 3DnpAg/SPE.		■	■	
Comparação entre os eletrodos desenvolvidos em relação a performance eletroquímica e analítica dos flavonoides.			■	
Desenvolvimento e aplicação do dispositivo portátil com conexão wi-fi, para análise em campo e em tempo real.	■	■	■	■
Relatórios, publicações e participações em eventos.	■	■	■	■
Solicitação de bolsa BEPE.		■		

Referencias

1. Barfi, B.; Asghari, A.; Rajabi, M.; Barfi, A.; Saeidi, I. ;*J. Chromatogr. A* **2013**, *1311*, 30.
2. Pereira, R. M. S.; López, B. G.-C.; Diniz, S. N.; Antunes, A. A.; Moreno Garcia, D.; Rocha Oliveira, C.; Marcucci, M. C. ;*Agric. Sci.* **2017**, *08*, 631.
3. Molina-Calle, M.; Priego-Capote, F.; Luque De Castro, M. D. ;*Talanta* **2015**, *144*, 349.
4. Marozzi, C. A.; Chialvo, A. C. ;*Electrochim. Acta* **2000**, *45*, 2111.
5. Yu, X.; Wang, M.; Wang, Z.; Gong, X.; Guo, Z. ;*Appl. Surf. Sci.* **2016**, *360*, 502.
6. Herraiz-Cardona, I.; Ortega, E.; Vázquez-Gómez, L.; Pérez-Herranz, V. ;*Int. J. Hydrogen Energy* **2012**, *37*, 2147.
7. Abdullah, A. A.; Yardım, Y.; Şentürk, Z. ;*Talanta* **2018**, *187*, 156.
8. Wu, J.; Wang, L.; Wang, Q.; Zou, L.; Ye, B. ;*Talanta* **2016**, *150*, 61.
9. Rossiter, B. W.; Hamilton, J. F. *Physical methods of chemistry*; 1986.
10. Laviron, E. ;*J. Electroanal. Chem.* **1979**, *101*, 19.
11. Bard, A. J.; Faulkner, L. R. *Electochemical Method: Fundamentlas and Applications*; 2nd ed.; Wiley, 2000.
12. Anson, F. C. ;*Anal. Chem.* **1964**, *36*, 932.
13. Zhupanova, A.; Guss, E.; Ziyatdinova, G.; Budnikov, H. ;*Anal. Lett.* **2020**, *53*, 2170.
14. Ferreira, R. D. Q.; Greco, S. J.; Delarmelina, M.; Weber, K. C. ;*Electrochim. Acta* **2015**, *163*, 161.
15. Enache, T. A.; Oliveira-Brett, A. M. ;*J. Electroanal. Chem.* **2011**, *655*, 9.
16. Ferreira, M.; Varela, H.; Torresi, R. M.; Tremiliosi-Filho, G. ;*Electrochim. Acta* **2006**, *52*, 434.
17. Xing, T.-L.; Wang, F.; Mao, Y.-Y.; Wang, L.-P.; Ye, B.-X. ;*J. Chinese Chem. Soc.* **2009**, *56*, 303.
18. YANG, B.; ARAI, K.; KUSU, F. ;*Anal. Sci.* **2001**, *17*, 987.
19. Ziyatdinova, G.; Yakupova, E.; Ziganshina, E.; Budnikov, H. ;*Electroanalysis* **2019**, *31*, 2130.
20. Sims, M. J.; Li, Q.; Kachoosangi, R. T.; Wildgoose, G. G.; Compton, R. G. ;*Electrochim. Acta* **2009**, *54*, 5030.
21. Laviron, E. ;*J. Electroanal. Chem.* **1979**, *101*, 19.
22. Cho, H. E.; Ahn, S. Y.; Kim, S. C.; Woo, M. H.; Hong, J.-T.; Moon, D. C. ;*Anal. Lett.* **2014**, *47*, 1299.
23. Seo, C.-S.; Shin, H.-K. ;*Appl. Sci.* **2020**, *10*, 1713.
24. Zhao, X. J.; Chen, D.; Kilmartin, P. A.; Jiao, B. N. ;*Anal. Lett.* **2019**, *52*, 1926.

APENDICE I

Tabela A1. Gradiente da eluição cromatográfico dos flavonoides.

t/min	% ACN + 0.1 % AF
0.01	20
14	50
14,5	100

ACN: Acetonitrila. AF: Ácido fórmico

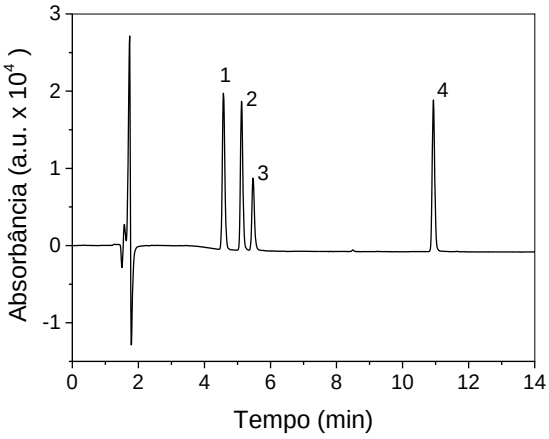

Fig.A1. Cromatograma dos padrões de (1) narirutina, (2) hesperidina, (3) naringina e (4) naringenina.

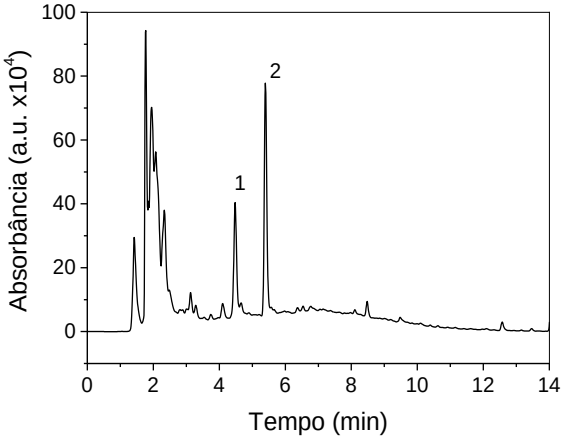

Fig.A2. Cromatograma da amostra de água amarela. Em (1) o tempo de retenção característico da narirutina e (2) da hesperidina.

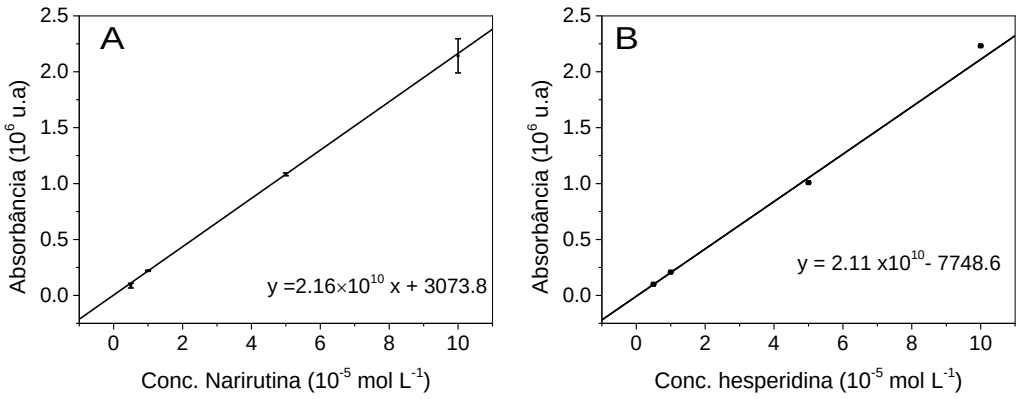

Fig.A3. Curva analítica para análise por HPLC obtida na faixa de $5{,}0 \times 10^{-6}$ mol L^{-1} - $1{,}0 \times 10^{-4}$ mol L^{-1} para (A) narirutina e (B) hesperidina.

Tabela A2. Determinação cromatográfica de narirutina e hesperidina em amostras de água amarela, (n = 3).

Molécula	Área do pico	Quantidade encontrada (10^{-5} mol L^{-1})
Narirutina		
1	1910512	8,8
2	1832054	8,4
3	1808043	8,3
Hesperidina		
1	3698884	17,4
2	3731592	17,6
3	3722160	17,6

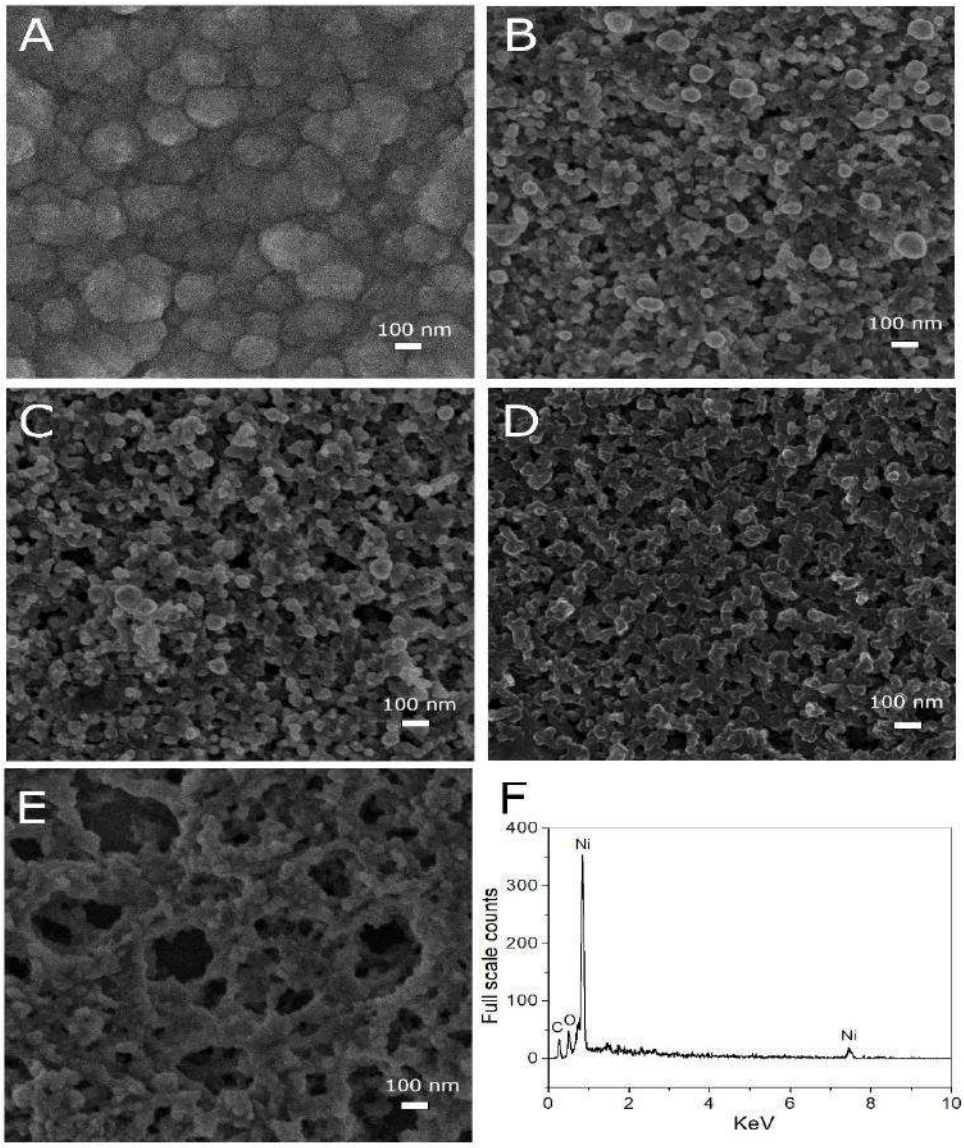

Fig.A4. FEG-SEM para (A) SPE e para 3DnpNi/SPE formada com a aplicação de densidade de corrente de: (B) 0,08, (C) 0,2, (D) 0,6 e (E) 0, 8 A cm^{-2}. Ampliação 50.000 x. Em (F) EDS relacionado à imagem D.

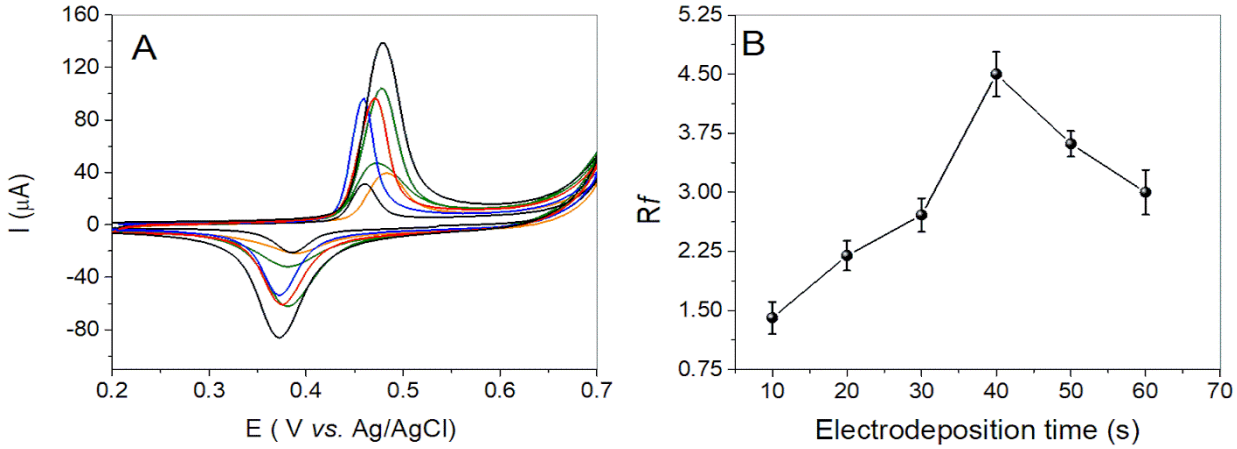

Fig.A5. (A) CV para 3DnpNi/SPE em NaOH 0,1 mol L^{-1} na faixa de potencial de 0,2 a 0,7 V, υ = 50 mVs^{-1} para diferentes tempos de eletrodeposição. Em (B), o fator de rugosidade para cada um dos tempos estudados, entre 10 e 60 s.

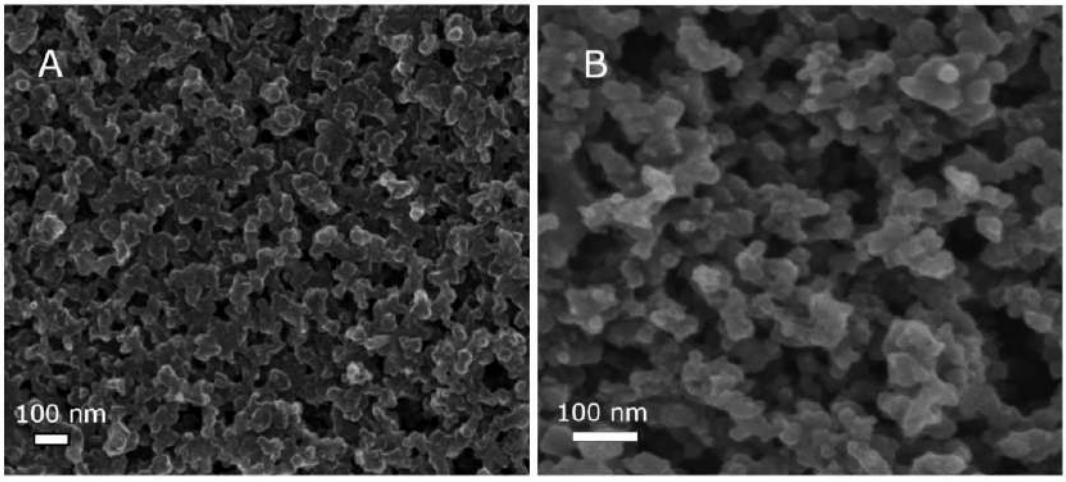

Fig.A6. FEG-SEM para 3DnpNi/SPE com ampliação (A) 50.000 e (B) 100.000.

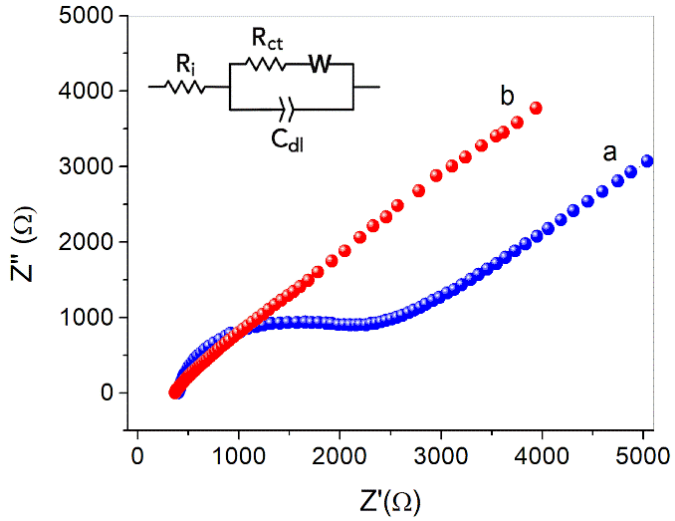

Fig.A7. Gráfico de Nyquist para (a) SPE e (b) 3DnpNi/SPE em 5,0 × 10^{-3} mol L^{-1} de Fe $(CN)_6^{3-/4-}$ em 0,1 mol L^{-1} de KCl na faixa de frequência de 0,1 Hz a 100 kHz. Inserção: circuito equivalente usado para análise dos dados de impedância.

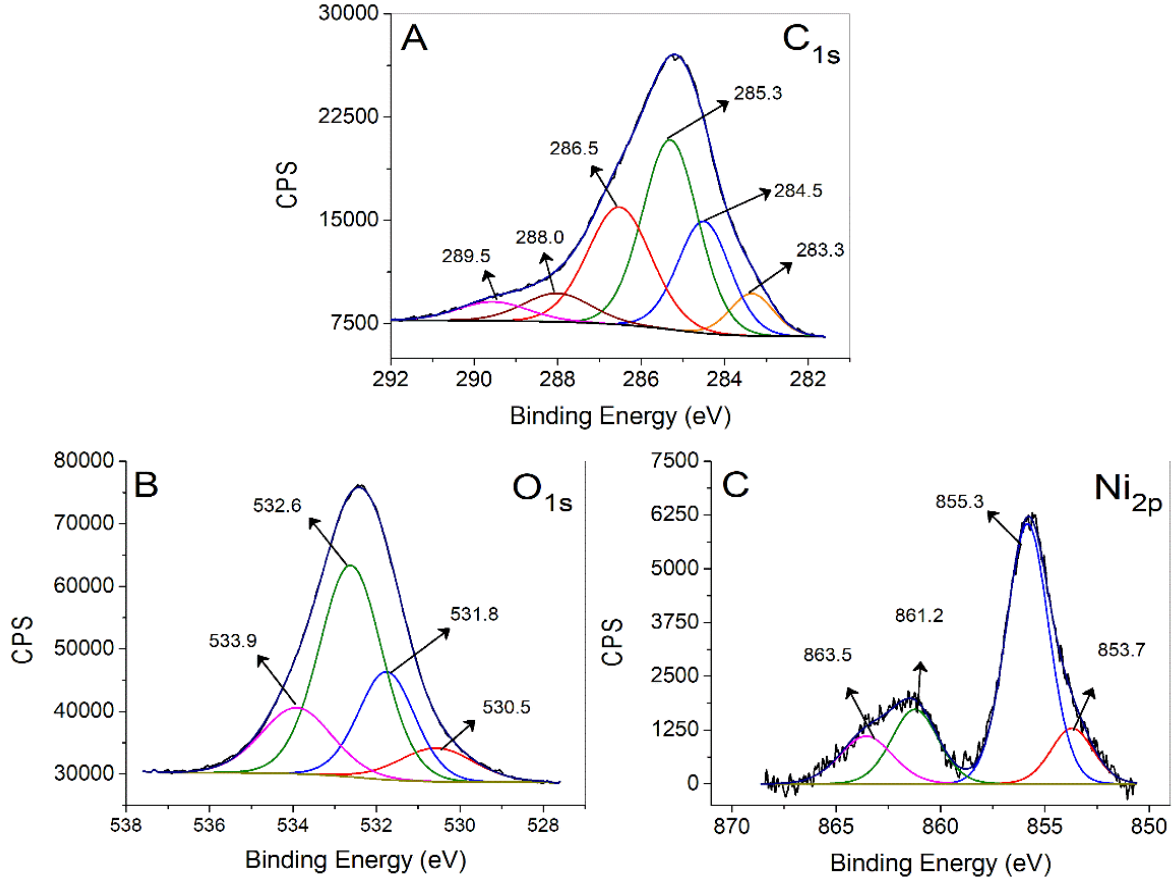

Fig.A8. Espectros de XPS para (A) C1s, (B) O1s e (C) Ni_{2p} referente a superfície do 3DnpNi/SPE.

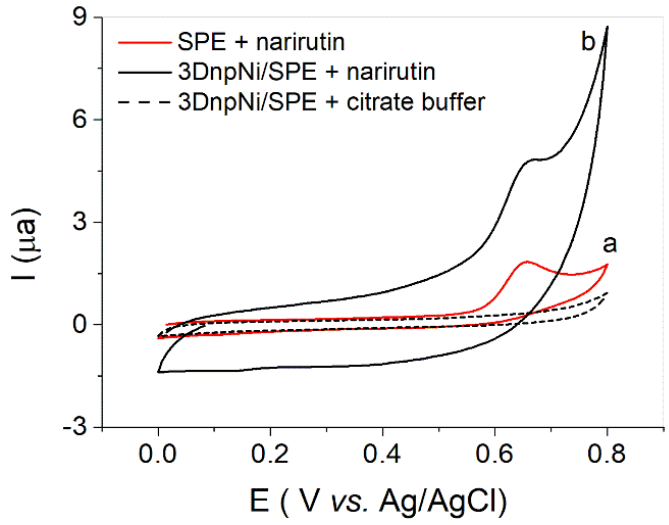

Fig.A9. CV de 1,0 × 10^{-5} mol L^{-1} de narirutina em solução tampão citrato pH 4,0, em (a) SPE e (b) 3DnpNi/SPE. Em (c) SPE somente em eletrólito de suporte. υ= 50 mV s^{-1}.

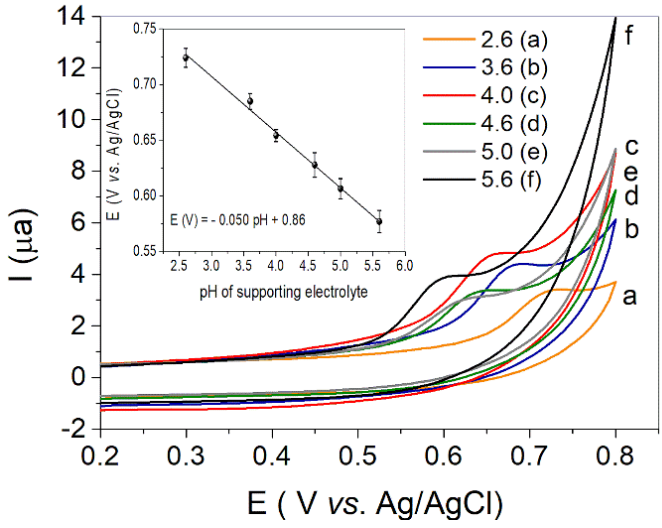

Fig.A10. CVs de 3DnpNi/SPE em solução contendo 1,0 × 10^{-5} mol L^{-1} de narirutina preparada em tampão de citrato 0,1 mol L^{-1} em diferentes valores de pH (2,6 a 5,6), υ = 50 mV s^{-1}. Inserção: Gráfico do potencial anódico da narirutina *versus* pH.

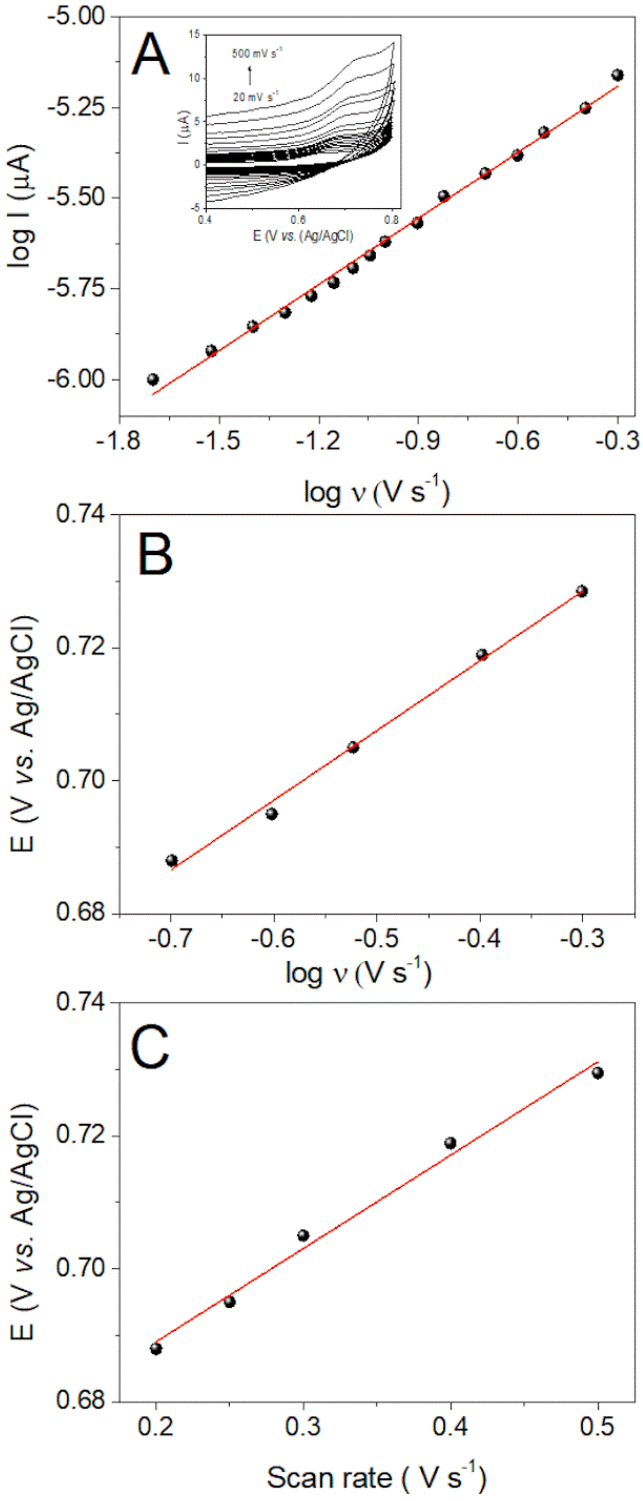

Fig.A11. (A) Dependência de log I (A) com log υ. Inserção: gráfico de corrente de oxidação de 1,0 × 10^{-5} mol L^{-1} de narirutina *versus* a velocidade de varredura em solução tampão de citrato (pH 4,0), entre 20 - 500 mV s^{-1}. (B) Relação entre o potential de pico *E* de 5,0 × 10^{-5} mol L^{-1} de narirutina e log υ. (C) Relação entre *E versus* υ. υ = 200 - 500 mV s^{-1}.

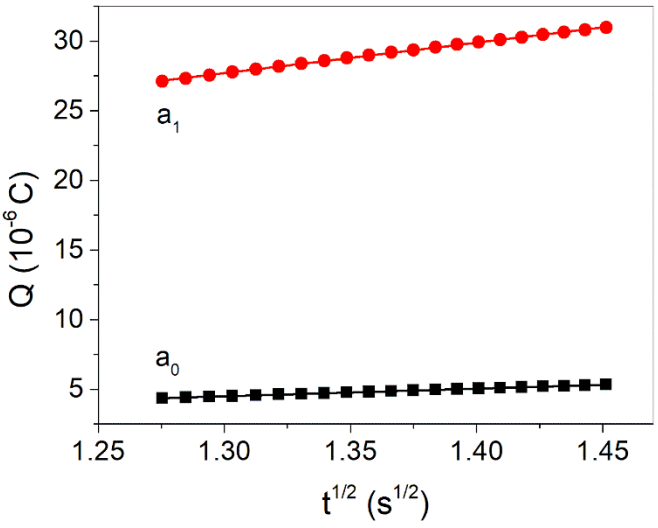

Fig.A12. Gráfico de Q versus $t^{1/2}$ para os experimentos cronocoulométricos realizados em solução tampão de citrato (pH 4,0) na ausência (a0) e na presença (a1) de 1,0 × 10^{-5} mol L^{-1} de narirutina. Potencial aplicado de 0,65 V.

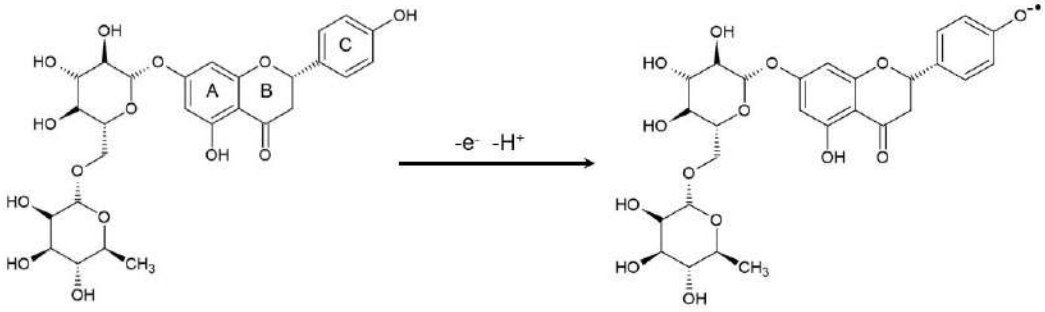

Esquema A1. Mecanismo proposto para eletrooxidação da narirutina.

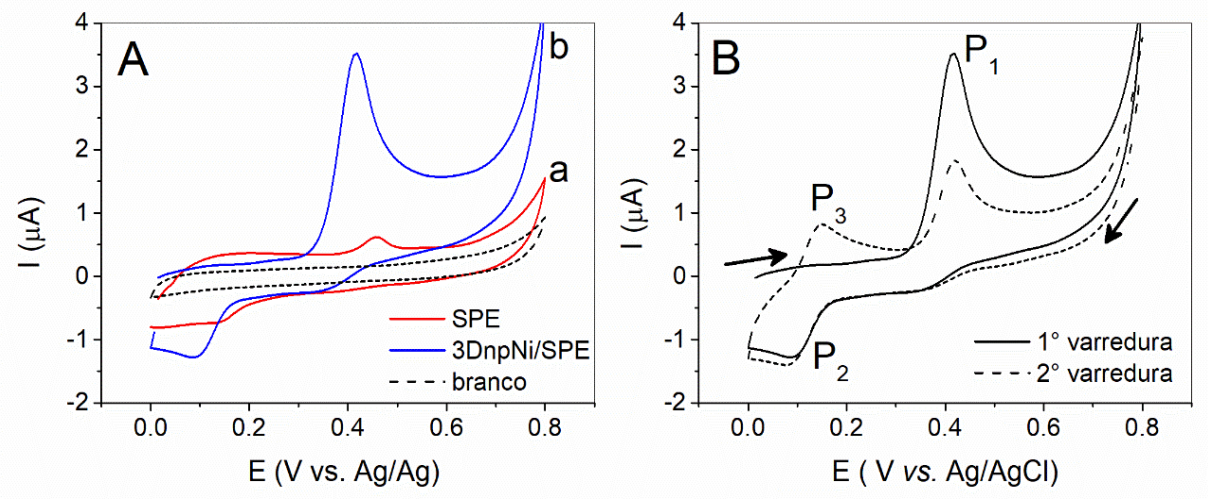

Fig.A13. (A) Voltamograma cíclico de 1,0 × 10^{-4} mol L^{-1} de hesperidina em SPE (curva a) e em 3DnpNi/SPE (curva b) em solução de 0,1 mol L^{-1} tampão citrato (pH 4,0). (B) Primeira e segunda varredura cíclica de hesperidina em 3DnpNi/SPE. υ = 50 mV s^{-1}.

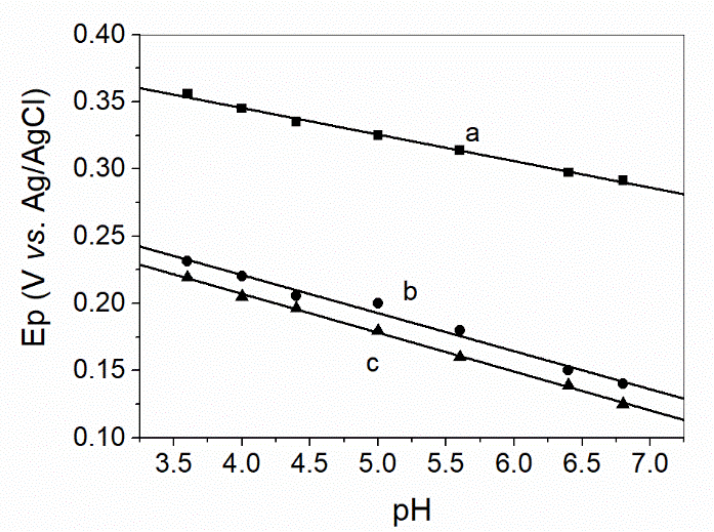

Fig.A14. Gráfico do potencial anódico da hesperidina *versus* pH para curva a (P_1), curva b (P_2) e curva c (P_3).

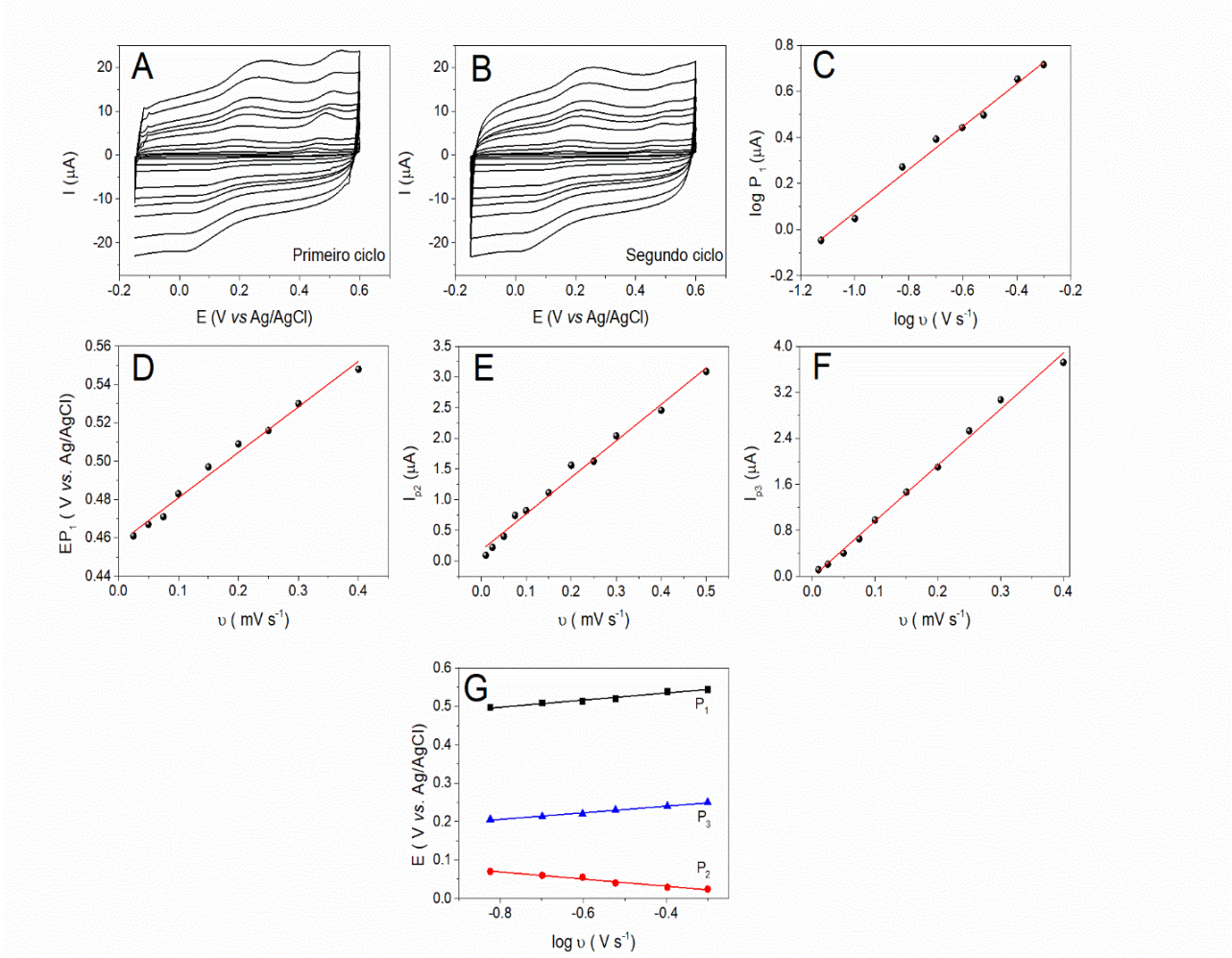

Fig.A15. (A) Primeiro e (B) segundo ciclo do CV de 5,0 × 10^{-5} mol L^{-1} de hesperidina em solução tampão citrato (pH 4,0), entre 10 - 500 mV s^{-1}. (C) Dependência de log P_1 com log υ. (D) Relação entre o potencial de pico EP_1 e υ. Relação da corrente de pico para (E) IP_2 e (F) IP_3 versus υ. (G) Dependência entre E vs. logυ para cada pico.

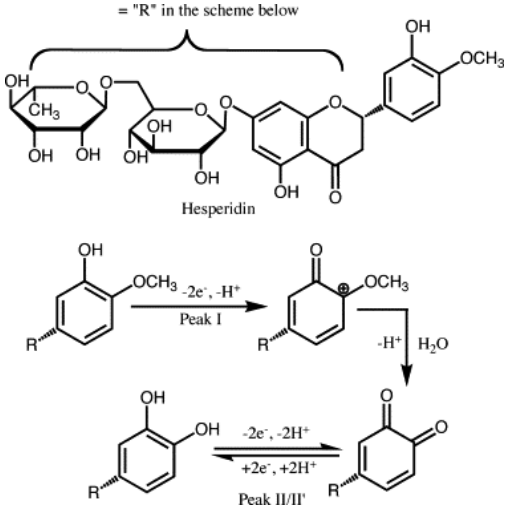

Esquema A2. Mecanismo $EC_{irrev}E$ da hesperidina proposto por Compton et al., [14] para explicar os picos observados por voltametria cíclica.

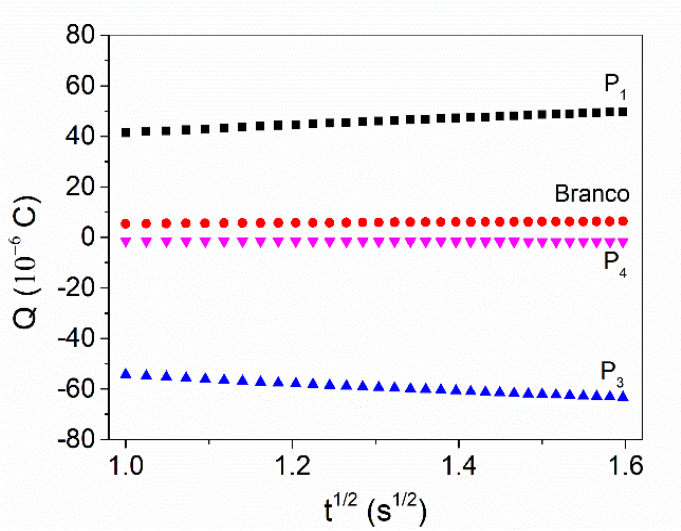

Fig.A16. Gráfico de Q *versus* $t^{1/2}$ para os experimentos cronocoulométricos realizados em solução tampão citrato (pH 4,0) na ausência (branco) e na presença de hesperidina ($1,0 \times 10^{-5}$ mol L^{-1}) para os picos P_1, P_2 e P_3.

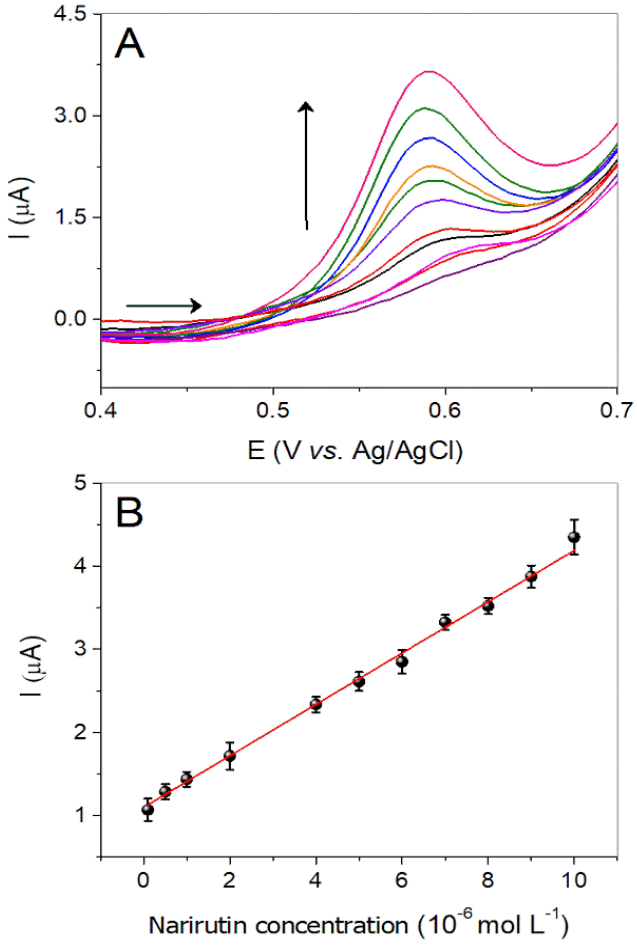

Fig.A17. (A) Curvas de DPV em diferentes concentrações de narirutina ($1,0 \times 10^{-7}$ mol L^{-1} a $1,0 \times 10^{-5}$ mol L^{-1}), obtidas em 3DnpNi/SPE em solução tampão de citrato 0,1 mol L^{-1} (pH 4,0). (B) Respectiva curva de calibração da corrente *versus* concentração de narirutina.

Tabela A3. Comparação entre o método desenvolvido em 3DnpNi/SPE e outros métodos analíticos relatados para a determinação de narirutina.

Técnica Analítica	Faixa linear (mol L^{-1})	LOD (mol L^{-1})	Ref.
HPLC-PDA	$3.45 \times 10^{-5} – 1.38 \times 10^{-3}$	1.21×10^{-5}	[9]
HPLC-UV	$2.43 \times 10^{-7} – 2.82 \times 10^{-4}$	8.06×10^{-8}	[8]
HPLC-ESI-MS	$3.45 \times 10^{-9} – 1.72 \times 10^{-6}$	1.72×10^{-9}	[12]
HPLC-PDA	$1.34 \times 10^{-6} – 8.61 \times 10^{-5}$	2.93×10^{-7}	[10]
LC–MS/MS	$1.72 \times 10^{-8} – 1.72 \times 10^{-5}$	8.63×10^{-10}	[10]
UPLC–PDA	$1.72 \times 10^{-7} – 1.72 \times 10^{-5}$	2.87×10^{-8}	[67]
HPLC–PDA	$1.34 \times 10^{-6} – 8.61 \times 10^{-5}$	8.61×10^{-8}	[11]
UHPLC-QqQ-MS	$1.05 \times 10^{-8} – 5.70 \times 10^{-6}$	3.45×10^{-9}	[13]
LC	$3.45 \times 10^{-4} – 1.72 \times 10^{-7}$	4.12×10^{-8}	[68]
3DnpNi/SPE	$1.00 \times 10^{-7} – 1.00 \times 10^{-5}$	3.96×10^{-8}	-

HPLC: high-performance liquid chromatographic; UV: ultraviolet; ESI: electrospray ionization; MS: mass spectrometry; UHPLC-QqQ-MS: ultra-high performance liquid chromatography coupled with triple-quadrupole mass spectrometry; PDA: photodiode array detector; UPLC: ultra-performance liquid chromatography; LC: liquid chromatography.

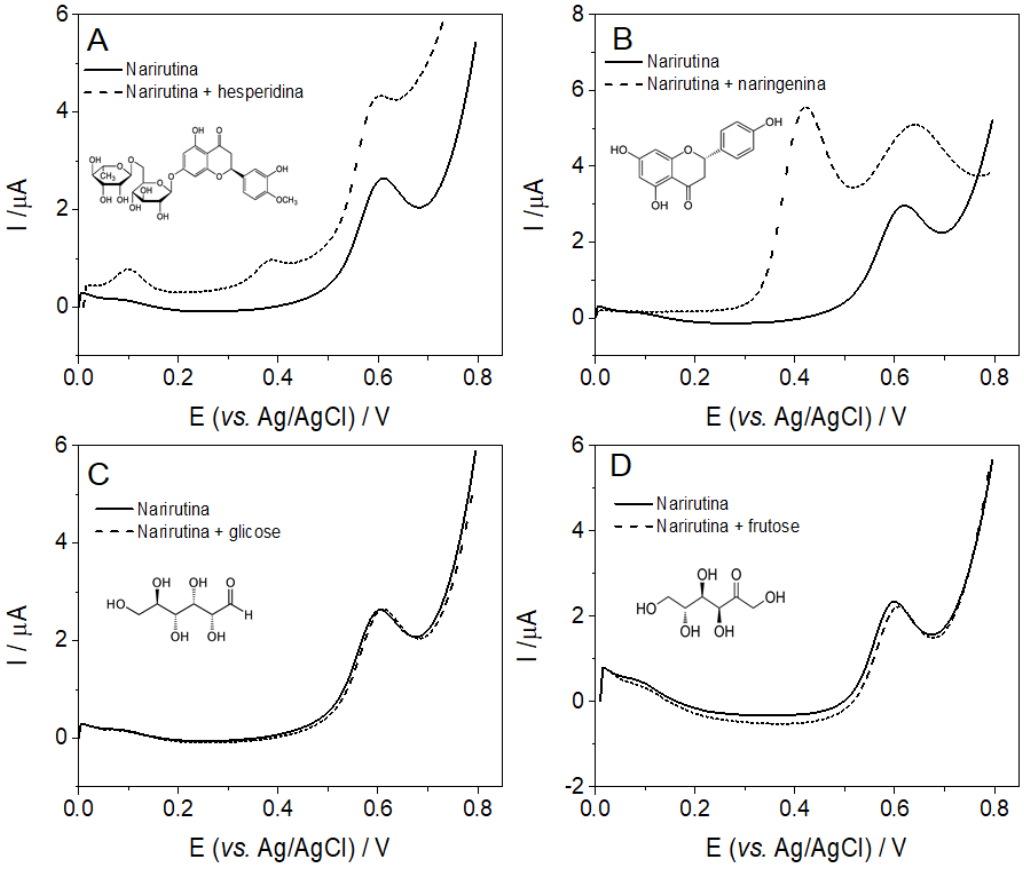

Fig.A18. Efeito dos possíveis interferentes (A) hesperidina, (B) naringenina, (C) glicose e (D) frutose, na resposta por DPV para a determinação de 1,0 × 10^{-6} mol L^{-1} de narirutina em solução tampão citrato 0,1 mol L^{-1} (pH 4,0). A taxa de concentração da solução interferente foi 1:10 (narirutina: interferente), usando 3DnpNi/SPE.

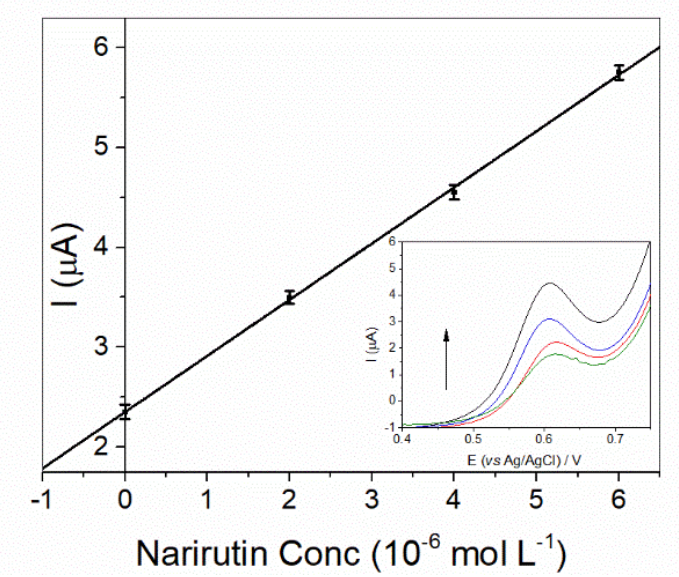

Fig A19. Relação linear entre o pico de corrente *versus* concentração adicionada de narirutina de 2,0 × 10^{-6} mol L^{-1} a 6,0 × 10^{-6} mol L^{-1}. Insert: DPVs correspondentes.

Tabela A4. Determinação de narirutina em amostras de água amarela (n=3).

Quantidade Adicionada (10^{-6} mol L^{-1})	Quantidade encontrada (10^{-6} mol L^{-1})	Recuperação (%)	RSD (%)
2,0	2,0 ± 0,1	101.6± 6.7	6,6
4,0	3,9 ± 0,1	98,4 ± 3,0	3,0
6,0	5,9 ± 0,03	99,8 ± 0,6	0,57

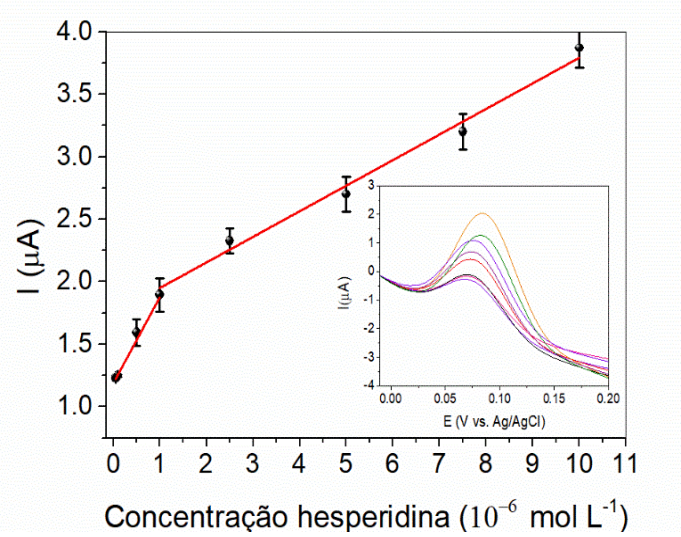

Fig.A20. Curva de calibração corrente *versus* concentração de hesperidina na faixa de 5,0 × 10^{-8} mol L^{-1} a 1,0 × 10^{-5} mol L^{-1}. Insert: Curvas de SWV em diferentes concentrações obtidas em 3DnpNi/SPE.

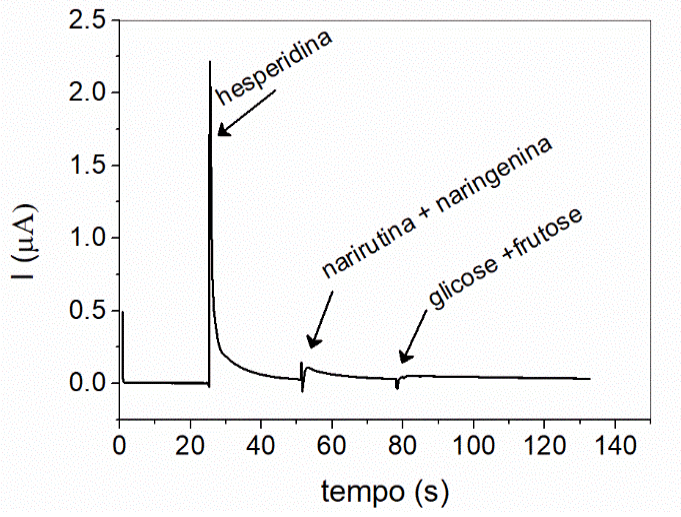

Fig.A21. Croanoamperometria para estudo da seletividade da hesperidina. Potencial aplicado de 0.075 V durante 130 s com adição de 1,0 ×10^{-5} mol L^{-1} de hesperidina no tempo de 20s, narirutina e naringenina no tempo de 50 s e frutose e glicose aos 80 s.

Tabela A5. Determinação de hesperidina em amostras de água amarela (n=3).

Quantidade Adicionada (10^{-6} mol L^{-1})	Quantidade encontrada (10^{-6} mol L^{-1})	Recuperação (%)	RSD (%)
1,0	0,96 ± 0,11	96 ± 11	11
5,0	5,6 ± 0,035	113 ± 1,3	1,3
10	9,6 ± 0,071	96,5 ± 0,71	0.73

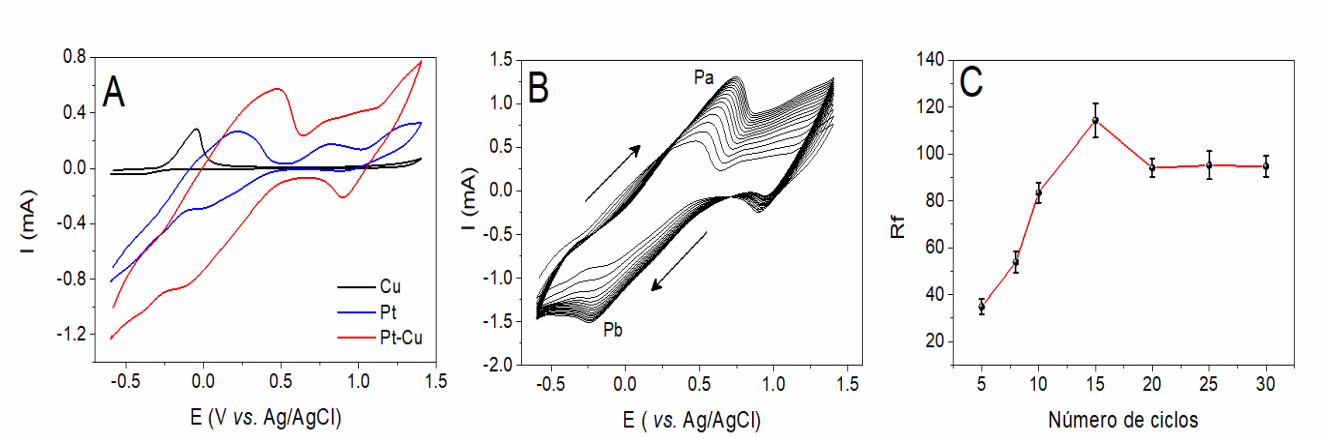

Fig.A22. (A) Curvas de CV para Cu. Pt e Pt-Cu em meio de 0,5 mol L^{-1} H_2SO_4, υ = 50 mV s^{-1}. (B) Sucessivos voltamogramas cíclicos durante a formação do 3DnpPt/SPE**.** (C) Gráfico do R*f* do eletrodo modificado em relação ao número de ciclos da liga de Pt-Cu.

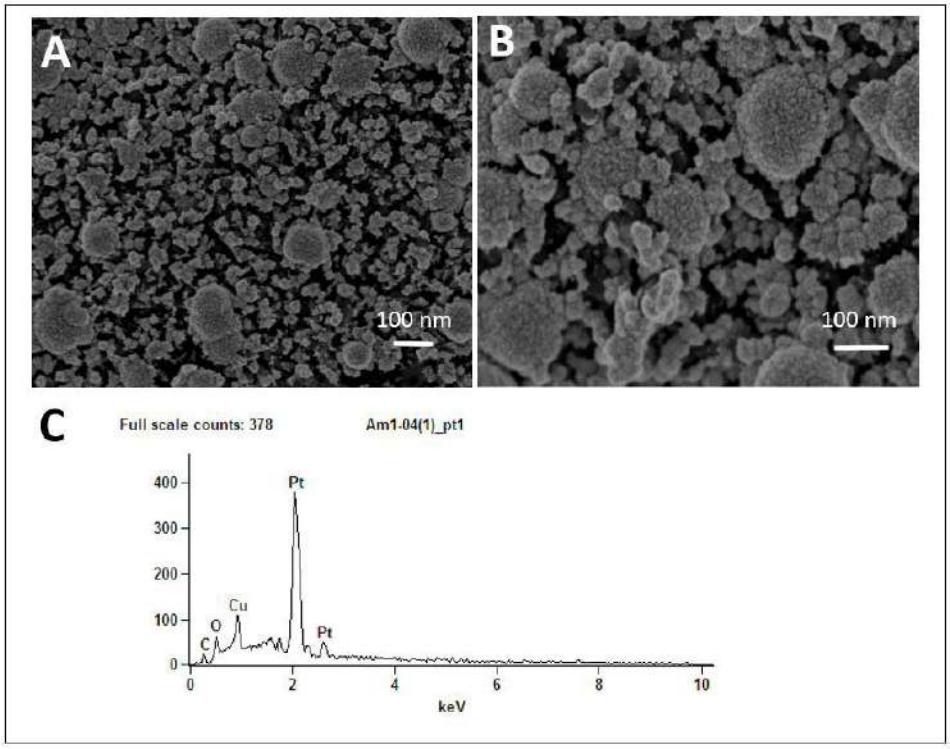

Fig.A23. FEG-SEM para 3DnpPt/SPE (A) Ampliação 50.000 x (B) 100.000 x e (C) EDS relacionado à imagem B.

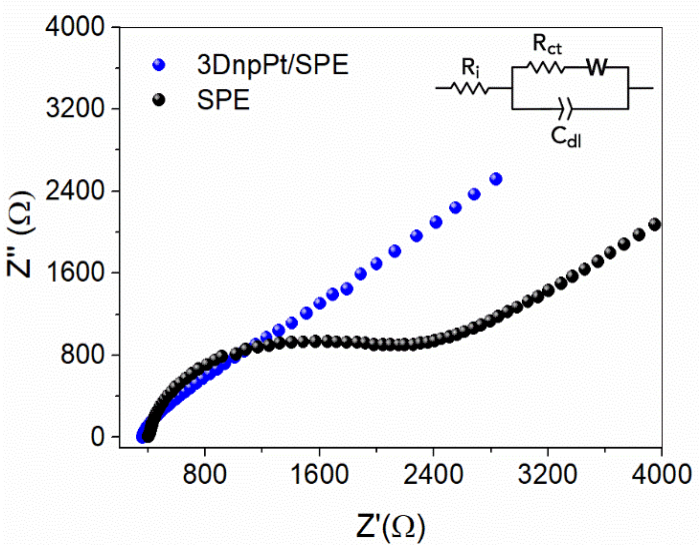

Fig.A24. Gráfico de Nyquist para (a) SPE e (b) 3DnpPt/SPE em 5,0 × 10^{-3} mol L^{-1} de $Fe(CN)_6^{3-/4-}$ em 0,1 mol L^{-1} de KCl na faixa de frequência de 0,1 Hz a 100 kHz.

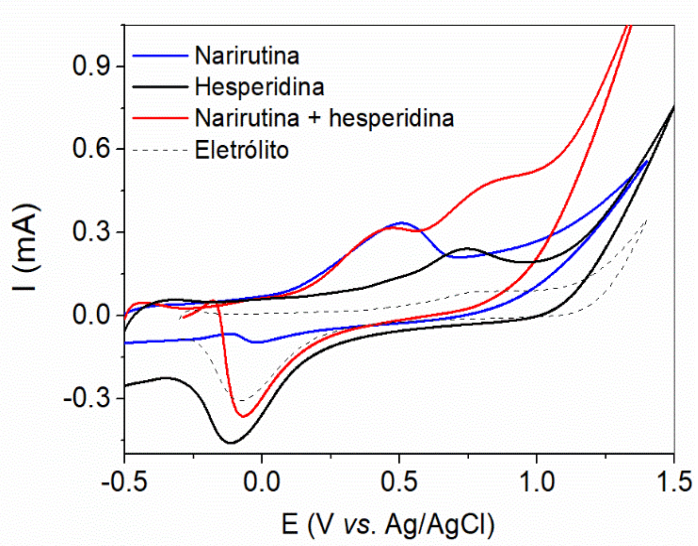

Fig.A25. CVs para 5,0 × 10^{-5} mol L^{-1} de narirutina, hesperidina e solução contendo ambas, em solução de 0,1 mol L^{-1} tampão citrato (pH 4,0). υ = 50 mV s^{-1}.

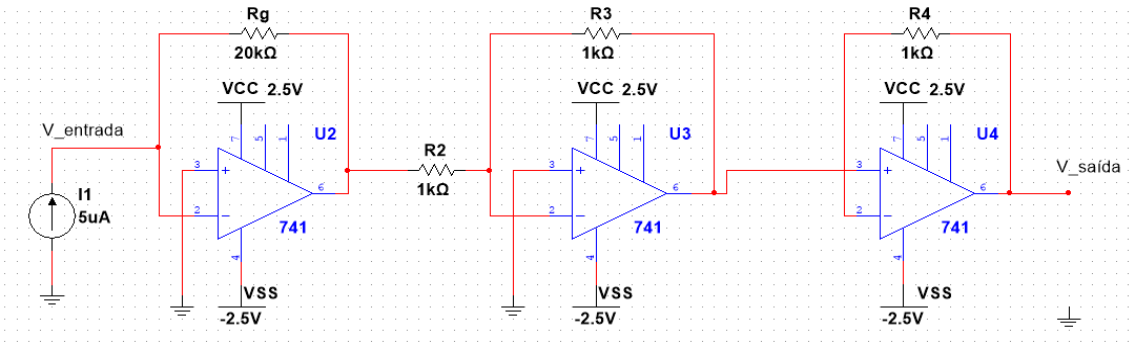

Fig.A26. Circuito de amplificação montado no software de simulação com LM741.

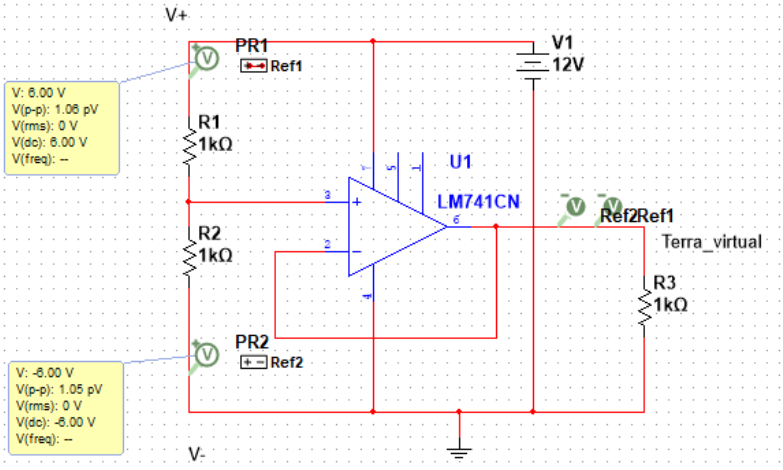

Fig.A27. Circuito gerador de tensão simétrica montado no software de simulação.

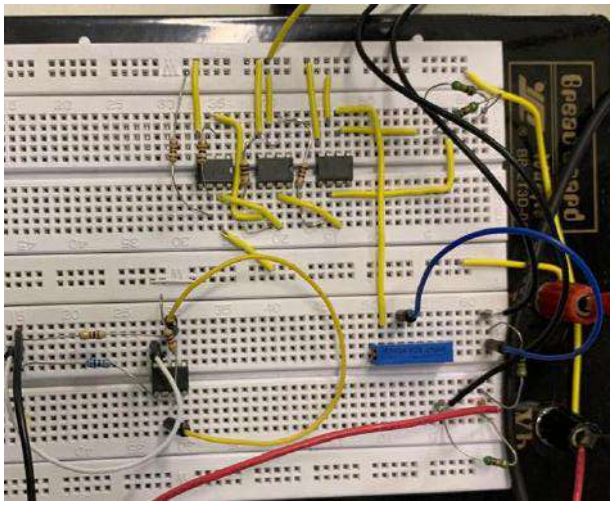

Fig.A28. Circuitos de amplificação e geração de tensão simétrica conectados.

6) Participação em evento científico.

[1] Beluomini, M.A.; Karimian, N.; Zanoni, M. V. B.; Stradiotto, N. R.; Ugo, P. Determinação de polióis em eletrodo modificado com nanopartículas de cobre em grafeno por técnicas voltamétricas**.** XXII Simpósio Brasileiro de Eletroquímica e Eletroanalítica, 2019. Ribeirão Preto, Brasil.

[2] Beluomini, M.A. Participação na “Bath Electrochemical Winter School”, 2020. Bath. Reino Unido.

[3] Beluomini, M.A.; Buffon, E.; Falone, M.; Stradiotto, N.R.; Boldrin, M.V. Sensores para Resíduos de Fruto-Refinarias. II Workshop INCT-DATREM, 2020. Araraquara. Brasil.

[4] Beluomini, M.A participação online no "I Fronteiras em eletroquímica e eletroanalítica: avanços realizados por jovens cientistas". 2020.

[5] Beluomini, M.A.; Stradiotto, N.R.; Boldrin, M.V. Seletiva determinação de hesperidina em eletrodo nanoporoso tridimensional de níquel para determinação de hesperidina em águas residuais da indústria cítrica. Submetido ao XXIV Congresso de La Sociedad Iberoamericana de Electroquímica. Evento Virtual que ocorrerá em novembro de 2020.

Tailor-made 3D-gold nanoelectrode ensembles modified with molecularly imprinted polymer for the detection of L-arabitol

M. A. Beluomini [1,2*], N. Karimian[2], M. V. B. Zanoni[1], N. R. Stradiotto[1], P. Ugo[2]

[1]São Paulo State University, Rua Prof. Francisco Degni 55, Araraquara- SP, Brazil.
[2] University Ca' Foscari of Venice, via Torino 155, Venice, Italy.

Abstract: L-arabitol is classified as one of the top 12 biomass-derivable building block chemicals, with low-calorific, low-glycemic, anticariogenic, and prebiotic character. In humans, abnormal concentrations of arabitol indicate the existence of infections by *Candida spp*. or other pathological conditions. The sensor reported here aims to decentralize analysis (on-site process control or patient bed-side monitoring) and improving the analytical performances for L-arabitol determination. For this, a sensor was developed combining the advantages of 3D nanostructured electrodes, namely, 3D-ensembles of gold nanowires (3DNEE), with the recognition capability of molecularly imprinted polymer (MIP). The MIP process involves the polymerization of functional monomers in the presence of the analyte which acts as template. The monomer should interact with the analyte during the polymerization, and after that, subsequent template extraction from the polymer network leaves cavities able to capture the target molecule. As a substrate for electropolymerization, gold nanowires were grown inside polycarbonate membranes (PC) with 80 nm pore diameter. PC was used for the electroless preparation of nanoelectrode ensembles (NEEs), as previously described [1]. Briefly, the PC was immersed in an Au plating bath for electroless deposition for 24 h. After this period, the golden membrane was washed with water and dried. The metallized membrane is sealed with an insulating film in which it contains a circular hole with a diameter of 2.1 mm (geometric area of NEE). For obtaining the 3DNEEs, NEEs were dipped in 9:1 (*v/v*) CH_2Cl_2/ethanol as etching agent for dissolution of PC membrane and exposure of 3D-nanowires. The analytical measurements were performed in a conventional three electrodes cell, with an Ag|AgCl|KCl_{sat} reference electrode, Pt wire auxiliary and 3DNEE as working electrode. The electropolymerization on 3DNEEs was carried out in acetate buffer (0.2 M, pH=4.8), containing 1.0 mM L-arabitol and 2.0 mM o-phenylenediamine, for 30 cycles between -0.4 and 1.0 V, υ= 50 mV s^{-1}. To remove the L arabitol template from the polymer matrix, MIP was washed with ethanol/water 70% (*v/v*). The sensor was characterized by scanning electron microscopy and dispersive energy X-ray spectroscopy while its electrochemical properties are examined by cyclic voltammetry (CV), differential pulse voltammetry (DPV) and electrochemical impedance spectroscopy (EIS). Analytically signals were obtained using the ferrocenyl methytrimethylammonium cation (FA^+) as an electroactive probe by competing for the binding sites with L-arabitol. The linear range was 1.0 to 150.0 nM, with LOD of 0.75 nM and LOQ of 2.5 nM. The sensor showed considerable reproducibility with 5.7 % RSD (n=3) and high stability (after 12 days the sensor kept 82% of the initial sensitivity). The selectivity factor was 2.5-fold higher for L-arabitol in comparison with interfering molecules. The applicability of the MIP/3DNEE in real samples was demonstrated by successfully quantifying L-arabitol in sugarcane vinasse ($2.96 \pm 0.03 \times 10^{-4}$ g L^{-1}). This can open the way to further studies aimed at exploring the MIP/3DNEE.

Acknowledgments: FAPESP (2018/12131-6 and 2014/23846-5), Capes/PDSE, São Paulo State University and University Ca'Foscari of Venice.

References:

[1] M. A. Beluomini, et al., *Sensors & Actuators: B. Chemical* 284 (2019) 250–257.

* **e-mail:** maisa.beluomini@unesp.br

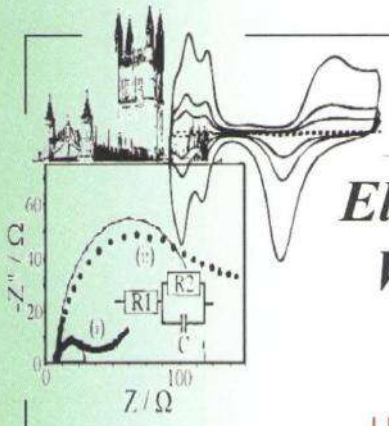

Bath Electrochemistry Winter School 2020

University of Bath

Certificate of Completion

is hereby granted to

Maisa Beluomini

to certify that he/she has completed the following course

Electrochemical Theory and Practical Applications 2020

Granted: 17th January 2020

Professor Frank Marken,
Course Director

Área: Sensores

Sensores para Resíduos de Fruto-Refinarias

Maísa Beluomini Azevedo[1] (PQ), Edervaldo Buffon[1] (PG), Max Fabrício Falone[1] (PG), Nelson Ramos Stradiotto (PQ),[1,2] Maria Valnice Boldin (PQ)[1] *mabeluomini@gmail.com

[1]Instituto de Química, UNESP; [2]Instituto de Pesquisa em Bioenergia (IPBEN)
Palavras-Chave: *Laranja, Banana, Goiaba, Ácidos Fenólicos, Flavonoides, Sensores Eletroquímicos.*

Resumo

A Fruticultura é um dos setores mais lucrativos da economia brasileira, contribuindo significativamente para produção de frutas frescas, produção e exportação de alimentos industrializados (sucos, doces, geleias e outros) e geração de empregos em toda sua cadeia produtiva. Entretanto, o beneficiamento de frutas é gerador de quantidades elevadas de resíduos, que, por sua vez, contribui para o agravamento da problemática ambiental. Entre as principais frutas produzidas no Brasil, são destaques laranja, banana e goiaba, sendo a laranja responsável por 39,7% de toda a produção nacional, seguida pela banana com cerca de 7.1 milhões de toneladas. Além disso, a goiaba também se destaca com 360 mil toneladas por ano [1]. Nos últimos anos, o estado de São Paulo produziu cerca de 13.275.125 toneladas de frutas cítricas, onde a laranja correspondeu aproximadamente 90% desse total. Além disso, a produção de banana e goiaba atingiu 1.2 milhões e 136.9 mil toneladas, respectivamente. No cenário mundial, cerca de 36% da produção de frutas é transformada em suco, entretanto, no caso de grandes produtores, como Brasil e Estados Unidos, essa porcentagem chega a 96%, levando a geração de um grande volume de resíduos, tais como casca, polpa, sementes, folhas e frutas que não atingiram os requisitos de qualidade. Estes resíduos, na maioria das vezes, são descartados no solo em áreas adjacentes aos locais de produção, aterros sanitários, ou até mesmo queimados para co-geração de energia. No entanto, os resíduos da fruticultura possuem uma composição rica em ácidos fenólicos, tais como ácidos ferúlico, gálico, cafeico, vanílico e p-cumárico, e flavonoides como hesperidina e narirutina. Assim, dentro do contexto de biorrefinarias, esses compostos podem ser utilizados pelas indústrias farmacêuticas, comésticas e alimentícias para obtenção de produtos com maior valor agregado. Neste contexto, é essencial que esses resíduos sejam caracterizados para posterior reutilização e melhor reaproveitamento. Os sensores eletroquímicos são dispositivos simples, sensíveis, seletivos, portáteis e de baixo custo, o que viabiliza sua utilização para determinação de compostos de interesse em matrizes complexas, como resíduos oriundos da fruticultura. Para aumentar a sensibilidade dos métodos eletroanalíticos, a superfície de eletrodos tem sido modificada com materiais nanoestruturados, tais como óxido de grafeno reduzido, nanopartículas e nanoporos metálicos. Estes nanomateriais apresentam baixo custo, elevada condutividade térmica e elétrica, bem como excelente estabilidade térmica e mecânica. Adicionalmente, a seletividade dos métodos analíticos tem sido aprimorada pela incorporação de polímeros molecularmente impressos às superfícies eletródicas. Estes polímeros são materiais sintéticos capazes de reconhecer seletivamente a molécula de interesse em uma matriz complexa. Neste sentido, o objetivo deste trabalho é apresentar metodologias eletroanalíticas baseadas em nanomateriais para caracterização dos resíduos da fruticultura, com o intuito de proporcionar a estes substratos um destino mais rentável e ambientalmente amigável. Os eletrodos impressos são dispositivos portáteis que permitem a realização de análise *in situ*. Dessa maneira, esses eletrodos foram utilizados para o desenvolvimento de dois métodos eletroanalíticos. No primeiro, a superfície eletródica foi modificada com óxido de grafeno reduzido, nanopartículas de ouro e um polímero molecularmente impresso de polifenol para detecção e quantificação de ácido ferúlico em cascas de frutas. Além disso, para a determinação de hesperidina e narirutina nos resíduos líquidos da indústria cítrica, como por exemplo a água amarela, um eletrodo impresso foi modificado com nanoporos de níquel através de técnicas eletroquímicas de deposição, como o processo *dealloying*[2] e de geração de hidrogênio[3]. Após a construção dos sensores, um dispositivo portátil capaz de reconhecer o sinal de oxidação desses compostos e enviar o sinal via wi-fi foi desenvolvido. Estes métodos mostraram-se adequados para quantificação dos analitos de interesse nas matrizes propostas.

[1] B.B. KIST, Anuário brasileiro de horti&fruti 2019, Santa Cruz do Sul: Editora Gazeta Santa Cruz, 2018, 96.
[2] L. SUN et al., Fabrication of Nanoporous Nickel by Electrochemical Dealloying, Chem. Mater, 2004, 16, 3125-3129.
[3] C.A. Marozzi, A.C. Chialvo, Electrodeposited porous nickel electrodes. Electrochimica Acta, 2000, 45, 2111–2120.

Agradecimentos

Os autores agradecem ao INCT-DATREM, à CAPES e a FAPESP (Processos 2017/22401-8, 2019/13818-8 e 2018/12131-6).

Certificado
de participação

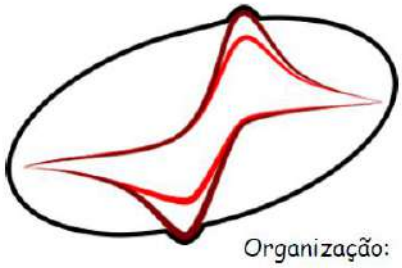

Certificamos que

Maisa Azevedo Beluomini

Participou do "I Fronteiras em eletroquímica e eletroanalítica: avanços realizados por jovens cientistas", realizado online, nos dias 16, 17, 24 e 25 de junho de 2020, perfazendo um total de 20 horas.

Bruno Campos Janegitz

Alex da Silva Lima

Organização:

Apoio:

Seletiva determinação de hesperidina em águas residuais da indústria cítrica usando eletrodos impressos modificados com nanoporos de níquel tridimensional.

Maísa Azevedo Beluomini[1], Nelson Ramos Stradiotto[1], Maria Valnice Boldrin[1]*
[1] Departamento de Química Analítica, Instituto de Química, Universidade Estadual Paulista (UNESP), Rua Prof. Francisco Degni, 55, Araraquara, São Paulo, Brasil. (10 pt. Arial, Cursiva)
e-mail: maisa.beluomini@unesp.br

A água amarela é um efluente gerado pela industria cítrica que pode causar impactos ambientais se lançado ao meio ambiente sem tratamento. Por outro lado, a presença de flavonóides, como a hesperidina, pode agregar valor ao efluente devido às suas propriedades anticâncer, antiviral (estudos demostram seu uso promissor no tratamento e prevenção de COVID-19) e antiinflamatório (1). Neste trabalho, o eletrodo impresso de carbono (SPE) foi modificado com nanoporos de níquel tridimensionais (3DnpNi/SPE) e utilizado para a determinação de hesperidina na água amarela. O eletrodo foi construído pelo método de geração de bolhas de hidrogênio, através da aplicação de densidade de corrente constante (0.6 A cm^{-2}) em uma solução contendo 0,01 mol L^{-1} de $NiCl_2$, 0,1 mol L^{-1} de NaCl e 0,2 mol L^{-1} de NH_4Cl. O 3DnpNi/SPE foi caracterizado por microscopia eletrônica de varredura (SEM), espectroscopia de energia dispersiva de raios-X (EDS), espectroscopia de fotoelétrons de raios-X (XPS), espectroscopia de impedância eletroquímica (EIS). Os resultados mostraram que os nanoporos foram distribuídos homogeneamente no SPE, apresentando diâmetros entre 70 - 120 nm. A oxidação da hesperidina no 3DnpNi/SPE foi consistente com o mecanismo $EC_{irrev}E$, apresentando dois picos anódicos e um pico catódico, atribuidos a oxidação eletroquímica irreversível da unidade guaiacol da molécula, com a formação do par *o*-benzoquinona/catecol quase reversível. Em comparação ao SPE, o 3DnpNi/SPE apresentou um aumento de 4 vezes na corrente de oxidação, o que pode ser atribuído a maior rugosidade da superficie. Para obtenção da curva analítica o par redox quase reversível foi avaliado por voltametria de onda quadrada (SWV), na faixa de -0.05 a 0,2 V, frequência de 15 Hz, amplitude e incremento de potencial de 25 mV. Duas faixas lineares foram obtidas, entre $5,0 \times 10^{-8}$ mol L^{-1} – $1,0 \times 10^{-6}$ mol L^{-1} e entre $1,0 \times 10^{-6}$ mol L^{-1} – $1,0 \times 10^{-5}$ mol L^{-1}. O LOD foi de $8,3 \times 10^{-9}$ mol L^{-1} e o LOQ de $2,8 \times 10^{-8}$ mol L^{-1}. A seletividade do eletrodo foi avaliada por cronoamperometria, no potencial de 0.075 V, na presença das moléculas de narirutina, naringenina, glicose e frutose. Os resultados indicaram excelente seletividade do 3DnpNi/SPE. Além disso, o 3DnpNi/SPE mostrou boa repetibilidade e estabilidade a longo prazo. A determinação de hesperidina na amostra foi realizada por adição padrão na faixa de $1,0 \times 10^{-6}$ mol L^{-1} a $1,0 \times 10^{-5}$ mol L^{-1}. A equação de regressão linear média foi I (μA) = $2,8 \times 10^{-5}$ $C_{hesperidina}$ + 1,9 e a concentração de hesperidina encontrada na água amarela foi de $15,4 \pm 2,19 \times 10^{-5}$ mol L^{-1} (n = 3). As porcentagens de recuperação variaram entre 96 % a 111 %, com RSD menor que 11 %, indicando que o método apresenta excelente precisão. Em comparação com a concentração de hesperidina encontrada pela técnica de cromatográfica liquida de alta eficiencia (CLAE/DAD), o RSD foi de 0,15 %, mostrando boa concordância entre as técnicas e confiabilidade do 3DnpNi/SPE para a determinação de hesperidina.

Referências

[1] A. Yusuf et al., Medical Hypotheses. 144 (2020) 11.

7) Lista das publicações resultantes no período a que se refere o Relatório Científico

[1] Moraes, T. M.; Beluomini, M.A., Stradiotto, N.R. Molecularly Imprinted Polypyrrole on Glassy Carbon Electrode Modified with Reduced Graphene Oxide and Gold Nanoparticles for Isoamyl Alcohol Analysis in Fusel Oil. J. Braz. Chem. Soc. 2020. https://dx.doi.org/10.21577/0103-5053.20200174

[2] Beluomini,M.A; Da Silva, J.L.; De Sá, A.C.; Buffon, E.; Pereira, T.C., Stradiotto,N.R. Electrochemical sensors based on molecularly imprinted polymer on nanostructured carbon materials: A review. Journal of electroanalytical Chemistry, v. 840, p. 343-366, 2019. https://doi.org/10.1016/j.jelechem.2019.04.005

8) Para as publicações listadas no item 7, inclua cópias das primeiras páginas.

https://dx.doi.org/10.21577/0103-5053.20200174

J. Braz. Chem. Soc., Vol. 00, No. 00, 1-11, 2020
Printed in Brazil - ©2020 Sociedade Brasileira de Química

Article

Molecularly Imprinted Polypyrrole on Glassy Carbon Electrode Modified with Reduced Graphene Oxide and Gold Nanoparticles for Isoamyl Alcohol Analysis in Fusel Oil

Thiago M. Mariano,[a] *Maísa A. Beluomini*[a] *and Nelson R. Stradiotto*[b,*]

[a]*Instituto de Química, Universidade Estadual Paulista (Unesp), 14800-060 Araraquara-SP, Brazil*

[b]*Instituto de Pesquisa em Bioenergia, Universidade Estadual Paulista (Unesp), 14800-060 Araraquara-SP, Brazil*

A molecularly imprinted electrochemical sensor for determination of isoamyl alcohol was successfully constructed by modifying the glassy carbon electrode (GCE) with gold nanoparticles (AuNPs) and reduced graphene oxide (RGO). The modification of the GCE increased the electron transfer rate and the electrode surface area, which, consequently, made more room available for the formation of the molecularly imprinted polymer (MIP). The development of the MIP on the modified surface was carried out via electropolymerization of the pyrrole in acetate buffer solution in the presence of the target molecule. The MIP-AuNPs-RGO/GCE showed low limit of detection (8.4×10^{-4} mol L^{-1}), satisfactory quantification range, amperometric sensitivity of 1.1 A L mol^{-1}, excellent reproducibility and stability. Even when in the presence of analogous molecules, the sensor exhibited excellent selectivity. These results suggest that the proposed sensor is suitable for the detection of isoamyl alcohol in fusel oil samples.

Keywords: molecularly imprinted polypyrrole, reduced graphene oxide, gold nanoparticles, isoamyl alcohol, fusel oil

Introduction

The search for alternative fuels has become inevitable and urgent in the deeply seek to reduce the environmental impacts associated with the use of fossil fuels. In this sense, bioethanol plants and their byproducts have grown significantly in recent years as vital alternatives for lessening the use and even replacing fossil fuels and other harmful chemical substances employed as sources of energy.[1] Bioethanol has proved to be economically useful in addition to being renewable. These are relevant features that explain the fact that it is being internationally marketed to satisfy countries with limited biomass resources.

The production of bioethanol generates byproducts such as fusel oil, obtained after fermentation and distillation of biomass, composed mainly of higher alcohols containing three or more carbon atoms, including isoamyl alcohol, isobutanol, propanol, butanol, among others.[2,3] The fact that higher alcohols present in fusel oil are considered natural products provides these alcohols high commercial values. Since these alcohols are high octane and low in exhaust gas emissions, they occupy an important place among alternative fuels. The separation of these compounds is regarded essentially important, since the market value of fusel oil is directly related to the amount of higher alcohols, especially of isoamyl alcohol. In a commercial plant, for example in Brazil, the yield of the fusel oil may vary from 1 to 11 L *per* 1000 L of alcohol produced, depending on the fermentation and distillation conditions as well as on the amount of nitrogen.[4]

Chromatographic methods are the predominant mechanism employed when it comes to the determination of fusel oil constituents in the literature. Pérez *et al.*[5] quantified fusel oil constituents by gas chromatography for alcohols and esters, and liquid chromatography for carbonyl compounds using fusel oil samples from 3 different plants. The isoamyl (390 g L^{-1}), isobutyl (158 g L^{-1}), ethyl (28.4 g L^{-1}), methyl (16.6 g L^{-1}) and *n*-propyl (11.9 g L^{-1}) alcohols represent approximately 77% of the fusel oil composition. Neale[6] used high performance liquid chromatography to determine ethanol, isoamyl alcohol, isobutyl alcohol and L-propanol in alcoholic beverages.

*e-mail: nrstradi@gmail.com

Journal of Electroanalytical Chemistry 840 (2019) 343–366

Contents lists available at ScienceDirect

Journal of Electroanalytical Chemistry

journal homepage: www.elsevier.com/locate/jelechem

Review

Electrochemical sensors based on molecularly imprinted polymer on nanostructured carbon materials: A review

Maísa Azevedo Beluomini[a], José Luiz da Silva[a], Acelino Cardoso de Sá[a], Edervaldo Buffon[a], Thulio César Pereira[a], Nelson Ramos Stradiotto[a,b,c,*]

[a] São Paulo State University (UNESP), Institute of Chemistry, Araraquara, São Paulo, CEP: 14800-060, Brazil
[b] Bioenergy Research Institute, São Paulo State University (UNESP), Rio Claro, São Paulo CEP: 13500-230, Brazil
[c] School of Industrial Metallurgical Engineering, Fluminense Federal University (UFF), Volta Redonda, Rio de Janeiro, CEP: 27255-125, Brazil

ARTICLE INFO

Keywords:
Molecularly imprinted polymer
Electrochemical sensor
Carbon nanotubes
Graphene
Fullerenes

ABSTRACT

This review provides a comprehensive overview of recent research on electrochemical sensors based on molecularly imprinted polymers (MIPs) on nanostructured carbon material surfaces for electrochemical detection. The combination of polymers and carbon nanomaterials for the development of electrochemical sensors unfolds new research opportunities in this area by virtue of the underlying properties of this class of sensors which include biocompatibility and excellent sensitivity, selectivity and stability. Furthermore, the aim of this review is to highlight recent achievements in analytical applications of these MIP-based electrochemical sensors in nanostructured carbon material for a wide range of sensing technologies.

1. Introduction

The molecularly imprinted technique (MIT) was first reported by Wulff and Sarhan in their work published in 1972 [1], where they described the preparation of synthetic polymers (functional monomers) with properties of sugar derivative receptors (template molecule) in appropriate solution. After this preparation process, by simple washing, the molecules stuck in the polymer matrix are then removed and the specific and complementary impressions are formed in the structure. Since the report published by Wulff and Sarhan, molecularly imprinted polymers (MIP) have played an outstanding role as an analytical tool in the development of tailor-made sensors. Among the pioneering works is Arshady and Mosbach [2], who reported a simple template strategy of the synthesis of custom-made polymers, based on complementary interactions. These MIP-based sensors exhibit a full range of properties including high selectivity, sensitivity, great reliability, low cost and mechanical, thermal and chemical stability [3], in addition to being employed as biological receptors (antigen and antibody).

The formation of MIP in general is based on the polymerization of one or more functional monomers with a cross-linker that polymerizes in the presence of a target molecule (usually the molecule of interest in detection, also referred to as template) through covalent or non-covalent interactions. After polymerization, the molecule of interest is extracted from the polymer matrix. The removal of the molecule leads to the creation of cavities in the structure with size, shape and interaction complementary to the template that can rebind reversibly and selectively in the presence of interferents [4].

MIPs may be prepared by bulk polymerization, photopolymerization, sol-gel and surface grafting polymerization mechanisms. In general the response time of the sensors based on MIP are longer because of the difficulties associated with diffusion. The shortest response times have involved grafting polymerization [5,6]. The sensitivity and efficiency of MIP-based sensors are directly related to the number of imprinted cavities present on the sensor surface. Indeed, MIPs formed in planar electrodes suffer from some obstacles such as irregular polymerization, restricted mobility and crowding of the cavities, which tend to compromise their selectivity due to poor accessibility, causing low electrochemical signal [7,8]. Nonetheless, the formation of nanostructured surfaces seems to be a promising way to overcome these problems through the improvement of sensibility and selectivity of these sensors.

Compared with planar surfaces, nanostructured surfaces present high surface-to-volume ratio and this essentially makes nanostructured materials extremely attractive when it comes to the development of MIP sensors. This vital property contributes to the increase in number and proportion of the imprint sites accessible for bonding, raising the MIP capacity by up to 15 times and the electron transfer ability from the binding sites to the surface of the electrode [9,10].

* Corresponding author at: São Paulo State University (UNESP), Institute of Chemistry, Araraquara, São Paulo CEP: 14800-060, Brazil.
E-mail address: nrstradi@iq.unesp.br (N.R. Stradiotto).

https://doi.org/10.1016/j.jelechem.2019.04.005
Received 27 September 2018; Received in revised form 12 February 2019; Accepted 1 April 2019
Available online 03 April 2019

9) Lista dos trabalhos preparados ou submetidos (e ainda não aceitos, pois os aceitos devem estar listados no item 7) para publicação, acompanhada de cópias destes trabalhos.

[1] Beluomini, M.A.; Stradiotto, N.R., Boldrin, M.V. Synthesis of three-dimensional nanoporous nickel based on dynamic hydrogen bubble template used for electrochemical detection of narirutin in citrus wastewater. Electrochimica Acta. EA20-04756. Submetido em Setembro de 2020.

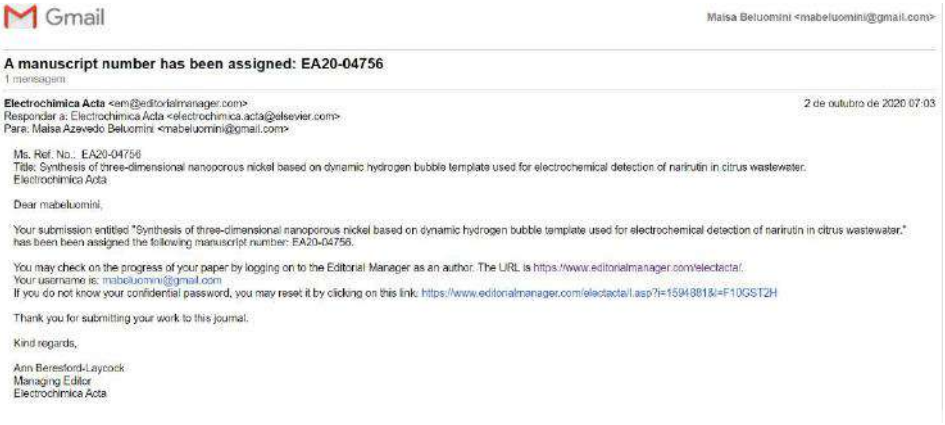

Gmail — Maisa Beluomini <mabeluomini@gmail.com>

A manuscript number has been assigned: EA20-04756
1 mensagem

Electrochimica Acta <em@editorialmanager.com> — 2 de outubro de 2020 07:03
Responder a: Electrochimica Acta <electrochimica.acta@elsevier.com>
Para: Maisa Azevedo Beluomini <mabeluomini@gmail.com>

Ms. Ref. No.: EA20-04756
Title: Synthesis of three-dimensional nanoporous nickel based on dynamic hydrogen bubble template used for electrochemical detection of narirutin in citrus wastewater.
Electrochimica Acta

Dear mabeluomini,

Your submission entitled "Synthesis of three-dimensional nanoporous nickel based on dynamic hydrogen bubble template used for electrochemical detection of narirutin in citrus wastewater." has been been assigned the following manuscript number: EA20-04756.

You may check on the progress of your paper by logging on to the Editorial Manager as an author. The URL is https://www.editorialmanager.com/electacta/.
Your username is: mabeluomini@gmail.com
If you do not know your confidential password, you may reset it by clicking on this link: https://www.editorialmanager.com/electacta/l.asp?i=1594881&l=F10GST2H

Thank you for submitting your work to this journal.

Kind regards,

Ann Beresford-Laycock
Managing Editor
Electrochimica Acta

[2] Garcia, M. B.; Beluomini, M.A.; Boldrin, M.V. Using an Electrochemical MIP Sensor for Selective Determination of 1-Naphthol in Oilfield Produced Water. J. Petrol.Science and Engineering. PETROL21864. Submetido em junho de 2020.

Track your recent Co-Authored submission to PETROL
1 mensagem

J. Petrol.Science and Engineering <eesserver@eesmail.elsevier.com> — 23 de julho de 2020 12:19
Responder a: "J. Petrol.Science and Engineering" <petrol-eo@elsevier.com>
Para: mabeluomini@gmail.com

*** Automated email sent by the system ***

Dear Dr. Maisa Azevedo Beluomini,

You have been listed as a Co-Author of the following submission:

Journal: Journal of Petroleum Science and Engineering
Title: Using an Electrochemical MIP Sensor for Selective Determination of 1-Naphthol in Oilfield Produced Water
Corresponding Author: Mariana Bartlotti Garcia
Co-Authors: Maisa Azevedo Beluomini, Ph.D.; Maria Valnice Boldrin, Ph.D.

To be kept informed of the status of your submission, register or log in (if you already have an Elsevier profile).

Register here: https://ees.elsevier.com/petrol/default.asp?acw=&pg=preRegistration.asp&user=cowithor&lname=Maisa Azevedo&lname=Beluomini&email=mabeluomini@gmail.com

Or log in: https://ees.elsevier.com/petrol/default.asp?acw=&pg=login.asp&email=mabeluomini@gmail.com

If you did not co-author this submission, please do not follow the above link but instead contact the Corresponding Author of this submission at mbartlottig@gmail.com.

Thank you,

Journal of Petroleum Science and Engineering

[3] Silva, J.L.; Buffon, E.; Beluomini, M.A.; Pradela-Filho, L.A, Araujo, D.A.G.; Santos, A.L.; Takeuchi, R.M.; Boldrin, M.V.; Stradiotto, N.R. Non-enzymatic lactose molecularly imprinted sensor based on disposable graphite paper electrode. Analytica Chimica Acta, ACA-20-2500, Submetido em agosto de 2020.

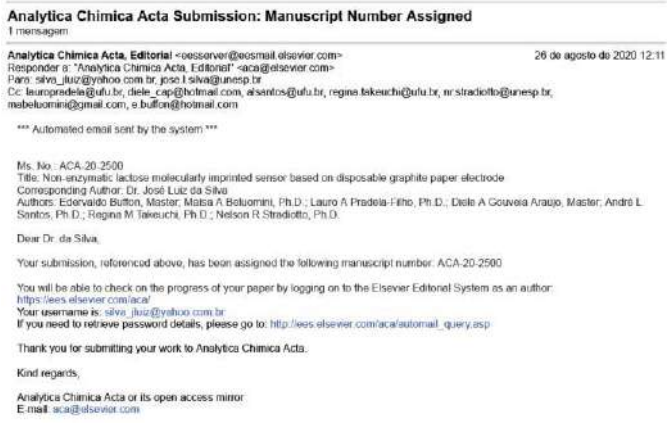

Analytica Chimica Acta Submission: Manuscript Number Assigned
1 mensagem

Analytica Chimica Acta, Editorial <eesserver@eesmail.elsevier.com> — 26 de agosto de 2020 12:11
Responder a: "Analytica Chimica Acta, Editorial" <aca@elsevier.com>
Para: silva_jluiz@yahoo.com.br, jose.l.silva@unesp.br
Cc: lauropradela@ufu.br, diele_cap@hotmail.com, alsantos@ufu.br, regina.takeuchi@ufu.br, nr.stradiotto@unesp.br, mabeluomini@gmail.com, e.buffon@hotmail.com

*** Automated email sent by the system ***

Ms. No.: ACA-20-2500
Title: Non-enzymatic lactose molecularly imprinted sensor based on disposable graphite paper electrode
Corresponding Author: Dr. José Luiz da Silva
Authors: Edervaldo Buffon, Master; Maisa A Beluomini, Ph.D.; Lauro A Pradela-Filho, Ph.D.; Diele A Gouveia Araujo, Master; André L Santos, Ph.D.; Regina M Takeuchi, Ph.D.; Nelson R Stradiotto, Ph.D.

Dear Dr. da Silva,

Your submission, referenced above, has been assigned the following manuscript number: ACA-20-2500

You will be able to check on the progress of your paper by logging on to the Elsevier Editorial System as an author:
https://ees.elsevier.com/aca/
Your username is: silva_jluiz@yahoo.com.br
If you need to retrieve password details, please go to: http://ees.elsevier.com/aca/automail_query.asp

Thank you for submitting your work to Analytica Chimica Acta.

Kind regards,

Analytica Chimica Acta or its open access mirror
E-mail: aca@elsevier.com

Synthesis of three-dimensional nanoporous nickel based on dynamic hydrogen bubble template used for electrochemical detection of narirutin in citrus wastewater.

Maísa Azevedo Beluomini[a], Nelson Ramos Stradiotto[a,b], Maria Valnice Boldrin[a,c].

[a] Analytical Chemistry Department, Institute of Chemistry, São Paulo State University (UNESP), 55 Prof. Francisco Degni St., Araraquara 14800-060, São Paulo State, Brazil.

[b] Bioenergy Research Institute (IPBEN), São Paulo State University (UNESP), 55 Prof. Francisco Degni St., Araraquara 14800-060, São Paulo State, Brazil.

[c] National Institute of Alternative Technologies for Detection, Toxicological Evaluation and Removal of Micropollutants and Radioactive Substances (INCT-DATREM), São Paulo State University (UNESP), 55 Prof. Francisco Degni St., Araraquara 14800-060, São Paulo State, Brazil.

* Corresponding author: maisa.beluomini@unesp.br

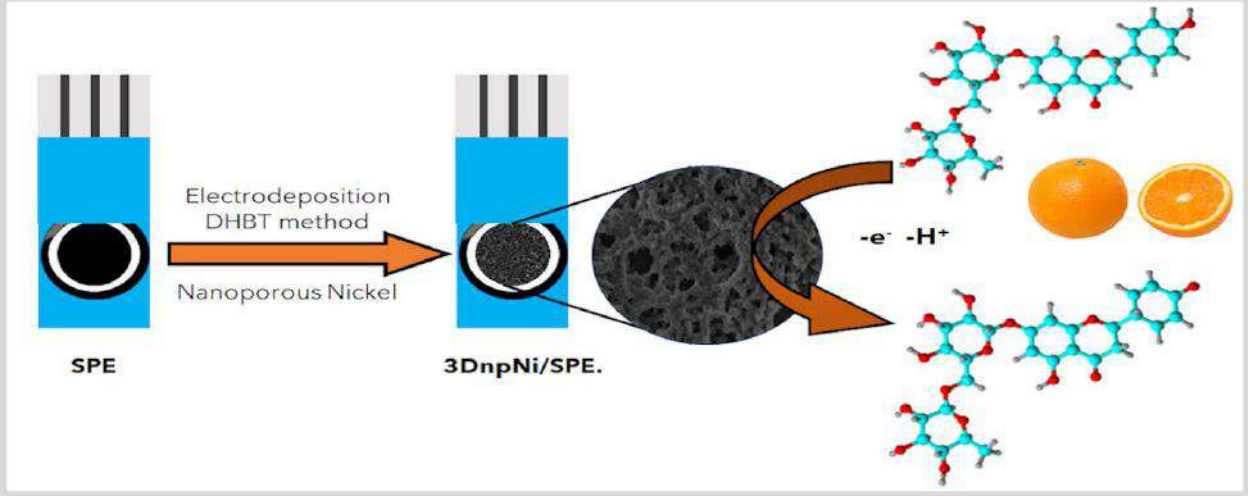

Abstract

This paper reports for the first time the electrochemical determination of narirutin using three-dimensional nanostructured porous nickel with high surface area on screen-printed electrode (3DnpNi/SPE). The modified electrode was successfully synthesized by the dynamic hydrogen bubble template (DHBT) method. The 3DnpNi/SPE was characterized by scanning electron microscopy (SEM), energy-dispersive x-ray spectroscopy (EDS), X-ray photoelectron spectroscopy (XPS), electrochemical impedance spectroscopy (EIS), and cyclic voltammetry. The results showed that the 3DnpNi/SPE presents excellent electrocatalytic activity for the oxidation of narirutin. To have a better understanding of the electrooxidation process of narirutin, the parameters involved in the process were investigated. The quantification of narirutin was conducted by differential pulse voltammetry (DPV), which showed a wide concentration range (1.0×10^{-7} – 1.0×10^{-5} mol L^{-1}), with low detection limit (3.9×10^{-8} mol L^{-1}), and excellent sensitivity (0.31 A L mol^{-1}). The good electrochemical performance of the proposed electrode was attributed to the high density of the nanostructured porous nickel on the SPE. Furthermore, the 3DnpNi/SPE showed good repeatability, long-term stability, and considerable selectivity. The electrode was applied toward the determination of narirutin in yellow water samples from the citrus industry, where it presented an excellent degree of accuracy. The results obtained by the application of the proposed method were in good agreement with those of the comparative HPLC/DAD method.

Keywords: Nanoporous nickel; Three-dimensional nanostructure; Narirutin; Wastewater; Citrus industry.

1. Introduction

The orange industry is one of the most important industries in the world owing to the high consumption of orange, orange juice and its derivatives worldwide. The orange production industry produces approximately 70 thousand tons of orange annually, with Brazil being the largest producer, followed by the United States, India, and China. In the orange industry, approximately 70 % of the orange produced is transformed into juice, marmalade, and other products, while a significant portion of the remaining 30% ends up as solid and liquid wastes [1]. It is estimated that the citrus industry produces nearly forty million tons of waste annually [2]. Yellow water is the term given to liquid residues produced from the washing of orange fruits, distilling activities of distilleries, and the production of essential oil from orange; the handling and disposal of these residues are a matter of great concern to orange industries worldwide. An average size orange plant produces about 100 m3 of yellow water daily [3]. This wastewater has a considerable amount of flavonoids, phenolic acids, sugars and pectin. Due to the high concentration of organic matter present therein, this waste becomes a highly polluting agent. Citrus processing industries are commercially interested in recovering significant quantities of some usefully relevant compounds present in yellow water. Among the compounds that have high added value, phytochemicals have great commercial importance [4]. One of the relevant groups of phytochemicals that deserves mentioning is citrus flavonoids; these flavonoids are a major class of secondary metabolites which has been extensively studied due to its important biological activities, such as anticancer, antioxidant, antiviral, anti-inflammatory and neuro-cardio protective effect and antiplatelet activity [5]. One of these citrus flavonoids that merits attention is narirutin (naringenin-7-O-rutinoside) - a flavanone glucoside, which, in recent years, has been shown to present interesting therapeutic properties in studies related to the protection of alcohol-induced damage [6], Alzheimer's disease therapy [7], and the reduction of airway inflammation in mice [8]. In addition, several studies have shown that flavonoids have therapeutic effects against the

coronavirus disease 2019 (COVID-19). The studies have demonstrated that flavonoids can bind with high affinity to the receptor angiotensin-converting enzyme 2 (ACE2) in the respiratory tract, causing a conformational change that inhibits the entry of coronaviruses in the human body [9–11].

In view of the biological and pharmacological importance of narirutin, the development of reliable methods for its determination is found to be essentially vital. Taking that into consideration, several studies published in the literature have employed a wide range of techniques aiming at the determination of narirutin and other flavonoids in solid and liquid waste samples. Some of the techniques that have been employed toward the determination of these compounds include the following: high performance liquid chromatography (HPLC) [12], reverse phase high performance liquid chromatography with photodiode array detector (HPLC-PAD) [13–15], liquid chromatography–mass spectrometry with tandem mass spectrometry (LC-MS/MS) [14], high-performance liquid chromatography-electrospray ionization-tandem mass spectrometry (HPLC-ESI-MS) [16], and ultra-high performance liquid chromatography coupled with triple-quadrupole mass spectrometry (UHPLC-QqQ-MS) [17]. Although the aforementioned methods offer high sensitivity, selectivity, and low detection limits, they are also found to present some non-negligible disadvantages including the use of non-environmentally friendly high volume of reagents and solvents, time-consuming sample preparation involving extraction, purification and filtration steps, and high cost of equipment for analysis. In view of that, there has been a considerable interest among researchers toward the development of an efficient, faster and less costly method that consumes low amount of chemical reagents. The use of electrochemical methods for compounds determination in wastewater has been shown to be advantageous because of their outstanding merits including fast response, operational simplicity, high sensitivity and low detection limits, apart from requiring low sample volume for analyses. Nevertheless, to date, there have been no reports in the literature regarding the application of an electrochemical technique for

the detection of narirutin and a thorough investigation about the electrochemical behavior of this compound.

Compared to unmodified electrodes, the use of modified electrodes has led to a significantly improved electrochemical response in the detection of compounds [18]. Materials with high electrical conductivity and large surface area have been widely employed for the construction of electrochemical sensors and biosensors. Nanomaterials are among the most widely used materials for the modification of electrodes; these materials include nanoparticles [19], quantum dots [20], magnetic nanoparticles [21], carbon-based nanomaterials [22] and polymers [23]. More recently, the use of metallic nanoporous materials for electrodes modification has drawn considerable attention among researchers in the field [24]. Compared to metallic nanoparticles, metallic nanoporous (np) materials have a spongy three-dimensional morphology which offers greater surface area, lower density, and larger active sites [25]. These properties contribute toward elevating the faradaic current (related to the electrode area) in nanoporous-modified electrodes compared to unmodified electrodes. In addition, the possibility of building a three-dimensional nanoporous structure (3Dnp) has been widely studied in electrocatalysis [26], supercapacitors [27], and for the construction of electrochemical sensors [26,28,29] and biosensors [30].

The 3Dnp can be constructed through the following ways: i) via electrochemical dealloying using metal alloys, such as Pt-Cu [31], Al-Cu [32] , Ni-Cu [33], and Zr-Cu [26]; ii) via the use of porous alumina commercial templates [34]; and iii) by anodization techniques [35]. Another efficient technique that has been extensively explored for the construction of 3Dnp is the dynamic hydrogen bubble template method (DHBT). This method involves the evolution of hydrogen bubbles together with the metal deposition process. The H+ ions are reduced to H2, which are agglomerated into bubbles. These bubbles become a dynamic template for the electrochemical deposition of metals. While metallic nanoparticles are electrodeposited between the hydrogen

bubbles, three-dimensional nanostructured metallic porous films are formed on the electrode surface [36]. The key advantages of this method lie in its simplicity, low cost, facile control of structures, one-step synthesis process, and production of clean nanostructures devoid of template contamination. Nanoporous materials synthesized by the DHBT method have presented excellent electrocatalytic activity for nitrite oxidation [36], non-enzymatic electrochemical detection of glucose[37], hydrogen evolution reaction [38], apart from their successful application as a host for the enhancement of the performance of Li metal anodes [39]. Interestingly, there have been no reports in the literature regarding the use of the DHBT method for the development of a three-dimensional nanostructured porous nickel (3DnpNi) on screen-printed electrode (SPE). Nickel is a low cost metal characterized by high electrical conductivity, good stability, and high catalytic activity; this metal has widely been used as electrode modifier for electroanalytical applications [40]. Within the context of developing new and highly efficient analytical techniques, the use of SPEs has been shown to enhance the efficiency of electrodes compared to the application of conventional electrodes; among the known qualities of SPEs include portability, simplicity of use, low cost, good reproducibility and repeatability, apart from requiring low volumes of solution for the conduct of analyses [41].

Thus, the present work reports the development and characterization of a three-dimensional structure of nanoporous nickel on a screen-printed electrode surface (3DnpNi/SPE) using the DHBT method. Compared to the non-modified SPE, the modified SPE presented better electrochemical performance in terms of the oxidation of narirutin. To the best of our knowledge, this is the first report involving a thorough study on the electrochemical behavior of narirutin. The proposed electrode was applied toward the determination of narirutin, where it presented excellent results with low detection limit and high sensitivity, apart from allowing the conduct of analysis at low volume (only 50 µl). The application of differential pulse voltammetry (DPV) for the quantification of narirutin in wastewater from the citrus industry yielded promising results

2. Experimental

2.1 Instruments and reagents

Narirutin ≥ 98 % ($C_{27}H_{32}O_{14}$), naringenin ($C_{15}H_{12}O_5$) ≥ 95%, hesperidina ($C_{28}H_{34}O_{15}$) ≥ 80%, D-glucose ($C_6H_{12}O_6$) ≥99.5 %, D-fructose ($C_6H_{12}O_6$) ≥ 99%, nickel (II) chloride hexahydrate > 98 % ($NiCl_2 \cdot 6\ H_2O$) and ammonium chloride (NH_4Cl) ≥ 99.5 % were obtained from Sigma – Aldrich. Citric acid ≥ 99.5 % ($C_6H_8O_7$), sodium citrate dihydrate ($C_6H_5Na_3O_7 \cdot 2\ H_2O$), potassium ferricyanide 99% ($K_3[Fe(CN)_6]$), potassium chloride 99 % (KCl), were purchased from Synth. The electrochemical measurements were performed in a potentiostat Autolab PGSTAT30. The data were recorded and stored in the Nova 2.0 software coupled to the laptop. The screen-printed electrodes (SPE) were acquired from DropSens (DRP - C110). The SPE consisted of a carbon working surface (4.0 mm diameter), silver/silver chloride reference electrode, and counter electrode made of carbon. All solutions were prepared using deionized water with resistivity not less than 18.2 $M\Omega cm^{-1}$. All the experiments were carried out at room temperature (25 ± 1.0 °C).

2.2 Construction of 3DnpNi/SPE

Prior to its modification, the SPE was activated by several voltammetry cycles in the potential range of − 0.2 V to 1.2 V, at scan rate of 50 mVs^{-1}, using 0.5 mol L^{-1} H_2SO_4 solution until a stable voltammogram was obtained. Nanoporous nickel was electrochemically deposited through the application of a cathodic current density of - 0.2 A cm^{-2} for 20 s, in a solution containing 0.01 mol L^{-1} $NiCl_2$, 0.1 mol L^{-1} NaCl, and 0.2 mol L^{-1} NH_4Cl. The electrodeposition process was carried out in an electrolyte solution without stirring or N_2 bubbling. All experiments were performed at least three times.

2.3 Determination of surface roughness of nickel nanoporous electrodes

The analysis of roughness of the nanoporous nickel on the SPE surface was carried out by cyclic voltammetry using 0.1 mol L^{-1} NaOH, with the application of potential range of 0.2 to 0.7 V and scan rate of 50 mV s^{-1}. The charge, associated with the area of the first nickel oxide reduction peak (related to NiOOH and $Ni(OH)_2$) in the first complete cyclic scan, was divided by a conversion factor of 257 μC cm^{-2}; this helped obtain the actual electrode area (cm^2) [42]. The real area was divided by the geometric area of the SPE (0.126 cm^2), and the result obtained was taken as the surface roughness factor. This parameter was evaluated in order to choose the best conditions for the formation of 3DnpNi/SPE.

2.4 Characterization of the 3DnpNi/SPE

The characterization of the 3DnpNi/SPE was performed by electrochemical impedance spectroscopy (EIS) with the application of the potential of 0.20 V and frequency range of 0.10 Hz to 100 kHz. The morphological characterization of the original surface was carried out by field-emission scanning electron microscopy (FEG-SEM; Jeol, model JSM 7500F) operated at 2 kV. The energy-dispersive X-ray spectroscopy (EDS) analysis detector, attached to the microscope, was used. The X-ray photoelectron spectroscopy analysis (XPS) was performed in a commercial spectrometer (UNI-SPECS UHV) at a pressure below 5.0×10^{-7} Pa using the Al Kα line (hν=1253.6 eV) with the analyzer pass energy applied at 10 eV. The inelastic background C 1s, O 1s, Ni $2p_{3/2}$ electron core-level spectra was subtracted using the Shirley's method. The composition (at. %) of the near surface region was determined with an accuracy of ± 5 % from the ratio of the relative peak areas corrected by Scofield's sensitivity factors of the corresponding elements. The spectra were deconvoluted using a Voigtian function, with Gaussian (70 %) and Lorentzian (30 %) combinations. The width at half maximum (FWHM) varied between 1.2 and 2.1 eV, and the accuracy of the peak positions was ± 0.1 eV.

2.5 Analytical measurements

The stock solution of narirutin was prepared in 40 % (*v/v*) ethanol and heated to 45 °C in an ultrasound bath for 15 min. After that, the solution was put in an amber bottle and kept in the refrigerator. Citrate buffer solution (pH = 4.0) was used as the supporting electrolyte for conducting the electrochemical studies by cyclic voltammetry (CV) in the potential range of 0.0 and 0.8 V, and scan rate of 50 mV s^{-1}. The DPV technique was employed in order to define the analytical method using the potential range of 0.2 to 0.8 V, modulation amplitude of 50 mV, step potential of 4.0 mV, and modulation time of 50 ms.

The figures of merit, such as limit of detection (LOD), limit of quantification (LOQ), and amperometric sensitivity (As), were determined. The limits were calculated using the following equation: LOD = $3S_b/m$ and LOQ = $10S_b/m$, where S_b stands for the standard deviation obtained from three measurements of the blank signal, and *m* is the analytical sensitivity [43].

2.6 Sample preparation

The yellow water samples were supplied by an agribusiness company from the city of Araraquara, São Paulo State, Brazil (21° 47′ 40″ S, 48° 10' 32″ W). The samples were centrifuged at 4000 rpm for 20 min to remove any solid particles. The supernatant was collected and filtered using filters with porosity of 0.47 and 0.22 μm, and was kept frozen until use. The sample was diluted 20 times in 0.1 mol L^{-1} citrate buffer solution (pH 4.0) and used for narirutin detection. The concentrations of narirutin in the samples were determined by the standard addition method. The same procedure was adopted for the recovery experiment where known concentrations of standard narirutin were added to the samples.

2.7 Chromatographic analysis

Chromatographic analyses were performed in a Shimadzu UV-1800 spectrophotometer using a technique similar to the one described by Barfi et al. [12]. The following conditions were applied: C18 HPLC column with temperature of 35˚C and flow rate of 1 ml min $^{-1}$. The wavelength was kept at 280 nm. Water (A) and acetonitrile containing 0.1% formic acid (B) were used for the mobile phase composition. The following chromatographic gradients were employed: 0 - 0.01 min, 80 % A – 20 % B; 0.01 - 10 min, 50 % A – 50 % B. Prior to use, the mobile phase was filtered with 0.45 and 0.22 μm membrane filters and degassed in an ultrasound bath. The injected volume of 50 μL (of the sample) was applied. The calibration curve was constructed by plotting the peak area as a function of narirutin concentration. The analytical curve for the HPLC analysis was obtained in the concentration range of 5.0×10^{-6} mol L^{-1} to 1.0×10^{-4} mol L^{-1} of narirutin (Fig. S2). The detection limit obtained was 3.4×10^{-6} mol L^{-1} (n = 3).

3. Results and discussion

3.1. Electrosynthesis and characterization of 3DnpNi

The electrodeposition of nanoporous nickel on the SPE was carried out at constant current density in a solution containing 0.01 mol L^{-1} $NiCl_2$, 0.1 mol L^{-1} NaCl and 0.2 mol L^{-1} NH_4Cl. The reduction of nickel ions and hydrogen evolution reaction occurred simultaneously. The parameters found to affect the formation of the porous nanomaterial include the following: the source and concentration of H^+; the applied current density; the substrate; and the metallic salt. In order to deposit the nickel on the SPE in a single step, one needs to choose an appropriate supporting electrolyte because this solution exerts a strong influence over the morphology and property of the film. With that in mind, NH_4Cl was chosen as one of the electrolytes because its presence provides a source of hydrogen (from hydrolysis process that decreases the pH of the electrolyte solution), which can increase the rate of hydrogen evolution, leading to the formation of porous nanostructures and the improvement of the mechanical resistance of the material. In addition, NaCl

contributes to the formation of $NiCl^+$, impeding the formation of $Ni(OH)_2$, while keeping the nickel freely available for the electrodeposition process [44,45].

It is worth noting that under the one-phase electrodeposition mechanism, the hydrogen bubble density increases with the applied current density and the random nucleation of the dissolved hydrogen produces microbubbles bound to the SPE surface. In this sense, the hydrogen evolution reaction occurs alongside the metal electrodeposition process. Unlike the conventional two-phase (liquid-solid) electrodeposition systems, this system involves a gas-liquid-solid mechanism, in a three-phase interface. For the electrodeposition of the nickel, the current density in the potential range of 0.08 to 0.6 A cm $^{-2}$ was applied for 20 s. The field emission gun scanning electron microscopy (FEG-SEM) images of the electrode surface are shown in Fig. 1. Fig. 1A shows the bare SPE (without modification); Fig. 1B shows the electrodeposition conducted at the current density of 0.08 A cm^{-2}; Fig. 1C shows the electrodeposition conducted at the current density of 0.2 A cm^{-2}; Fig. 1D shows the electrodeposition conducted at the current density of 0.6A cm^{-2}; and Figure 1E shows the electrodeposition conducted at the current density of 0.8 A cm^{-2}. The morphology of the porous nanostructure is defined by the dynamics of the diffusion layer along the electrode surface. Due to the rapid change of the diffusion layer with time, higher applied current densities produce porous nanostructures with better morphology. On the other hand, extremely high densities lead to the generation of large hydrogen bubbles, and the coalescence between them produces large porous nanostructures, with low mechanical resistance, as can be noted in the image in Fig.1E. Looking at the images, one can see that the application of the current density of 0.6 A cm^{-2} led to a better formation of the porous nanostructure, characterized by the homogeneous distribution of the porous nanostructure on the electrode surface, with diameter ranging between 70 - 120 nm. Fig.1F shows the energy dispersion spectroscopy (EDS) related to image D, which confirms the presence of nickel on the electrode surface.

The 3DnpNi is formed due to the fact that the internal pores have a smaller diameter than those located on the surface. The enlargement of the porous nanostructure is indicative of the coalescence of the hydrogen bubbles. Thus, the smaller pores are covered by the larger pores, forming hierarchical structures with different size, which change very quickly over time.

The surface roughness was evaluated during the electrodeposition time between 10 to 60 s, at the current density of 0.6 A cm^{-2}, as shown in Fig. 2. To determine the surface roughness for each time, the 3DnpNi/SPE was evaluated by CV in 0.1 mol L^{-1} NaOH solution, in the potential range of 0.2 to 0.7 V, with scan rate of 50 mVs^{-1}. A typical nickel electrochemical response was observed, as shown in equation 1. The oxidation of nickel occurred at the potential of 0.46 V, with the formation of Ni(II) species on the electrode surface. Through cathodic scanning, the peak of reduction from Ni(II) to Ni(0) occurred at the potential of - 0.38 V [46].

$Ni + 2OH^{-} \rightarrow Ni(OH)_2 + 2e^{-}$ (1).

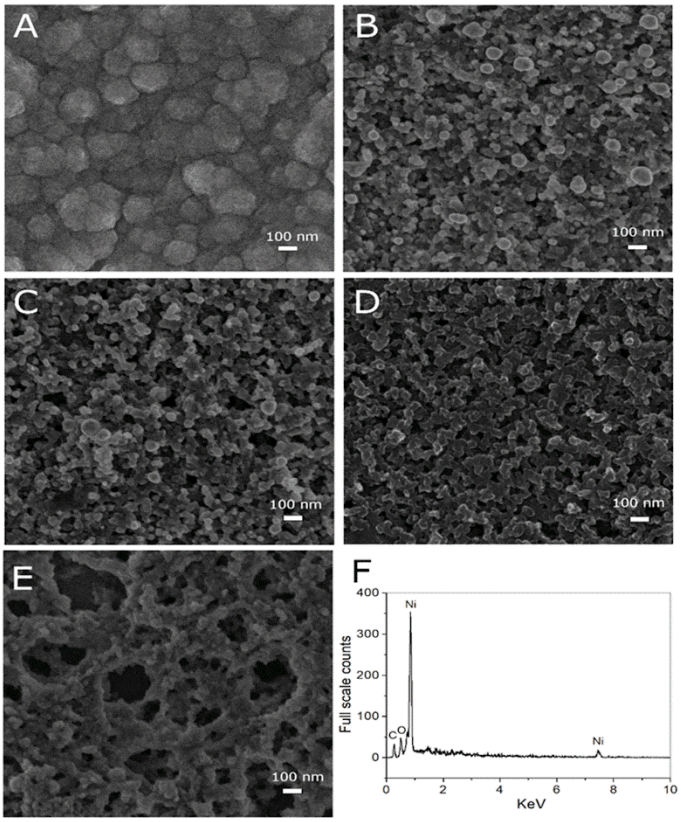

Fig. 1. FEG-SEM images for (A) SPE and 3DnpNi/SPE under different current densities: (B) 0.08, (C) 0.2, (D) 0.6 and (E) 0.6 A cm^{-2}. Magnification of 50 000 x. (F) EDS related to image D.

The surface roughness factor (R*f*) is derived from the division of the electrochemical area by the geometric area. So, the electrochemical area was determined by dividing the peak area of the nickel oxide reduction (μC) (Fig. 2A) by a correction factor of 257 μC [42] (as described in *section 2.3*). The geometric area obtained for the SPE (used as substrate) was 0.126 cm^2. This method of calculation is applied to metals that have a well-defined region in the formation and reduction of their oxide monolayers [47]. Based on the aforementioned method, the R*f* was calculated by dividing the electrochemical surface area (cm^2) by the geometric area (cm^2); the result obtained is a good indicator for monitoring the evolution of the electrode [48].

The surface of the 3DnpNi/SPE exhibited an increase in roughness up to the electrodeposition time of 40 s, with R*f* of 4.8 (four times greater compared to the period of 10 s). After 40 s, the electrode surface presented a decrease in roughness (Fig. 2B), which is attributed to the coalescence of the hydrogen bubbles, with the formation of larger pores that decrease the surface roughness [38]. Thus, for the formation of 3DnpNi/SPE, a current density of 0.6 A cm^{-2} and a deposition time of 40 s were applied. The FEG-SEM images of these optimal conditions are shown in Fig. S1.

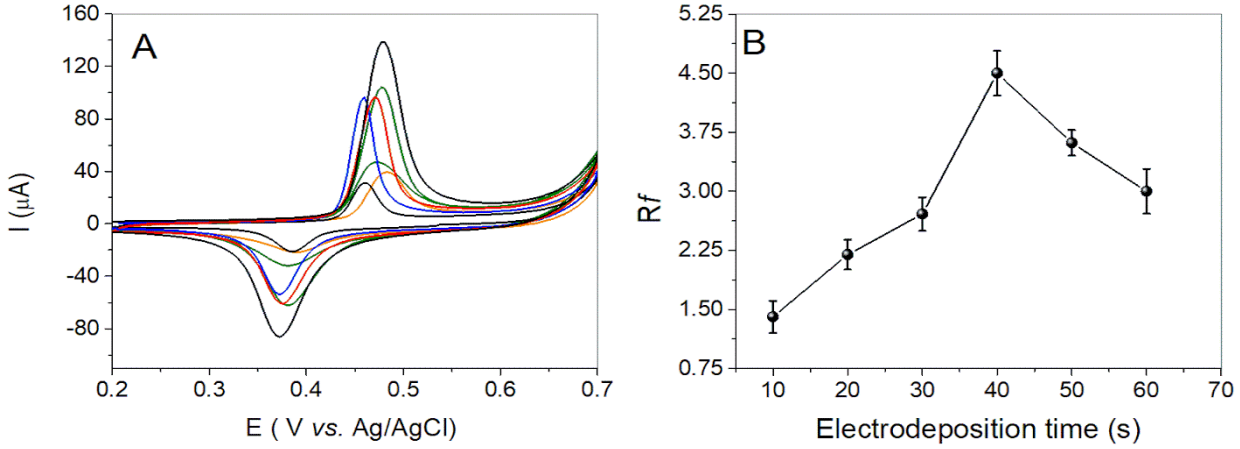

Fig. 2. (A) CV for 3DnpNi/SPE in NaOH 0.1 mol L^{-1} in the potential range of 0.2 to 0.7 V, at scan rate of 50 mVs^{-1} for different electrodeposition times. In (B), the roughness factor for each of the times investigated, between 10 and 60 s.

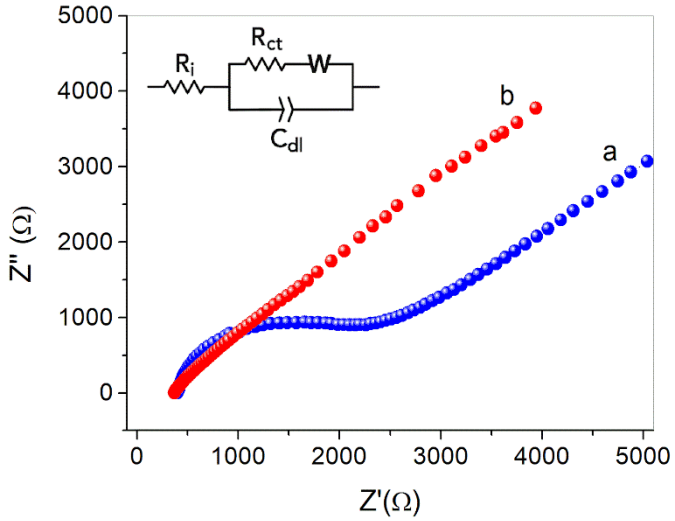

Fig. 3. Nyquist plot for (a) SPE and (b) 3DnpNi/SPE using 5.0×10^{-3} mol L^{-1} $Fe(CN)_6^{3-/4-}$ solution prepared in 0.1 mol L^{-1} of KCl in the frequency range of 0.1 Hz to 100 kHz. Insertion: equivalent circuit used for impedance data analysis.

The EIS technique was applied for the electrochemical characterization of the 3DnpNi/SPE. The electron-transfer resistance was analyzed using a solution of 5.0×10^{-3} mol L^{-1} $[Fe(CN)_6]^{3-/4-}$ in 0.1 mol L^{-1} KCl. A typical impedance arc (Nyquist plot) with the compatible circuit is shown in Fig. 3. In the circuit, R_i represents the resistance of the solution, C_{dl} is related to the double layer capacitance, and R_{ct} refers to the charge-transfer resistance. The results obtained were discussed in terms of R_{ct} from the equivalent circuits. This parameter (R_{ct}) has a simple meaning in physics and can be used for the comparison of the electrodes in order to evaluate the characteristics of the electrode/solution interface.

Looking at the Nyquist diagram in Fig. 3, one can observe the presence of a semicircle for the unmodified SPE (curve a), with R_{ct} of 2.3 KΩ. When the SPE was modified with nanoporous nickel, the electrochemical response appeared to be close to a straight line (curve b), and the R_{ct} value was notably lower, 39 Ω; this shows that the modification of the electrode facilitated the transfer of electrons between the redox probe and the electrode surface.

The surface chemistry of 3DnpNi/SPE was also characterized by XPS; this was done in order to study the oxidation level as well as the nature of the chemical bonding of the electrode (Fig. 4). The signal at 285.3 eV can be mainly associated with aliphatic carbon (C-H and / or C sp^3), while the signal at 284.5 eV is related to aromatic C-C bonds. The signal at 283.4 eV is associated with C-Ni bonds, as shown in Fig. 4A. One can observe the presence of oxygenated groups of alcohol/ether (C-O), carbonyl (C=O), and carboxyl/ester (O-C=O) at 286.5 eV, 288.0 eV, and ~ 289.5 eV, respectively. The oxygen content was monitored by the O_{1s} signal. The high-resolution O_{1s} spectra of the electrode surface was deconvoluted into three components corresponding to oxygen atoms in different functional groups; these groups included the following: the O-C bonds at ~ 532.2 eV, O=C, -OH groups at ~ 531.7 eV, and O-C=O at 533.9 eV (Fig. 4B). The Ni spectrum of the spin-orbit ($Ni2p_{3/2}$ and $Ni2p_{1/2}$) was deconvoluted into two components (Fig. 4C), associated with metallic nickel (853.7 eV) and Ni_2O_3 (855.3 eV). The shake-up satellites were found to be related to the effect of the final Ni (III) state (861.2 and 863.5 eV).

3.2 Electrochemical behavior of narirutin

Since no systematic studies have been reported in the literature regarding the electrochemical oxidation mechanism of narirutin, its electrochemical behavior was investigated by CV. Fig. 5 shows the voltammetric response for bare SPE (curve a) and 3DnpNi/SPE (curve b), based on the application of 1.0×10^{-5} mol L^{-1} of narirutin in citrate buffer solution, with pH = 4.0. One can observe the presence of anodic peak at the potential of 0.64 V. An analysis of the reverse scan showed the presence of no peaks; this implies that the oxidation process of narirutin was irreversible. In addition, the oxidation product did not show a peak of re-oxidation or reduction in the potential range evaluated; this shows that the oxidation product was not electroactive.

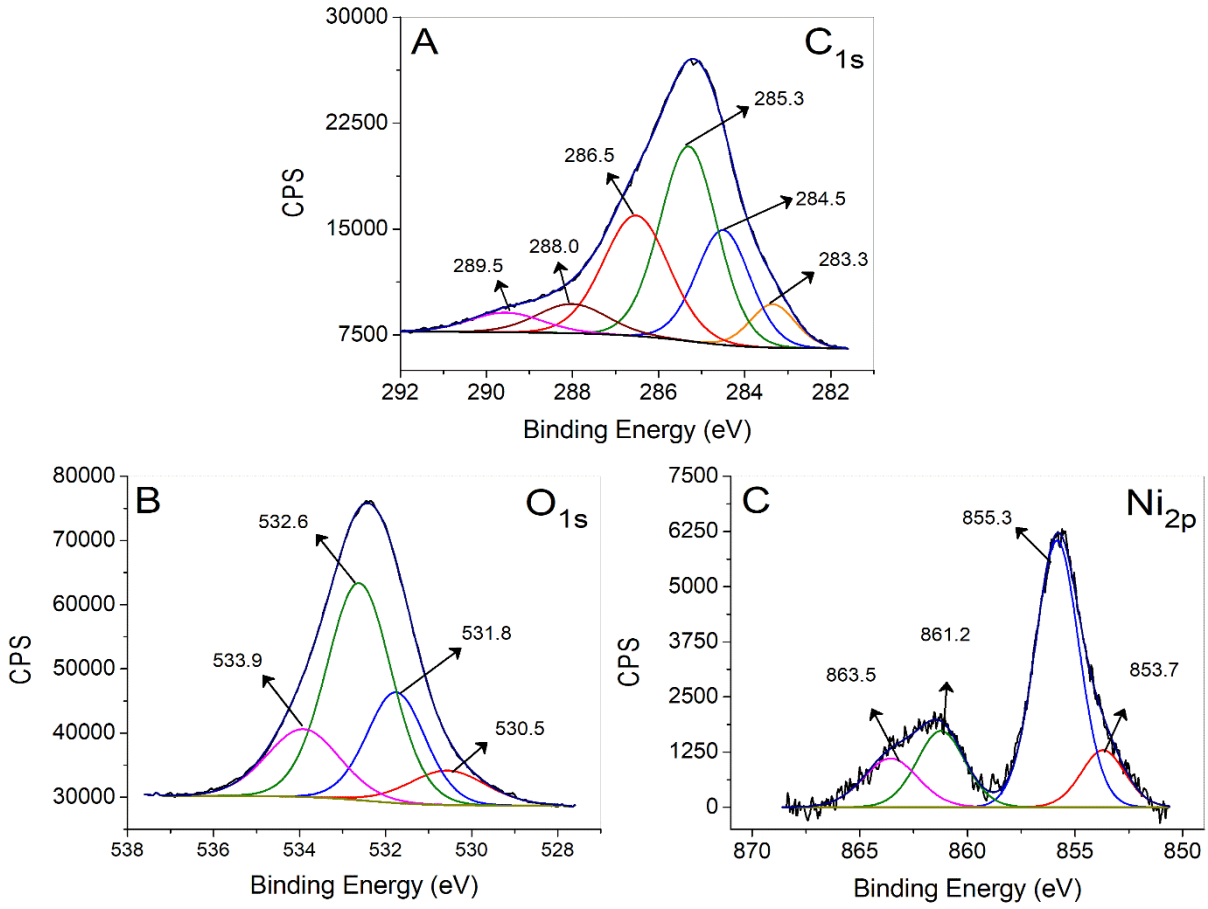

Fig. 4. Deconvoluted and Gaussian fitted XPS spectrum of (A) C1s (B) O1s and (c) Ni2p curves related to 3DnpNi/SPE.

The 3DnpNi/SPE exhibited a peak current which was 2.2 times greater than that of bare SPE; this shows that the electrode modification enhanced the electrocatalytic activity of narirutin. Thus, the improved behavior of the SPE surface in the oxidation of narirutin is related to the increased porosity derived from the incorporation of 3DnpNi.

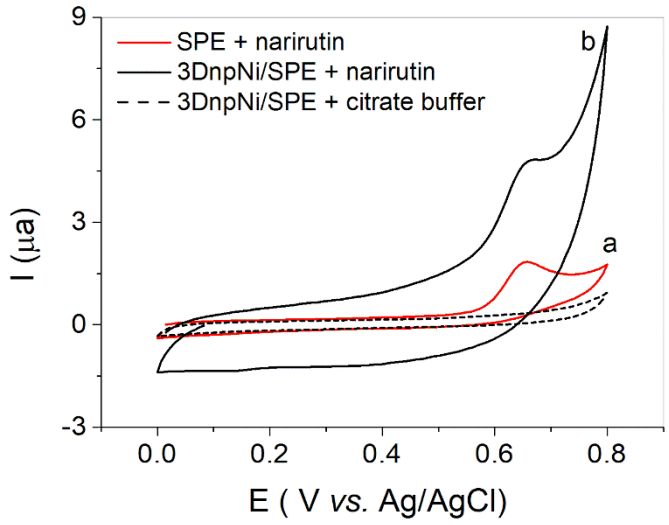

Fig. 5. Cyclic voltammograms of 1.0×10^{-5} mol L^{-1} of narirutin in citrate buffer solution of pH 4.0, on (a) SPE and (b) 3DnpNi/SPE. In (c) SPE applied in supporting electrolyte solution. Scan rate applied: 50 mV s^{-1}.

3.3 Effect of the solution pH

Owing to the presence of hydroxyl groups in the aromatic rings of the narirutin molecule, the influence of pH on the electrochemical performance was evaluated. The influence of the pH was investigated in the pH range of 2.6 to 5.6 using 0.1 mol L^{-1} citrate buffer solution. A 1.0×10^{-5} mol L^{-1} concentration of narirutin was employed in this analysis. The CV related to the application of 3DnpNi/SPE for narirutin determination can be found in Fig. 6; as can be observed, the highest current peak, with good definition, was found at pH 4.0. Thus, this pH value was adopted in subsequent experiments. All peaks shifted negatively with the variation of the pH value; this indicates that narirutin oxidation was accompanied by proton transfer. In addition, a good linear relationship was observed between the oxidation potential of narirutin and the pH of the citrate buffer solution. The corresponding regression equation obtained was E (V) = - 0.050 pH + 0.86 (R= 0.999). The slope of the linear correlation was based on the following equation: -2.303 *m*RT/*n*F, where *m* and *n* represent the number of protons and electrons, respectively [49]. The slope of -0.050 V/pH was found to be in good agreement with the theoretical value of -0.059 V/pH at 25˚C, as demonstrated by the Nernst equation, when *m* = *n*. Thus, the electron-transfer number

during the oxidation of narirutin was accompanied by an equal proton-transfer number. Furthermore, for pH values higher than 9.0, the CV did not exhibit a well-defined peak (not shown); as a result, it was impossible to accurately measure the values of the potential. A similar voltammetric behavior was also observed in the oxidation of other flavonoids [49,50].

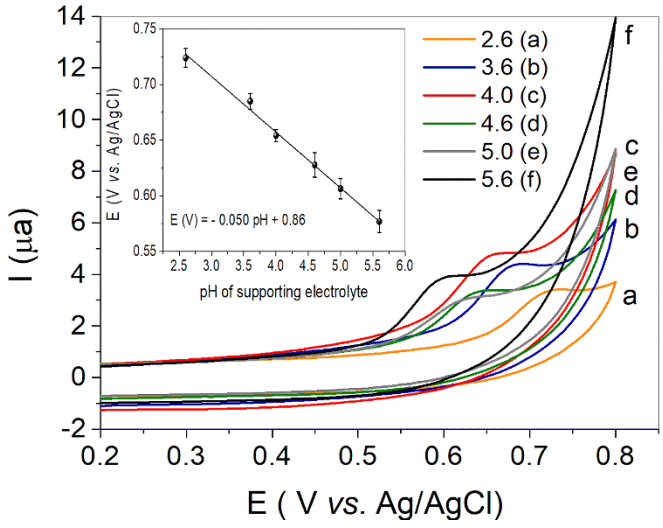

Fig. 6. CVs obtained for 3DnpNi/SPE using 1.0×10^{-5} mol L^{-1} of narirutin containing citrate buffer solution at different pH values (ranging from pH 2.6 to pH 5.6), with scan rate of 50 mV s^{-1}. Insert: Plot of the anodic potential of narirutin versus pH.

3.4 Influence of scan rate

The influence of scan rate (υ) on the electrooxidation of 5.0×10^{-5} mol L^{-1}narirutin on 3DnpNi/SPE was investigated based on the variation of scan rate from 20 to 500 mV s^{-1}. Fig. 7A shows that there was a good linear relationship between the logarithm of I (A) and the logarithm of υ; and the insert in the figure shows the respective voltammogram. The equation can be expressed as log I (A) = 0.61 log υ (mV s^{-1}) – 6.8, (R= 0.997). According to the literature, a slope of log I vs. log *v* close to 0.50 is indicative of the occurrence of a diffusional process, while a slope of 1.0 is associated with adsorption processes [51]. As can be seen from the equation, the value of 0.61 lies between 0.50 and 1.0; this indicates that the oxidation of narirutin was controlled by a mixed adsorption–diffusion process on the surface of the 3DnpNi/SPE. This result is in agreement

with the results obtained for similar flavonoids in studies previously reported in the literature [50,52].

Fig 7B shows the plot of peak potential *E versus* log υ; here, one can observe that the *E* values shifted to more positive values when the scan rate was increased; this points to the irreversibility of the electrode reaction [53]. The relationship between *E* and log υ is expressed by the Laviron's equation [54], when the scan rate is larger than 200 mV s^{-1}, according to the following equation:

$E = E^0 + 2.303RT/\alpha nF (\log RTk_o/ \alpha nF - \log\upsilon)$ (2),

where 'α' is the charge transfer coefficient for the oxidation step, 'k_0' is the standard heterogeneous rate constant of the reaction (cm s^{-1}), 'υ' is the scan rate (V s^{-1}), 'E^0' is the formal redox potential (V), 'T' is the temperature (K), '*R'* is the universal gas constant (8.314 J K^{-1} mol^{-1}), *n* is the number of electrons involved in the rate determining step, and *'F'* is the Faraday constant (96,485 C mol^{-1}). Based on the experiments conducted, the relationship between the oxidation peak potentials and log υ (200 – 500 mV s^{-1}) can be described as follows: $E = 0.11 \log\upsilon + 0.76$, R = 0.997 (Fig. 7B). Hence, one can calculate *αn* based on the slope of *E vs* log υ. *Here,* the value obtained for *αn was 0.56*. In general, the theoretical value of *α* for an irreversible electrode process *is* 0.50, according to Bard and Faulkner [55]. So, the value of *n* can be said to be 1. The value of *n* indicates that one electron was involved in narirutin oxidation in 0.1 mol L^{-1} citrate buffer solution.

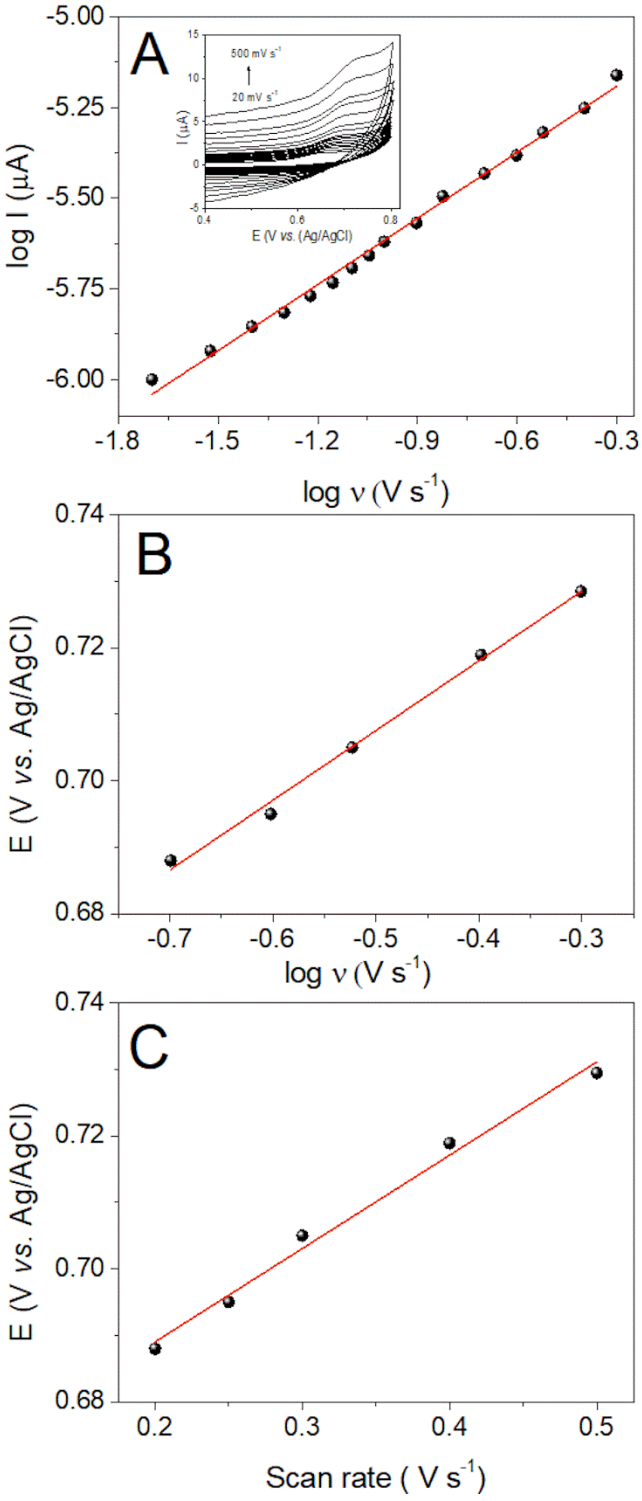

Fig. 7. (A) Relationship between log I(A) and log υ. Insert: plot of current versus scan rates in citrate buffer solution (pH = 4.0) containing 1.0×10^{-5} mol L^{-1} of narirutin (20 - 500 mV s^{-1}). (B) Relation between the peak current of 5.0×10^{-5} mol L^{-1} of narirutin and the logarithm of the scan rates. (C) Relation between potential and scan rate. (Scan rates 200 - 500 mV s^{-1}).

The value of k_0 provides us with the information regarding the speed of electron transfer between a molecule and the electrode surface; this value can be determined from equation (2) if the value of E^0 is known. To obtain the value of E^0, the graph of E^0 versus υ was plotted; and based on the value of the intercept (Fig. 7C), by extrapolating to the vertical axis at υ = 0, the value of E^0 was obtained [56]. The linear regression equation obtained for the curve was E= 0.14 υ + 0.67, R = 0.997. In this system, the value obtained for E^0 was 0.66 V *vs* Ag/AgCl; based on this value, k_0 was found to be 1.0 x 10^{-3} cm s^{-1} at 298 K.

3.5 Chronocoulometry studies

Chronocoulometric analysis was conducted aiming at investigating the adsorption capacity (Γ^*) and the diffusion coefficient (D) of narirutin oxidation on 3DnpNi/SPE, since the electrode reaction of narirutin was controlled by both processes. The experiments were carried out at the constant potential of 0.63 V in the presence and absence of 1.0 × 10^{-5} mol L^{-1} of narirutin, respectively. The charge (Q) versus $t^{1/2}$ curves obtained are shown in Fig. 7. The a_0 curve is related to the blank solution and a_1 is related to the narirutin solution. The linear equations obtained for curves a_0 and a_1 were Q (10^{-6} C) = 5.49 $t^{1/2}$ - 2.64 (R = 0.999) and Q (10^{-6} C) = 22.8 $t^{1/2}$ - 1.28 (R = 0.999), respectively. One will observe that the slope and the intercept of the two straight lines are different. This confirms the previous result obtained which showed that the oxidation of narirutin was controlled by both adsorption and diffusion processes. Based on the equation given by Anson [57],

$$Q = [2nFAC(Dt)^{1/2}]/\pi^{1/2} + Q_{dl} + Q_{ads} \quad (3),$$

where A is the active area of the 3DnpNi/SPE, C is the concentration of substrate, F is the Faraday constant, n is the number of electrons, Q_{dl} is the double-layer charge, and Q_{ads} is the Faradaic charge due to the oxidation of adsorbed narirutin. Here, Q_{ads} represents the difference between the

two intercepts. In addition, the surface coverage (Γ^*) of narirutin on 3DnpNi/SPE was calculated based on the Farady law equation below [58]:

$Q_{ads}= nFA\Gamma^*$ (4).

The value obtained for Γ^* was 1.1×10^{-10} mol cm^{-2}. Based on the slope of curve a_1 and equation 3, the value of *D* obtained was 2.8×10^{-8} cm^2 s^{-1}.

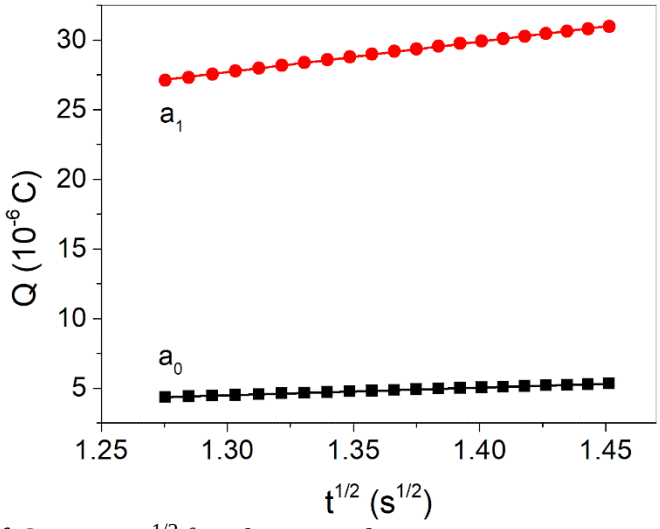

Fig. 8. The plot of Q versus $t^{1/2}$ for chronocoulometric experiments in citrate buffer solution (pH 4.0) in the absence of narirutin (a_0) and in the presence (a_1) of 1.0×10^{-5} mol L^{-1} narirutin. Applied potential of 0.65 V.

According to the literature, the phenol groups of the B ring in flavonoids are considered the electroactive moiety of the molecule [59,60]. Hence, one can say that the peak observed in the narirutin voltammogram is related to the electrooxidation of the 4-hydroxyl group of ring B. The oxidation process involved 1 electron and 1 proton in a single irreversible step, with the formation of phenoxyl radical (peak observed), which was adsorbed on the electrode surface due to the irreversible reaction (dimerization), to form dimer products [61,62]. Analogous patterns of behavior have been reported for structurally similar phenolic compounds, such as naringin, apigenin, and kaempferol [63–65]. Based on these results, the proposed mechanism for the electrochemical oxidation of narirutin in 0.1 mol L^{-1} citrate buffer solution (pH= 4.0) is shown in scheme 1.

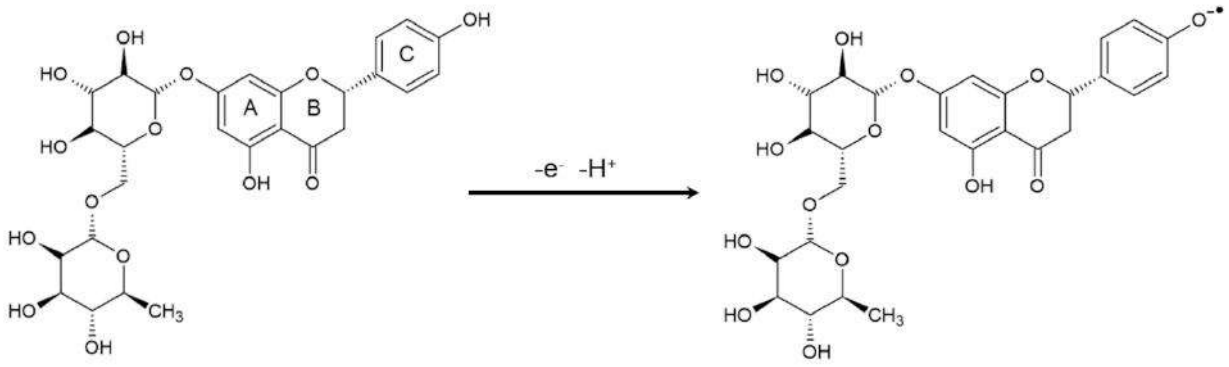

Scheme 1. Proposed mechanism for electrooxidation of narirutin.

3.6 Analytical performance

The DPV technique was applied in order to evaluate the analytical performance and the practical feasibility of 3DnpNi/SPE in terms of narirutin oxidation. This technique was chosen due to its sensitivity and precision, coupled with the fact that it has a lower background current compared to other voltammetric techniques. The overlapped cyclic voltammograms of narirutin in the concentration range of 1.0×10^{-7} mol L^{-1} to 1.0×10^{-5} mol L^{-1} are shown in Fig. 9A. The relationship between the variation in peak current and narirutin concentration is shown in Fig. 9B. The linear regression equation and correlation coefficient obtained were I(A) = 0.31 x + 1.06×10^{-6}, and R= 0.998, respectively. The relative standard deviation (RSD) values obtained for the slope and the intercept were 1.6 % and 3.7 %, respectively. The values obtained for LOD, LOQ, and analytical sensitivity were 3.9×10^{-8} mol L^{-1}, 1.3×10^{-7} mol L^{-1}, and 0.31 A L mol^{-1} (n =3), respectively.

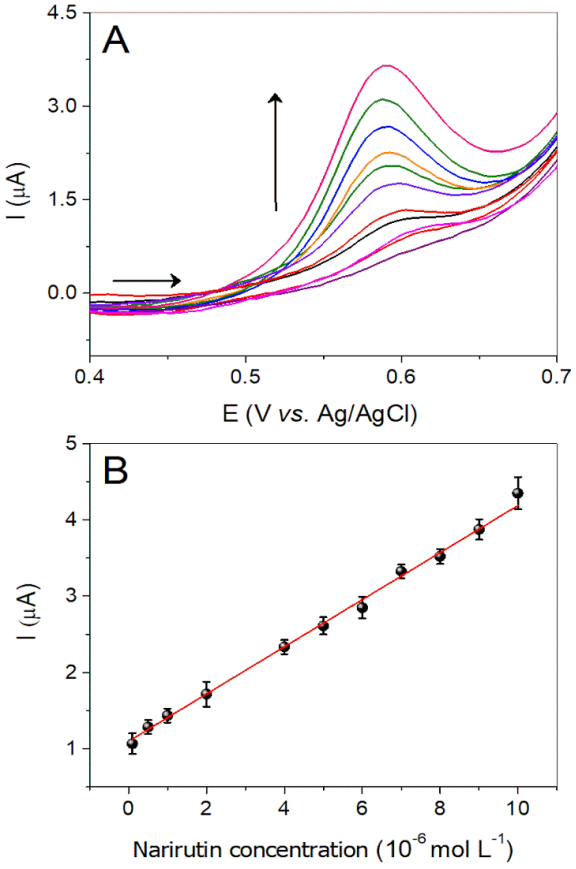

Fig. 9. (A) DPV curves for different concentrations of narirutin obtained through the application of 3DnpNi/SPE in 0.1 mol L^{-1} citrate buffer solution (pH= 4.0). Narirutin concentration in the range of 1.0×10^{-7} mol L^{-1} to 1.0×10^{-5} mol L^{-1}. (B) Calibration plot of peak current versus narirutin concentration.

Considering that the present work reports the development and application of the first electroanalytical method for narirutin determination, a comparison was made between the method proposed in this work and other analytical methods described in the literature; this can be found in Table 1. The parameters analyzed in this comparative study included the linear range and the LOD.

Table 1. Comparison of the 3DnpNi/SPE and other analytical methods previously reported for the determination of narirutin.

Analytical technique	Linear range (mol L^{-1})	LOD (mol L^{-1})	Ref.
HPLC-PDA	$3.45 \times 10^{-5} – 1.38 \times 10^{-3}$	1.21×10^{-5}	[13]
HPLC-UV	$2.43 \times 10^{-7} – 2.82 \times 10^{-4}$	8.06×10^{-8}	[12]
HPLC-ESI-MS	$3.45 \times 10^{-9} – 1.72 \times 10^{-6}$	1.72×10^{-9}	[16]
HPLC-PDA	$1.34 \times 10^{-6} – 8.61 \times 10^{-5}$	2.93×10^{-7}	[14]
LC–MS/MS	$1.72 \times 10^{-8} – 1.72 \times 10^{-5}$	8.63×10^{-10}	[14]
UPLC–PDA	$1.72 \times 10^{-7} – 1.72 \times 10^{-5}$	2.87×10^{-8}	[66]
HPLC–PDA	$1.34 \times 10^{-6} – 8.61 \times 10^{-5}$	8.61×10^{-8}	[15]
UHPLC-QqQ-MS	$1.05 \times 10^{-8} – 5.70 \times 10^{-6}$	3.45×10^{-9}	[17]
LC	$3.45 \times 10^{-4} – 1.72 \times 10^{-7}$	4.12×10^{-8}	[67]
3DnpNi/SPE	$1.00 \times 10^{-7} – 1.00 \times 10^{-5}$	3.96×10^{-8}	This work

HPLC: high-performance liquid chromatographic; UV: ultraviolet; ESI: electrospray ionization; MS: mass spectrometry; UHPLC-QqQ-MS: ultra-high performance liquid chromatography coupled with triple-quadrupole mass spectrometry; PDA: photodiode array detector; UPLC: ultra-performance liquid chromatography; LC: liquid chromatography.

As can be observed in Table 1, with the exception of the methods developed by Cho et al [16], Seo et al. [15], and Zhao et al. [17], the electroanalytical method proposed in this work exhibited an excellent analytical performance with a wider linear range and a significantly lower LOD compared to most of the methods reported in the literature. It is worth noting that, when it comes to chromatographic methods, the proposed electrode is found to be comparatively cheaper, and does not require the use of large volumes of solvents, complex mobile phase or long periods of analysis. Taking these factors into account, the 3DnpNi/SPE-based electroanalytical method can be regarded an environmentally friendly technique, since only 50 µl solution is required to be applied on the electrode surface in order to perform the analysis. Certainly, the use of low amount of solution minimizes the generation of waste. In addition, the proposed method does not require sample purification steps and/or lengthy filtration processes.

The inter-electrode repeatability (n = 5) was investigated by CV using the concentration of 5.0×10^{-6} mol L^{-1} of narirutin in 0.1 mol L^{-1} citrate buffer solution (pH 4.0). The average oxidation current obtained was 2.2 µA, with RSD of 5.9 %. In addition, the 3DnpNi/SPE was stored for 10 days in contact with air at room temperature (25 °C). The current response relative to narirutin

detection was found to be 94.2 % of its initial peak current value. These results show that the 3DnpNi/SPE has good repeatability and long-term stability.

3.7 Interferences studies

To be regarded satisfactorily suitable for use, the proposed 3DnpNi/SPE is required to have a reasonable anti-interference ability. For the evaluation of selectivity of the 3DnpNi/SPE for narirutin determination, the influence of some interfering flavonoids, such as naringenin and hesperidin, as well as glucose and fructose, were investigated in the presence of narirutin. The current signals obtained by DPV using 1.0×10^{-6} mol L^{-1} narirutin in 0.1 mol L^{-1} citrate buffer solution (pH= 4.0) were compared in the absence and presence of the aforementioned interfering molecules (at the concentration of 1.0×10^{-5} mol L^{-1}). The species were considered to have an interfering effect when the current value causes a relative error $\leq \pm$ 5.0 % (tolerance limit) for the current response of narirutin. The results showed a relative error percentage of - 4.7 %, - 3.8 %, 3.2 % and 2.9 % at peak current for the analyses conducted in the presence of hesperidin, naringenin, glucose, and fructose, respectively. The effect of the presence of hesperidin in the solution can be found in Fig. S3A; one can observe that the oxidation peak occurred at 0.10 and 0.38 V, and there was no interfering effect on the oxidation peak of narirutin (at 0.60 V). The analysis involving naringenin (see Fig. S3B) showed the oxidation peak at 0.42 V. For the analyses involving glucose and fructose, (Fig. S3C and S3D), apart from the peak related to narirutin, no peak was observed for the sugars investigated. Based on these results, the 3DnpNi/SPE electrode was found to present good selectivity for the detection of narirutin molecules.

3.8 Determination of narirutin in yellow water

The analytical applicability of 3DnpNi/SPE for the determination of narirutin in yellow water samples from the orange industry was examined using the DPV technique. The samples

were prepared as described in *Section 2.5*. The standard addition method was used for determining the concentration of narirutin in the samples; this method was employed once it can minimize to the maximum the matrix interferences. The results obtained are presented in Table 2. The samples were spiked with known concentrations of standard narirutin in the range of 2.0×10^{-6} mol L^{-1} to 6.0×10^{-6} mol L^{-1} (Fig. S4). A linear relationship was observed between the current peak and the added concentration of narirutin. The regression equation was as follows: $y = 0.56\ x + 2.3 \times 10^{-6}$ ($R = 0.999$). From the standard addition curve, and based on the extrapolation of the straight line (Fig. S3) and the sample dilution (20-fold), the concentrations of narirutin found in the yellow water samples were $(8.3 \pm 0.39) \times 10^{-5}$ mol L^{-1} (n = 3). To determine the analytical accuracy of the proposed method, recovery experiments were performed in standard solutions. The recovery rates obtained ranged from 97.1% to 100.9%, with RSD lower than 7.0 %. These results show that the method presents an excellent degree of accuracy.

Table 2. Determination of narirutin in yellow water samples (n=3).

Added (10^{-6} mol L^{-1})	Found (10^{-6} mol L^{-1})	Recovery (%)	RSD (%)
2.0	2.0 ± 0.1	101.6 ± 6.7	6.6
4.0	3.9 ± 0.1	98.4 ± 3.0	3.0
6.0	5.9 ± 0.03	99.8 ± 0.6	0.57

The concentration of narirutin in the yellow water samples was also determined by HPLC. The concentration value obtained was $(8.6 \pm 0.25) \times 10^{-5}$ mol L^{-1} (Table S1), and the RSD obtained between the two techniques was 0.16 %. These results demonstrate a good agreement between the proposed method and the comparative method (HPLC); essentially, this points to the reliability of the method proposed in this work. Thus, the findings of the present study show that the proposed 3DnpNi/SPE-based electroanalytical method can certainly be used for the determination of narirutin in yellow water.

4 Conclusions

The present work reported the development of a simple and complete electrochemical method based on three-dimensional nanoporous nickel deposited on the surface of SPE and its successful application for the determination of narirutin. Compared to bare SPE, the modification of SPE with nanoporous nickel significantly enhanced the electrochemical performance of the electrode in terms of the oxidation of narirutin. The present work also investigated the electrochemical behavior of narirutin and the mechanism for its electrochemical oxidation. The high surface area and good electrical conductivity of the 3DnpNi/SPE sensor contributed to the excellent analytical performance of the device. Being the first electrochemical sensor applied toward the determination of narirutin, the sensor presented good sensitivity and low detection limit. The proposed method was found to exhibit good selectivity, and there was no significant interference in the application of the electrode for narirutin detection in the sample analyzed. The results obtained from the application of the proposed 3DnpNi/SPE-based electroanalytical method were compared with those of the HPLC technique, where an excellent agreement was found between the two techniques. The experimental analyses conducted using real samples showed that the 3DnpNi/SPE is an effective, sensitive, and reliable electrode suitable for the determination of narirutin in yellow water samples.

Declaration of conflicts interest

The authors declare no conflicts of interest.

Acknowledgments

M.A. Beluomini is particularly grateful to the São Paulo Research Foundation (FAPESP) for the pos-doctorate scholarship (grant #2018/12131-6). The authors are also grateful for FAPESP for

the financial support granted in the course of this research (grants #2014/50945-4 and #2017/22401-8).

References

[1] P.S. Calabrò, L. Pontoni, I. Porqueddu, R. Greco, F. Pirozzi, F. Malpei, Effect of the concentration of essential oil on orange peel waste biomethanization: Preliminary batch results, Waste Manag. 48 (2016) 440–447.

[2] P. Deng, Z. Xu, Y. Kuang, Electrochemical determination of bisphenol A in plastic bottled drinking water and canned beverages using a molecularly imprinted chitosan-graphene composite film modified electrode, Food Chem. 157 (2014) 490–497.

[3] A. Di Mauro, B. Fallico, A. Passerini, E. Maccarone, Waste Water from Citrus Processing as a Source of Hesperidin by Concentration on Styrene−Divinylbenzene Resin, J. Agric. Food Chem. 48 (2000) 2291–2295.

[4] C. Feng, J.F. García-Martín, M. Broncano Lavado, M. del C. López-Barrera, P. Álvarez-Mateos, Evaluation of different solvents on flavonoids extraction efficiency from sweet oranges and ripe and immature Seville oranges, Int. J. Food Sci. Technol. 55 (2020) 3123–3134.

[5] K. Sharma, N. Mahato, M.H. Cho, Y.R. Lee, Converting citrus wastes into value-added products: Economic and environmently friendly approaches, Nutrition. 34 (2017) 29–46.

[6] H.-Y. Park, S.K. Ha, H. Eom, I. Choi, Narirutin fraction from citrus peels attenuates alcoholic liver disease in mice, Food Chem. Toxicol. 55 (2013) 637–644.

[7] S. Chakraborty, S. Basu, Multi-functional activities of citrus flavonoid narirutin in Alzheimer's disease therapeutics: An integrated screening approach and in vitro validation, Int. J. Biol. Macromol. 103 (2017) 733–743.

[8] N. Funaguchi, Y. Ohno, B.L.B. La, T. Asai, H. Yuhgetsu, M. Sawada, G. Takemura, S. Minatoguchi, T. Fujiwara, H. Fujiwara, Narirutin inhibits airway inflammation in an allergic mouse model, Clin. Exp. Pharmacol. Physiol. 34 (2007) 766–770.

[9] W. Ngwa, R. Kumar, D. Thompson, W. Lyerly, R. Moore, T.-E. Reid, H. Lowe, N. Toyang, Potential of Flavonoid-Inspired Phytomedicines against COVID-19, Molecules. 25 (2020) 2707. doi:10.3390/molecules25112707.

[10] F. Meneguzzo, R. Ciriminna, F. Zabini, M. Pagliaro, Hydrodynamic Cavitation-based Rapid Expansion of Hesperidin-rich Products from Waste Citrus Peel as a Potential Tool Against COVID-19, Preprints. (2020) 2020040152. .

[11] H. Tutunchi, F. Naeini, A. Ostadrahimi, M.J. Hosseinzadeh-Attar, Naringenin, a flavanone with antiviral and anti-inflammatory effects: A promising treatment strategy against <scp>COVID</scp> -19, Phyther. Res. (2020) 6781.

[12] B. Barfi, A. Asghari, M. Rajabi, A. Barfi, I. Saeidi, Simplified miniaturized ultrasound-assisted matrix solid phase dispersion extraction and high performance liquid chromatographic determination of seven flavonoids in citrus fruit juice and human fluid samples: Hesperetin and naringenin as biomarkers, J. Chromatogr. A. 1311 (2013) 30–40.

[13] M.L. Calabrò, V. Galtieri, P. Cutroneo, S. Tommasini, P. Ficarra, R. Ficarra, Study of the extraction procedure by experimental design and validation of a LC method for determination of flavonoids in Citrus bergamia juice, in: J. Pharm. Biomed. Anal., Elsevier, 2004: pp. 349–363.

[14] C.S. Seo, H.K. Shin, Quality assessment of traditional herbal formula, Hyeonggaeyeongyo-tang through simultaneous determination of twenty marker components by HPLC–PDA and LC–MS/MS, Saudi Pharm. J. 28 (2020) 427–439.

[15] C.-S. Seo, H.-K. Shin, Simultaneous Determination of 12 Marker Components in

Yeonkyopaedok-san Using HPLC–PDA and LC–MS/MS, Appl. Sci. 10 (2020) 1713.
[16] H.E. Cho, S.Y. Ahn, S.C. Kim, M.H. Woo, J.-T. Hong, D.C. Moon, Determination of Flavonoid Glycosides, Polymethoxyflavones, and Coumarins in Herbal Drugs of *Citrus* and *Poncirus* Fruits by High Performance Liquid Chromatography–Electrospray Ionization/Tandem Mass Spectrometry, Anal. Lett. 47 (2014) 1299–1323.
[17] X.J. Zhao, D. Chen, P.A. Kilmartin, B.N. Jiao, Simultaneous Determination of Phenolics and Polymethoxylated Flavones in Citrus Fruits by Ultra-High Performance Liquid Chromatography Coupled with Triple-Quadrupole Mass Spectrometry (UHPLC-QqQ-MS), Anal. Lett. 52 (2019) 1926–1938.
[18] J. Li, L. He, J. Jiang, Z. Xu, M. Liu, X. Liu, H. Tong, Z. Liu, D. Qian, Facile syntheses of bimetallic Prussian blue analogues (KxM[Fe(CN)6]·nH2O, M=Ni, Co, and Mn) for electrochemical determination of toxic 2-nitrophenol, Electrochim. Acta. 353 (2020) 136579.
[19] I.M. Apetrei, C. Apetrei, A modified nanostructured graphene-gold nanoparticle carbon screen-printed electrode for the sensitive voltammetric detection of rutin, Meas. J. Int. Meas. Confed. 114 (2018) 37–43.
[20] Z. Zhou, P. Zhao, C. Wang, P. Yang, Y. Xie, J. Fei, Ultra-sensitive amperometric determination of quercetin by using a glassy carbon electrode modified with a nanocomposite prepared from aminated graphene quantum dots, thiolated β-cyclodextrin and gold nanoparticles, Microchim. Acta. 187 (2020) 1–9.
[21] Q. He, Y. Wu, Y. Tian, G. Li, J. Liu, P. Deng, D. Chen, Facile Electrochemical Sensor for Nanomolar Rutin Detection Based on Magnetite Nanoparticles and Reduced Graphene Oxide Decorated Electrode, Nanomaterials. 9 (2019) 115.
[22] N. Sebastian, W.C. Yu, D. Balram, Synthesis of amine-functionalized multi-walled carbon nanotube/3D rose flower-like zinc oxide nanocomposite for sensitive electrochemical detection of flavonoid morin, Anal. Chim. Acta. 1095 (2020) 71–81.
[23] M.A. Beluomini, J.L. da Silva, N.R. Stradiotto, Amperometric determination of myo-inositol by using a glassy carbon electrode modified with molecularly imprinted polypyrrole, reduced graphene oxide and nickel nanoparticles, Microchim. Acta. 185 (2018) 170.
[24] Y. Pei, M. Hu, Y. Xia, W. Huang, Z. Li, S. Chen, Electrochemical preparation of Pt nanoparticles modified nanoporous gold electrode with highly rough surface for efficient determination of hydrazine, Sensors Actuators, B Chem. 304 (2020) 127416.
[25] X. Gao, Y. Gao, C. Bian, H. Ma, H. Liu, Electroactive nanoporous gold driven electrochemical sensor for the simultaneous detection of carbendazim and methyl parathion, Electrochim. Acta. 310 (2019) 78–85.
[26] D. Zhu, C. Xia, Z. Yang, X. Wang, T. Yang, C. Liang, F. Yin, Q. Li, Fabrication of non-enzyme glucose sensor via dealloying amorphous Zr-Cu alloy and anodic oxidation, Mater. Lett. 245 (2019) 49–52.
[27] M. Mirzaee, C. Dehghanian, Preparation of dendritic nanoporous Ni-NiO foam by electrochemical dealloying for use in high-performance supercapacitors, J. Solid State Electrochem. 22 (2018) 3639–3645.
[28] H. Wang, D. Qian, X. Xiao, S. Gao, J. Cheng, B. He, L. Liao, J. Deng, A highly sensitive and selective sensor based on a graphene-coated carbon paste electrode modified with a computationally designed boron-embedded duplex molecularly imprinted hybrid membrane for the sensing of lamotrigine, (2017).
[29] S. Lee, J. Lee, S. Park, H. Boo, H.C. Kim, T.D. Chung, Disposable non-enzymatic blood glucose sensing strip based on nanoporous platinum particles, Appl. Mater. Today. 10 (2018) 24–29.
[30] C.W. Bae, P.T. Toi, B.Y. Kim, W. Il Lee, H.B. Lee, A. Hanif, E.H. Lee, N.E. Lee, Fully

Stretchable Capillary Microfluidics-Integrated Nanoporous Gold Electrochemical Sensor for Wearable Continuous Glucose Monitoring, ACS Appl. Mater. Interfaces. 11 (2019) 14567–14575.
[31] H. Liu, P. He, Z. Li, J. Li, High surface area nanoporous platinum: facile fabrication and electrocatalytic activity, Nanotechnology. 17 (2006) 2167–2173.
[32] C. Tian, S. Zhang, H. Wang, C. Chen, Z. Han, M. Chen, Y. Zhu, R. Cui, G. Zhang, Three-dimensional nanoporous copper and reduced graphene oxide composites as enhanced sensing platform for electrochemical detection of carbendazim, J. Electroanal. Chem. 847 (2019) 113243.
[33] L.S. Yuan, Y.X. Zheng, M.L. Jia, S.J. Zhang, X.L. Wang, C. Peng, Nanoporous nickel-copper-phosphorus amorphous alloy film for methanol electro-oxidation in alkaline medium, Electrochim. Acta. 154 (2015) 54–62.
[34] Y. Yi, S. Uhm, J. Lee, Electrocatalytic Oxidation of Ethanol on Nanoporous Ni Electrode in Alkaline Media, Electrocatalysis. 1 (2010) 104–107.
[35] K. Nishio, H. Masuda, Anodization of Gold in Oxalate Solution To Form a Nanoporous Black Film, Angew. Chemie. 123 (2011) 1641–1645. doi:10.1002/ange.201005700.
[36] M.R. Majidi, S. Ghaderi, Hydrogen bubble dynamic template fabrication of nanoporous Cu film supported by graphene nanaosheets: A highly sensitive sensor for detection of nitrite, Talanta. 175 (2017) 21–29.
[37] Y. Li, Y.Y. Song, C. Yang, X.H. Xia, Hydrogen bubble dynamic template synthesis of porous gold for nonenzymatic electrochemical detection of glucose, Electrochem. Commun. 9 (2007) 981–988.
[38] I. Herraiz-Cardona, E. Ortega, L. Vázquez-Gómez, V. Pérez-Herranz, Double-template fabrication of three-dimensional porous nickel electrodes for hydrogen evolution reaction, Int. J. Hydrogen Energy. 37 (2012) 2147–2156.
[39] H. Qiu, T. Tang, M. Asif, X. Huang, Y. Hou, 3D Porous Cu Current Collectors Derived by Hydrogen Bubble Dynamic Template for Enhanced Li Metal Anode Performance, Adv. Funct. Mater. 29 (2019) 1808468.
[40] M.A. Beluomini, J.L. da Silva, A.C. de Sá, E. Buffon, T.C. Pereira, N.R. Stradiotto, Electrochemical sensors based on molecularly imprinted polymer on nanostructured carbon materials: A review, J. Electroanal. Chem. 840 (2019) 343–366.
[41] H. Beitollahi, S.Z. Mohammadi, M. Safaei, S. Tajik, Applications of electrochemical sensors and biosensors based on modified screen-printed electrodes: A review, Anal. Methods. 12 (2020) 1547–1560.
[42] E.C. Serban, A. Balan, A.M. Iordache, A. Cucu, C. Ceaus, M. Necula, G. Ruxanda, C. Bacu, E. Mamut, I. Stamatin, Urea/ hydrogen peroxide fuel cell, Dig. J. Nanomater. Biostructures. 9 (2014) 1647-1654. 661
[43] B. Dinesh, K.S. Shalini Devi, A.S. Kumar, Curcumin-quinone immobilised carbon black modified electrode prepared by in-situ electrochemical oxidation of curcumin-phytonutrient for mediated oxidation and flow injection analysis of sulfide, J. Electroanal. Chem. 804 (2017) 116–127.
[44] C.A. Marozzi, A.C. Chialvo, Development of electrode morphologies of interest in electrocatalysis. Part 1: Electrodeposited porous nickel electrodes, Electrochim. Acta. 45 (2000) 2111–2120.
[45] X. Yu, M. Wang, Z. Wang, X. Gong, Z. Guo, The structure evolution mechanism of electrodeposited porous Ni films on NH 4 Cl concentration, Appl. Surf. Sci. 360 (2016) 502–509.
[46] Š. Trafela, J. Zavašnik, S. Šturm, K.Ž. Rožman, Formation of a Ni(OH)2/NiOOH active redox couple on nickel nanowires for formaldehyde detection in alkaline media, Electrochim. Acta. 309 (2019) 346–353.

[47] S. Trasatti, O.A. Petrii, International Union of Pure and Applied Chemistry Physical Chemistry Division Commission on Electrochemistry: Real Surface Area Measurements in Electrochemistry, Pure Appl. Chem. 63 (1991) 711–734.
[48] W. McCormick, D. McCrudden, Development of a highly nanoporous platinum screen-printed electrode and its application in glucose sensing, J. Electroanal. Chem. 860 (2020) 113912.
[49] H.R. Zare, N. Nasirizadeh, A study of the electrochemical behavior of hematoxylin as an important bioactive flavonoid, Electrochim. Acta. 56 (2011) 3920–3925.
[50] J. Wu, L. Wang, Q. Wang, L. Zou, B. Ye, The novel voltammetric method for determination of hesperetin based on a sensitive electrochemical sensor, Talanta. 150 (2016) 61–70.
[51] L.R.F. A.J. Bard, Electrochemical Methods Fundamentals and Application, 2nd ed, Wiley, 2004.
[52] A.A. Abdullah, Y. Yardım, Z. Şentürk, The performance of cathodically pretreated boron-doped diamond electrode in cationic surfactant media for enhancing the adsorptive stripping voltammetric determination of catechol-containing flavonoid quercetin in apple juice, Talanta. 187 (2018) 156–164.
[53] B.W. Rossiter, J.F. Hamilton, Physical methods of chemistry, 1986.
[54] E. Laviron, General expression of the linear potential sweep voltammogram in the case of diffusionless electrochemical systems, J. Electroanal. Chem. 101 (1979) 19–28.
[55] A.J. Bard, L.R. Faulkner, Electochemical Method: Fundamentlas and Applications, 2nd ed., Wiley, 2000.
[56] Y. Wu, X. Ji, S. Hu, Studies on electrochemical oxidation of azithromycin and its interaction with bovine serum albumin, Bioelectrochemistry. 64 (2004) 91–97.
[57] F.C. Anson, Application of Potentiostatic Current Integration to the Study of the Adsorption of Cobalt(III)-(Ethylenedinitrilo(tetraacetate) on Mercury Electrodes, Anal. Chem. 36 (1964) 932–934.
[58] C. Hu, C. Yang, S. Hu, Hydrophobic adsorption of surfactants on water-soluble carbon nanotubes: A simple approach to improve sensitivity and antifouling capacity of carbon nanotubes-based electrochemical sensors, Electrochem. Commun. 9 (2007) 128–134.
[59] A. Zhupanova, E. Guss, G. Ziyatdinova, H. Budnikov, Simultaneous Voltammetric Determination of Flavanones Using an Electrode Based on Functionalized Single-Walled Carbon Nanotubes and Polyaluminon, Anal. Lett. 53 (2020) 2170–2189.
[60] R.D.Q. Ferreira, S.J. Greco, M. Delarmelina, K.C. Weber, Electrochemical quantification of the structure/antioxidant activity relationship of flavonoids, Electrochim. Acta. 163 (2015) 161–166.
[61] T.A. Enache, A.M. Oliveira-Brett, Phenol and para-substituted phenols electrochemical oxidation pathways, J. Electroanal. Chem. 655 (2011) 9–16.
[62] M. Ferreira, H. Varela, R.M. Torresi, G. Tremiliosi-Filho, Electrode passivation caused by polymerization of different phenolic compounds, Electrochim. Acta. 52 (2006) 434–442.
[63] T.-L. Xing, F. Wang, Y.-Y. Mao, L.-P. Wang, B.-X. Ye, Electrochemical Behavior of Apigenin at a Glassy Carbon Electrode and its Analytical Application, J. Chinese Chem. Soc. 56 (2009) 303–309.
[64] B. YANG, K. ARAI, F. KUSU, Electrochemical Behaviors of Quercetin and Kaempferol in Neutral Buffer Solution., Anal. Sci. 17 (2001) 987–989. doi:10.2116/analsci.17.987.
[65] G. Ziyatdinova, E. Yakupova, E. Ziganshina, H. Budnikov, First Order Derivative Voltammetry on the *in situ* Surfactant Modified Electrode for Naringin Quantification, Electroanalysis. 31 (2019) 2130–2137.

Supplementary Information (SI)

Synthesis of three-dimensional nanoporous nickel based on dynamic hydrogen bubble template used for electrochemical detection of narirutin in citrus wastewater.

Maísa Azevedo Beluomini[a,c], Nelson Ramos Stradiotto[a,b], Maria Valnice Boldrin[a,c].

[a] Analytical Chemistry Department, Institute of Chemistry, São Paulo State University (UNESP), 55 Prof. Francisco Degni St., Araraquara 14800-060, São Paulo State, Brazil.

[b] Bioenergy Research Institute (IPBEN), São Paulo State University (UNESP), 55 Prof. Francisco Degni St., Araraquara 14800-060, São Paulo State, Brazil.

[c] National Institute of Alternative Technologies for Detection, Toxicological Evaluation and Removal of Micropollutants and Radioactive Substances (INCT-DATREM), São Paulo State University (UNESP), 55 Prof. Francisco Degni St., Araraquara 14800-060, São Paulo State, Brazil.

* Corresponding author: maisa.beluomini@unesp.br

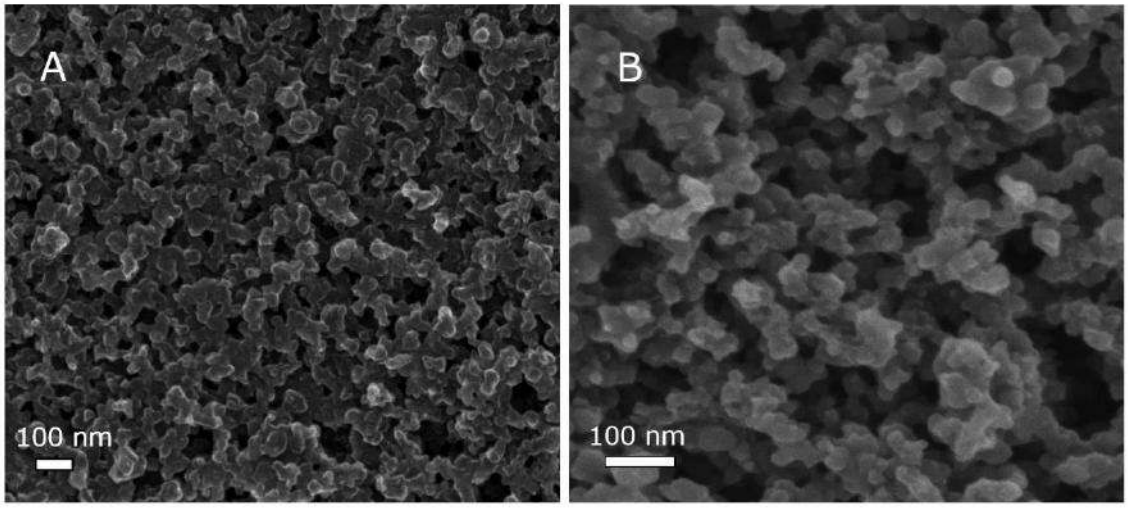

Figure S1. FEG-SEM images for 3DnpNi/SPE with magnification (A) 50,000 and (B) 100,000.

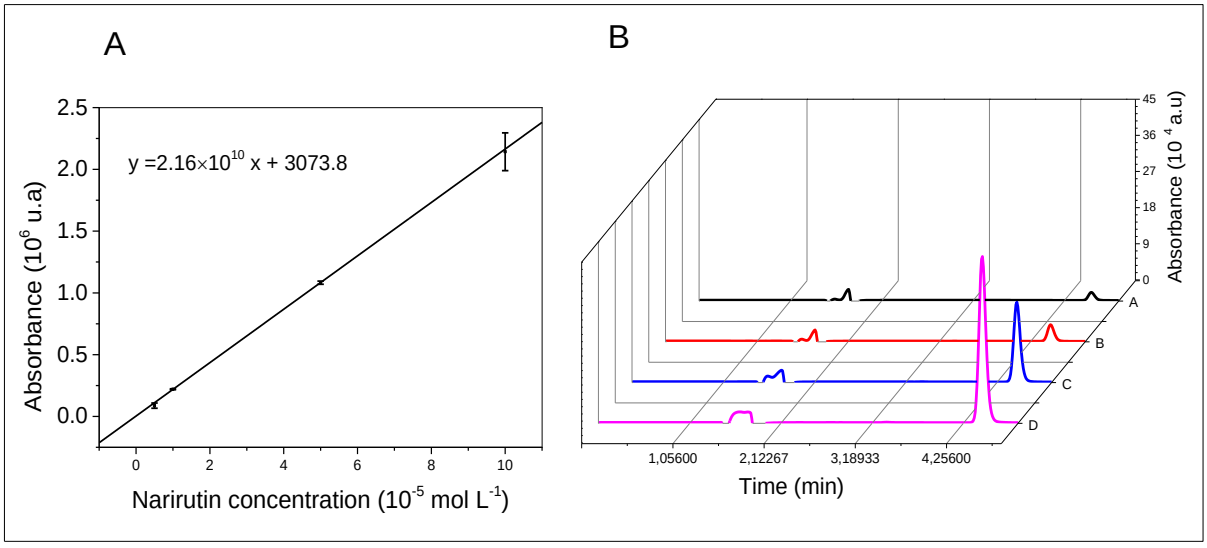

Fig. S2. (A) The analytical curve for HPLC analysis was obtained in the range of 5.0×10^{-6} mol L^{-1} to 1.0×10^{-4} mol L^{-1} of the narirutin standard. The linear regression equation and correlation coefficient were I (a.u) = 2.16×10^{-10} x + 3037.8, R= 0.999, (n=3). (B) Chromatogram of the analytical curve of narirutin (retention time: 4.63 min).

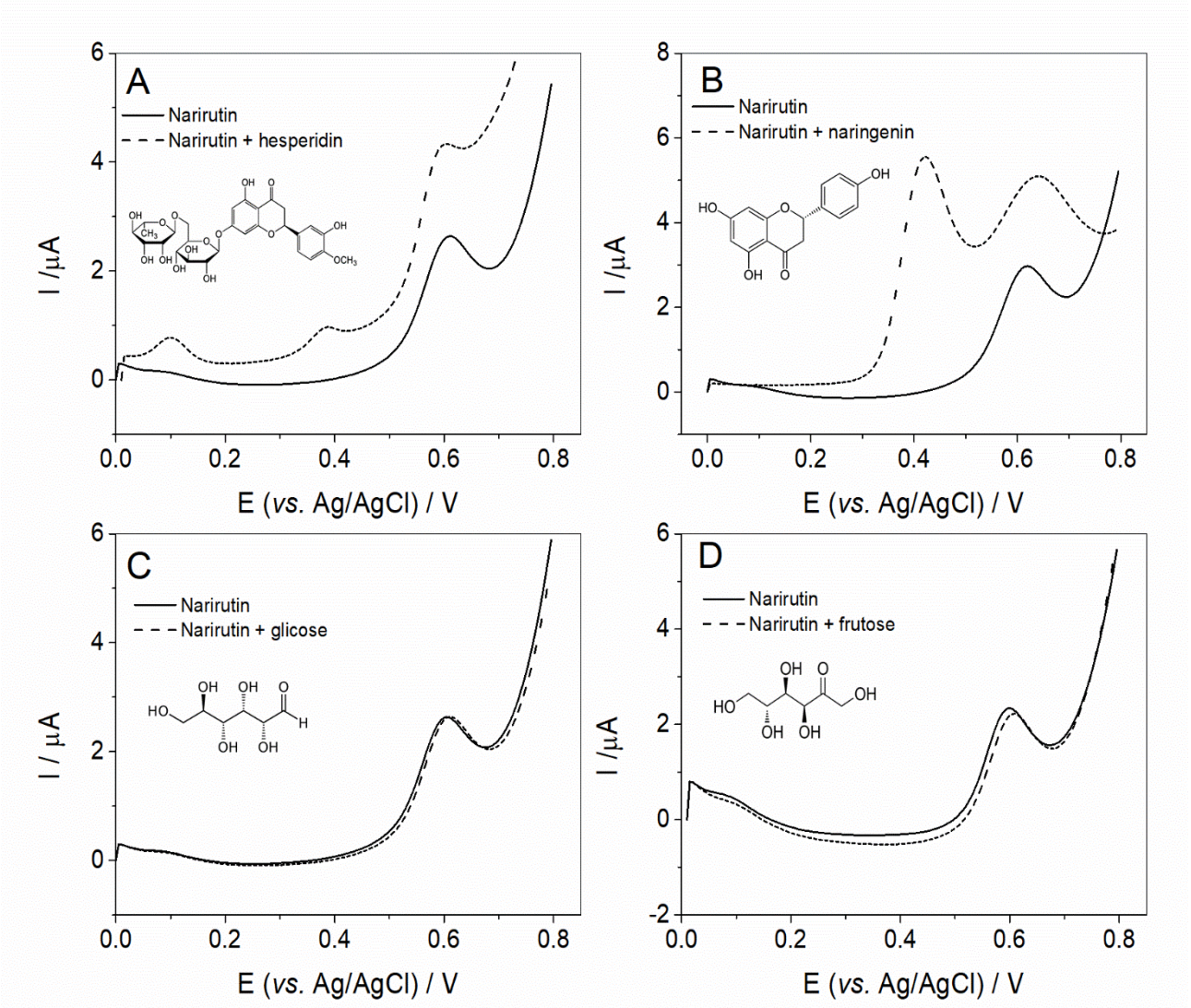

Fig. S3. Effect of possible interference (A) hesperidin, (B) naringenin, (C) glucose and (D) fructose, in the DPV response for the determination of 1.0×10^{-6} mol L^{-1} of narirutin in 0.1 mol L^{-1} citrate buffer solution (pH= 4.0). The concentration rate of the interfering solution was 1:10 (narirutin: interferent), using 3DnpNi/SPE.

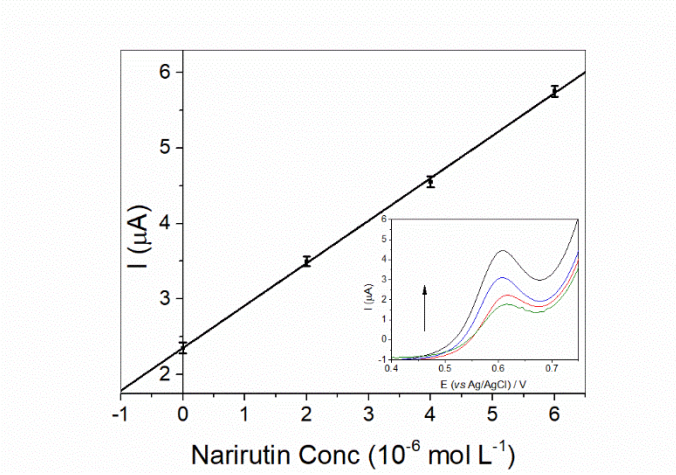

Figure S4. Linear relationship between a current peak plotted against the added concentration of narirutin from 2.0 × 10^{-6} mol L^{-1} to 6.0 × 10^{-6} mol L^{-1}, and the corresponding differential pulse voltammograms.

Sample application in HPLC.

Sample application was performed through the area obtained for the peak reference to narirutin (retention time of 4.63 min), using the analytical curve method. The areas with the respective quantities found are shown in Table S1. The value found was (8.6 ± 0.25) × 10^{-5} mol L^{-1} narirutin.

Table S1. Chromatographic determination of narirutin in yellow water samples, (n=3)

Analysis	**Peak area**	**Found (10^{-5} mol L^{-1})**
1	1910512	8.83
2	1832054	8.46
3	1808043	8.36

Using an Electrochemical MIP sensor for Selective Determination of 1-Naphthol in Oilfield Produced Water

Mariana Bartilotti Garcia[1,2*], Maísa Azevedo Beluomini[1,2], Maria Valnice Boldrin Zanoni[1,2]

[1]National Institute of Alternative Technologies for Detection, Toxicological Evaluation and Removal of Micropollutants and Radioactive Substances (INCT-DATREM), São Paulo State University (UNESP), 55 Prof. Francisco Degni St., Araraquara 14800-060, São Paulo State, Brazil.

[2] Analytical Chemistry Department, Institute of Chemistry, São Paulo State University (UNESP), 55 Prof. Francisco Degni St., Araraquara 14800-060, São Paulo State, Brazil.

*Corresponding author: mbartilottig@gmail.com;

ORCID: 0000-0002-6345-4419

HIGHLIGHTS

1. A novel electrochemical MIP sensor for 1-naphthol detection in producer water;
2. GCE-MIP was effectively constructed via electropolymerization technique;
3. High affinity and selectivity for the 1-naphthol was successfully achieved;
4. The proposed technique helped obtain well-shaped cavities for the MIP film;
5. The sensor was successfully applied in oilfield produced water sample.

ABSTRACT

A molecularly imprinted polymer (MIP) sensor was successfully constructed on glassy carbon electrode for determination of 1-naphthol (1-Nph). The sensor was constructed through the technique of electropolymerization on bare GCE in the presence of 1-naphthol (template molecule). The recognition of the target molecule was conducted indirectly using $[Fe(CN)_6]^{3-/4-}$ as electrochemical probe. The best conditions for the formation of the MIP sensor were evaluated by electrochemical techniques. After the construction and characterization of the sensor, an analytical curve was constructed for 1-Nph, where linear concentration range of 5.0 x 10^{-9} mol L^{-1} to 2.5 x 10^{-8} mol L^{-1} was obtained. The application of the NIP and MIP sensors led to significantly different results in terms of analyte recognition. The MIP sensor presented better selectivity for 1-Nph compared to the NIP; this implies that the cavities formed on the surface of the proposed electrode have good conformation. The limits of detection and quantification obtained were 1.5×10^{-9} mol L^{-1} and 4.9×10^{-9} mol L^{-1}, respectively, with amperometric sensitivity of $2.5\pm 0.07\times10^{7}$ μA L mol^{-1} (n=2). The MIP sensor was used to determine 1-Nph in oilfield produced water and the results obtained show that the sensor is a suitable device for the sensitive and selective quantification of the molecule in complex chemical environments.

Keywords: 1-Naphthol electroanalysis; molecularly imprinted electrochemical sensor; oilfield produced water; 1-Nph detection sensor.

1. Introduction

The petroleum industry is regarded one of the ten largest sources of toxic wastes emission in the environment (Varjani and Upasani, 2017). Considering that the oil extraction process is a great contributor to toxic wastes emission, there have been growing concerns regarding the discharge of oilfield produced water (OPW) into the environment, once OPW is generated as a by-product of the process. The oil extraction process uses water injection in the process in order to maintain enough pressure and to aid the flow of liquid and gases from the ground to the surface of the oilfield. Oilfield produced water (OPW) is thus simply the term given to the wastewater produced in this oil extraction process. OPW contains considerable amounts of dissolved organic and inorganic compounds; as such, its disposal into the environment requires rigorous control of the content of OPW. The content and disposal of OPW is regulated by environmental legislations and guidelines established by environmental agencies and regulatory bodies at both national and international levels. In Brazil, OPW disposal is regulated by the National Council of the Environment (CONAMA) under the Resolution n°393/207; based under the international threshold adopted worldwide, this resolution has set the medium standard maximum concentration of 29 mg L^{-1} /month for oil content in OPW disposed into the environment (2007). As OPW contains huge amounts of dissolved pollutants, their disposal into surface waters can be potentially harmful to human health and to all organisms in the entire aquatic ecosystem (Aidar et al., 1999).

A sample of raw wastewater from the oilfield industry is an extraordinarily complex matrix, which generally consists of a mixture of organic substances, salts, gases, metals, oils, and grease (Hansen BR and Davies SR, 1994; Stephenson, 1992). There have been huge concerns regarding the health and environmental risks posed by some of the hazardous substances which are part of the components of the oilfield wastewater. Among these hazardous substances include BTEX (benzene, toluene, etilbenzene and xylenes); phenols; and particularly polycyclic aromatic hydrocarbons (PAHs), which include anthracene, fluoranthene and naphthalene (Hansen BR and

Davies SR, 1994). With regard to naphthalene, in spite of its high degree of toxicity, its occurrence in wastewater is compromised due to its low stability under aqueous system in direct contact with UV-Vis light (Bernardo et al., 2016; McConkey et al., 2002). The organic compound 1-naphthol (1-Nph) is one of the main compounds derived from the degradation of naphthalene (McConkey et al., 2002); it is known to present higher stability and environmental toxicity (Cajaraville et al., 1989).

The analytical methods employed for the quantification of 1-Nph concentration in real and synthetic samples are mainly carried out using gas chromatography with mass spectrometer (Serdar et al., 2003); high performance liquid chromatography with an UV detector (Chin-Chen et al., 2012; Wang and Kuo, 1999), fluorescence detection ("Direct Determination of 1-Naphthol in Human Urine by Coupled-Column Liquid Chromatography with Fluorescence Detection," 2003), and magnetic solid phase extraction method (Zhou et al., 2016). Although electrochemical techniques applied toward the detection of analytes have presented fast and reliable results with high sensitivity and selectivity, virtually few studies reported in the literature have employed these techniques for the determination of 1-Nph [14–16, 17, 18–21].

Most electroanalytical methods reported in the literature and which have been capable of detecting 1-Nph are based on solid electrodes strategically modified to improve the interaction with naphthol (Nph) [14, 17, 20, 21]. In their work, Zhao et al. (2007) (Zhao et al., 2007) developed a biosensor through the immobilization of acid-denatured DNA on pre-treated glassy carbon electrode (GCE) surface, where the sensor contributed toward enhancing the recognition of 1-Nph with a detection limit (LOD) of 5.0×10^{-9} mol L^{-1} yet lacked stability. Tsai and Chen (2007) (Tsai and Chen, 2007) also developed Tosflex film-modified GCE sensor for the determination of 2-Nph, which yielded a LOD of 2×10^{-7} mol L^{-1}. Two other related studies worth mentioning involved the development of oxide-based sensors using meso-$NiCo_2O_4$ and High-Index Facet SnO_2, which resulted in amperometric detection of 7×10^{-9} mol L^{-1} and 5×10^{-9} mol

L^{-1}, respectively (Huang et al., 2012; Zhang et al., 2017). To date, when one takes into account analyses involving simultaneous and selective detection of 1-Nph and 2-Nph, there have been no reports in the literature about the development of a sensor for the quantification of 1-Nph and 2-Nph along with the interfering agents in complex matrices containing PAHs which are present in OPW.

The last decade has witnessed a great popularization of electrochemical sensors based on molecularly imprinted polymer (MIP) constructed on electrode surfaces; these MIP-based sensors have been used for the advance of the selectivity and sensitivity of electroanalytical methods (Beluomini et al., 2019). The formation of MIP is carried out through the polymerization of functional monomers with the target molecule, which may be the molecule that will be properly analyzed or which has a similar structure. After the formation of the film, the target molecule is extracted from the polymer matrix, generating cavities which will be used for the recognition of the analyte (Beluomini et al., 2019). In this context, the electropolymerization process occurs through the formation of free radicals, stemming from oxidation reactions that take place on the electrode surface. The coating of the electrode by electropolymerization has become more widely applied in the field compared to chemical techniques; this is because through electropolymerization it is possible to control the thickness of the polymeric film under voltammetric or amperometric conditions (Sharma et al., 2012). Specifically, the use of o-phenylenediamine (o-PD) for the construction of compact (rigid), continuous and thin polymer film on glassy carbon electrode has become well established in the literature (Beluomini et al., 2017; Buffon and Stradiotto, 2019; Liu et al., 2012; Shekarchizadeh et al., 2013). The polymer is easily obtainable and offers hydrophilic sites on the electrode surface, which can help improve the detection of analytes, such as 1-Nph, in complex matrices.

The present work shows the development of a MIP sensor by electropolymerization of o-PD in the presence of 1-Nph on the glassy carbon electrode (GCE), and the application of the sensor

in OPW sample. The conditions for the removal and rebinding of the molecule were optimized; these conditions help control the sensor thickness and directly affect the sensor quality. Selectivity study was conducted in order to evaluate the selectivity of the sensor for application in complex samples. The polymeric films were characterized by voltammetric techniques and electrochemical impedance spectroscopy (EIS). For the recognition of 1-Nph by the MIP and NIP sensor, $[Fe(CN)_6]^{3-/4-}$ was employed as electrochemical probe through the application of differential pulse voltammetry (DPV).

2. Experimental

2.1. Reagents and equipment

1-naphthol (1-Nph, purity: ≥ 98%), o-Phenylenediamine (o-PD, purity: ≥ 98%), potassium ferricyanide ($K_3[Fe(CN)_6]$), potassium dihydrogen, dipotassium hydrogen phosphates, potassium chloride, sodium acetate, acetonitrile and acetic, sulfuric and nitric acids (purities: 99%) were purchased from Sigma–Aldrich. Ultrapure water was used to prepare the solutions.

A potentiostat PalmSens®, coupled to a laptop which records the electrochemical measurements obtained through the software PSTrace. A conventional electrochemical cell was employed. The electrochemical cell consisted of reference, auxiliary and working electrodes. Silver chloride, Ag|AgCl (KCl 3 mol L^{-1}), was used as reference electrode, a platinum wire as auxiliary electrode, and GCE with diameter 3.0 mm was used as working electrode. A magnetic stirrer was employed for the mass convective transport during some steps in the construction and application of the MIP. The measurements and experiments described in the next sections were performed at 25 ± 1.0 °C.

2.2. Development of the MIP on GCE

Initially, the GCE was polished with paper sheet on glass support and was electrochemically cleaned by cyclic voltammetry (CV) using successive scans at 50 mV s^{-1} in the potential range of −1.5 and +1.0 V in nitric acid 20% (*v/v*); this was done until the voltammogram characteristics matched with those of clean GCE.

The electropolymerization procedure was carried out by CV using a solution of 5.0×10^{-4} mol L^{-1} 1-Nph as template molecule and 5.0×10^{-4} mol L^{-1} o-PD as polymeric molecule in acetate buffer solution (ABS), pH = 5.0. The CVs were recorded from −0.4 to +1.0 V during 20 consecutive cycles at scan rate of 50 mV s^{-1}. After that, the electrode was washed with ultrapure water and was then immersed into a solution containing sulfuric acid and acetonitrile in the ratio 1:3 (*v/v*) for 45 s under stirring in order to remove the 1-Nph. A non-imprinted polymer (NIP) was also constructed in the same procedures but without 1-Nph in the electropolymerization process.

The parameters, such as electropolymerization cycles, concentration of template molecule and times of extraction and rebinding of the 1-Nph, were investigated in order to obtain optimum film thickness and physical stability, apart from promoting the formation of well-shaped cavities in the polymer film. After the extraction and rebinding procedures, all the optimization parameters were investigated using $[Fe(CN)_6]^{3-/4-}$ as analytical probe. The electrodes were analyzed by DPV, in terms of the difference between the currents obtained, aiming for the best conditions that lead to the formation of the MIP sensor. The repeatability was evaluated by two successive repetitions for the same electrode in line with the report published in the JCGM 200:2012 International vocabulary of metrology; as such, the analysis was conducted based on the described procedures of cleaning, electroplolymerization, extraction and rebinding.

2.4. Electroanalytical measurements

The GCE-MIP was evaluated by DPV in the potential range from −0.2 to +0.5 V, with step potential of 4.0 mV, modulation time of 50 ms and modulation amplitude of 50 mV. The sensor

performance was evaluated through the electrochemical active probe $K_3[Fe(CN)_6]$ in concentration of 5.0 x 10^{-3} mol L^{-1} in 0.1 mol L^{-1} KCl. The imprinted cavities on the GCE surface become a path for the oxidation of the probe. When these cavities are occupied by the molecules of interest (1-Nph molecules in this case), the probe is prevented from reaching the electrode surface, and this produces a difference in the electrochemical signal after the rebinding of the GCE-MIP. The first current measurement was carried out after the extraction of the 1-Nph molecule from the polymer matrix and washing it with ultra-pure water. The next measurement was performed after the rebinding of the 1-Nph molecule in the cavities formed; this measurement was performed by placing of the GCE-MIP in a PBS (at pH 6.5) containing different concentrations of 1-Nph under stirring for 10 min (optimization) or 20 min (further experiments). For the purposes of distinction, the suffix "-reb" was added to the wording of GCE-MIP and GCE-NIP to indicate that they have been subjected to rebinding.

The electrochemical characterization of the GCE-MIP was performed using the CV and EIS techniques. Cyclic voltammetries were recorded at potentials ranging from -0.2 and +0.6 V, scan rate of 50 mV s^{-1}. Faraday cage was used for the EIS, the data were recorded at the potential of 0.22 V (vs. Ag|AgCl), in the frequency range of 0.1 Hz to 100 kHz.

The selectivity of the GCE-MIP was conducted by DPV technique in a solution containing 1-Nph in the absence and presence of one selected interferent at a time; the interferents employed included fluoranthene, naphthalene, phenol and toluene. These interferents were chosen due to the fact that they belong to the same functional group, are of similar size, and are simultaneously present in OPW. The analysis of selectivity was conducted by comparing the interference in the current delta response of the probe solution $[Fe(CN)_6]^{3-/4-}$ through DPV and under the aforementioned optimized conditions. The rebinding procedure was performed as described above but using molar concentration of 5.0×10^{-9} mol L^{-1} for each molecule: 1-Nph and interferent.

Calibration curves were constructed using optimized parameters for the GCE-MIP sensor; here, the values related to limit of detection (LOD) and limit of quantification (LOQ), as well as the standard deviation of the intercept (SD) and slope of the calibration curve (S) were determined using the classical statistics approach based on the IUPAC and ACS definitions (Mocak et al., 1997) which show that the limits = k×(SD/S) with factor k = 3 and 10, respectively.

The unknown concentrations of 1-Nph in OPW were determined by the standard addition method using the optimized MIP sensors, which were analyzed by DPV based on the measurement conditions described previously.

2.6. Analysis of 1-naphthol in oilfield produced water

The sample of OPW was acquired from the Petrobrás® offshore platform in Natal/RN-Brazil in April, 2017. The sample was stored in polypropylene bottles and kept in a refrigerator.

The original sample was diluted 1:1000 (*v/v*) in 0.2 mol L^{-1} PBS (at pH 6.5) and spiked by known amounts of 1-Nph standard solutions. The quantification of 1-Nph in the real sample was determined by the standard addition method (n=2); the quantified 1-Nph concentration is presented in terms of average value of added concentration.

3. Results and discussion

3.1. Molecular Imprinted Polymer (MIP) films on GCE

Figure 1 (Curve a) shows the electrooxidation of o-PD in ABS (at pH 5.0) by CV; it is possible to observe two irreversible anodic peaks at 0.45 and 0.7 V (vs. Ag | AgCl), attributed to the dimer state of o-PD. This dimer refers to univalent cationic radical that oxidizes to a divalent cationic radical, initiating the electropolymerization process as reported in the literature (Buffon and Stradiotto, 2019). The successive cycles showed a decrease in peak currents, suggesting the formation of a non-electroactive film on the GCE surface; this film was attributed to NIP (also see

Fig. A.1). Curve (c) in Figure 1 shows that the oxidation of 1-Nph exhibits an anodic peak around +0.5 V (*vs.* Ag|AgCl); this peak is attributed to the oxidation of phenolic group in its corresponding radical, leading to a process of electropolymerization. This electropolymerization process can lead to passivation on the electrode surface (Abdelaal, 2005; Ferreira et al., 2006; Zheng et al., 2015), (see Fig A.3). The distinguishable electropolymerization profile observed in curve (b) shows that the MIP formation is altered by the presence of the template molecule during the process.

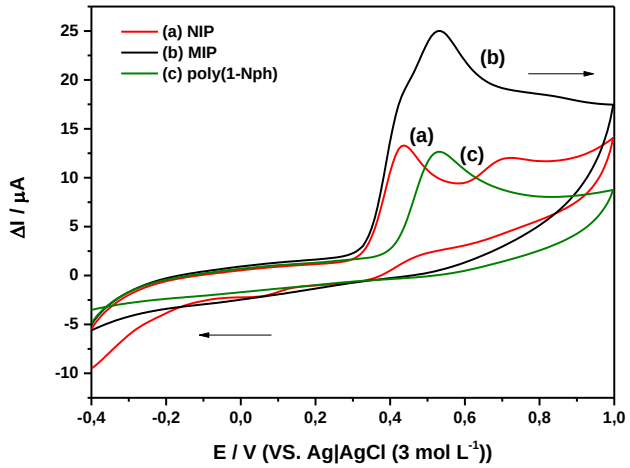

Figure 1. First cycle of CV during electropolymerization of o-phenylenediamine (o-PD) and/or 1-naphthol (1-Nph) for (a) NIP, (b) MIP, and (c) poly(1-Nph). 1-Nph and o-PD concentrations of 5.0×10^{-4} mol L^{-1} each were applied in ABS at pH 5.

Many studies related to MIP electropolymerization (Bozal-Palabiyik et al., 2019; Buffon and Stradiotto, 2019; Liu et al., 2016; Ozcelikay et al., 2019; Wang et al., 2014; Yan et al., 2012) show that the template molecule does not interfere in this process; this means that the interference of 1-Nph needs to be investigated in terms of its proportion relative to the functional molecules. The interference of 1-Nph affects the formation of cavities because of the presence of oxidized and non-oxidized 1-Nph during the imprinting process.

3.2. Electrochemical behavior of the GCE-MIP sensor

For the analysis involving the recognition of the probe solution, the CV and DPV techniques were evaluated in Figure 2. The redox probe $[Fe(CN)_6]^{3-/\ 4-}$ monitored the changes on the GCE surface through the evaluation of its electrochemical behavior during the sensor modification steps.

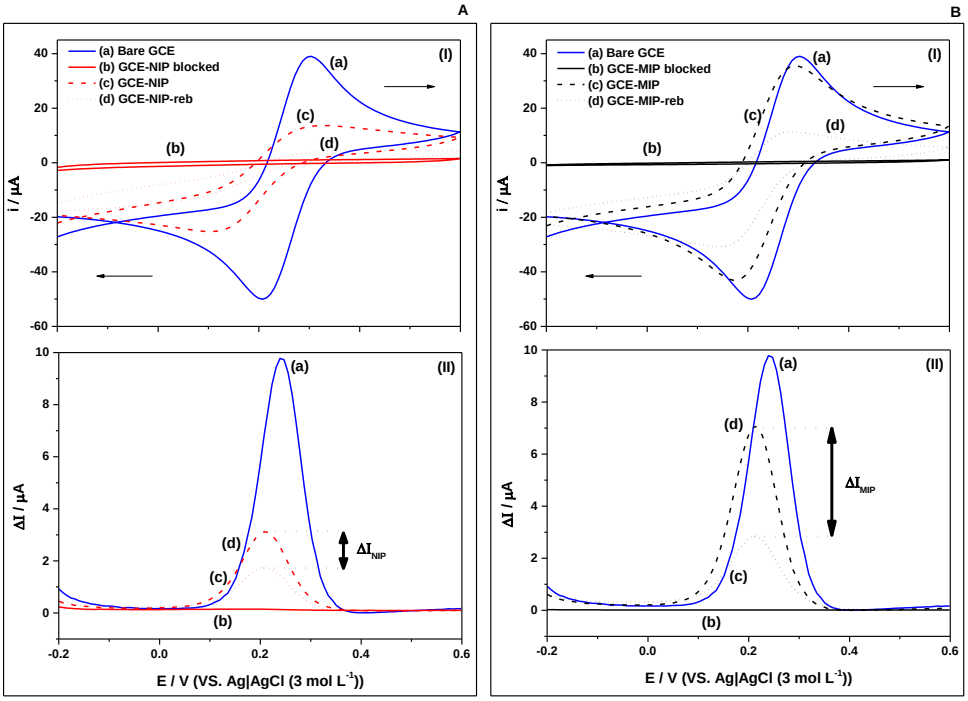

Figure 2. (I) CVs and (II) DPV for A: (a) GCE (b) blocked GCE-NIP, (c) GCE-NIP and (d) rebinding of GCE-NIP. B: (a) GCE (b) blocked GCE-MIP, (c) GCE-MIP, and (d) rebound GCE-MIP. Conditions: rebinding was done using PBS (pH = 6.5) in 5.0×10^{-6} mol L^{-1} of 1-Nph for 20 min. The analyses were conducted in solution containing 5.0×10^{-3} mol L^{-1} $[Fe(CN)_6]^{3-/4-}$ in 0.1 mol L^{-1} KCl.

Looking at curves b (I) in *Figure 2* sections A and B, one will notice the presence of a couple of typical redox peaks of $[Fe(CN)_6]^{3-/\ 4-}$ on the bare GCE which is found to be suppressed after electropolymerization, forming a compact and non-conductive film, identified as NIP and MIP. The re-appearance of the voltammetric signal from the redox probe after the removal of the target molecule is considerably higher for the MIP film compared to the NIP film (see *Figure 2*, curve c). The smaller voltammetric signal from the redox probe observed for the NIP film may be attributed to microscopic cracks in the poly(o-PD), while the higher voltammetric signal observed for the

MIP film is related to the rupture of the hydrogen bonds that occurs in the extraction stage of the 1-Nph, resulting in the formation of the cavities. This is evidenced by the decrease in signal from the redox probe after the rebinding process of the target molecule (curve d), giving rise to Δ_{NIP} and Δ_{MIP}. One will also notice the occurrence of a weak adsorption of cavities for the poly(1-Nph) films (see Fig. B.1).

Taking into consideration that DPV is characterized by better peak resolution, greater sensitivity and lower double-layer charge current effects, this technique was chosen to conduct further investigation regarding the conditions involving the GCE-MIP and for the evaluation of the sensor performance in the detection of 1-Nph. The DVP technique was found to be efficient with remarkable peak resolution and relatively higher current delta for the MIP sensor compared to the NIP sensor, as shown in *Figure 2* section A(II) and B(II). The proper use of the voltammetry technique allows the quantitative analysis of the sensor performance during optimization and the proper recognition of analytes during application, ensuring lower detection limit and higher electrochemical response (Wang et al., 2014).

To obtain additional information about the surface-modified electrodes, the MIP electrode was subjected to EIS analysis. Figure 3 illustrates the Nyquist plots based on Randles circuit, where R_s represents the solution resistance, CPE being the constant phase element, representing the double layer capacitance, W is Warburg impedance and R_{ct} is the charge-transfer resistance. The values were examined in terms of R_{ct} for each step of the building of MIP sensor (Cesiulis et al., 2016).

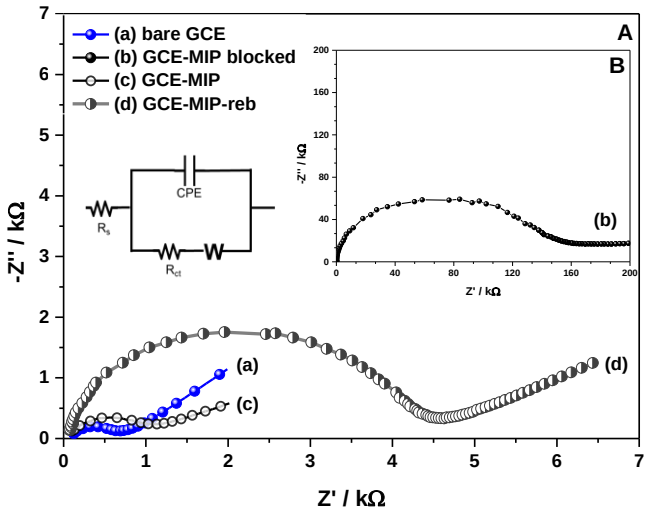

Figure 3. (A): Nyquist plots for (a) bare GCE, (c) MIP after extraction (GCE-MIP), and (d) GCE-MIP after rebinding (GCE-MIP-reb). Inset B: (b) MIP after electropolymerization (blocked GCE-MIP). Inset: Randles equivalent circuit. The supporting electrolyte was 5.0×10^{-3} mol L^{-1} $[Fe(CN)_6]^{3-/4-}$ in 0.1 mol L^{-1} KCl. Inset: Randles equivalent circuit.

The EIS behavior of the redox probe solution $[Fe(CN)_6]^{3-/\,4-}$ on the GCE surface is shown in Figure 3 during the formation of MIP sensor. The bare GCE presented R_{ct} value of 678 Ω (Curve a). However, the blocked GCE-MIP present a significant increase in its resistance (Curve b), recording R_{ct} value of 169,600 Ω; this means that the imprinted film generated poor conductivity on the surface of the electrode. In this sense, the significant increase in resistance suggests that 1-Nph may also be trapped in the polymer matrix in the same way as the o-PD monomer. Thus, the modified electrode presented a R_{ct} value of 1,173 Ω after the removal of the template (Curve c), indicating the presence of gaps formed by the removal of 1-Nph, which the redox probe approaches the surface of the electrode. In contrast, the GCE-MIP electrode after the rebinding process presented a R_{ct} value of 4,532 Ω (Curve d), demonstrating that the 1-Nph molecule was capable of rebinding into the selective cavities formed on the electrode surface. Thus, the results confirm the previously observed behavior of the MIP and further studies were carried out in order to optimize the MIP sensor performance in the detection of 1-Nph.

3.3. Film formation: optimization

3.3.1. Concentration of template molecule

The concentration of the template molecule (1-Nph) plays a vital role in the formation of the MIP and it directly influences the quality of the cavities on the GCE. In view of that, three concentrations of 1-Nph were chosen for the study of the influence of the template molecule concentration: 2.0×10^{-4} mol L^{-1}, 2.5×10^{-4} mol L^{-1} and 5.0×10^{-4} mol L^{-1}. Higher concentrations were disregarded due to the insolubility of 1-Nph and low repeatability of the voltammetric signal. The results showed that the application of 5.0×10^{-4} mol L^{-1} concentration presented no change in 1-Nph recognition; this implies that the ideal number of imprinted cavities on the electrode surface has already been adopted in other steps involving the optimization of the MIP sensor.

3.3.2. Electropolymerization

The number of cycles applied for the electropolymerization of o-PD in the presence of 1-Nph can influence the sensor stability and sensitivity by changing the thickness of the film formed on the sensor surface. The electrochemical behavior of the MIP sensor was investigated through the number of the applied electropolymerization cycles in the range of 10 to 30 cycles. The results are shown in Figure B.1. As can be observed, the application of 10 cycles of electropolymerization resulted in an extremely thin polymeric film, which undermined the sensor repeatability. On the other hand, a very thick film formed after the application of more than 20 cycles led to lower molecular recognition of 1-Nph as a result of the badly formed cavities. In essence, an increase in the thickness of the polymeric film was found to provoke a higher R_{ct} on the electrode surface. Thus, the number of 20 cycles was selected for the electropolymerization process.

3.3.3. Extraction of the target molecule

The extraction of an imprinted molecule in a polymer chain is a quite delicate process. This process involves the ability to form suitable sites while simultaneously maintaining the cavities in the rigid polymer film and ensuring good repeatability and sensitivity of the sensor. Several solvents have been employed toward the removal of template molecules in MIP; these include alcoholic (Yan et al., 2012), basic (Ozcelikay et al., 2019) and acid (Dechtrirat et al., 2018; Liu et al., 2016) aqueous solution. With regard to the extraction of the template molecule (1-Nph), the best performance was obtained under the solution containing 0.01×10^{-3} mol L^{-1} of H_2SO_4 and acetonitrile in the ratio of 1:3 (*v/v*, 3< pH < 4). The affinity of the solvents with the polymer allows their penetration into the polymeric mass and the acid solution promotes the release of the target molecule (1-Nph) by weakening the hydrogen bonds [29,35,37]. The effect of different periods of time applied for the removal of the template molecule was analyzed in the range of 10 to 240 s using the previously optimized parameters with the rebinding of the template molecule for 10 min. As seen in Figure 4C, the current delta rapidly decreases when the electrode is immersed for more than 45 s, indicating the bad formation of the cavities. Furthermore, longer extraction times results in low repeatability of 1-Nph recognition; this is mainly attributed to the swelling of the polymer, which makes the cavities less selective in relation to the target molecule. Thus, the extraction time of 45 s was kept for further experiments.

3.3.4. Rebinding time

For the purpose of finding the adsorption equilibrium for the rebinding of the analyte in the MIP, an investigation was conducted regarding the influence of time by testing 1.0×10^{-6} mol L^{-1} of 1-Nph for the periods ranging from 5 to 30 min (see Figure 4D). The MIP sensors for this analysis were electropolymerized by CV for 20 cycles using 5.0×10^{-4} mol L^{-1} of 1-Nph in ABS pH 5.0 and template extraction time of 45 s. The response was measured by DPV in the oxidation

probe solution. The maximum current and stable response were reached after 20 min; so this time was selected for posterior experiments.

The maximum current variation and repeatability response were obtained in 20 min; as such, this time was chosen for the conduct of subsequent studies through the application of GCE-MIP.

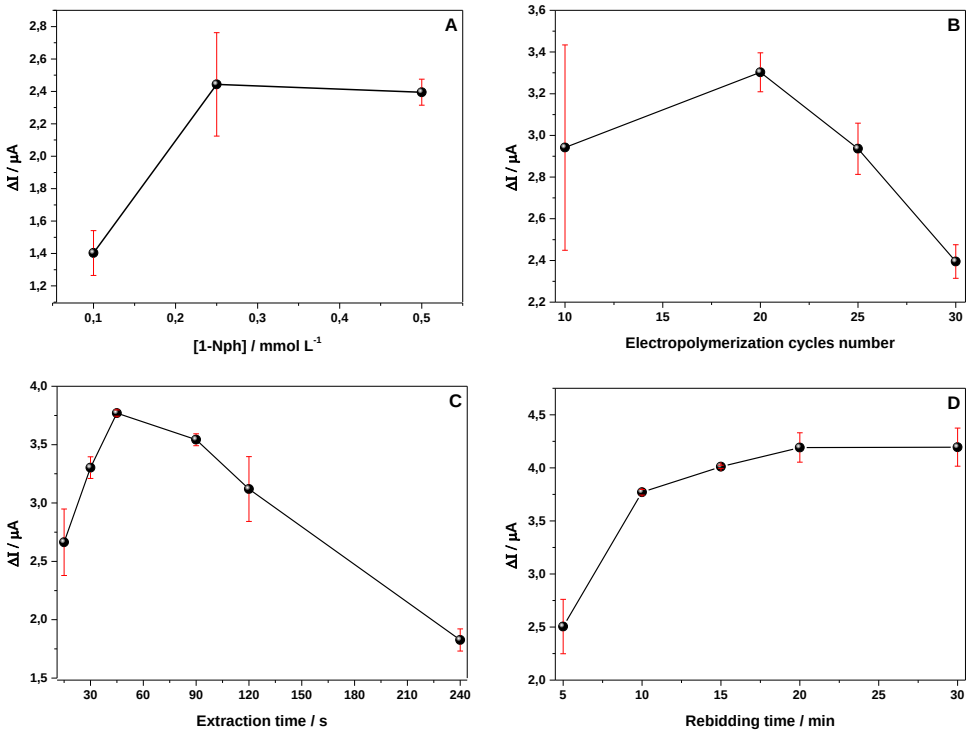

Figure 4. Effect of the following parameters: (A) concentration of 1-Nph and (B) number of cycles applied in electropolymerization, and exposure times for (C) removal and (D) rebinding of template molecule in ABS (pH = 5.0) and PBS (pH = 6.5), respectively. The response was measured by DPV using the probe solution.

3.4. Analytical performance

3.4.1. Construction of the analytical curve

Under optimized conditions, analytical curves for GCE-MIP and GCE-NIP were constructed after rebinding varying concentrations of 1-Nph in aqueous medium using DPV. Briefly, 20 cycles of DPV were applied for the electropolymerization process using 5.0×10^{-4} mol L^{-1} of 1-Nph in ABS (at pH 5.0). The extraction of the template molecule from the polymer chain was carried out

after 45 s of the electrode exposure to H_2SO_4 solution/acetonitrile in the ratio of 1:3 (v/v); the rebinding of 1-Nph in the cavities formed occurred in 20 min.

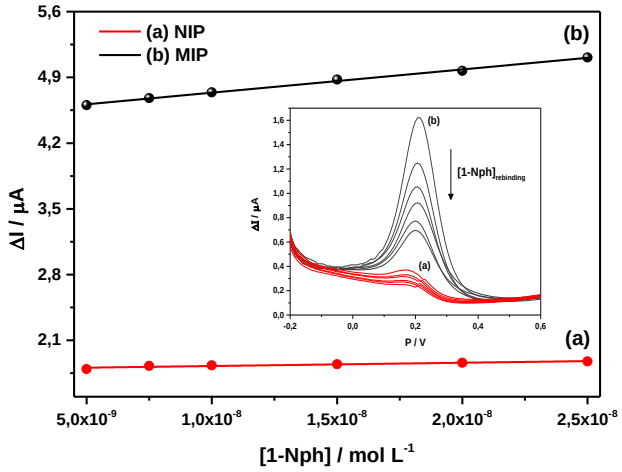

Figure 5. Calibration curves for 1-naphthol (1-Nph) determination (5.0×10^{-9} to 2.5×10^{-8} mol L^{-1}) using (a) NIP and (b) MIP in probe solution after 20 min of rebinding in PBS (pH = 6.5). Inset: DPVs of MIP and NIP sensors.

The inset in *Figure 5* shows the corresponding DPV voltammograms for the $[Fe(CN)_6]^{3-/4-}$ probe when GCE-MIP was previously exposed to 5.0×10^{-9} mol l^{-1} to 2.5×10^{-8} mol L^{-1} of 1-Nph. With the increase in the concentration of 1-Nph, the intensity of the peaks decreased; this shows that some cavities were rebound to the target molecule, hindering the access of the redox probe to the electrode surface. The difference between the results obtained in terms of the performance of the NIP and MIP electrodes reinforces the existence of imprinted site shown in the graph in *Figure 5*. For the MIP, the linear regression equation was $\Delta I\ (\mu A) = 2.5 \times 10^7\ C_{1\text{-Nph}} + 4.5$ (R = 0.998), LOD and LOQ of 1.5×10^{-9} mol L^{-1} and 5.0×10^{-9} mol L^{-1}, respectively, and AS of $2.5 \pm 0.07 \times 10^7$ μA L mol^{-1} (n=2).

In order to assess the performance of the GCE-MIP in relation to other electroanalytical sensors reported in the literature for the quantification of 1-Nph, the analytical parameters and the complexity of samples detected were compared in *Table 1*. Although the LOD obtained under the

proposed method is comparable to that of other reported methods, the sensor developed in this work presents superior advantages including rapid fabrication, low cost and fast analysis.

Table 1. Comparison of the merit figures and target sample between the method proposed and the methods reported in the literature for electrochemical determination of 1-Nph.

Electrode	**Linear range (mol L^{-1})**	**LOD (mol L^{-1})**	**Sample**	**Reference**
HS-β-CD/AuNPs/HNCMS[a]	2.0×10^{-9} – 1.5×10^{-7}	1.0×10^{-9}	River water	Zhu et al., 2012
TFGCE[b]	8.0×10^{-7} - 1.0×10^{-5}	2.0×10^{-7}	Tap and ground water	Tsai e Chen, 2007
HIF SnO_2/GCE[c]	2.0×10^{-8} - 4.0×10^{-7}	5.8×10^{-9}	River, landscape and sewage water	Huanga et al., 2012
GCE-MIP	5.0×10^{-9} - 1.0×10^{-8}	1.5×10^{-9}	Produced water	This work

a Gold nanoparticles (AuNPs)/hollow nitrogen-doped carbon microspheres (HNCMS) hybrids functionalized with thiolated-β-cyclodextrin (HS-β-CD);

b Tosflex polymer film (TF);

c SnO2 nanooctahedron with {221} high-index facet (HIF).

Another point worth mentioning is the ability of the proposed sensor to detect analytes in complex samples with the presence of a wide range of interfering molecules. As aforementioned, the oxidation of pollutants in produced water may occur during the storage of the sample; this can change the character of the sample to basic or acidic and may likewise lead to changes in polarity that occurs in the transformation of naphthalene to Nph (Neff, 2002). Thus, the study of the sensor selectivity is essentially important in the sense that it helps evaluate the ability of the MIP sensor to monitor the pollutant in complex samples.

3.4.2. Selectivity performance

Considering the risks posed by organic compounds (such as, BTEX, PAHs and phenol along with their oxidized species) to human health and the environment as a whole (Jiménez et al., 2018), it is essentially relevant to evaluate whether the developed sensor has good selectivity when it comes to the detection of small molecules like 1-Nph. In view of that, the selectivity of the GCE-MIP sensor was investigated by testing its recognition efficiency through the cavities formed in the presence of 5.0×10^{-9} mol L^{-1} 1-Nph with the application of potential interferents, including

fluoranthene, naphthalene, toluene and phenol, in the same concentration as 1-Nph. The results obtained (by the application of the proposed GCE-MIP) in solution containing 1-Nph and also in solution containing 1-Nph + interfering, are shown in Figure 6. The GCE-NIP was checked in the same solution for comparison and control.

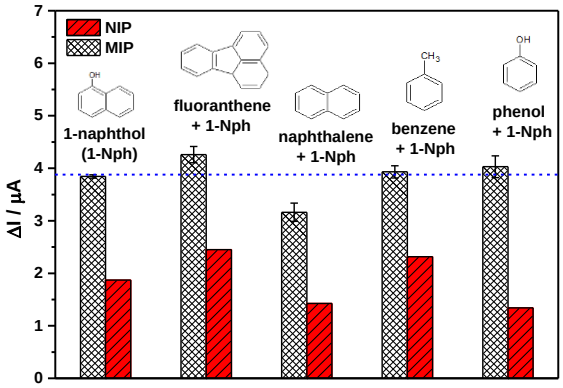

Figure 6. Evaluation of selectivity for GCE-MIP and GCE-NIP sensors. Concentrations of 5.0×10^{-9} mol L^{-1} for each molecule analyzed in PBS at pH 6.5 and rebinding time of 20 min. The blue dotted line indicates the current variation for 1-Nph. Analyses conducted by DPV in 0.1 mol L^{-1} KCl containing 5.0×10^{-3} mol L^{-1} $[Fe(CN)_6]^{3-/4-}$.

The factors related to selectivity were also evaluated. To conduct this analysis, three parameters were tested and compared in Table 2. The parameters included the interference coefficient, the imprinted factor, and the selectivity factor. The interference coefficient (θ) was studied in order to determine the sensor selectivity for 1-Nph, considering a real applicable scenario. The analysis of the imprinting factor (α) was aimed at finding out the manner in which the sensor response to 1-Nph is affected by the interfering molecules in the cavities. The selectivity factor (β) was studied aiming at evaluating the selectivity of effective imprinted sites for 1-Nph in the presence of each interfering molecule. The interference coefficient and the selectivity factor obtained for the proposed GCE-MIP sensor were compared with those of the GCE-NIP sensor. The sensitivity of the GCE-MIP sensor was tested based on the convergence of the values obtained from the recognition of 1-Nph in the presence of the interfering molecules and those obtained for

the recognition of only the template molecule. The recognition of 1-Nph generated the following reference values: θ = 0%, α = 2.0, β = 1.0.

Table 2. Selectivity of GCE-MIP for 1-naphthol and interfering molecules.

Molecule(s)	θ[a]	α[b]	β[c]
1-Naphthol (1-Nph)	0%	2.0	1.0
Fluoranthene + 1-Nph	11%	1.7	1.2
Naphthalene + 1-Nph	18%	2.2	0.92
Phenol + 1-Nph	4.8%	3.0	0.68
Toluene + 1-Nph	2.3%	1.7	1.2

[a] $\theta = [\ |\ \Delta I_{MIP:\ 1\text{-}Nph} - \Delta I_{MIP:\ 1\text{-}Nph+interferent}\ |\ /\ (\Delta I_{MIP:\ 1\text{-}Nph})]$ x 100 %;
[b] $\alpha = (\Delta I_{MIP}) / (\Delta I_{NIP})$;
[c] $\beta = (\alpha_{1\text{-}Nph}) / (\alpha_{1\text{-}Nph+interferent})$.

The analysis of the coefficient θ showed that the presence of fluoranthene and naphthalene slightly affected the performance of the MIP sensor relative to the selectivity for 1-Nph. This can be attributed to the similarity of the molecules, in size and shape, and the likely occurrence of Van der Walls-type interactions. With regard to the analysis of interference in 1-Nph detection in the presence of fluoranthene and naphthalene, the NIP sensor exhibited a higher interference of fluoranthene compared to naphthalene. Hence, this requires the conduct of a comparative analysis of the factors of imprinting and selectivity, which will enable one to evaluate the quality of the cavities constructed on the GCE and the electrostatic attractions that occur between the interferents and poly(o-PD) during the competitive rebinding process. Phenol is the only molecule that provides significant differences for those two factors – imprinting (α) and selectivity (β); this confirms the influence of electrostatic attractions π-π as well as hydrogen bonds in the recognition of the analytes. The intermolecular interaction between hydroxyl and amine groups played a negligible role in the competition for the molecule recognition. The GCE-NIP presented interference in the presence of phenol, and it is likely that this kind of interactions occurs on the polymer surface. It is also worth noting that both the MIP and NIP sensors presented a decrease in

recognition in the presence of naphthalene without a significant change in the cavities formed or selectivity, confirming the influence of the aromatic rings in the rebinding process due to superficial interactions.

Based on the results obtained from the selectivity studies, one can conclude that the GCE-MIP has good selectivity for 1-Nph; this implies that the cavities constructed on the electrode surface have good conformation and are capable of recognizing the target molecule with considerable degree of accuracy. In addition, as can be observed in Table 1, the results show that the GCE-MIP presents a relatively higher degree of recognition for the template molecule compared to other sensors reported in the literature when it comes to analytes detection in complex chemical environments such as produced water.

3.5. Quantification of 1-Nph in real sample

The determination of the presence of 1-Nph concentration in OPW was carried on by standard addition method. The collected samples were spiked with standard 1-Nph concentrations in the range of 5.0×10^{-9} to 1.0×10^{-8} mol L^{-1} and detected by DPV. The results related to the added and detected concentrations in the samples are presented in *Table 3*

Table 3. Determination of 1-naphthol in samples of oilfield produced water (n=2).

Amount (10^{-9} mol L^{-1})		**Recovery (%)**
Added	**Found**	
-	22 ± 8	-
5.0	5.1 ± 0.008	102 ± 1
7.5	7.8 ± 0.2	104 ± 3
10.0	9.7 ± 0.1	97 ± 1

The amount of 1-Nph concentration found in the original sample was 22 ± 0.8 $\times10^{-9}$ mol L^{-1}. The recovery rate was measured in the OPW sample by spiking it with three different

concentrations of 1-Nph. The values obtained were between 97 % and 104 %, indicating a good degree of accuracy of the method employed.

Boitsov, Mjøs and Meier (2007) (Boitsov et al., 2007) identified naphthol (Nph) and other molecules in produced water at low concentrations through the application of the chromatography technique. The concentrations of Nph obtained were 10 to 50 times lower than the concentrations of alkylphenols with quite similar molar mass. Studies reported in the literature have pointed out difficulties in the identification of aromatic compounds with low molar mass in produced water; this is attributed to the tiny quantity of these compounds in produced water, as well as their similarity in terms of size and polarity, making this matrix a complex sample for the detection of this kind of compounds (Beens and Tijssen, 1997; Malins et al., 1980; Thomson et al., 1997). Thus, the proposed method shows that one can determine 1-Nph concentration in OPW sample with high reliability, good recovery rate, excellent selectivity and under previously optimized conditions.

Conclusion

The present study describe the development of a selective GCE-MIP based on the electropolimerization of *o*-phenylenediamine on GCE and its application for the quantification of 1-Nph in OPW. The optimization of the film played a key role in the improvement of the sensor performance monitored by redox probe $[Fe(CN)_6]^{3-/4-}$. MIP film presented well-formed cavities which were found to be selective for the 1-Nph molecule even in solution containing interfering molecules. The results obtained showed that the GCE-MIP has good repeatability, selectivity, sensitivity and low LOD and LOQ. Based on the experimental results, the proposed method using GCE-MIP for the detection of 1-Nph showed excellent sensitive, selectivity and accuracy. This GCE-MIP can be considered of great interest, since demonstrated promising results for the determination of 1-Nph in the OPW sample.

Appendix A. Supporting information

Supplementary data associated with this article can be found in the online version.

Competing interests

The authors of this research do not have any competing interests to declare.

Acknowledgment

The authors would like to thank the Brazilian research funding agencies including the São Paulo Research Foundation (FAPESP, process n° 2018/12131-6 and n° 2014/50945-4) and the National Council for Scientific and Technological Development (CNPq process n° 143222/2017-1) for the financial support granted. Thanks are also due to Dr. José Luiz da Silva for his invaluable remarks and contribution toward improving the quality of the work.

References

Abdelaal, M.Y., 2005. ELECTROCHEMICAL POLYMERIZATION OF NAPHTHOLS IN AQUEOUS MEDIUM. International Journal of Polymeric Materials 54, 151–159. https://doi.org/10.1080/00914030390207237

Aidar, E., Sigaud-Kutner, T.C.S., Bicega, M.C., Schinke, K.P., Gianesella, S.M.F., Braga, E.S., 1999. Evaluation of produced water toxicity from an oil maritime terminal through Skeletonema costatum toxicity tests. Rev. Bras. Oceanogr. 47, 137–144. https://doi.org/10.1590/S1413-77391999000200003

Beens, J., Tijssen, R., 1997. The characterization and quantitation of sulfur-containing compounds in (heavy) middle distillates by LC-GC-FID-SCD. J. High Resol. Chromatogr. 20, 131–137. https://doi.org/10.1002/jhrc.1240200303

Beluomini, M.A., da Silva, J.L., Sedenho, G.C., Stradiotto, N.R., 2017. D-mannitol sensor based on molecularly imprinted polymer on electrode modified with reduced graphene oxide decorated with gold nanoparticles. Talanta 165, 231–239. https://doi.org/10.1016/j.talanta.2016.12.040

Beluomini, M.A., Karimian, N., Stradiotto, N.R., Ugo, P., 2019. Tailor-made 3D-nanoelectrode ensembles modified with molecularly imprinted poly(o-phenylenediamine) for the sensitive detection of L-arabitol. Sensors and Actuators B: Chemical 284, 250–257. https://doi.org/10.1016/j.snb.2018.12.091

Bernardo, D.L., Barros, K.A., Silva, R.C., Pavão, A.C., 2016. CARCINOGENICITY OF POLYCYCLIC AROMATIC HYDROCARBONS. Química Nova. https://doi.org/10.5935/0100-4042.20160093

Boitsov, S., Mjøs, S.A., Meier, S., 2007. Identification of estrogen-like alkylphenols in produced water from offshore oil installations. Marine Environmental Research 64, 651–665. https://doi.org/10.1016/j.marenvres.2007.07.001

Bozal-Palabiyik, B., Erkmen, C., Uslu, B., 2019. Molecularly imprinted electrochemical sensors: Analytical and pharmaceutical applications based on ortho-phenylenediamine polymerization. CPA 15. https://doi.org/10.2174/1573412915666190304150159

Buffon, E., Stradiotto, N.R., 2019. Electrochemical sensor based on molecularly imprinted poly(ortho-phenylenediamine) for determination of hexahydrofarnesol in aviation biokerosene. Sensors and Actuators B: Chemical 287, 371–379. https://doi.org/10.1016/j.snb.2019.02.059

Cajaraville, M.P., Marigomez, J.A., Angulo, E., 1989. Stability of 1-naphthol in sea water solutions and its uptake by the marine prosobranch gastropodLittorina littorea (L.). Bull. Environ. Contam. Toxicol. 42, 799–806. https://doi.org/10.1007/BF01701618

Cesiulis, H., Tsyntsaru, N., Ramanavicius, A., Ragoisha, G., 2016. The Study of Thin Films by Electrochemical Impedance Spectroscopy, in: Tiginyanu, I., Topala, P., Ursaki, V. (Eds.), Nanostructures and Thin Films for Multifunctional Applications. Springer International Publishing, Cham, pp. 3–42. https://doi.org/10.1007/978-3-319-30198-3_1

Chin-Chen, M.-L., Rambla-Alegre, M., Durgbanshi, A., Bose, D., Mourya, S.K., Esteve-Romero, J., Carda-Broch, S., 2012. Micellar Liquid Chromatographic Determination of Carbaryl and 1-Naphthol in Water, Soil, and Vegetables. International Journal of Analytical Chemistry 2012, 1–7. https://doi.org/10.1155/2012/809513

Dechtrirat, D., Sookcharoenpinyo, B., Prajongtat, P., Sriprachuabwong, C., Sanguankiat, A., Tuantranont, A., Hannongbua, S., 2018. An electrochemical MIP sensor for selective detection of salbutamol based on a graphene/PEDOT:PSS modified screen printed carbon electrode. RSC Adv. 8, 206–212. https://doi.org/10.1039/C7RA09601A

Direct Determination of 1-Naphthol in Human Urine by Coupled-Column Liquid Chromatography with Fluorescence Detection, 2003. . Chromatographia 58, 565–569.

Ferreira, M., Varela, H., Torresi, R.M., Tremiliosi-Filho, G., 2006. Electrode passivation caused by polymerization of different phenolic compounds. Electrochimica Acta 52, 434–442. https://doi.org/10.1016/j.electacta.2006.05.025

Hansen BR, Davies SR, 1994. Review of Potential Technologies for the Removal of Dissolved Components from Produced Water. Chem. Eng. Res. Des. 72, 176–188.

Huang, X., Zhao, G., Liu, M., Li, F., Qiao, J., Zhao, S., 2012. Highly sensitive electrochemical determination of 1-naphthol based on high-index facet SnO2 modified electrode. Electrochimica Acta 83, 478–484. https://doi.org/10.1016/j.electacta.2012.08.008

Jiménez, S., Micó, M.M., Arnaldos, M., Medina, F., Contreras, S., 2018. State of the art of produced water treatment. Chemosphere 192, 186–208. https://doi.org/10.1016/j.chemosphere.2017.10.139

Liu, J., Tang, H., Zhang, B., Deng, X., Zhao, F., Zuo, P., Ye, B.-C., Li, Y., 2016. Electrochemical sensor based on molecularly imprinted polymer for sensitive and selective determination of metronidazole via two different approaches. Anal Bioanal Chem 408, 4287–4295. https://doi.org/10.1007/s00216-016-9520-1

Liu, P., Zhang, X., Xu, W., Guo, C., Wang, S., 2012. Electrochemical sensor for the determination of brucine in human serum based on molecularly imprinted poly-o-phenylenediamine/SWNTs composite film. Sensors and Actuators B: Chemical 163, 84–89. https://doi.org/10.1016/j.snb.2012.01.011

Malins, D.C., Krahn, M.M., Brown, D.W., MacLeod, W.D., Collier, T.K., 1980. Analysis for petroleum products in marine environments. Helgolander Meeresunters 33, 257–271. https://doi.org/10.1007/BF02414751

McConkey, B.J., Hewitt, L.M., Dixon, D.G., Greenberg, B.M., 2002. Natural Sunlight Induced Photooxidation of Naphthalene in Aqueous Solution. Water, Air, and Soil Pollution 136, 347–359. https://doi.org/10.1023/A:1015223806182

Ministery of Environment, 2007. CONAMA Resolution nº 393.

Mocak, J., Bond, A.M., Mitchell, S., Scollary, G., 1997. A statistical overview of standard (IUPAC and ACS) and new procedures for determining the limits of detection and quantification: Application to voltammetric and stripping techniques (Technical Report). Pure and Applied Chemistry 69, 297–328. https://doi.org/10.1351/pac199769020297

Neff, J.M., 2002. Produced Water, in: Bioaccumulation in Marine Organisms. Elsevier, pp. 1–35. https://doi.org/10.1016/B978-008043716-3/50002-6

Ozcelikay, G., Kurbanoglu, S., Zhang, X., Kosak Soz, C., Wollenberger, U., Ozkan, S.A., Yarman, A., Scheller, F.W., 2019. Electrochemical MIP Sensor for Butyrylcholinesterase. Polymers 11, 1970. https://doi.org/10.3390/polym11121970

Serdar, B., Waidyanatha, S., Zheng, Y., Rappaport, S.M., 2003. Simultaneous determination of urinary 1- and 2-naphthols, 3- and 9-phenanthrols, and 1-pyrenol in coke oven workers. Biomarkers 8, 93–109. https://doi.org/10.1080/1354750021000046570

Sharma, P.S., Pietrzyk-Le, A., D'Souza, F., Kutner, W., 2012. Electrochemically synthesized polymers in molecular imprinting for chemical sensing. Anal Bioanal Chem 402, 3177–3204. https://doi.org/10.1007/s00216-011-5696-6

Shekarchizadeh, H., Ensafi, A.A., Kadivar, M., 2013. Selective determination of sucrose based on electropolymerized molecularly imprinted polymer modified multiwall carbon nanotubes/glassy carbon electrode. Materials Science and Engineering: C 33, 3553–3561. https://doi.org/10.1016/j.msec.2013.04.052

Stephenson, M.T., 1992. A Survey of Produced Water Studies, in: Ray, J.P., Engelhardt, F.R. (Eds.), Produced Water. Springer US, Boston, MA, pp. 1–11. https://doi.org/10.1007/978-1-4615-2902-6_1

Thomson, J.S., Green, J.B., McWilliams, T.B., 1997. Determination of Sulfides and Thiols in Petroleum Distillates Using Solid-Phase Extraction and Derivatization with Pentafluorobenzoyl Chloride. Energy Fuels 11, 909–914. https://doi.org/10.1021/ef960165m

Tsai, M.-C., Chen, P.-Y., 2007. Electrochemical Detection of 2-Naphthol at a Glassy Carbon Electrode Modified with Tosflex Film. Electroanalysis 19, 1315–1321. https://doi.org/10.1002/elan.200703857

Varjani, S.J., Upasani, V.N., 2017. A new look on factors affecting microbial degradation of petroleum hydrocarbon pollutants. International Biodeterioration & Biodegradation 120, 71–83. https://doi.org/10.1016/j.ibiod.2017.02.006

Wang, L.-H., Kuo, Y.-P., 1999. Simultaneous quantitative determination of resorcinol and 1-Naphthol in haircolor products by high-performance liquid chromatography. Chromatographia 49, 208–211. https://doi.org/10.1007/BF02575287

Wang, Q., Paim, L.L., Zhang, X., Wang, S., Stradiotto, N.R., 2014. An Electrochemical Sensor for Reducing Sugars Based on a Glassy Carbon Electrode Modified with Electropolymerized Molecularly Imprinted Poly-*o*-phenylenediamine Film. Electroanalysis 26, 1612–1622. https://doi.org/10.1002/elan.201400114

Wang, X.-G., Wu, Q.-S., Ding, Y.-P., 2006. Direct Simultaneous Determination of α- and β-Naphthol Isomers at GC-Electrode Modified with CNTs Network Joined by Pt Nanoparticles Through Derivative Voltammetry. Electroanalysis 18, 517–520. https://doi.org/10.1002/elan.200503412

Yan, X., Deng, J., Xu, J., Li, H., Wang, L., Chen, D., Xie, J., 2012. A novel electrochemical sensor for isocarbophos based on a glassy carbon electrode modified with electropolymerized molecularly imprinted terpolymer. Sensors and Actuators B: Chemical 171–172, 1087–1094. https://doi.org/10.1016/j.snb.2012.06.038

Zhang, J., Mei, Q., Ding, Y., Guo, K., Yang, X., Zhao, J., 2017. Ordered Mesoporous $NiCo_2O_4$ Nanospheres as a Novel Electrocatalyst Platform for 1-Naphthol and 2-Naphthol Individual Sensing Application. ACS Appl. Mater. Interfaces 9, 29771–29781. https://doi.org/10.1021/acsami.7b08497

Zhang, Y., Zhuang, H., 2009. Poly (acridine orange) film modified electrode for the determination 1-naphthol in the presence of 2-naphthol. Electrochimica Acta 54, 7364–7369. https://doi.org/10.1016/j.electacta.2009.07.067

Zhao, J., Hu, G. -Z., Yang, Z. -S., Zhou, Y. -Y., 2007. Determination of 1-Naphthol with Denatured DNA–Modified Pretreated Glassy Carbon Electrode. Analytical Letters 40, 459–470. https://doi.org/10.1080/00032710600964759

Zheng, X., Duan, S., Liu, S., Wei, M., Xia, F., Tian, D., Zhou, C., 2015. Sensitive and simultaneous method for the determination of naphthol isomers by an amino-functionalized, SBA-15-modified carbon paste electrode. Anal. Methods 7, 3063–3071. https://doi.org/10.1039/C5AY00027K

Zhou, Q., Lei, M., Li, J., Zhao, K., Liu, Y., 2016. Determination of 1-naphthol and 2-naphthol from environmental waters by magnetic solid phase extraction with Fe@MgAl-layered double hydroxides nanoparticles as the adsorbents prior to high performance liquid chromatography. Journal of Chromatography A 1441, 1–7. https://doi.org/10.1016/j.chroma.2016.02.061

Zhu, G., Gai, P., Yang, Y., Zhang, X., Chen, J., 2012. Electrochemical sensor for naphthols based on gold nanoparticles/hollow nitrogen-doped carbon microsphere hybrids functionalized with SH-β-cyclodextrin. Analytica Chimica Acta 723, 33–38. https://doi.org/10.1016/j.aca.2012.02.034

Non-enzymatic lactose molecularly imprinted sensor based on disposable graphite paper electrode

José Luiz da Silva [a, *], Edervaldo Buffon [a], Maísa Azevedo Beluomini [a], Lauro Antonio Pradela-Filho [b], Diele Aparecida Gouveia Araújo [b], André Luiz Santos [b], Regina Massako Takeuchi [b], Nelson Ramos Stradiotto [a, c]

[a] Analytical Chemistry Department, Institute of Chemistry, São Paulo State University (UNESP), 55 Prof. Francisco Degni St., Araraquara 14800-060, São Paulo State, Brazil

[b] Institute of Exact and Natural Sciences of Pontal, Federal University of Uberlandia, 1600 20 St., Ituiutaba 38304-402, Minas Gerais State, Brazil

[c] Bioenergy Research Institute (IPBEN), São Paulo State University (UNESP), 55 Prof. Francisco Degni St., Araraquara 14800-060, São Paulo State, Brazil

* Corresponding author.

E-mail address: jose.l.silva@unesp.br; silva_jluiz@yahoo.com.br

Abstract: Lactose (LAC) is a disaccharide - major sugar, present in milk and dairy products. LAC content is an important indicator of milk quality and abnormalities in food industries, as well as in human and animal health. The present study reports the development of an innovative imprinted voltammetric sensor for sensitive detection of LAC. The sensor was constructed using electropolymerized pyrrole (Py) molecularly imprinted polymer (MIP) on graphite paper electrode (PE). The MIP film was constructed through the electrosynthesis of polypyrrole (PPy) in the presence of LAC (template molecule) on PE (PPy/PE). To optimize the detection conditions, several factors affecting the PPy/PE sensor performance were assessed by multivariate methods (Plackett–Burman design and central composite design). Under optimized conditions, the

proposed analytical method was applied for LAC detection in whole and LAC-free milks, where it demonstrated high sensitivity and selectivity, with two dynamic linear ranges of concentration (1.0 to 10 nmol L^{-1} and 25 to 125 nmol L^{-1}) and a detection limit of 0.88 nmol L^{-1}. The MIP sensor showed selective molecular recognition for LAC in the presence of structurally related molecules. The proposed PPy/PE sensor exhibited good stability, as well as excellent reproducibility and repeatability. Based on the results obtained, the PPy/PE is found to be highly promising for sensitive detection of LAC.

Keywords: paper-based electrode, molecularly imprinted polymers, electropolymerization, experimental design, non-enzymatic electroanalysis, lactose sensing.

1. Introduction

Lactose (LAC) is the major carbohydrate (sugar) found in the milk of mammals (with the exception of sea lions and walruses that produce LAC-free milk) and in dairy products [1]. This sugar is formed by a disaccharide composed of two monosaccharides (glucose and galactose) bonded through a β-1→4 glycosidic linkage. LAC content is an important indicator of milk quality and it is used for the detection of abnormalities in wastewater control, veterinary medicine (animal health), food industries, as well as in public health [2–5]. Mastitis in cows has been reported to cause lower LAC levels in cow milk and a reduction in milk production [3,5,6]. In addition, about 65-70% of the adult population in the world present symptoms of poor LAC digestion caused by LAC malabsorption (LAC intolerance). The main symptoms of LAC intolerance include abdominal pain, bloating and diarrhoea, which occur due to low or no production of the enzyme lactase (β-galactosidase), found to be responsible for LAC degradation in the small intestine after the ingestion of dairy products [1,7,8]. Hence, the sensitive determination of LAC levels in dairy products such as LAC-free milk is regarded essential for a better quality of life.

Several analytical techniques have been used for the development of methods and sensors for LAC determination; these include gravimetry, polarimetry, spectrophotometry, infrared spectroscopy (IR), high-performance liquid chromatography (HPLC), and capillary electrophoresis [9–12], apart from specially designed electrochemical sensors [7] and biosensors [2–6,13–15]. Even though some of these methods offer good sensitivity, they are usually dependent on expensive instrumentation, complex pre-treatment steps and time-consuming analysis. Electrochemical techniques, on the other hand, are highly attractive because they offer fast and sensitive detection of analytes with simple and relatively low-cost instrumentation. However, lack of selectivity has been found to be the main drawback of electrochemical techniques, and this is certainly one of the main challenges to overcome in electroanalysis.

The use of electrochemical biosensors is an alternative approach toward tackling the selectivity problems found in electrochemical techniques; this is done through the application of biological receptors with specific molecular affinity. Nonetheless, these devices are also found to present some limitations including complexity of execution and high costs associated with the protocols required to be followed in order to immobilize the bioactive sensing layer, apart from their lack of stability and reproducibility [16–18].

To circumvent these shortcomings, molecular imprinting technology has been widely applied for the development of synthetic receptors with improved ability for molecular recognition. Besides exhibiting great selectivity, molecularly imprinted devices have other outstanding advantages; these include low cost, high specificity and mechanical/chemical stability, and robustness under harsh conditions [16–19]. Electropolymerization has been extensively applied in the preparation of electrochemical sensors based on molecularly imprinted polymers (MIP); this is because the electropolymerization preparation method is simple, cost-effective, and produces polymeric layers with controlled thickness, fast response, and high sensitivity. Electrosynthesis of MIPs occurs through the electropolymerization of functional monomers in the

presence of template molecules. After the removal of the template molecule, the MIP film is obtained with three-dimensional imprinted cavities which exhibit characteristics complementary to the spatial structure of the template molecule [16,17,20–22].

Allied to MIP technology, paper-based electrochemical sensors have emerged as a recent trend in the development and application of electroanalytical methods [23,24]. Paper substrates are accessible, flexible, recyclable, biodegradable, and have eco-friendly properties [25–28]. These characteristics make paper electrodes attractive alternative substrates for the preparation of electrochemical MIP sensors. So far, few studies published in the literature have reported the use of paper-based electrodes for the construction of electrochemical MIP sensors. Phenol, pyrrole, o-phenylenediamine and aniline functional monomers were used as electropolymerized MIP for the respective determination of 3-nitrotyrosine, tert-butyl-hydroquinone, D-glutamic acid and heptachlor in biological and food samples [29–32]. To date, no electrochemical MIP sensors have been developed for LAC determination.

Bearing that in mind, the present work sought to develop a sensitive electrochemical sensor based on molecularly imprinted polypyrrole film electropolymerized on graphite paper electrode (PE), which was applied for the selective determination of lactose (LAC). Pyrrole (Py) was selected as functional monomer due to its stability, biocompatibility, ease of preparation and electropolymerization, thickness controllability and good conductivity [21,33]. The influence of some factors on the sensitivity of the electrosynthesized MIP sensor were evaluated using Plackett – Burman design and optimized by the central composite design. The work also reports the results obtained from the morphological and electrochemical characterizations of the proposed modified sensor, as well as its analytical performance and application toward the quantification of LAC in milk samples.

2. Experimental section

2.1 Reagents and materials

Lactose (LAC; purity: ≥ 99.0%), fructose (purity: ≥ 99.0%), glucose (purity: ≥ 99.5%), galactose (purity: ≥ 99.0%), sucrose (purity: ≥ 99.5%), monobasic potassium phosphate (purity: ≥ 98.0%), potassium bibasic phosphate (purity: ≥ 98.0%), potassium chloride (purity: ≥ 99.0%), potassium ferricyanide (purity: 99.0%), pyrrole (Py; purity: ≥ 98.0%), sodium hydroxide (purity: ≥ 98.0%), sodium hydroxide solution (NaOH, 50-52% in H_2O) and graphite powder (particle diameter: < 20 μm) were purchased from Sigma-Aldrich (São Paulo, Brazil). Acetone (purity: ≥ 99.5%) was acquired from Alphatec (Rio de Janeiro, Brazil). Quantitative filter paper with particles retention of 1.0 to 2.0 μm (model: C42; diameter: 9.0 cm) and glass varnish were obtained from Unifil (Alvorada, Rio Grande do Sul, Brazil) and Acrilex (São Paulo, Brazil), respectively. All aqueous solutions were prepared using ultrapure water with resistivity not less than 18.2 MΩ cm, obtained from a Milli-Q system.

2.2 Apparatus

The electrochemical measurements, including cyclic voltammetry (CV), differential pulse voltammetry (DPV) and electrochemical impedance spectroscopy (EIS) were performed using a potentiostat (PGSTAT204, Metrohm, Switzerland) controlled by NOVA 1.11 software. A 10 mL electrochemical cell containing three electrodes was used. The electrochemical cell consisted of an Ag/AgCl (3.0 mol L^{-1} KCl) reference electrode, a platinum wire auxiliary electrode and a paper electrode (PE) modified with MIP film used as working electrode. STATISTICA 10 software and Microsoft Office Excel 2007 were employed for data analysis, experimental design, statistical evaluation, and model fitting.

The morphological characterization of the modified electrode was performed using a scanning electron microscope with field emission gun (SEM-FEG) from JEOL, model JSM7500F.

High performance anion-exchange chromatography (HPAEC) analyses were performed using an ion chromatograph 850 Professional IC Cation-HP-Gradient (Metrohm, Switzerland) with extender module 872 (post-column) and 863 compact autosampler (Metrohm, Switzerland). Pulsed amperometric detection (PAD) was carried out using Model IC Amperometric detector (Metrohm, Switzerland) with an electrochemical Wall-Jet cell containing three electrodes: Au used as working electrode, palladium (Pd|PdO) as reference electrode, and stainless steel employed as counter electrode. A CarboPac PA1 anion-exchange column (4 × 250 mm I.D., 10 μm, DIONEX) coupled to guard column CarboPac PA1 column (4 × 50 mm I.D., 10 μm) was used for chromatographic separation.

2.3 Preparation of the paper-based electrodes

The PEs were prepared according to the procedure previously described in the literature [34]. An amount of 150 mg of the conductive carbon ink was manually produced by mixing carbon powder and glass varnish in the proportion of 50:50% (m:m). After that, an amount of 500 μL of acetone was added to the ink to obtain a suitable viscosity. Subsequently, the ink was spread on a piece of quantitative filter paper (5.0 × 1.0 cm) using a paint-brush (Figure 1A). The paper substrate containing the conductive ink was left to dry for 12 h at room temperature and was then cut into pieces of 0.50 × 1.0 cm (Figure 1B). The electroactive area of the electrodes was delimited by using an adhesive tape with a circular orifice of 0.30 cm in diameter. An insulating layer was applied on the back of the paper substrate to prevent the occurrence of capillary water absorption. Finally, the electrical contact of the electrodes was established using copper foils (Figure 1C).

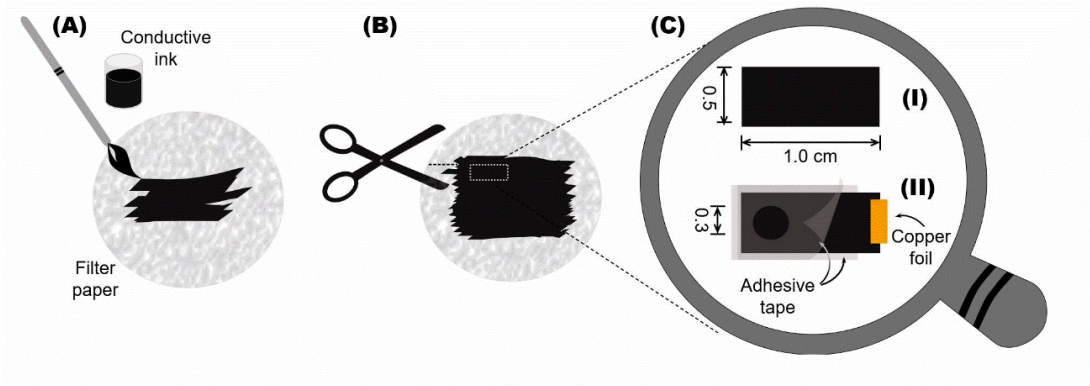

Figure 1. Schematic representation of the construction of the paper-based electrode. A) Spreading of the carbon conductive ink onto the paper substrate with a paint-brush. B) Cutting of electrodes. C) Painted paper piece (I) and adhesive tape layers of the final device (II) were used to define the geometric area of the working electrode and prevent the occurrence of capillary water absorption. The copper foil was used to provide the electrical contact with the potentiostat.

2.4 Modification of the electrode with molecularly imprinted polypyrrole film

To modify the PE with a molecularly imprinted polypyrrole (PPy) film, the electrode was placed in a 200 mmol L^{-1} phosphate buffer (PB) solution (pH= 6.0) containing 2.0 mmol L^{-1} LAC and 41.0 mmol L^{-1} Py. The electropolymerization process was performed by CV using 5 voltammetric cycles in the potential range of 0.0 to 1.2 V at 50 mV s^{-1}. The PPy film was overoxidized in 100 mmol L^{-1} NaOH solution to produce the imprinted cavities. The overoxidation process was performed using five voltammetric cycles in the potential range of 0.0 to 1.6 V at 50 mV s^{-1}. This procedure enabled the removal of the LAC template molecule from the polymeric structure. Thereafter, the preparation of the PPy/PE was completed. For comparison purposes, an electrode modified with non-imprinted polymer (NIP) was prepared using the same experimental procedure in the absence of LAC.

2.5 Electroanalytical measurements

The PPy/PE electrode was placed in a PB solution (200 mmol L^{-1}, pH= 8.0) containing different concentrations of LAC for 15 min. The measurements were performed by DPV in the potential range of − 0.20 to 0.50 V under the following conditions: pulse amplitude: 50 mV; pulse width: 50 ms; pulse time: 0.50 s and scan rate: 10 mV s^{-1}. To perform this analysis, a solution of 5.0 mmol L^{-1} $[Fe(CN)_6]^{3-}$ in 1.0 mol L^{-1} KCl was used as an electrochemical probe.

The performance of the electrode in terms of LAC detection was evaluated through the current difference (ΔI) of this device before and after the rebinding process. The figures of merit, such as sensitivity (S), and detection (LOD) and quantification limits (LOQ) were obtained by the following equations: LOD = 3 × SD/S and LOQ = 10 × SD/S, where SD corresponds to the standard deviation of the intercept and S refers to the slope of the analytical curve.

2.6 Chromatographic method

The HPAEC separation was performed using a mobile phase mixture of 150 mmol L^{-1} NaOH/ultrapure water (40:60 v/v) at flow rate of 1.0 mL min^{-1} (isocratic elution). The mobile phase was filtered (0.22 μm PTFE Millipore membrane) and degassed by ultrasonication for 10 min. Column oven and detector temperatures applied were 30 and 35 °C, respectively, and the injection volume was 20 μL. The triple potential (E) waveforms employed for PAD were as follows: E_1, 0.050 V for 300 ms (integration time: 100 ms); E_2, 0.55 V for 50 ms; and E_3, -0.10 V for 200 ms.

2.7 Sample preparation

The liquid milk samples were purchased from a local supermarket and pre-processed based on reports in the literature [9]. The milk samples were diluted with ultrapure water (1:10 v/v). After vortexing for 1 min, a 5.0 mL aliquot of each sample was centrifuged at room temperature for 12 min at 4000 rpm (K14-4000 centrifuge, Kasvi). Thereafter, supernatants were collected,

filtered (0.22 µm Titan3™ PVDF filter, Thermo Fisher Scientific) and diluted with ultrapure water for detection.

3. Results and discussion

3.1 Preparation and morphological characterization of the PPy/PE

Figure S1 shows the cyclic voltammograms obtained during the electropolymerization of the Py on the electrode surface. An anodic peak can be observed at 0.95 V due to the electrooxidation of Py. In this process, the Py monomer loses an electron to form a cationic radical, which, in turn, couples with another cationic radical to generate a PPy dimer. Subsequently, this dimer couples with other cationic radicals to form the polymeric matrix of PPy [35].

During the electropolymerization process, the LAC molecule is trapped in the polymeric structure through molecular interactions with Py units. These interactions are essentially important for the formation of the imprinted cavities and they probably occur between the hydroxyl groups of the LAC molecule and the amine group of the Py units. In Figure S1, a decrease in current intensity can be clearly observed as the number of cycles increases. The same behaviour was noted during the preparation of the non-imprinted PPy/PE (Figure S2); this shows that the LAC molecule is not electroactive in the potential range employed in the electropolymerization process.

The modified electrode was characterized by SEM-FEG (Figure 2). Figure 2A shows the PE surface without any modification, where the carbon ink can be found covering the entire paper substrate. In addition, one will observe that the PE has a rough and non-homogeneous surface, which favours the adhesion of the PPy film on this electrode. Figs. 2B and 2C show the PPy/PE and non-imprinted PPy/PE surfaces, respectively. In both images, one can observe that the PPy film has covered the entire PE surface; however, this polymeric structure presented a higher degree of coverage for the non-imprinted PPy/PE. This can be attributed to the absence of the LAC molecule during the electropolymerization procedure, since this molecule strongly affects the

formation of the PPy polymer chains. The SEM-FEG images clearly show that the electropolymerization process was efficient for the electrosynthesis of the PPy film on the PE surface.

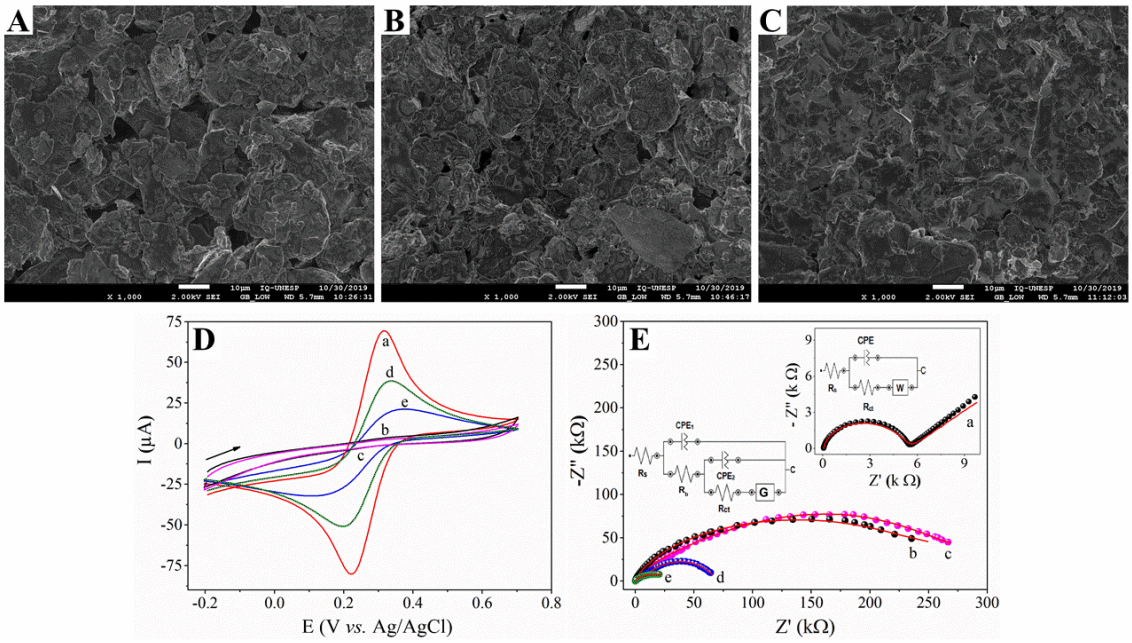

Figure 2. SEM-FEG images for (A) PE, (B) PPy/PE and (C) non-imprinted PPy/PE; (D) CV measurements at 50 mV s^{-1} and (E) Nyquist diagrams at fixed potential of 0.23 V, frequency range of 100 kHz to 10 mHz and potential amplitude of 10 mV for (a) PE, (b) PPy/PE; (c) non-imprinted PPy/PE, (d) PPy/PE after the formation of the imprinted cavities, and (e) PPy/PE after the rebinding procedure using 200 mmol L^{-1} PB solution (pH= 8.0) containing 10 nmol L^{-1} LAC for 15 min. Inset: corresponding equivalent circuits. The CV and EIS measurements were performed using a solution of 5.0 mmol L^{-1} $[Fe(CN)_6]^{3-}$ in 1.0 mol L^{-1} KCl as an electrochemical probe.

3.2 Electrochemical characterization of the PPy/PE

The modified electrode was electrochemically characterized by CV and EIS using a solution of 5.0 mmol L^{-1} $[Fe(CN)_6]^{3-}$ in 1.0 mol L^{-1} KCl as an electrochemical probe. Figure 2D shows a pair of redox peaks corresponding to the $[Fe(CN)_6]^{3-/4-}$ redox couple (curve a). These peaks are not observed after the formation of the PPy film on the PE surface (curve b), which implies that the polymeric film prevented the access of the electrochemical probe to the electrode surface. As a result, no electron transfer occurred at the electrode/solution interface. The same behaviour was observed for the non-imprinted PPy/PE electrode (curve c).

For the formation of imprinted cavities, the LAC molecules need to be removed from the polymeric matrix. This procedure was carried out by subjecting the PPy film to an overoxidation process in a 100 mol L^{-1} NaOH solution. This solution was chosen since strong nucleophiles, such as OH^-, favour the PPy film overoxidation, which would not occur in acidic or neutral medium [33]. During the overoxidation process, oxygenated groups (such as carbonyl and carboxyl) were inserted in the PPy structure, which promoted the removal of LAC molecules from the polymeric film [33].

The presence of voltammetric peaks related to the electrochemical probe after the removal of the LAC molecules (Figure 2D, curve d) showed that the overoxidation process was efficient in forming the imprinted cavities. Consequently, the $[Fe(CN)6]^{3-}$ species were able to permeate the PPy film through these cavities and reach the electrode surface. However, when the electrode was placed in a 200 nmol L^{-1} PB solution (pH= 8.0) containing 10 nmol L^{-1} LAC for 15 min, there was a noticeable decrease in the current intensities of the redox probe (Figure 2D, curve e). This behaviour indicates that during the rebinding process, the LAC molecules occupied some imprinted cavities, decreasing the number of sites available for the electrochemical probe to access the electrode surface.

Figure 2E shows the Nyquist diagrams obtained after each step involving the electrode preparation and the equivalent circuits used to fit the experimental data. The Nyquist diagram for the PE without any modification can be seen in the inset of Figure 2E (curve a). A well-defined semicircle is observed at high frequencies followed by a linear region at low frequencies. The equivalent circuit for this diagram consists of the constant phase element (CPE), solution resistance (R_s), charge-transfer resistance (R_{ct}) and Warburg diffusion element (W).

After the formation of the PPy film on the electrode surface, the equivalent circuits required to fit the experimental data were formed by CPE_1, CPE_2, R_s, R_{ct}, bulk resistance (R_b) and Gerischer impedance element (G). In this context, CPE_1 and R_b were attributed to the presence of the PPy

film on the PE surface, while G was used to simulate the characteristics of a porous electrode [22]. It is worth noting that the experimental data were well fitted with the proposed circuit; this occurs due to the presence of imprinted cavities in the polymeric structure of PPy, which gives a porous aspect to the PPy/PE electrode.

For the equivalent circuits presented in Figure 2E, the R_{ct} value is found to be proportional to the semicircle size and it is the element of the circuit that best describes the charge-transfer between the $[Fe(CN)_6]^{3-}$ species and the electrode surface [20]. After the electropolymerization process, an increase was observed in the R_{ct} value from 5.3 kΩ to 284 kΩ and 322 kΩ for the PPy/PE (curve b) and non-imprinted PPy/PE (curve c) electrodes, respectively. This shows that the PPy polymeric film on the PE surface restricted the charge-transfer at the electrode-solution interface.

After the overoxidation of the PPy film and the consequent formation of the imprinted cavities, the R_{ct} value exhibited a remarkable decrease from 284 kΩ to 32.4 kΩ (Figure 2E, curve d); this indicates that the cavities formed in the polymeric structure allowed the electrochemical probe to reach the PE surface. On the other hand, after the electrode was placed in a 200 mmol L^{-1} PB solution (pH= 8.0) containing 10 nmol L^{-1} LAC for 15 min, an increase was observed in the R_{ct} value from 32.4 kΩ to 70 kΩ (Figure 3B, curve e); this evidently points to the fact that, during the rebinding process, the LAC molecules occupied some imprinted cavities and blocked the sites available for the $[Fe(CN)_6]^{3-}$ probe to access the electrode surface. These EIS results are in agreement with the CV measurements, which together confirm that the imprinted cavities for LAC recognition were successfully formed in the PPy polymeric structure.

3.3 PPy/PE sensor optimization

A large number of potential factors can influence the development and sensitivity of electrosynthesized MIP sensors. The effects of these factors are usually evaluated by univariate

optimization. However, this procedure generally consumes time and chemicals; as such, for additional optimization, Plackett–Burman design (PBD) was employed as a screening and selection method of variables that can statistically influence the construction of the PP/PE.

Based on studies previously reported in the literature [33,36,37], 7 factors, including LAC (A) and Py concentrations (B), number of cycles employed in electropolymerization (C) and LAC extraction (D; overoxidation), pH of MIP electropolymerization solution (E), LAC rebinding time (F) and pH for LAC rebinding on the PPy/PE (G), were selected and subjected to analysis. The factors were tested at two parameter levels, high (+) and low (–), as shown in Table 1. The PBD experimental matrix was conducted for the 7 factors (2^{7-3}), with 16 randomized runs in triplicate. The PPy/PE response expressed as average ΔI for the redox probe is presented in Table S1.

The Pareto chart of the standardized main effect (Figure 3) displays the estimated effects of the 7 factors and their statistical significance with a minimum *t*-value of 2.3 at 95.0% confidence level. The Pareto chart includes a vertical dashed reference line (*t*-value, $\alpha = 0.05$) used for separating the statistically significant effects and bars proportional to the absolute values of the estimated effects. Among the factors evaluated, only E presented a negative effect (white bar); this indicates an improvement in the sensor response at a lower level of this factor. The effects of other factors (A, B, C, D, F and G) were positive, which implies that there were improvements in peak currents at their higher levels.

Table 1. High (+) and low parameter levels (–) for factors chosen for PBD experimental field.

Factor	Symbol	Low (–)	High (+)
LAC concentration (mmol L^{-1})	A	2	10
Py concentration (mmol L^{-1})	B	5	50
No. of cycles used in electropolymerization	C	5	15
pH of MIP electropolymerization solution	D	6	8
No. of cycles used in LAC extraction	E	5	15
LAC rebinding time (min)	F	5	25
pH for LAC rebinding on PPy/PE	G	5	8

Based on the screening design results (Figure 3), the factors G (45.3%), B (20.1%) and F (17.8%) were found to represent 83.2% of the current response of PPy/PE, which shows that these factors were the most important for the development of the sensor. Thus, these most relevant factors were thoroughly evaluated. The other factors, i.e., A (5.0%), C (1.0%), D (8.3%) and E (2.5%), were not statistically significant.

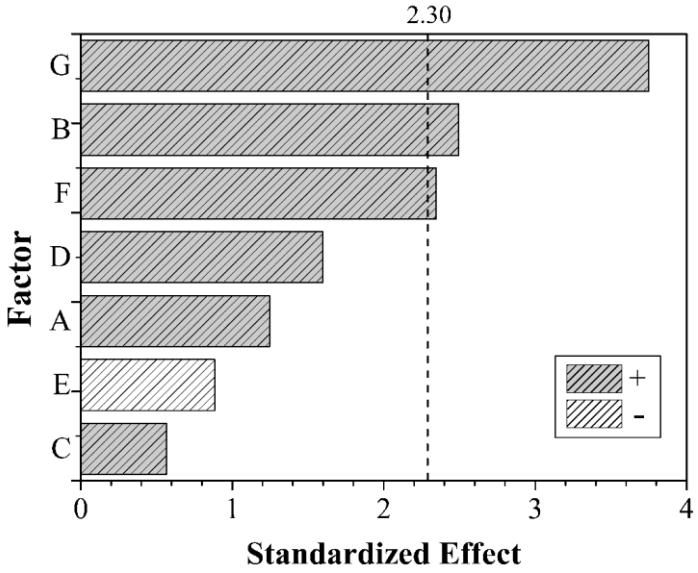

Figure 3. Pareto chart analysis of the standardized main effect for PBD (α= 0.05).

After screening (using PBD), the Py concentration (B), LAC rebinding time (F) and pH for LAC rebinding on the PPy/PE (G) were optimized using the central composite design (CCD) to obtain the best conditions for the sensor performance. Five-level CCD experiments (2^3) with 18 runs and 4 replicates at the central point were carried out; the corresponding peak current (ΔI) of each run is presented in Table S2. The results were converted into individual desirability based on a study reported in the literature [38]. Figure 4 presents the desirability diagrams obtained for the factors B, F and G used in the construction of the PPy/PE with optimized conditions. The best conditions were 41 mmol L^{-1} for Py concentration (B), 5 min for LAC rebinding time (F) and pH 8.0 for LAC rebinding on the PPy/PE (G).

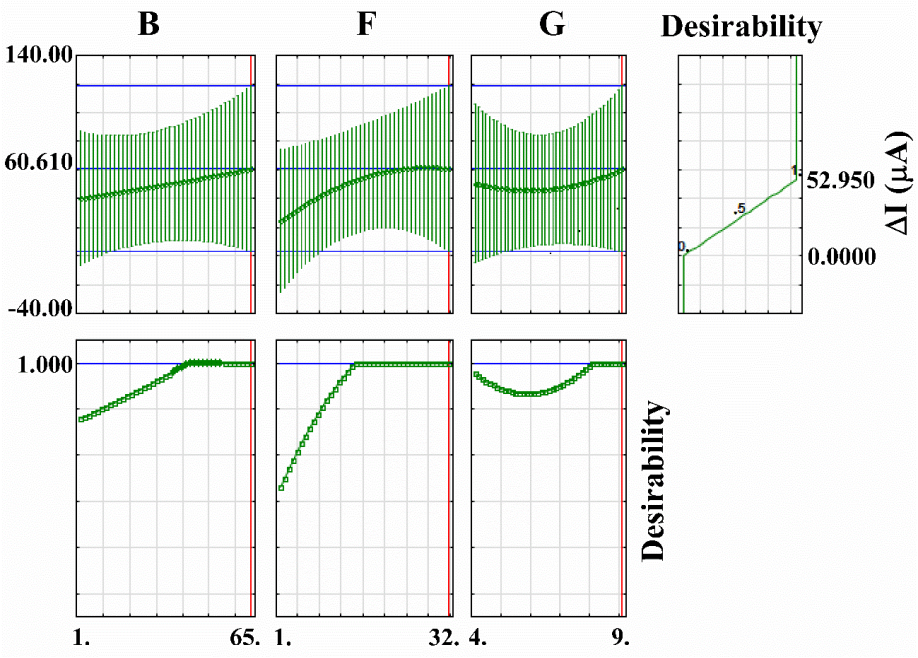

Figure 4. Desirability diagrams for CCD matrix responses with 95% confidence level.

3.4 Analytical performance

After optimizing the parameters and characterizing the sensor, quantitative analyses were performed using DPV (see Figure 5). After the removal of the template, the PPy/PE was placed in 200 mmol L^{-1} PB solution (pH= 8.0) containing different concentrations of LAC for 15 min. As shown in Figure 5A, the peak current response was found to decrease when LAC concentration was increased. This result indicates that the cavities formed on the sensor surface were occupied by the LAC molecules which blocked the diffusion of the $[Fe(CN)_6]^{3-/4-}$. Accordingly, the current of the $[Fe(CN)_6]^{3-/4-}$ electrochemical probe was proportionally reduced as the LAC concentration in solution was increased. The ΔI value was proportional to the LAC concentration in two linear ranges: 1.0 to 10 nmol L^{-1} and 25 to 125 nmol L^{-1}, as shown in Figure 5B. The first linear range (Inset in Figure 5B) was used to obtain the figures of merit. The linear regression equation obtained was ΔI (μA) = 0.51 C_{LAC} (nmol L^{-1}) + 15, with correlation coefficient of 0.9997, LOD of 0.88 nmol L^{-1}, LOQ of 29 nmol L^{-1} and sensitivity of 0.51 μA L $nmol^{-1}$.

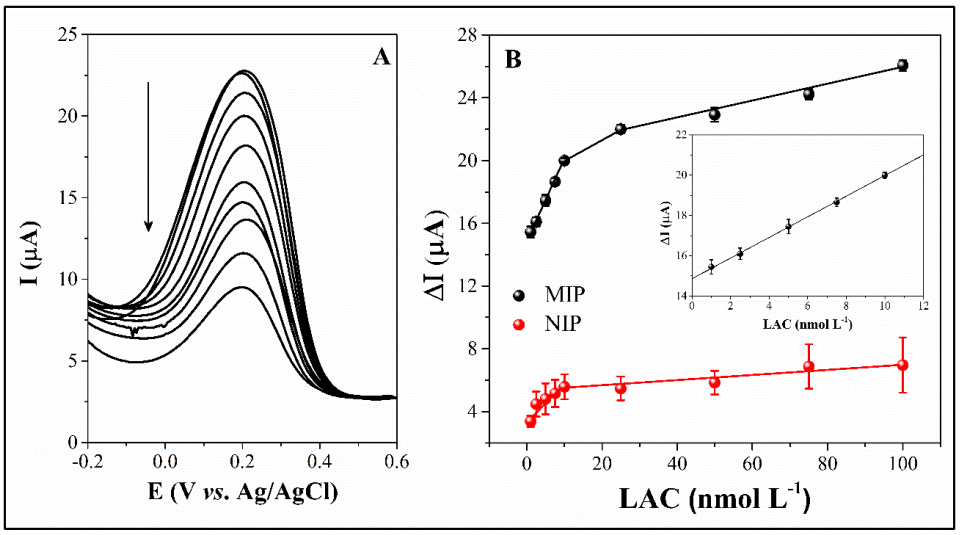

Figure 5. (A) DPVs of PPy/PE after 15 min of incubation with different concentrations of LAC ranging from 1.0 to 125 nmol L^{-1} in 5.0 mmol L^{-1} $[Fe(CN)_6]^{3-/4-}$ containing 1.0 mol L^{-1} KCl. (B) Respective calibration curves for MIP and NIP. Inset: first linear range of 1.0 to 10 nmol L^{-1}.

The existence of two linear ranges in the analytical response of the MIP sensor can be explained by the difference in affinity between the cavities formed in the polymer and the LAC molecule. When the LAC concentration in the solution is low, the molecules will preferably occupy the high affinity imprinted sites, which are located on the surface of the MIP. Conversely, when the LAC concentration is higher in the solution, the low-affinity sites, which are usually more deeply located, are occupied, causing a decline in the slope of the calibration curve [33,39].

The comparison of the proposed sensor with other sensors employed for LAC determination found in the literature (Table 2) shows that the PPy/PE presented a relatively better analytical performance, with good linear working range and lower detection limit. In addition, considering that the PPy/PE is a non-enzymatic sensor, it is inexpensive and easy to prepare, apart from exhibiting relatively higher stability.

Table 2. Comparison of PPy/PE performance with other reported sensors for lactose determination.

Detection method	Linear range	Detection limit	References

Pt/graphene/P(1,5-DAN) electrode [a]	0 – 1.7 mmol L^{-1}	2.9 µmol L^{-1}	[14]
PPy-DBSb enzyme electrode [b]	0.3 – 1.22 mmol L^{-1}	2.0 µmol L^{-1}	[2]
Lactose biosensor	1.0 – 3.0 mmol L^{-1}	1.0 µmol L^{-1}	[15]
bi-enzyme (β-Gal + GOx) electrodes [c]	0.1 – 14 mmol L^{-1}	< 1.0 µmol L^{-1}	[5]
β-Gal-GOD-HRP-TTF-MPA-AuE [d]	1.5 –120 µmol L^{-1}	0.46 µmol L^{-1}	[3]
Cu foam electrode	0.18 – 3.5 mmol L^{-1}	2.6 µmol L^{-1}	[7]
CtCDH-PVA-TLFCL-GPH [e]	0.25 – 5.0 mmol L^{-1}	0.18 mmol L^{-1}	[13]
CDH [f]	10 – 100 µmol L^{-1}	-	[4]
PPy/PE	1.0 – 10 nmol L^{-1}	0.88 nmol L^{-1}	This Work

[a] Polydiaminonaphthalene [P(1,5-DAN)].
[b] PPy and DBS stand for polypyrrole and dodecylbenzenesulfonate.
[c] β-Galactosidase (β-Gal) and glucose oxidase (GOx).
[d] β-Galactosidase (β-Gal), glucose oxidase (GOD), peroxidase (HRP) and the mediator tetrathiafulvalene (TTF), 3-mercaptopropionic acid (MPA).
[e] Photocrosslinkable polymer (PVA), Thin layer flow-cell (TLFCL) and graphene (GHP).
[f] Cellobiose dehydrogenase (CDH).

3.5 Binding Selectivity for LAC

To evaluate the selectivity of the PPy/PE for LAC detection (Figure 6), the sensor was placed in a solution containing the main interfering species, including sucrose, glucose, galactose and fructose, which are structurally similar to LAC and are usually present in considerable quantities in milk samples. It is worth noting that the selectivity of MIP-based sensors is influenced by 2 factors: the position and type of the functional groups and the size of the molecule. Larger molecules with different chemical structure do not usually interfere in the analysis. For the evaluation of the sensor selectivity, an analysis was conducted regarding the changes in current response (ΔI) of $[Fe(CN)_6]^{3-/4-}$ on the MIP and NIP electrodes containing the same concentration (10 nmol L^{-1}) of each potentially interfering molecule, as shown in Figure 6A. As can be noted, the PPy/PE was able to recognize the LAC molecule with a current response of about 3.7 times greater compared with molecules of similar chemical structure. This result shows that the proposed sensor is suitable for the selective determination of LAC even in complex samples.

The proposed sensor response to LAC and the interfering molecules employed at the same concentration was also evaluated in terms of the imprinting factor (α) and selectivity factor (β), as shown in Table 3. The values related to the imprinting factor (α) obtained for the LAC were

relatively greater; this shows that the sensor has a relatively better ability to interact with this molecule than with the interferents. The selectivity factor shows that the PPy/PE has higher affinity for the LAC molecule, which implies that the cavities created in the polymer matrix are selective. These parameters indicate that the size and conformation of the cavities formed in the PPy/PE are selective for LAC detection.

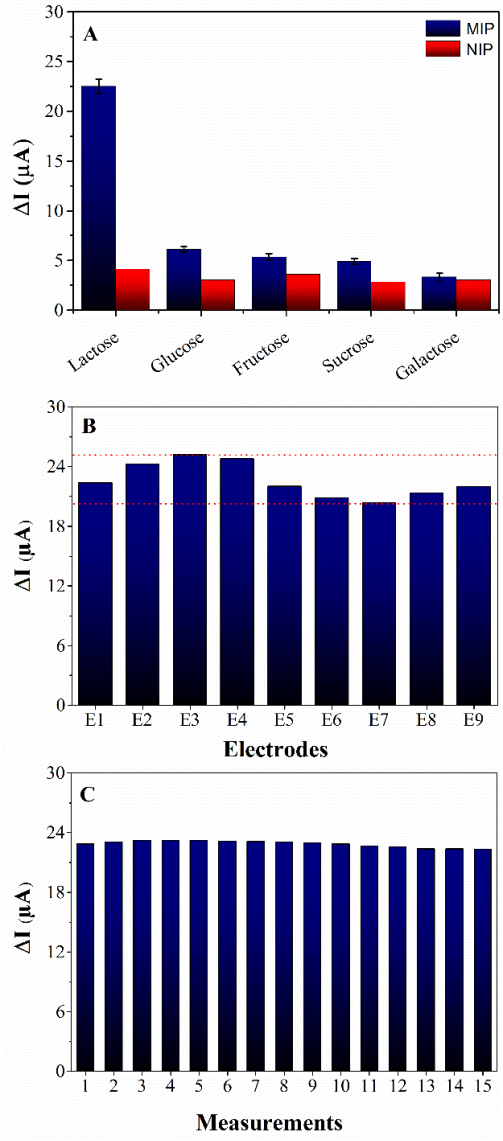

Figure 6. (A) Selectivity comparison of the MIP and NIP sensors: Concentration of 10 nmol L^{-1} in PB solution (pH= 8.0) for each molecule analyzed (rebinding time: 15 min). (B) Reproducibility measurements for 10 nmol L^{-1} LAC detection using nine different electrodes, and (C) Repeatability measurements for consecutive 10 nmol L^{-1} LAC detections using the same electrode. DPV response for solution containing 5.0 mmol L^{-1} $[Fe(CN)_6]^{3-/4-}$ in 1.0 mol L^{-1} KCl.

Table 3. Parameters of PPy/PE selectivity for lactose detection.

Molecule	Imprinted PPy/PE (µA)	Non-imprinted PPy/PE (µA)	α[a]	β[b]
Lactose	23	4.1	5.6	1.0
Glucose	5.9	3.0	2.0	2.9
Frutose	5.1	3.6	1.4	4.0
Sucrose	4.7	2.8	1.7	3.3
Galactose	3.0	3.0	1.2	4.7

[a] $\alpha = (\Delta I_{MIP})/(\Delta I_{NIP})$
[b] $\beta = (\alpha_{Lactose}/\alpha_{interferent})$

3.6 Repeatability, reproducibility and stability of the PPy/PE

The studies regarding the repeatability, reproducibility and stability of the PPy/PE were performed according to the experimental conditions described in *Section 2.5*, using a 200 mmol L^{-1} PB solution (pH= 8.0) containing 10 nmol L^{-1} LAC. The sensor reproducibility was evaluated by comparing the current response of different electrodes during LAC detection. To perform this analysis, nine electrodes were independently prepared and used for the detection of LAC. Figure 6B shows that the current responses of the electrodes varied from 24.4 to 30.2 µA and presented a relative standard deviation (RSD) of 7.3% (n= 9). To evaluate the sensor repeatability, 15 consecutive measurements were performed using the same electrode in the presence of LAC (Figure 6C). The RSD value obtained was 1.4% (n = 15), which demonstrates that the PPy/PE electrode has good repeatability for LAC determination.

The stability of the PPy/PE electrode was investigated as a function of time. An electrode was prepared and used for the detection of LAC for several consecutive days. During the analysis period, this device was stored in a dry place at room temperature (25 °C). The results showed that the current response of this electrode decreased 5.7, 15.3 and 24.4% after 5, 10 and 12 days of use, respectively. Considering that the proposed electrode consists of a disposable paper-based platform, this study demonstrated that the PPy/PE electrode has good stability for LAC detection.

3.7 LAC determination in milk samples

For the quantification of LAC in LAC-free products containing low contents of this molecule, one requires a sensitive and selective method capable of detecting LAC at concentrations below 0.1% [4]. With this in mind, the proposed sensor was applied for the determination of LAC in four samples of Ultra High Temperature (UHT) cow milk cow from different brands. One of these samples was labeled LAC-containing whole milk and the other three samples were labeled LAC-free milk. The first sample labeled whole milk was named sample A, and the other three samples were named as follows: LAC-free whole milk was named sample B; LAC-free semi-skim milk was named sample C, and LAC-free skim milk was named sample D. The determination of LAC was performed using the standard addition method, which involves the addition of known concentration of the analyte in a specific quantity of the sample. The study was carried out by DPV under optimized conditions, and the concentration of LAC used in these experiments ranged from 25 to 75 nmol L^{-1}. The samples were prepared as described in *Section 2.7*, and they were diluted as follows: 2.2×10^7 (sample A) and 8.8×10^5 times (sample B, C and D). The standard addition curves for each sample and the respective linear regression equations are shown in Figure S3. All the measurements were performed in triplicate with four different electrodes based on the proposed method (n=3). The average recovery rate obtained for the 12 measurements performed was 100 ± 8 %; this shows that the proposed sensor has good practical applicability, making it suitable to be used for the reliable and selective determination of LAC in milk samples.

The amounts (g L^{-1}) of LAC found in samples A, B, C and D were 47.2 ± 1.8, 0.13 ± 0.01, 0.13 ± 0.00 and 0.11 ± 0.01, respectively (Table 4). Under the Brazilian Health Regulatory Agency legislation [40,41], dairy products are legally classified as LAC-free when the amount of LAC in them is <1.0 g L^{-1} . For the EU Member States, the established LAC content threshold for dairy products to be considered LAC-free varies from 0.10 to 1.0 g L^{-1} [42]. Dairy products above this

threshold of 1.0 g L^{-1} are said to contain LAC. Another relevant information worth mentioning here is that, according to the International Dairy Federation [43], UHT milk contains less than 60 g L^{-1} of LAC. All the samples tested in this study presented LAC levels within the ranges recommended by the regulatory agencies. Thus, from the results obtained, one can conclude that the proposed sensor presented good performance in terms of LAC determination in both low LAC content milk samples (LAC-free products) and in high LAC content whole milk samples.

Table 4. Lactose determination in milk samples at 95% confidence level (n = 3).

Brand codification	PPy/PE (g L^{-1})	HPAEC (g L^{-1})	[a] F-test		[b] t-test	
			$F_{Calculated}$	$F_{Critical}$	$t_{calculated}$	$t_{Critical}$
Sample A	47.2 ± 1.8	47.0 ± 1.5	1.6	19.0	0.16	2.8
Sample B	0.13 ± 0.01	0.14 ± 0.00	8.1		2.6	
Sample C	0.13 ± 0.00	0.14 ± 0.00	8.1		2.7	
Sample D	0.11 ± 0.01	0.11 ± 0.01	2.5		1.1	

[a] Degrees of freedom (D. F.) = 2.
[b] D. F.= 4.

The results were validated using High performance anion-exchange chromatography (HPAEC) method with electrochemical detection. The samples A, B, C and D were diluted 3548.4, 71.9, 73.2 and 78.1 times, respectively, and LAC determination was conducted by the standard addition method. The results obtained are summarized in Table 4. The amounts of LAC found in the samples through the application of the PPy/PE sensor were in agreement with those found by the HPAEC method. To check for precision and accuracy, the results obtained under the two methods were statistically compared using *F*-test and paired Student's *t*-test at 95% confidence level (Table 4). The *F*-test revealed that the PPy/PE and HPAEC methods provided an equivalent level of precision. All the $F_{Calculated}$values were less than the standard value ($F_{Critical}$= 19.0). Similarly, the results obtained from the *t*-test showed that there were no significant differences between the HPAEC method and the proposed analytical method ($t_{Calculated} < t_{Critical}$); this

shows that the PPy/PE sensor can be accurately applied for LAC determination in milk samples under the optimized conditions described in this study.

4. Conclusions

This work reported the development of a simple, low-cost, disposable paper-based non-enzymatic voltammetric sensor for lactose (LAC) determination using the electropolymerized molecular imprinting technique. The imprinting of LAC molecules in the PPy film on the PE surface was successfully conducted through a multivariate optimization strategy. The results showed that Py concentration, LAC rebinding time, and pH for LAC rebinding on the PPy/PE exhibited the most important effects on the efficiency of the MIP sensor. Under the optimized conditions applied, PPy/PE presented high analytical performance for LAC determination compared with other existing electrochemical sensors. In addition, the sensor exhibited high stability, excellent selectivity for LAC, and good reproducibility. The proposed MIP sensor was successfully applied for the determination of LAC in whole and LAC-free milk samples. The application of the PPy/PE sensor coupled with an electroanalytical technique is a cost-effective approach which can be employed successfully as an alternative to more expensive analytical methods based on liquid chromatography or biosensors.

Declaration of competing interests

The authors declare that they have no known competing financial interests or personal relationships that could have appeared to influence the work reported in this paper.

Credit authorship contribution statement

José Luiz da Silva: Conceptualization, Methodology, Investigation, Formal Analysis, Validation, Project Administration, Writing - Original Draft. **Edervaldo Buffon**: Methodology, Investigation,

Formal Analysis, Validation, Writing - Original Draft. **Maísa Azevedo Beluomini**: Methodology, Investigation, Formal Analysis, Validation, Writing - Original Draft. **Lauro Antônio Pradela-Filho**: Methodology, Investigation, Resources. **Diele Aparecida Gouveia Araújo**: Methodology, Investigation, Resources. **André Luiz Santos**: Conceptualization, Supervision, Resources, Funding Acquisition, Writing - Review & Editing. **Regina Massako Takeuchi**: Conceptualization, Resources, Supervision, Funding Acquisition, Writing - Review & Editing. **Nelson Ramos Stradiotto**: Conceptualization, Resources, Supervision, Funding Acquisition, Writing - Review & Editing.

Acknowledgments

The authors are grateful to São Paulo Research Foundation (FAPESP: 2019/13818-8, 2018/12131-6 and 2017/25329-6), Minas Gerais Research Foundation (FAPEMIG: APQ-02905-15 and APQ-02078-15), Coordination for the Improvement of Higher Education Personnel (CAPES: 88887.368610/2019-00) and National Council of Technological and Scientific Development (CNPq: 408783/2018-4, 447668/2014-5 and 443315/2014-0) for the financial support and scholarships granted in the course of this work.

Appendix A. Supplementary data

Supplementary data to this article can be found online at https://doi.org/.

References

[1] B. Misselwitz, M. Butter, K. Verbeke, M.R. Fox, Update on lactose malabsorption and intolerance: Pathogenesis, diagnosis and clinical management, Gut. 68 (2019) 2080–2091. https://doi.org/10.1136/gutjnl-2019-318404.

[2] O. Gürsoy, G. Çelik, S.Ş. Gürsoy, Electrochemical biosensor based on surfactant doped polypyrrole (PPy) matrix for lactose determination, J. Appl. Polym. Sci. 131 (2014) 1–7. https://doi.org/10.1002/app.40200.

[3] F. Conzuelo, M. Gamella, S. Campuzano, M.A. Ruiz, A.J. Reviejo, J.M. Pingarrón, An integrated amperometric biosensor for the determination of lactose in milk and dairy

products, J. Agric. Food Chem. 58 (2010) 7141–7148. https://doi.org/ 10.1021/jf101173e.
[4] F. Lopez, S. Ma, R. Ludwig, W. Schuhmann, A. Ruff, A Polymer Multilayer Based Amperometric Biosensor for the Detection of Lactose in the Presence of High Concentrations of Glucose, Electroanalysis 29 (2017) 154–161. https://doi.org/ 10.1002/elan.201600575.
[5] M. Ammam, J. Fransaer, Two-enzyme lactose biosensor based on β-galactosidase and glucose oxidase deposited by AC-electrophoresis: Characteristics and performance for lactose determination in milk, Sensor. Actuator. B Chem. 148 (2010) 583–589. https://doi.org/10.1016/j.snb.2010.05.027.
[6] F. Tasca, R. Ludwig, L. Gorton, R. Antiochia, Determination of lactose by a novel third generation biosensor based on a cellobiose dehydrogenase and aryl diazonium modified single wall carbon nanotubes electrode, Sensor. Actuator. B Chem. 177 (2013) 64–69. https://doi.org/10.1016/j.snb.2012.10.114.
[7] J. Jin, Y. Ge, G. Zheng, Y. Cai, W. Liu, G. Hui, D-Glucose, D-Galactose, and D-Lactose non-enzyme quantitative and qualitative analysis method based on Cu foam electrode, Food Chem. 175 (2015) 485–493. https://doi.org/10.1016/ j.foodchem.2014.11.148.
[8] T.M. Bayless, E. Brown, D.M. Paige, Lactase non-persistence and lactose intolerance, Curr. Gastroenterol. Rep. 19 (2017) 23. https://doi.org/10.1007/ s11894-017-0558-9.
[9] N. Gonzaga, L.S. Watanabe, J. Mareze, T.B. Madeira, R. Tamanini, E.A. Rios, S.L. Nixdorf, V. Beloti, Green method using water for lactose and lactulose extraction and determination in milk by high-performance liquid chromatography with refractive index detection, LWT - Food Sci. Technol. 113 (2019) 108288. https://doi.org/10.1016/j.lwt.2019.108288.
[10] M. Pokrzywnicka, R. Koncki, Disaccharides Determination: A Review of Analytical Methods, Crit. Rev. Anal. Chem. 48 (2018) 186–213. https://doi.org/10.1080/10408347.2017.1391683.
[11] L. Gambelli, Milk and its sugar-lactose: A picture of evaluation methodologies, Beverages 3 (2017) 35. https://doi.org/10.3390/beverages3030035.
[12] S. Jia, X. Dong, Recent advances in analytical techniques for the determination of lactose, Int. J. Curr. Res. Chem. Pharm. Sci. 3 (2017) 39–42. https://doi.org/10.22192/ijcrcps.
[13] H. Kanso, M.B.G. García, L.F. Llano, S. Ma, R. Ludwig, P.F. Bolado, D.H. Santos, Novel thin layer flow-cell screen-printed graphene electrode for enzymatic sensors, Biosens. Bioelectron. 93 (2017) 298–304. https://doi.org/ 10.1016/j.bios.2016.08.069.
[14] B.H. Nguyen, B.T. Nguyen, H. Van Vu, C. Van Nguyen, D.T. Nguyen, L.T. Nguyen, T.T. Vu, L.D. Tran, Development of label-free electrochemical lactose biosensor based on graphene/poly(1,5-diaminonaphthalene) film, Curr. Appl. Phys. 16 (2016) 135–140. https://doi.org/10.1016/j.cap.2015.11.004.
[15] O.O. Soldatkin, V.M. Peshkova, O.Y. Saiapina, I.S. Kucherenko, O.Y. Dudchenko, V.G. Melnyk, O.D. Vasylenko, L.M. Semenycheva, A.P. Soldatkin, S.V. Dzyadevych, Development of conductometric biosensor array for simultaneous determination of maltose, lactose, sucrose and glucose, Talanta 115 (2013) 200–207. https://doi.org/10.1016/j.talanta.2013.04.065.
[16] Z. Mazouz, M. Mokni, N. Fourati, C. Zerrouki, F. Barbault, M. Seydou, R. Kalfat, N. Yaakoubi, A. Omezzine, A. Bouslema, A. Othmane, Computational approach and electrochemical measurements for protein detection with MIP-based sensor, Biosens. Bioelectron. 151 (2020) 111978. https://doi.org/10.1016/j.bios.2019. 111978.
[17] I.A. Stoian, B.C. Iacob, C.L. Dudaș, L. Barbu-Tudoran, D. Bogdan, I.O. Marian, E. Bodoki, R. Oprean, Biomimetic electrochemical sensor for the highly selective detection of azithromycin in biological samples, Biosens. Bioelectron. 155 (2020) 112098. https://doi.org/10.1016/j.bios.2020.112098.

[18] T. Alizadeh, M. Zare, M.R. Ganjali, P. Norouzi, B. Tavana, A new molecularly imprinted polymer (MIP)-based electrochemical sensor for monitoring 2,4,6-trinitrotoluene (TNT) in natural waters and soil samples, Biosens. Bioelectron. 25 (2010) 1166–1172. https://doi.org/10.1016/j.bios.2009.10.003.
[19] E. Mazzotta, R.A. Picca, C. Malitesta, S.A. Piletsky, E. V. Piletska, Development of a sensor prepared by entrapment of MIP particles in electrosynthesised polymer films for electrochemical detection of ephedrine, Biosens. Bioelectron. 23 (2008) 1152–1156. https://doi.org/10.1016/j.bios.2007.09.020.
[20] E. Buffon, N.R. Stradiotto, Electrochemical sensor based on molecularly imprinted poly (ortho-phenylenediamine) for determination of hexahydrofarnesol in aviation biokerosene, S ensor. Actuator. B Chem. 287 (2019) 371–379. https://doi.org/ 10.1016/j.snb.2019.02.059.
[21] M.A. Beluomini, J.L. da Silva, A.C. de Sá, E. Buffon, T.C. Pereira, N.R. Stradiotto, Electrochemical sensors based on molecularly imprinted polymer on nanostructured carbon materials: A review, J. Electroanal. Chem. 840 (2019) 343–366. https://doi.org/10.1016/j.jelechem.2019.04.005.
[22] L.F.P.P. Moreira, E. Buffon, N.R. Stradiotto, Electrochemical sensor based on reduced graphene oxide and molecularly imprinted poly (phenol) for D -xylose determination, Talanta 208 (2020) 120379. https://doi.org/10.1016/j.talanta. 2019.120379.
[23] E. Noviana, C.P. McCord, K.M. Clark, I. Jang, C.S. Henry, Electrochemical paper-based devices: Sensing approaches and progress toward practical applications, Lab Chip. 20 (2020) 9–34. https://doi.org/10.1039/c9lc00903e.
[24] V.N. Ataide, L.F. Mendes, L.I.L.M. Gama, W.R. Araujo, T.R.L.C. Paixão, Electrochemical paper-based analytical devices: Ten years of development, Anal. Methods 12 (2020) 1030–1054. https://doi.org/10.1039/c9ay02350j.
[25] E.W. Nery, L.T. Kubota, Sensing approaches on paper-based devices: A review, Anal. Bioanal. Chem. 405 (2013) 7573–7595. https://doi.org/10.1007/s00216-013-6911-4.
[26] D.D. Liana, B. Raguse, J.J. Gooding, E. Chow, Recent advances in paper-based sensors, Sensors 12 (2012) 11505–11526. https://doi.org/10.3390/ s120911505.
[27] T. Ozer, C. McMahon, C.S. Henry, Advances in paper-based analytical devices, Annu. Rev. Anal. Chem. 13 (2020) 1–25. https://doi.org/10.1146/annurev-anchem-061318-114845.
[28] K. Ratajczak, M. Stobiecka, High-performance modified cellulose paper-based biosensors for medical diagnostics and early cancer screening: A concise review, Carbohydr. Polym. 229 (2020) 115463. https://doi.org/10.1016/j.carbpol. 2019.115463.
[29] G.V. Martins, A.C. Marques, E. Fortunato, M.G.F. Sales, Paper-based (bio)sensor for label-free detection of 3-nitrotyrosine in human urine samples using molecular imprinted polymer, Sens. Bio-Sensing Res. 28 (2020) 100333. https://doi.org/ 10.1016/j.sbsr.2020.100333.
[30] L. Fan, Q. Hao, X. Kan, Three-dimensional graphite paper based imprinted electrochemical sensor for tertiary butylhydroquinone selective recognition and sensitive detection, Sensor. Actuator. B Chem. 256 (2018) 520–527. https://doi.org/10.1016/j.snb.2017.10.085.
[31] L. Ge, S. Wang, J. Yu, N. Li, S. Ge, M. Yan, Molecularly imprinted polymer grafted porous Au-paper electrode for an microfluidic electro-analytical origami device, Adv. Funct. Mater. 23 (2013) 3115–3123. https://doi.org/10.1002/adfm. 201202785.
[32] P. Wang, G. Sun, L. Ge, S. Ge, J. Yu, M. Yan, Photoelectrochemical lab-on-paper device based on molecularly imprinted polymer and porous Au-paper electrode, Analyst 138 (2013) 4802–4811. https://doi.org/10.1039/c3an00694h.
[33] M.A. Beluomini, J.L. da Silva, N.R. Stradiotto, Amperometric determination of myo-inositol by using a glassy carbon electrode modified with molecularly imprinted polypyrrole, reduced graphene oxide and nickel nanoparticles, Microchim. Acta 185 (2018)

170. https://doi.org/10.1007/s00604-018-2710-0.
[34] L.A. Pradela-Filho, I.A.A. Andreotti, J.H.S. Carvalho, D.A.G. Araújo, L.O. Orzari, A. Gatti, R. M. Takeuchi, A. L. Santos, B. C Janegitz, Glass varnish-based carbon conductive ink: A new way to produce disposable electrochemical sensors, Sensor. Actuator. B Chem. 305 (2020) 127433. https://doi.org/10.1016/j.snb.2019.127433.
[35] S.K. Pang, Comprehensive study of polymerization of pyrrole: A theoretical approach, J. Electroanal. Chem. 859 (2020) 113886. https://doi.org/10.1016/ j.jelechem.2020.113886.
[36] A. Nezhadali, M. Mojarrab, Fabrication of an electrochemical molecularly imprinted polymer triamterene sensor based on multivariate optimization using multi-walled carbon nanotubes, J. Electroanal. Chem. 744 (2015) 85–94. https://doi.org/10.1016/j.jelechem.2015.03.010.
[37] A. Nezhadali, G.A. Bonakdar, Multivariate optimization of mebeverine analysis using molecularly imprinted polymer electrochemical sensor based on silver nanoparticles, J. Food Drug Anal. 27 (2019) 305–314. https://doi.org/10.1016/ j.jfda.2018.05.002.
[38] D.C. Lima, W.N. Guedes, V.C. Costa, F.A.C. Amorim, Application of factorial design and desirability function to develop a single analytical procedure for the determination of metals in different tissues of blue crab (Callinectes danae), J. Braz. Chem. Soc. 29 (2018) 1885–1893. https://doi.org/10.21577/0103-5053.20180064.
[39] M.A. Beluomini, J.L. da Silva, G.C. Sedenho, N.R. Stradiotto, D-mannitol sensor based on molecularly imprinted polymer on electrode modified with reduced graphene oxide decorated with gold nanoparticles, Talanta 165 (2017) 231–239. https://doi.org/10.1016/j.talanta.2016.12.040.
[40] Brazilian Health Regulatory Agency (ANVISA), 2017. Resolução RDC nº 135, de 08/02/2017. Brasília: Diário Oficial da União.
[41] Brazilian Health Regulatory Agency (ANVISA), 2017. Resolução RDC nº 136, de 08/02/2017. Brasília: Diário Oficial da União.
[42] L. Monti, S. Negri, A. Meucci, A. Stroppa, A. Galli, G. Contarini, Lactose, galactose and glucose determination in naturally “lactose free” hard cheese: HPAEC-PAD method validation, Food Chem. 220 (2017) 18–24. https://doi.org/10.1016/j.foodchem.2016.09.185.
[43] Bulletin of the International Dairy Federation (IDF), 2019. IDF Factsheet 010/2019-12. Brussels, Belgium.

Universidade Estadual Paulista (UNESP)

Instituto de Química

Departamento de Química Analítica

Relatório Científico de Pós-Doutorado

Sensores eletroquímicos baseados em eletrodos impressos modificados com nanoporos metálicos e monitorados por rede sem fio para determinação de flavonóides nos resíduos da indústria cítrica

Processo FAPESP n° 2018/12131-6

Período: 20 de outubro de 2020 - 31 de janeiro de 2022

Maísa Azevedo Beluomini
Pós-doutoranda

Profa. Dra. Maria Valnice Boldrin
Supervisora

Araraquara, outubro de 2021.

SUMÁRIO

1. Resumo do projeto proposto

A água residual da indústria cítrica é considerada um agente de alto poder poluente devido a sua rica composição orgânica. Por outro lado, o controle de modo rápido e eficiente destes compostos nos processos industriais é de alta relevância para a avaliação do reaproveitamento da biomassa, para fins mais econômicos, estratégicos e ambientalmente amigáveis. Neste contexto, os sensores eletroquímicos baseados em eletrodos impressos podem ser uma alternativa com respostas confiáveis, rápidas, de fácil manuseio e de baixo custo, pois permitem o desenvolvimento de métodos mais robustos, com elevado desempenho, portabilidade e superfícies livres de contaminantes. Assim, este projeto tem como objetivo desenvolver sensores eletroquímicos baseados em eletrodos impressos modificados com materiais metálicos nanoporosos para determinação dos flavonóides hesperidina, narirutina, sinensitina e naringenina. A oxidação destes analitos sobre os sensores de elevada condutividade elétrica e atividade eletrocatalítica proporcionará alta sensibilidade e seletividade na detecção desses flavonóides em resíduos da indústria cítrica. Além disso, pretende-se combinar a portabilidade desses sensores com a comunicação sem fio, através do desenvolvimento de plataformas que permitirá coletar, processar e enviar os dados via wi-fi para um smartphone/laptop, visando a aplicação em campo e em tempo real, através de dispositivos inteligentes, com baixo consumo de energia e robustos.

2. Realizações no período

Uma extensa revisão bibliográfica sobre a preparação de eletrodos baseados em nanoporos metálicos, comportamento eletroquímico dos flavonoides e dispositivos de detecção baseados em smartphone portáteis e com envio de sinal a distância, foi realizada. O primeiro sensor eletroquímico desenvolvido para a detecção de narirutina usando nanoporos de níquel estruturado tridimensionalmente em eletrodo impresso de carbono (3DnpNi/SPE) apresentou excelentes resultados, como descrito no relatório anterior, e foi publicado no jornal *Food Chemistry*, v 353, 129427, 2021, intitulado "*Electrosynthesis of three-dimensional nanoporous nickel on screen-printed electrode used for the determination of narirutin in citrus wastewater*" (https://doi.org/10.1016/j.foodchem.2021.129427), IF= 7.514.

O segundo sensor desenvolvido foi modificado com nanoporos de platina (3DnpPt) a partir do método de corrosão eletroquímica seletiva da liga Pt-Cu na superfície do SPE, e aplicado na determinação voltamétrica simultânea de hesperidina (HES) e narirutina (NAR) em água residual da indústria cítrica. A morfologia da superfície do eletrodo foi caracterizada por microscopia eletrônica de varredura por emissão de campo (FEG-SEM), difração de elétrons de raios X (EDX), espectroscopia de fotoelétrons de raios X (XPS) e pela técnica de espectroscopia de impedância

eletroquímica (EIS). Os resultados obtidos nos estudos voltamétricos realizados mostraram que o sensor possui boa atividade eletrocatalítica e seletividade para oxidação HES e NAR. A técnica de voltametria de varredura linear (LSV) apresentou faixas lineares de 10 μmol L^{-1} a 0,4 mmol L^{-1} e 10 μmol L^{-1} a 0,5 mmol L^{-1}, com limites de detecção de 6,61 μmol L^{-1} e 0,21 μmol L^{-1}, e sensibilidade amperométrica de 0,52 AL mol^{-1} e 0,79 AL mol^{-1} para HES e NAR, respectivamente. O sensor 3DnpPt-SPE também exibiu boa repetibilidade e alta seletividade, bem como estabilidade a longo prazo. O sensor foi aplicado em amostra de água residual da indústria cítrica para a quantificação simultânea de HES e NAR, apresentando taxas de recuperação entre 87 % e 104 %. Além disso, este trabalho acaba de ser aceito para publicação no *Journal of Electroanalytical Chemistry*, intitulado "*Simultaneous detection of hesperidin and narirutin in residual water using nanoporous platinum electrosynthesized by alloying-dealloying mechanism"*, JELECHEM-D-21-01066 (IF = 4.464), como pode ser visto no item 8 deste relatório.

Outro sensor que está sendo desenvolvido no momento, envolve a modificação do SPE com nanoporos de prata, e tem como objetivo explorar a resposta catódica dos flavonoides, visando maior seletividade para o sensor devido a formação do completo metal-flavonoide, que se forma na superfície do eletrodo. A redução dos flavonoides em eletrodos livres de mercúrio ainda não foi relatada na literatura.

Juntamente com a desenvolvimento dos sensores eletroquímicos, a colaboração com o Prof. Dr. Eduardo Paciência Godoy, do Instituto de Ciências e Tecnologia da UNESP campus Sorocaba, está sendo realizada, para a construção de um sistema que permitirá a comunicação sem fio entre o sinal fornecido pelos eletrodos na oxidação/redução dos flavonoides e um software, para análises em campo e em tempo real. Os testes realizados no circuito desenvolvido apresentaram resultados promissores, e a placa de aquisição ESP32 para transmissão dos dados sem fio está sendo executada. Atualmente, finalizamos a construção do circuito, utilizando a interface gráfica *LabView* da *National Instruments*. Neste software, foi possível visualizar em tempo real o sinal proveniente do eletrodo, devido a conexão entre a saída amplificada do circuito e a entrada analógica da placa de aquisição ligada a um computador. A calibração do dispositivo foi realizada através da comparação dos dados com o equipamento comercial PalmSens3. A próxima etapa envolve a aquisição e transmissão de dados sem fio. Esses dados serão enviados para um dispositivo de visualização gráfica, podendo ser em um laptop, celular ou tablet.

Além disso, estabelecemos colaboração com o Prof. Dr. Frank Marken da University of Bath, no Reino Unido, durante a participação da Dra. Maísa na escola de eletroquímica de Bath (Bath Electrochemical Winter School), em janeiro de 2020. O Prof. Dr. Frank desenvolve uma das principais pesquisas no campo de sensores eletroquímicos baseados no sistema "feedback redox",

através de um "small gap". O grupo do Prof. Frank é um dos poucos grupos de pesquisa no mundo que trabalham com este tipo de dispositivo, e esta parceria representa uma grande oportunidade para desenvolver sensores tecnológicos para detecção eletroquímica em nanoescala. O projeto BEPE intitulado "*Benchtop fabrication of microgap sensor based on carbon nanomaterials for selective detection of flavonoids*" foi submetido para a FAPESP (processo #2020/01822-8) porém foi cancelado em janeiro de 2021 devido às incertezas causadas pela pandemia de COVID-19. Submetemos novamente a proposta em julho de 2021, a proposta foi habilitada em 14/07/21, mas até o presente momento ainda não foi avaliada pela FAPESP. Assim, esperamos que a renovação da bolsa nos permita consolidar a parceria com o Prof. Frank Marken, para que a pós-doutoranda tenha a oportunidade de realizar o estágio de pesquisa no exterior, que muito contribuirá para o desenvolvimento deste projeto e para sua formação acadêmico-científica. Prof. Frank também demostrou seu apoio a renovação da bolsa, como pode ser verificado na carta que está anexada em "outros documentos".

Ademais, durante o período desde relatório, a Dra. Maísa também participou dos principais congressos da área, tendo a oportunidade de apresentar na forma oral o trabalho "*Screen-Printed Electrode Modified with 3-D Nanoporous Nickel for the Determination of Narirutin in Wastewater from Citrus Industry*", no 239th ECS Meeting with the 18th International Meeting on Chemical Sensors (IMCS), evento online realizado em Chicago - EUA (https://iopscience.iop.org/article/10.1149/MA2021-01571542mtgabs/meta). Também tivemos a oportunidade de divulgar nosso trabalho no "II Fronteiras em Eletroquímica e Eletroanalítica: avanços realizados por jovens mulheres cientistas". Gostaríamos também de mencionar os trabalhos que foram publicados através das colaborações científicas da pós-doutoranda e que constam nos itens 7 e 9 deste relatório.

3. Resultados e Discussão

Devido a restrição ao número de páginas, que deve conter no máximo 17 páginas até o item 5, segundo consta na nova norma sobre o formato dos Relatórios Científicos, (https://fapesp.br/14453/formato-para-os-relatorios-cientificos-anuais-e-final-bolsas-no-pais), todas as tabelas, figuras e esquemas constam no Apêndice I.

3.1 Determinação simultânea de hesperidina e narirutina em água residual da indústria cítrica usando eletrodo impresso modificado com nanoporos de platina eletrossintetizada pelo mecanismo de corrosão eletroquímica seletiva.

No relatório anterior havíamos mencionado o início da construção do eletrodo modificado com nanoporos de platina, porém o estudo do comportamento eletroquímico dos flavonoides nesse eletrodo foi retomado neste relatório devido a interferência do etanol, utilizado na diluição da hesperidina, que apresenta excelente eletroatividade na superfície de Pt, o que causou interferência na análise. Com isso, a hesperidina e a narirutina foram diluídas em ACN/água 1:1 *v/v*.

3.1.1. Eletrossíntese e caracterização do 3DnpPt/SPE

Os estudos eletroquímicos foram realizados em um potenciostato Autolab PGSTAT30 acoplado a um microcomputador utilizando o software de controle Nova 1.11 Os eletrodos impressos (SPE) foram adquiridos da DropSens (código: DRP - C11L).

A construção do SPE modificado com nanoporos de platina tridimensionais (3DnpPt-SPE) está detalhadamente reportada no artigo anexado no item 8, intitulado: "*Simultaneous detection of hesperidin and narirutin in residual water using nanoporous platinum electrosynthesized by alloying-dealloying mechanism",* aceito para publicação em outubro de 2021, na Journal of Electroanalytical Chemistry (JELECHEM-D-21-01066). Resumidamente, o eletrodo impresso foi modificado com nanoporos de platina através da eletrodeposição da liga Pt-Cu em uma solução contendo 1,0 mmol L^{-1} H_2PtCl_4, 1,0 mmol $L^{-1}CuSO_4$ e 0,5 mol L^{-1} H_2SO_4. Essa liga foi escolhida devido a diferença de potencial entre os elementos químicos, em que à corrosão seletiva do componente menos nobre, no caso o Cu, ocorre quando seu potencial é atingido. O processo de corrosão seletiva foi realizado através da técnica de voltametria cíclica (CV) durante a aplicação de 15 ciclos na faixa de potencial de 1,4 V a - 0,40 V, velocidade de varredura (υ) de 100 mVs^{-1}. Para cada ciclo, um filme de Pt-Cu é eletrodepositado na superfície do SPE durante a varredura catódica. Quando o ciclo voltamétrico é revertido, na direção da varredura anódica, o Cu é dissolvido da liga levando à formação dos nanoporos de Pt.

Os CVs apresentados na Figura A1A (ver apêndice) mostram a resposta do SPE em solução contendo $CuSO_4$ (curva preta), H_2PtCl_6 (curva azul) e $CuSO_4$ + H_2PtCl_6 (curva vermelha). Com relação ao voltamograma do Cu, pode-se observar a presença de dois picos; um pico em aproximadamente -0,18 V, correspondendo à oxidação do Cu, e o outro em aproximadamente -0,40 V, onde ocorre a redução do Cu. As curvas relacionadas ao Pt apresentam picos na região entre -0,10 e 0,10 V, os quais são atribuídos à adsorção e dessorção de hidrogênio [1] . A oxidação de Pt (Pt-OH) ocorre em potenciais maiores que 0,30 V e a redução do óxido ocorre na varredura

catódica em ~ 0,20 V. O CV da Figura A1B mostra a presença de um pico de redução na varredura catódica (Pa), que é atribuído à co-deposição da liga Pt-Cu na superfície do SPE. O pico observado na varredura anódica (Pb) é atribuído à corrosão do Cu na liga Pt-Cu. Durante cada CV, uma camada de liga de Pt-Cu é eletrodepositada durante a varredura catódica e, durante a varredura anódica, o cobre é removido da liga. Todo esse processo, portanto, resulta na formação de uma nanoestrutura porosa de Pt. Com isso, o número de ciclos voltamétricos aplicados na etapa de modificação do SPE está relacionado ao crescimento, forma e estrutura dos nanoporos, afetando diretamente a rugosidade da superfície. Assim, a influência do número de ciclos na formação do 3DnpPt-SPE foi estudada na faixa de 5 a 25. Após a eletrodeposição da Pt, o eletrodo foi submetido a sucessivos CVs em solução contendo 0,5 mol L^{-1} H_2SO_4, na faixa de potencial de −0,40 a 1,4 V, υ de 100 mV s^{-1}, até a estabilização da corrente. A carga (μC) associada à área do pico de redução do óxido de platina (Figura A1C) foi dividida por um fator de conversão de 420 μC cm^{-2} [2]. O valor obtido (área eletroquímica) foi dividido pela área geométrica do SPE (0,126 cm^2), resultando no fator de rugosidade da superfície (R*f*). A análise da rugosidade superficial do eletrodo é um importante parâmetro que permite a escolha das melhores condições para a formação dos nanoporos de Pt. O procedimento para o cálculo de R*f* pode ser aplicado quando o metal investigado possui uma região bem definida no CV relacionada à formação e redução da monocamada de óxido, como é o caso da Pt. Assim, esse fator é considerado um adequado indicador de rugosidade superficial. O R*f* obtido neste trabalho variou de 7 a 24 (Figura A1D), em que um aumento na rugosidade da superfície até 15 ciclos voltamétricos de eletrodeposição foi observado. Depois desse valor, houve uma diminuição no R*f,* que pode ser atribuído à formação de uma camada mais espessa, que pode ter afetado a remoção do cobre e causado a redução da rugosidade superficial. Assim, considerando que a aplicação de 15 ciclos voltamétricos resultou em uma maior área superficial, este número de ciclos foi escolhido para a construção do sensor.

A morfologia da superfície do 3DnpPt-SPE foi analisada por microscopia eletrônica de varredura (MEV). As Figuras A2A e A2B mostram a morfologia da superfície de nanoporos de Pt com 1 μm e 100 nm de escala. Observando as imagens é possível notar a presença de aglomerados de nanopartículas de Pt, assim como os espaços nanométricos entre os aglomerados, que podem estar relacionados aos íons Cu que foram dissolvidos da liga, levando à formação de lacunas na estrutura. A Figura A2C mostra o respectivo EDS, confirmando a presença predominante de Pt, e de Cu remanescente na estrutura (em menor proporção). O histograma de distribuição de tamanho de partícula é mostrado na Figura A2D. As nanopartículas de Pt foram calculadas contando 400 partículas, exibindo tamanhos variando de 20 a 240 nm com diâmetro médio de 96 ± 42 nm.

Para estudar as características eletroquímicas da superfície do sensor proposto, EIS foi utilizada na faixa de frequência de 0,10 Hz a 100 kHz, em solução contendo $5,0 \times 10^{-3}$ mol L^{-1} de $[Fe(CN)_6]^{3-/4-}$ em 0,1 mol L^{-1} KCl, aplicando o potencial de 0,2 V. O circuito equivalente de Randles foi utilizado para ajustar os dados obtidos pelo diagrama de Nyquist, e é apresentado na inserção superior esquerda da Figura A3. Neste circuito, Ri representa a resistência da solução, Cdl sendo o elemento de fase constante que está relacionado com a capacitância de camada dupla, Rct representando a resistência de transferência de carga e W a impedância de Warburg. Como pode ser observado na Figura A3, o diagrama de Nyquist para o SPE (curva a) mostra um semicírculo com Rct de 2,4 kΩ. Após a modificação da superfície com o 3DnpPt (curva b), o Rct diminuiu aproximadamente 2,6 vezes, atingindo o valor de 924 Ω. Esses resultados mostram que aos nanoporos de platina atuaram como um excelente mediador no processo de transferência de elétrons.

A fim de obter uma melhor compreensão do processo de deposição de Pt na superfície do SPE, análises de XPS foram realizadas conforme mostra a Figura A4. O espectro de C1s de alta resolução foi deconvoluído em cinco componentes; correspondendo a átomos de carbono presente em diferentes grupos funcionais, com energias de ligação de 285,4 (C-H), 286,3 (C-O), 287,9 (C = O) e 289,0 (O-C = O) eV. Os espectros de oxigênio foram monitorados pelo sinal de O1s; esses espectros foram deconvoluídos em quatro componentes que correspondem a átomos de oxigênio em diferentes grupos funcionais com energias de ligação de 531,4 (C = O e -OH), 532,3 (CO), 533,6 (OC = O) e 530,7 (O-Pt) eV. Os espectros de XPS para Pt, ou seja, os picos relacionados aos elétrons Pt4f7/2 e Pt4f5/2, podem ser encontrados em 71,2 e 74,3 eV, respectivamente; mostrando que a Pt na superfície SPE tem valência zero [2]. Os grupos $Pt(OH)_2$ 4f7/2 e Pt $(OH)_2$4f5/2 podem ser observados em 72,3 e 75,7 eV, respectivamente, e os sinais em 73,7 e 77,1 eV estão ligados aos grupos $PtO_2$4f7/2 e $PtO_2$4f5/2. Para mais detalhes sobre a caracterização do 3DnpPt/SPE, por favor consulte o artigo anexado no item 8.

3.1.2. Comportamento eletroquímico da hesperidina e narirutina em 3DnpPt-SPE.

As moléculas de hesperidina (HES) e narirutina (NAR) são estruturalmente semelhantes, caracterizadas pela presença de dois anéis benzeno ligados por um anel pirano, como mostrado Esquema A1. O comportamento eletroquímico de 0,2 mmol L^{-1} de HES, 0,2 mmol L^{-1} de NAR e 0,2 mmol L^{-1} da mistura de HES e NAR em 0,1 mol L^{-1} H_2SO_4, foi analisado por CV em SPE e em 3DnpPt-SPE. Ao analisar a primeira varredura anódica na Figura A5A, observa-se a presença de um pico em 0,46 V (P1). Já na varredura reversa, é possível observar a presença de uma onda redutiva em 0,22 V (P2). No segundo ciclo de varredura, há o surgimento de um novo pico (P3)

na região de 0,25 V e diminuição da intensidade do P1. Com base nesta observação, é possível afirmar que P1 (sistema I) é um pico anódico irreversível e P2/P3 (sistema II) é um par redox derivado do produto de oxidação de P1. Esses resultados são semelhantes aos observados por Sims et al., [3] e Manasa et al., [4], que concluíram que a oxidação da HES em eletrodos de carbono ocorre de acordo com o mecanismo ECirrevE. O primeiro pico observado no SPE é característico da oxidação irreversível da unidade guaiacol da molécula de HES, com a formação do par o-benzoquinona/catecol quase reversível. A modificação do SPE com 3DnpPt, levou a um aumento na intensidade das correntes, mas sem deslocamento dos picos. A corrente P1 aumentou cerca de 2,5 vezes, enquanto as correntes P2 e P3 aumentaram 2,0 e 1,4 vezes, respectivamente. Esses resultados podem ser atribuídos à maior área superficial proporcionada pela estrutura nanoporosa de Pt. A Figura A5B mostra o CV obtido para NAR no SPE e no 3DnpPt-SPE, em que é possível observar na primeira varredura a presença de um pico anódico no potencial de 0,72 V. Na análise da varredura reversa nenhum pico foi observado, indicando que o processo de oxidação da narirutina é irreversível, de acordo com os dados previamente relatados no relatório anterior e disponível na literatura [5]. Uma análise comparativa na oxidação da NAR em SPE e em 3DnpPt-SPE, mostra que o eletrodo modificado exibiu uma corrente de pico 2,2 vezes maior para o eletrodo modificado, confirmando que a maior porosidade da superfície resultou em uma corrente catalítica para a NAR. A Figura A5C mostra os CVs obtidos para uma mistura de 0,2 mmol L^{-1} HES e NAR em 0,1 mol L^{-1} de H_2SO_4 em SPE e em 3DnpPt-SPE. Ao comparar a resposta voltamétrica individual de cada molécula e em solução combinada de HES e NAR, nota-se um comportamento eletroquímico semelhante; em outras palavras, a resposta individual de HES e NAR foi semelhante à da solução combinada de HER e NAR. Esses resultados mostram que o eletrodo 3DnpPt-SPE pode ser usado para a determinação simultânea de HES e NAR, com melhor sensibilidade em comparação ao SPE. O sensor proposto neste trabalho (3DnpPt-SPE) é o primeiro relatado na literatura para a determinação simultânea de HES e NAR.

O efeito da velocidade de varredura no comportamento eletroquímico de HES e NAR também foi estudado por CV usando 0,2 mmol L^{-1} de uma mistura de HES e NAR em 0,1 mol L^{-1} de H_2SO_4. A Figura A6 mostra os CVs obtidos em diferentes velocidades de varredura (10 - 250 mVs^{-1}). Analisando os CVs, é possível observar que ambas as moléculas deslocaram o potencial de pico para potenciais mais positivos com o aumento da velocidades de varredura; indicando para a limitação cinética da reação eletroquímica [6]. Além disso, o gráfico de corrente de pico (I) *vs.* velocidade de varredura (υ) (Figura A7) apresentou uma relação linear característica de processos controlados por adsorção. Esses resultados estão de acordo com os relatados na literatura que envolvem o uso de eletrodos nanoporosos de Pt [3,5,7]. Além disso, esses eletrodos apresentam a

capacidade de melhorar as reações faradaicas heterogêneas de cinética lenta [8,9]. Assim, como as moléculas de HES e NAR não apresentam reações eletródicas rápidas o suficiente para serem controladas por difusão, o 3DnpPt-SPE desempenha um papel importante na detecção dessas moléculas.

3.2. Desempenho analítico do 3DnpPt-SPE na determinação simultânea de HES e NAR

3.2.1. Estudo para determinação simultânea de HES e NAR

Para demonstrar a aplicabilidade do 3DnpPt-SPE na determinação de HES e NAR, cada um dos dois analitos foi determinado usando a técnica de LSV, em solução contendo uma concentração constante do outro analito durante a análise, ou seja, para a construção da curva analítica para HES, a concentração de NAR foi mantida constante na concentração de 50 µmol L^{-1}. A Figura A8A mostra que a corrente de oxidação P3 para HES exibiu o melhor perfil voltamétrico e maior linearidade conforme o aumento da concentração. Uma vez que o P3 foi formado após a geração de P1, a corrente de pico analisada é correspondente à concentração adicionada anteriormente. Com isso, a corrente P3 aumentou linearmente com a concentração na faixa de 10 µmol L^{-1} a 0,4mmol L^{-1} (R = 0,9989). A equação linear correspondente foi I_{HES3} (µA) = 19082,40 C_{hes3} + 0,52 (R = 0,9977) (Figura A8A ') e o valor do desvio padrão relativo (RSD) obtido para a inclinação da curva foi de 3,9 %. O limite de detecção (LOD) foi de 6,61 µmol L^{-1}, e a sensibilidade analítica (As) foi de 0,52 A L mol^{-1} (n = 3). Da mesma forma, a corrente de pico de NAR aumentou linearmente com o aumento na concentração na faixa de 10 µmol L^{-1} a 0,5 mmol L^{-1} (Figura A8B), mesmo na presença de 50 µmol L^{-1} HES. A equação de regressão linear foi I_{NAR} (µA) = 18143,30 C_{NAR} + 0,79 (R = 0,9977) (Figura A8B '), e o valor do desvio padrão relativo (RSD) obtido para a inclinação da curva foi de 6,1%. O LOD foi de 0,21 µmol L^{-1} e o As foi de 0,79 A L mol^{-1} (n = 3).

A análise simultânea foi realizada utilizando concentrações de HES e NAR entre 20 µmol L^{-1} a 0,4 mmol L^{-1}, conforme pode ser observado na Figura A8C. Os resultados obtidos mostram que um aumento simultâneo na concentração de HES e NAR foi linear com as correntes de pico para P_{HES3} e P_{NAR}. As equações lineares e RSD obtidos para HES e NAR foram: I_{HES3} (µA) = 14.245,80 C_{HESP3} + 0,87 (R = 0,9979), com RSD de 7,6% para a inclinação; e I_{NAR} (µA) = 34433,90 C_{NAR} + 0,06 (R = 0,9989), com RSD de 6,3% para a inclinação (Figura A8C '). Quando esses resultados são comparados com os obtidos na determinação individual de HES e NAR, as inclinações foram na mesma magnitude, com RSD de 14,5% para HES e 20,3% para NAR, mostrando que a oxidação de HES no 3DnpPt-SPE não interferiu na quantificação de NAR e vice-versa. Assim, podemos concluir que os processos de detecção são independentes e o sensor

adequado para determinar simultaneamente HES e NAR sem interferências; além disso, o sensor também apresentou considerável sensibilidade.

Assim, considerando a técnica voltamétrica, faixa linear e LOD para HES e NAR, os resultados obtidos neste trabalho com o 3DnpPt-SPE, foram comparados com os demais eletrodos relatados na literatura e os dados são apresentados na Tabela A1. Embora alguns autores relatam bons resultados na determinação de HES e NAR [4,10–12], várias etapas foram utilizadas na construção do eletrodo. Além disso, em alguns estudos a energia aplicada para a oxidação da HES foi muito maior, chegando a 1,21 V [10]. Outro estudo interessante foi conduzido por Temerk et al., [13] em que foi utilizado um eletrodo gotejante de mercúrio para a redução de HES usando voltametria de onda quadrada com redissolução catódica, porém este tipo de eletrodo não é mais utilizado devido ao seu elevado grau de toxicidade. Além disso, a maioria dos métodos analíticos relatados usam a técnica AdSV e CASV ou uma abordagem de DPV com pré-concentração da molécula de interesse. Assim, essas técnicas requerem a aplicação de um tempo de acúmulo, o que, consequentemente, aumenta o tempo de análise. Essas desvantagens tornam a proposta desse trabalho comparativamente melhor, com a utilização da técnica LSV que é muito mais rápida e simples. Está é uma abordagem que leva à construção de uma plataforma de detecção portátil, prática e viável, e que até o momento não há relatos na literatura sobre o desenvolvimento e aplicação de sensores capazes de determinar simultaneamente HES e NAR. Também devemos considerar que em amostras como suco de laranja, resíduos de frutas cítricas e em formulações farmacêuticas, a quantidade encontrada de HES e NAR são da ordem de μM a mM. Isso mostra que não é necessário empregar métodos analíticos com valores muito baixos de LOD. Resumindo, as vantagens do 3DnpPt-SPE proposto são: i) facilidade de preparação do eletrodo - envolvendo uma única e rápida etapa eletroquímica; ii) o sensor é capaz de realizar detecção simultânea - o que demonstra a versatilidade do dispositivo; ii) a técnica envolve um mecanismo de detecção simples; iv) o sensor fornece resposta analítica sensível e seletiva; e v) a técnica envolve a utilização de baixo volume de solução (50 μL).

3.2.2. Repetibilidade, estabilidade, seletividade

A estabilidade do 3DnpPt-SPE foi avaliada por LSV usando uma solução contendo 0,1 mmol L^{-1} de HES e NAR em 0,1 mol L^{-1} de H_2SO_4 por 7 dias. As medidas foram realizadas a cada dia (e quando não em uso, o eletrodo foi armazenado em temperatura ambiente). Ao final do período de 7 dias, a corrente apresentou 82,1 % do seu valor inicial para HES (P3) e 89,8 % para NAR; mostrando que o eletrodo proposto tem considerável estabilidade. Para avaliar a repetibilidade entre eletrodos, três eletrodos foram preparados independentemente nas mesmas

condições; os eletrodos foram usados para detectar 0,1 mmol L^{-1} de HES e NAR, conforme mostrado na Figura A9 (n = 3). Os valores médios da corrente de oxidação correspondente a HES e NAR foram 2,4 μA e 4,3 μA, com RSD de 2,3 % e 5,7 %, respectivamente. Esses resultados mostram que o 3DnpPt-SPE tem satisfatória repetibilidade e estabilidade a longo prazo.

3.2.3 Seletividade do 3DnpPt-SPE

Para que uma molécula seja considerada interferente na análise, a variação da corrente de pico não deve ser ≤ ± 5,0% (limite de tolerância). Com base nos resultados voltamétricos obtidos na análise da mistura de 0,2 mmol L^{-1} de HES e NAR na presença da mesma quantidade de 0,1 mmol L^{-1} frutose (Figura A10A), glicose (Figura A10B) e arabinose (Figura A10C), essas moléculas não desempenharam papel significativo de interferência na análise de HES e NAR. Quando a molécula de naringenina foi adicionada, um aumento de 292,6% foi observado na corrente P1 da HES (Figura A10D), porém os picos P2 e P3 exibiram um aumento de corrente de 1,2% e 4,9%, respectivamente. Na presença de ácido ascórbico, a corrente de pico relacionada a P1 registrou uma queda acentuada de 66,9%; e as correntes de P2 e P3 não registraram alterações significativas - as correntes de pico exibiram uma oscilação de corrente de 2,19% e 4,9%, respectivamente. Os resultados obtidos sugerem que o sensor proposto possui boa seletividade quando aplicado na determinação simultânea de HES e NAR quando os picos P2 e P3 são analisados; além disso, esses picos apresentaram maior linearidade durante o estudo do desempenho analítico do sensor.

3.3. Aplicação do sensor na amostra

A amostra de água amarela foi coletada na indústria cítrica (Citrosuco®) e utilizada para investigar a aplicabilidade do método proposto. Antes da realização da análise, a amostra foi diluída 2,5 vezes em H_2SO_4 0,1 mol L^{-1} e a técnica LSV foi empregada. O método de adição de padrão foi utilizado, e as concentrações conhecidas de HES e NAR adicionadas na amostra foram na faixa de 0,075 a 0,2 mmol L^{-1}. Por meio da construção da curva de adição padrão, e a partir da extrapolação da reta (Figura A11), a concentração de HES e NAR (considerando a diluição da amostra) foi de 174 ± 1.1 mmol L^{-1} e 81,8 ± 0,99 μmol L^{-1} (n = 3), respectivamente. Conforme mostra a Tabela A2, os percentuais de recuperação variaram de 98,2% a 102,0% e de 95,0% a 103,8% para HES e NAR, respectivamente. Esses resultados mostram que o 3DnpPt-SPE apresenta um excelente grau de precisão na análise das moléculas em amostras reais.

O teste *t* de *Student* e o teste *F* foram utilizados para a análise estatística dos valores médios obtidos para as concentrações de HES e NAR presentes na amostra utilizando o método de HPLC

(apresentado no relatório 1 e disponível no anexo do artigo submetido) e pelo método proposto neste trabalho. Com nível de confiança de 95 %, conforme mostrado na Tabela A3, os valores calculados relativos ao teste *F* e ao teste *t* foram inferiores aos valores críticos; ou seja, não houve diferença estatística significativa entre os métodos. Assim, é possível concluir que o método proposto é altamente confiável para a análise de HES e NAR em amostra de água amarela.

3.4. Construção do dispositivo sem fio para determinação em campo dos flavonoides.

Está parte do projeto está sendo realizada em colaboração com o Prof. Dr. Eduardo Paciência Godoy, do Instituto de Ciências e Tecnologia, campus Sorocaba. O sistema que será utilizado para uma comunicação sem fio entre o sinal fornecido pelos eletrodos impressos modificados na oxidação dos flavonoides e o dispositivo sem fio, está sendo baseado em uma placa ESP32, para aquisição e envio de dados para um computador ou outro dispositivo que faça a interface com o usuário, de maneira a apresentar as curvas características de cada um dos flavonoides analisados. Uma vez que a corrente drenada pelo eletrodo é, na maioria das vezes, da escala de microampère (μA), foi necessário a elaboração de um circuito para tratamento e amplificação do sinal antes do mesmo ser enviado para placa de aquisição. Em comparação ao relatório anterior, alguns ajustes no circuito foram realizados no circuito, com o objetivo de melhorar a aquisição de sinal. Em todos os testes, a corrente obtida foi comparada com a gerada por uma solução de $5{,}0 \times 10^{-3}$ mol L^{-1} de $K_3[Fe(CN)_6)$ em 0,1 mol L^{-1} de KCl, obtida pelo equipamento PalmSens3 e registrados pelo software PStrace 4.8. Assim, o circuito de amplificação utilizando amplificadores operacionais, simples, eficazes e de baixo custo foram montados. O circuito foi composto por três amplicadores operacionais em cascata utilizando o software *Multisim* da National Instruments, de modo a conseguir uma melhor regulagem no fator de ganho da amplificação. O amplificador modelo LM741 foi utilizado e um novo circuito foi montado, como apresentado no circuito de amplificação da Fig A12. Com a realização dos testes foi observado que o circuito entregou bons resultados. A parte de alimentação do amplificador operacional, uma vez que o objetivo do projeto é ter apenas uma fonte simples de energia, provavelmente algum tipo de bateria, o circuito que gera uma tensão simétrica a partir de uma fonte de tensão simples também foi alterado. Após simulações necessárias, o circuito é mostrado na Fig.A13. A montagem dos circuitos em laboratório foi realizada em um *protoboard*, a fim de mitigar possíveis erros. Após isso, os primeiros testes de funcionalidade foram realizados. Os três circuitos integrados, (CI's) LM741, foram conectados entre si em forma de cascata, cada CI possui apenas um amplificador operacional interno e três resistores, as demais conexões nas extremidades foram entradas, saídas e alimentação. As saídas de tensão simétrica foram conectadas na alimentação dos amplificadores

operacionais do circuito de amplificação. O circuito foi alimentado com uma única fonte de tensão, com amplitude de 5,0 V. Assim, foi iniciado os testes utilizando o sinal de corrente do eletrodo impresso como corrente de entrada do circuito de amplificação. O eletrodo de trabalho forneceu a corrente que entra no circuito para ser amplificada e, nos eletrodos auxiliar (CE) e de referência (RE), uma tensão fixa é recebida, que terá seu valor definido de acordo com a substância que será analisada. Através da conexão do eletrodo no circuito, os testes foram realizados utilizando o sinal fornecido por 50 µL da solução de diferentes concentrações da sonda redox ferricianeto/ferrocianeto (1,0 – 5,0 mM) gotejada na superfície do SPE. Assim, o funcionamento do circuito foi monitorado por uma interface gráfica montada no software *LabView* da *National Instruments*. No software, foi possível visualizar em tempo real o sinal proveniente do eletrodo, devido a conexão entre a saída amplificada do circuito e a entrada analógica da placa de aquisição ligada a um computador. As curvas de corrente *vs* tempo fornecidas pelo dispositivo desenvolvido foram comparadas com as do equipamento comercial PalmSens3. Conforme pode ser observado na Figura A14, as curvas obtidas pelo sistema nas concentrações de 1,0 mM (curva a), 2,0 mM (curva (b), 3,0 mM (curva c), 4,0 mM (curva d) e 5,0 mM (curva e), foram muito similares com as obtidas pelo potenciostato comercial depois do tempo de 20 s. A Tabela A4 mostra os valores médios de corrente obtido pelo potenciostato comercial e pelo dispositivo desenvolvido nas cinco concentrações estudadas da sonda redox, assim como o desvio padrão entre elas. Além disso, o erro relativo entre os valores de corrente obtidos pelo aparelho comercial PalmSens3.0 e o dispositivo desenvolvido também foi calculado (Tabela A4), revelando a precisão das medidas.

A placa de aquisição e transmissão de dados sem fio, ESP32, está sendo testada para o envio do sinal da hesperidina utilizando o eletrodo 3DnpNi/SPE. O 3DnpNi/SPE foi escolhido como plataforma de detecção nesta etapa do projeto, por ter apresentado boa performance analítica e ser de baixo custo. Além disso, a boa sensibilidade do sensor (discutida no relatório anterior) será útil para converter reações eletroquímicas em sinais analógicos mensuráveis, que são registrados e convertidos em sinais digitais pelo detector portátil. A corrente gerada será enviada para um dispositivo de visualização gráfica, podendo ser laptop, smatphone ou tablet. Também será realizado o desenvolvimento de um firmware para recebimento e controle dos dados, de preferência usando a plataforma de programação simples e gratuita. Após a construção do hardware, firmware e aplicativos, a curva analítica para os flavonoides será feita e a determinação em campo e tempo real também será realizada.

3.5. Conclusão

Neste relatório, foi desenvolvido um novo sensor para determinação simultânea de HES e NAR a partir do eletrodo de SPE modificado com 3DnpPt, construído a partir de uma metodologia direta e rápida. Em comparação com o SPE não modificado, o eletrodo 3DnpP-SPE melhorou a eficiência de transferência de elétrons e a atividade eletrocatalítica de HES e NAR, sendo o primeiro sensor eletroquímico utilizado para a determinação simultânea dessas moléculas. O sensor desenvolvido neste estudo apresentou excelente desempenho analítico, ampla faixa linear de trabalho, excelente seletividade, sensibilidade amperométrica e estabilidade. O método analítico baseado em 3DnpPt-SPE e LSV requer a aplicação de apenas 50 μL da amostra para determinar a presença de HES e NAR, de forma relativamente mais rápida, simples e confiável comparável ao método de HPLC. As excelentes propriedades do 3DnpPt-SPE tornam o dispositivo adequado para uso como plataforma de detecção de HES e NAR, com potencial aplicação em amostra de águas residuais da indústria cítrica. Além disso, o desenvolvimento do dispositivo portátil mostrou que o sistema está operando de forma adequada pois dos dados obtidos através dos testes com diferentes concentrações da sonda redox ferri/ferro, são comparáveis aos obtidos pelo potenciostato comercial. As próximas etapas abrangem tornar o dispositivo capaz de transmitir os dados gerados via wireless para um smartphone, para análise em campo e em tempo real, em que o SPE modificado com os nanoporos metálicos sejam utilizados como sensores descartáveis para a detecção dos flavonoides. Além disso, o eletrodo modificado com nanoporos de prata (npAg-SPE) também deverá ser desenvolvido, com o objetivo de explorar a redução eletroquímica dos flavonoides, ainda não relatado na literatura para eletrodos livres de mercúrio.

4. Descrever como o Plano de Gestão de Dados está sendo seguido e eventuais modificações

Este item é aplicável somente para bolsas solicitadas a partir de 01/09/2020.

5. Plano de atividades para o próximo período

Para o próximo período, pretendemos explorar redução dos flavonoides, abrindo a possibilidade de detecção catódica. Para isso, será realizado a construção e caracterização de nanoporos de prata (npAg-SPE) e posterior aplicação do sensor. Também deverá ser realizada a comparação entre os eletrodos desenvolvidos em relação a performance eletroquímica e analítica dos flavonoides. Além disso, nosso maior foco será a finalização da placa ESP32 do dispositivo portátil e sua aplicação na análise em campo e em tempo real. Também pretendemos consolidar nossa parceria com o Prof. Dr. Frank Marken, da University of Bath - Inglaterra. Nós havíamos solicitado a bolsa BEPE (processo 2020/01822-8) em fevereiro de 2020, mas a solicitação foi

cancelada pela FAPESP devido às incertezas causadas pela COVID-19. Reconsideramos a proposta em 17/12/2020, e devido as recrudescimento da pandemia a proposta foi cancelada novamente pela FAPESP em 27/01/2021 (comunicado nº 9 da FAPESP sobre a COVID-19 – Solicitações de Bolsas BEPE e BPE). Através do comunicado nº 12, publicado em junho de 2021, foi enviado pela segunda vez um pedido de reconsideração da proposta BEPE em 12/07/2021, mas até o momento não houve prosseguimento da análise após a habilitação do pedido, conforme verificamos no histórico do SAGe. Devido a necessidade de respeitar o tempo mínimo restante de bolsa no país após o retorno da bolsista, acreditamos que a renovação da bolsa seja de fundamental importância para que a pós-doutoranda possa ter a oportunidade de realizar seu estágio de pesquisa no exterior, o que contribuirá tanto para sua formação acadêmico-científica, quanto para o grupo de eletroanalítica de Araraquara.

ATIVIDADES A SEREM DESEMPENHADAS	**TRIMESTRE**			
	1°	**2°**	**3°**	**4°**
Construção e desenvolvimento do método analítico utilizando o 3DnpAg/SPE.	■			
Caracterização morfológica, química e eletroquímica do sensor	■	■		
Desenvolvimento da metodologia analítica utilizando o 3DnpAg/SPE.		■	■	
Comparação entre os eletrodos desenvolvidos em relação a performance eletroquímica e analítica dos flavonoides.			■	
Finalização e aplicação do dispositivo portátil para análise em campo e em tempo real.	■	■	■	■
Relatórios, publicações e participações em eventos.	■	■	■	■
Solicitação de bolsa BEPE.	■			

Referencias

[1] C. Xu, F. Sun, H. Gao, J. Wang, Nanoporous platinum-cobalt alloy for electrochemical sensing for ethanol, hydrogen peroxide, and glucose, Anal. Chim. Acta. 780 (2013) 20–27. doi:10.1016/j.aca.2013.03.068.

[2] S. Trasatti, O.A. Petrii, International Union of Pure and Applied Chemistry Physical Chemistry Division Commission on Electrochemistry: Real Surface Area Measurements in Electrochemistry, Pure Appl. Chem. 63 (1991) 711–734. doi:10.1351/pac199163050711.

[3] M.J. Sims, Q. Li, R.T. Kachoosangi, G.G. Wildgoose, R.G. Compton, Using multiwalled carbon nanotube modified electrodes for the adsorptive striping voltammetric determination of hesperidin, Electrochim. Acta. 54 (2009) 5030–5034. doi:10.1016/j.electacta.2008.10.056.

[4] G. Manasa, R.J. Mascarenhas, A.K. Bhakta, Z. Mekhalif, Nano-graphene-platelet/Brilliant-green composite coated carbon paste electrode interface for electrocatalytic oxidation of flavanone Hesperidin, Microchem. J. 160 (2021) 105768. doi:10.1016/j.microc.2020.105768.

[5] M.A. Beluomini, N.R. Stradiotto, M.V. Boldrin, Electrosynthesis of three-dimensional nanoporous nickel on screen-printed electrode used for the determination of narirutin in citrus wastewater, Food Chem. (2021) 129427. doi:10.1016/j.foodchem.2021.129427.

[6] A.J. Bard, L.R. Faulkner, L.R.F. Allen J. Bard, Electrochemical methods: fundamentals and applications, 2nd ed., Wiley Global Education, New York, 2001. doi:10.1016/B978-0-12-381373-2.00056-9.

[7] D. Obendorf, E. Reichart, Determination of hesperidin by catholic stripping voltammetry in orange juice and helopyrin, a phytopharmaceutical preparation, Electroanalysis. 7 (1995) 1075–1081. doi:10.1002/elan.1140071115.

[8] S. Park, Y.J. Song, J.H. Han, H. Boo, T.D. Chung, Structural and electrochemical features of 3D nanoporous platinum electrodes, Electrochim. Acta. 55 (2010) 2029–2035. doi:10.1016/j.electacta.2009.11.026.

[9] S.A.G. Evans, J.M. Elliott, L.M. Andrews, P.N. Bartlett, P.J. Doyle, G. Denuault, Detection of hydrogen peroxide at mesoporous platinum microelectrodes, Anal. Chem. 74 (2002) 1322–1326. doi:10.1021/ac011052p.

[10] Y. Gao, X. Wu, H. Wang, W. Lu, M. Guo, Highly sensitive detection of hesperidin using AuNPs/rGO modified glassy carbon electrode, Analyst. 143 (2018) 297–303. doi:10.1039/C7AN01706E.

[11] B. Sun, X. Hou, D. Li, Y. Gou, F. Hu, W. Li, X. Shi, Electrochemical Sensing and High Selective Detection of Hesperidin with Molecularly Imprinted Polymer Based on Ultrafine Activated Carbon, J. Electrochem. Soc. 166 (2019) B1644–B1652. doi:10.1149/2.1141915jes.

[12] A. Zhupanova, E. Guss, G. Ziyatdinova, H. Budnikov, Simultaneous Voltammetric Determination of Flavanones Using an Electrode Based on Functionalized Single-Walled Carbon Nanotubes and Polyaluminon, Anal. Lett. 53 (2020) 2170–2189. doi:10.1080/00032719.2020.1732402.

[13] Y.M. Temerk, M.S. Ibrahim, M. Kotb, Square-wave cathodic adsorptive stripping

voltammetric determination of 3-hydroxyflavone, morin and hesperidin in bulk form and biological fluids in absence and presence of Cu(II), J. Braz. Chem. Soc. 22 (2011) 2056–2064. doi:10.1590/S0103-50532011001100006.

[14] D. Sun, F. Wang, K. Wu, J. Chen, Y. Zhou, Electrochemical determination of hesperidin using mesoporous SiO2 modified electrode, Microchim. Acta. 167 (2009) 35–39. doi:10.1007/s00604-009-0200-0.

[15] A. Yiğit, Y. Yardım, Z. Şentürk, Square-Wave Adsorptive Stripping Voltammetric Determination of Hesperidin Using a Boron-Doped Diamond Electrode, J. Anal. Chem. 75 (2020) 653–661. doi:10.1134/S1061934820050184.

[16] S. Šafranko, A. Stanković, A. Asserghine, M. Jakovljević, S. Hajra, S. Nundy, M. Medvidović-Kosanović, S. Jokić, Electroactivated Disposable Pencil Graphite Electrode – New, Cost-effective, and Sensitive Electrochemical Detection of Bioflavonoid Hesperidin, Electroanalysis. (2020) elan.202060511. doi:10.1002/elan.202060511.

[17] Y.M. Temerk, M.S. Ibrahim, M. Kotb, Square-wave cathodic adsorptive stripping voltammetric determination of 3-hydroxyflavone, Morin and Hesperidin in bulk form and biological fluids in absence and presence of Cu(II), J. Braz. Chem. Soc. 22 (2011) 2056–2064. doi:10.1590/S0103-50532011001100006.

[18] A. Zhupanova, E. Guss, G. Ziyatdinova, H. Budnikov, Simultaneous Voltammetric Determination of Flavanones Using an Electrode Based on Functionalized Single-Walled Carbon Nanotubes and Polyaluminon, Anal. Lett. 53 (2020) 2170–2189. doi:10.1080/00032719.2020.1732402.

APENDICE I

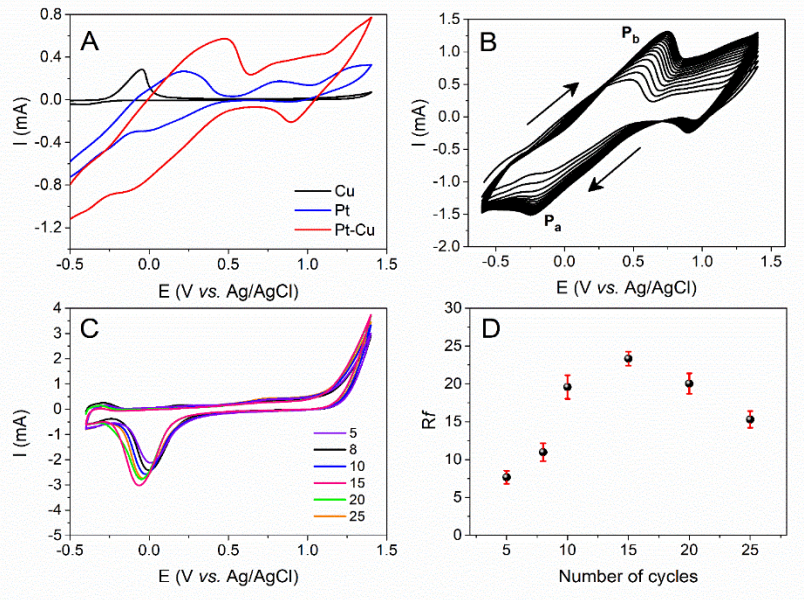

Figura A1. (A) CV para Cu, Pt e Pt-Cu em 0,5 mol L^{-1} H_2SO_4, υ = 50 mV s^{-1}. (B) CVs sucessivos durante a eletrodeposição de 3npPt-SPE. (C) Gráfico do fator de rugosidade superficial, R*f*, do eletrodo modificado em relação ao número de ciclos voltamétricos aplicados para a liga Pt-Cu. (D) CV de 3DnpPt-SPE em 0,5 mol L^{-1} H_2SO_4, a υ = 100 mV s^{-1}.

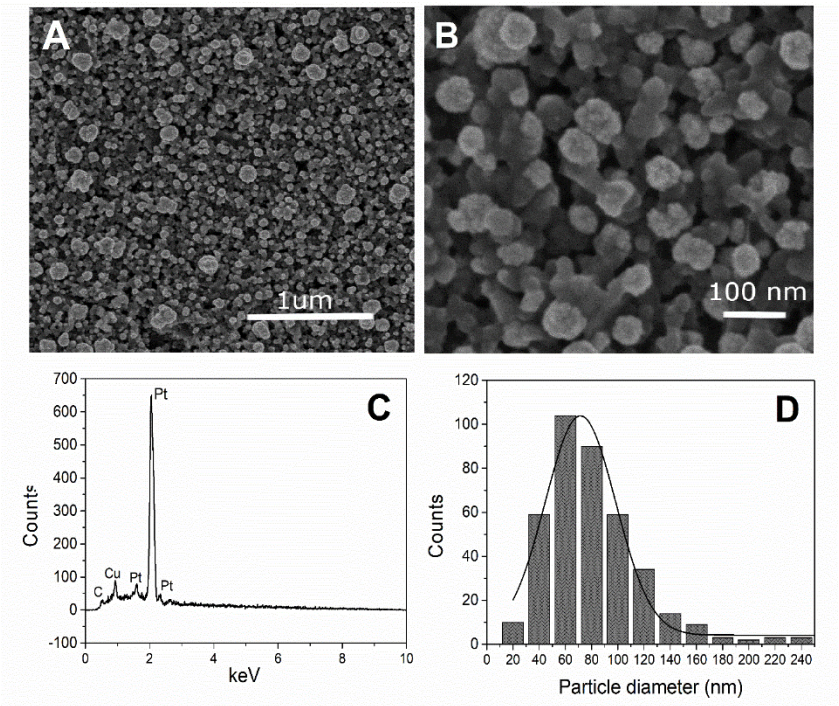

Figura A2. MEV obtida para o eletrodo 3DnpPt-SPE com magnificação de 50 000 x (A) e 100 000 x (B), (C) o respectivo EDS e (D) histograma da distribuição de tamanho das nanopartículas de Pt, em relação à imagem A

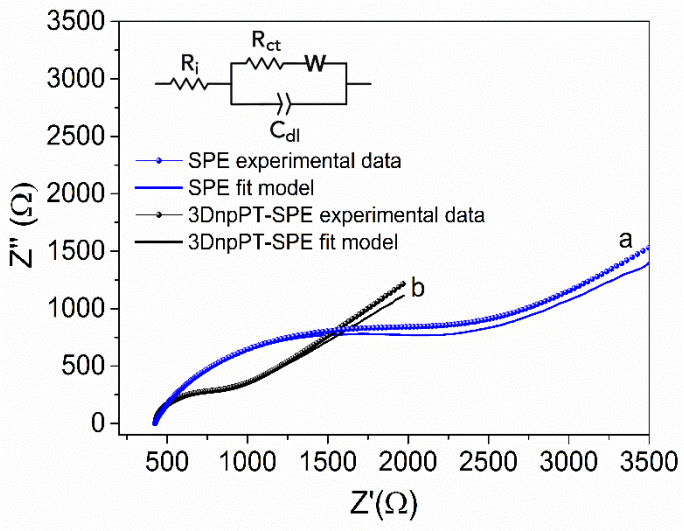

Figura 3A. Diagrama de Nyquist obtido para (a) SPE e (b) 3DnpPt-SPE em 5,0 mmol L^{-1} Fe $(CN)_6^{3-/4-}$ preparado em 0.1 mol L^{-1} KCl, na faixa de frequência de 0,1 Hz - 100 kHz; a linha curva representa o modelo fitting, calculado através do circuito equivalente inserido na figura.

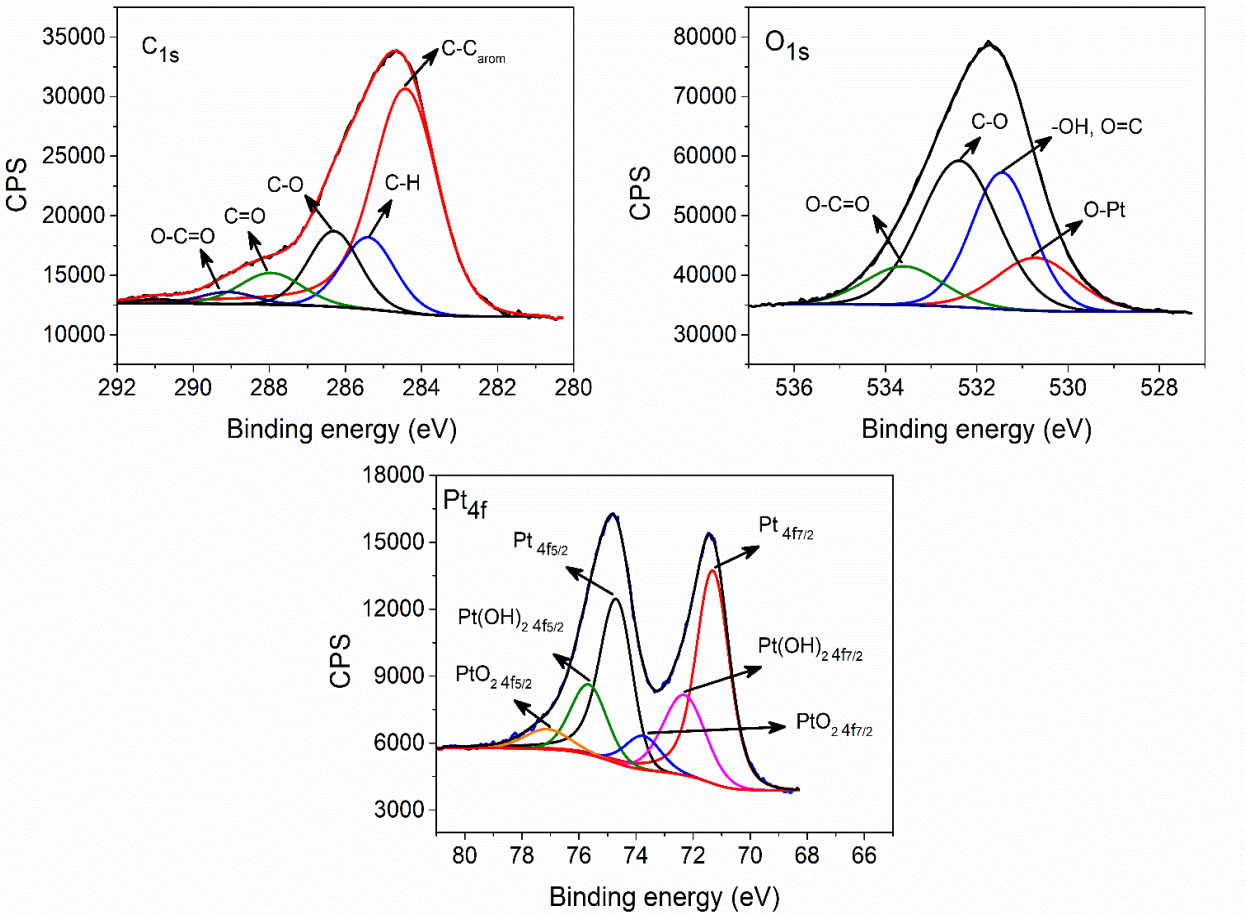

Figure A4. Deconvolucão do espectro de XPS para C1s, O1s, Pt4f para o 3DnpPt-SPE.

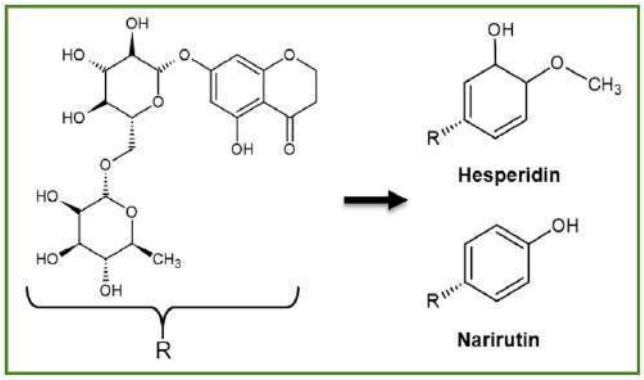

Esquema A1. Ilustração da estrutura química da hesperidina e narirutina.

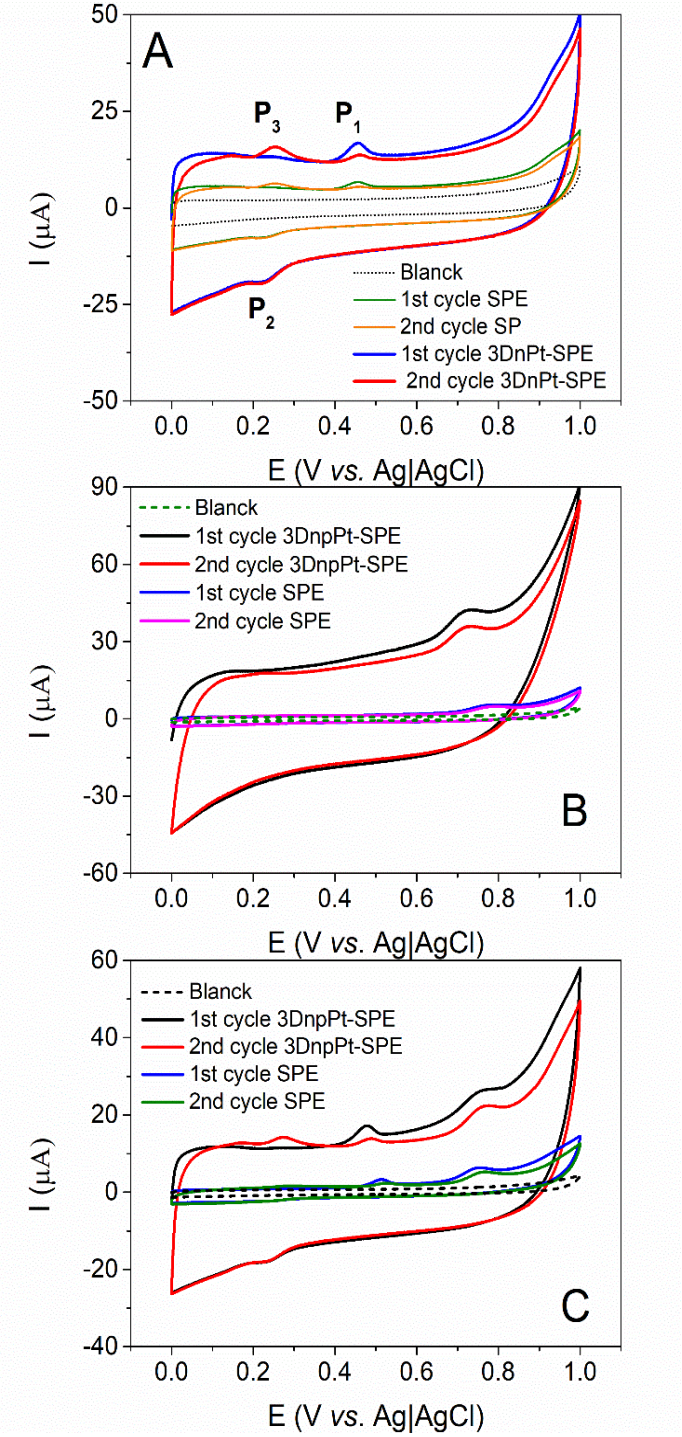

Figura A5. CVs obtidos para 0.2 mmol L^{-1} (A) HES, (B) NAR, e (C) HES and NAR, analisados em SPE e 3DnpPt-SPE.

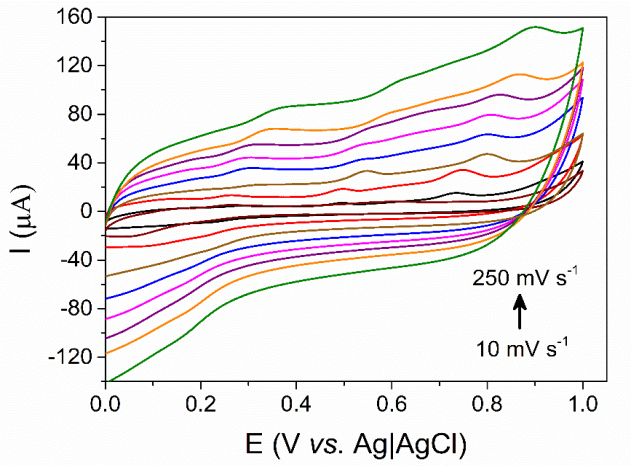

Figura A6. CV para 3DnpPt-SPE em diferentes velocidades de varredura (10 – 250 mV s^{-1}) para 0,2 mmol L^{-1} de HES e NAR em 0,1 mol L^{-1} de H_2SO_4.

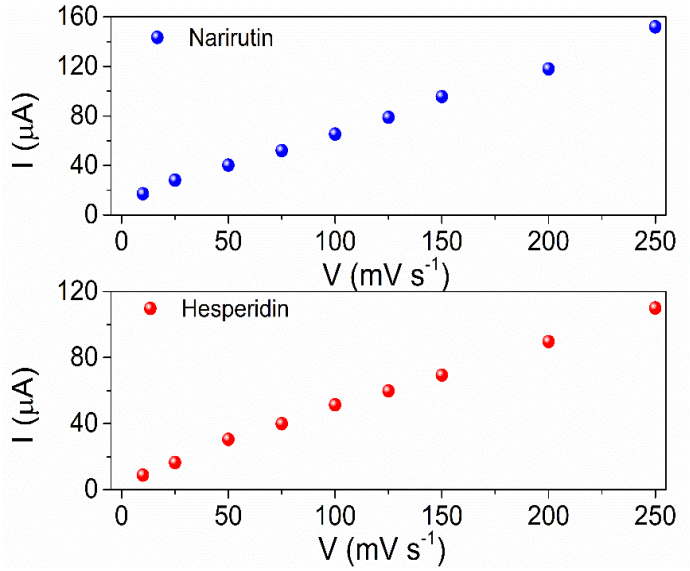

Figura A7. Gráfico da corrente de pico da narirutina e hesperidina *vs*. a velocidade de varredura (10 - 250 mVs^{-1}).

Tabela A1. Análise comparativa das figuras de mérito obtidas para o método proposto nesse trabalho utilizando 3DnpPt-SPE e outros métodos eletroanalíticos relatados na literatura e usados na determinação de HES e NAR.

Eletrodo	Técnica	Analito	Faixa linear (µM)	LOD (nM)	Ref.
3DnpPt-SPE	LSV	HES	10 – 400	6610	This work
		NAR	10 – 500	210	
AuNPs/rGO/GCE	AMP	HES	0,05–8,0	8,2	[10]
Mesoporous SiO_2-modified CPE	DPV	HES	0,5 – 25	250	[14]
MIP/AuNPs/UAC@GCE	DPV	HES	0,08–30,0	45	[11]
BDD	SW-AdSV	HES	4,1–120,0	120,0	[15]
3DnpNi/SPE	DPV	NAR	0,1 – 10	39	[5]
ePGE	DPV	HES	0,5 –10	200	[16]
MWCNT-BPPGE	SW-AdSV	HES	0,02–0,4 0,4–30,0	7,3	[3]
	CV-AdSV		0,5–15,0 15,0–40,0	610,0	
HMDE	SW-CASV	HES	0,019–0,654	7,54	[17]
nGp-Bg/MCPE	DPV	HES	0,1–7,0 7,0–100,0	50,0	[4]
Polyaluminon/f-SWCNT/GCE	DPV	HES	0,10–0,25	29,0	[18]

Abbreviations: AMP: Amperometry; DPV: Differential Pulse Voltammetry; SW-AdSV: Square-Wave Adsorptive Stripping Voltammetric; CV-AdSV: Cyclic voltammetric adsorptive voltammetry; SWCASV: Square wave cathodic adsorptive voltammetry; AuNPs/rGO/GCE: gold nanoparticles, reduced graphene oxide and modified glassy carbon electrode; CPE: carbon paste electrode; MIP/AuNPs/UAC@GCE: molecularly imprinted gold ultrafine activated carbon on glassy carbon electrode; BDD: Boron doped diamond; 3DnpNi/SPE: three-dimensional nanostructured porous nickel on screen-printed electrode; ePGE: pencil graphite electrode; MWCNT-BPPGE: Multiwalled carbon nanotube-Basal-Plane Pyrolytic graphite electrode; HMDE: hanging mercury dropping electrode; nGp-Bg/MCPE: nano-Graphene-platelets and π-e- of cationic Brilliant green on modified carbon paste electrode; Polyaluminon/f-SWCNT/GCE: polyaluminon/functionalized-single-walled carbon nanotubes/GCE.

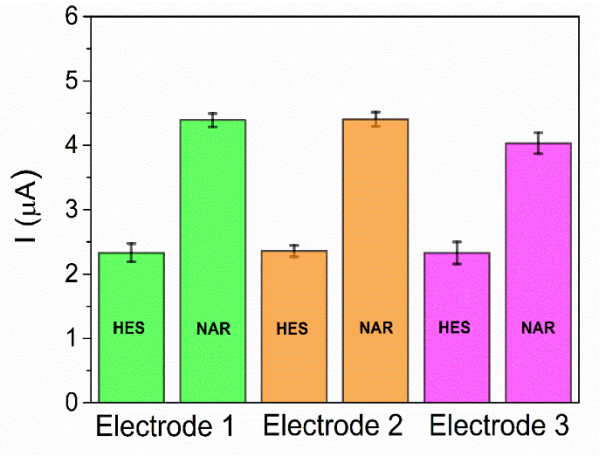

Figura A9. Repetibilidade entre eletrodos para HES e NAR (n=3).

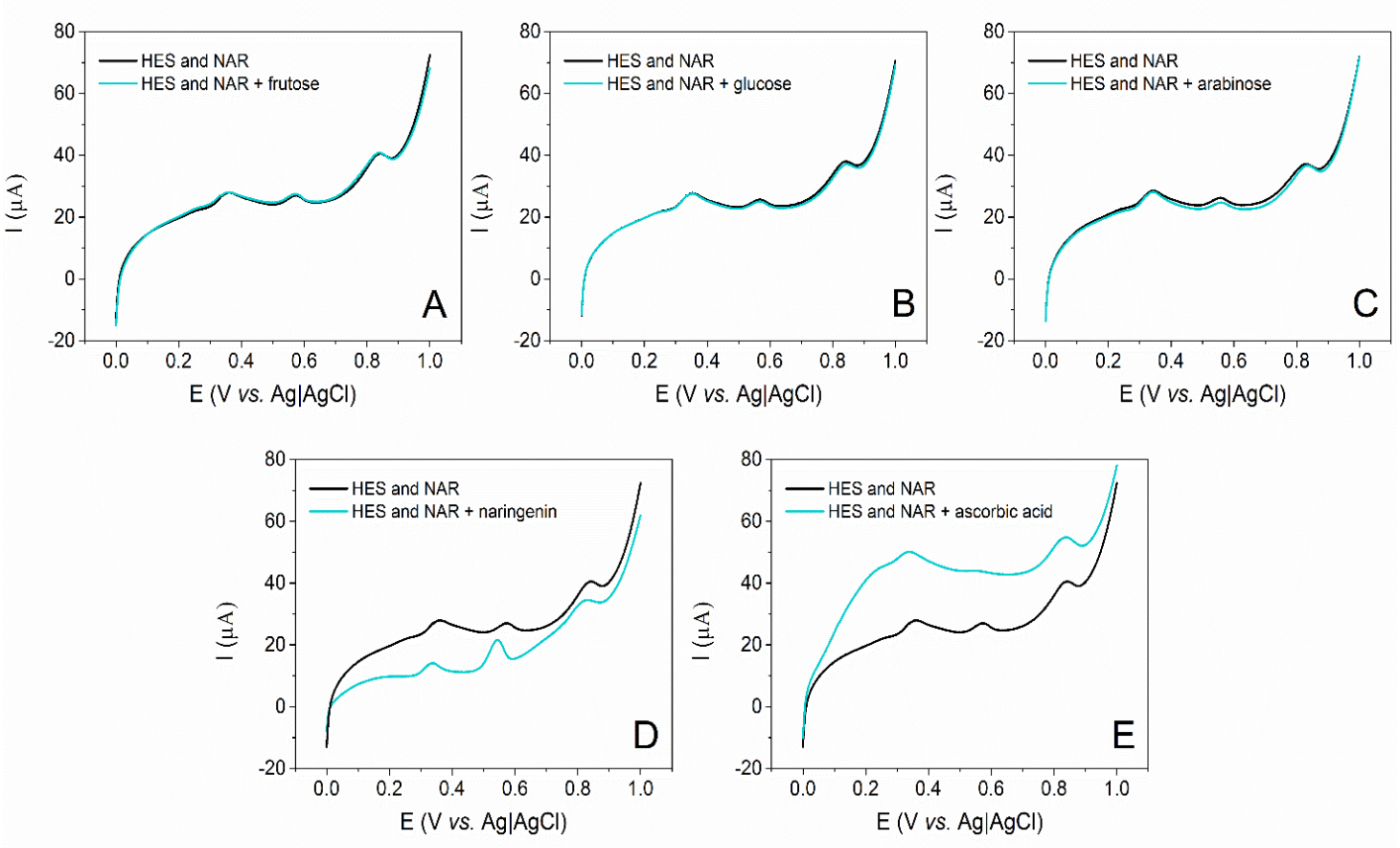

Figura A10. Estuda da seletivida do 3DnpPt-SPE na presença de (A) frutose, (B) glicose, (C) arabinose, (D) naringenina, (E) ácido ascórbico.

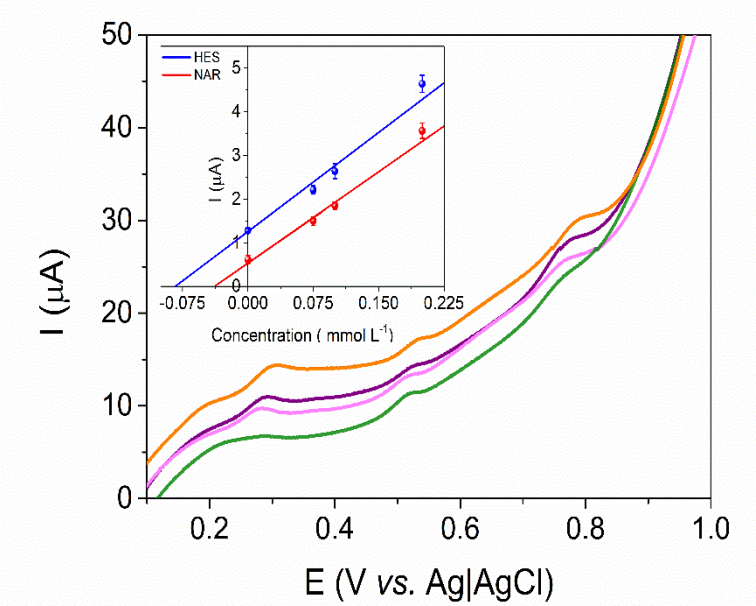

Figura A11. LSV para a determinação de HES e NAR. Inserção: Relação linear entre a corrente de pico *vs* concentração adicionada de HES e NAR de 0,075 a 0,2 mmol L^{-1}.

Tabela A2. Determinação de HES e NAR em amostra de água amarela (n=3).

Analito	Add (mmol L^{-1})	Encontrado (mmol L^{-1})	Recuperado (%)	RSD (%)
HES	0,075	0,065 ± 0,006	87,1	0,86
	0,10	0,091 ± 0,024	90,5	2,65
	0,20	0,208 ± 0,014	104,0	0,68
NAR	0,075	0,068 ± 0,003	90,7	0,42
	0,10	0,091 ± 0,17	91,7	1,85
	0,20	0,207 ± 0,007	103,2	0,34

Tabela A3. Valores obtidos a partir da análise estatística comparativa (usando t-student e test F) do método HPLC/DAD e do método de LSV em 3DnpPt-SPE proposto para a determinação de HES e NAR em amostras de água amarela (n = 3).

Analito	Método	Média (10^{-5} mol L^{-1})	Variância	*F-test*		*t-test*	
				Calculado	[a]Critico	Calculado	[b]Critico
HES	HPLC	17,6	0,00013	0,89	19,0	0,22	4,3
	LSV	17,4	0,0056				
NAR	HPLC	8,55	0,061	0,99	19,0	0,039	4,3
	LSV	8,54	0,28				

[a]$F_{critical}$: reported F value from *F-test* table with 95 % confidence level and 2/2 degrees of freedom,
[b]$t_{critical}$: reported t value from Student *t-test* table with 95 % confidence level,

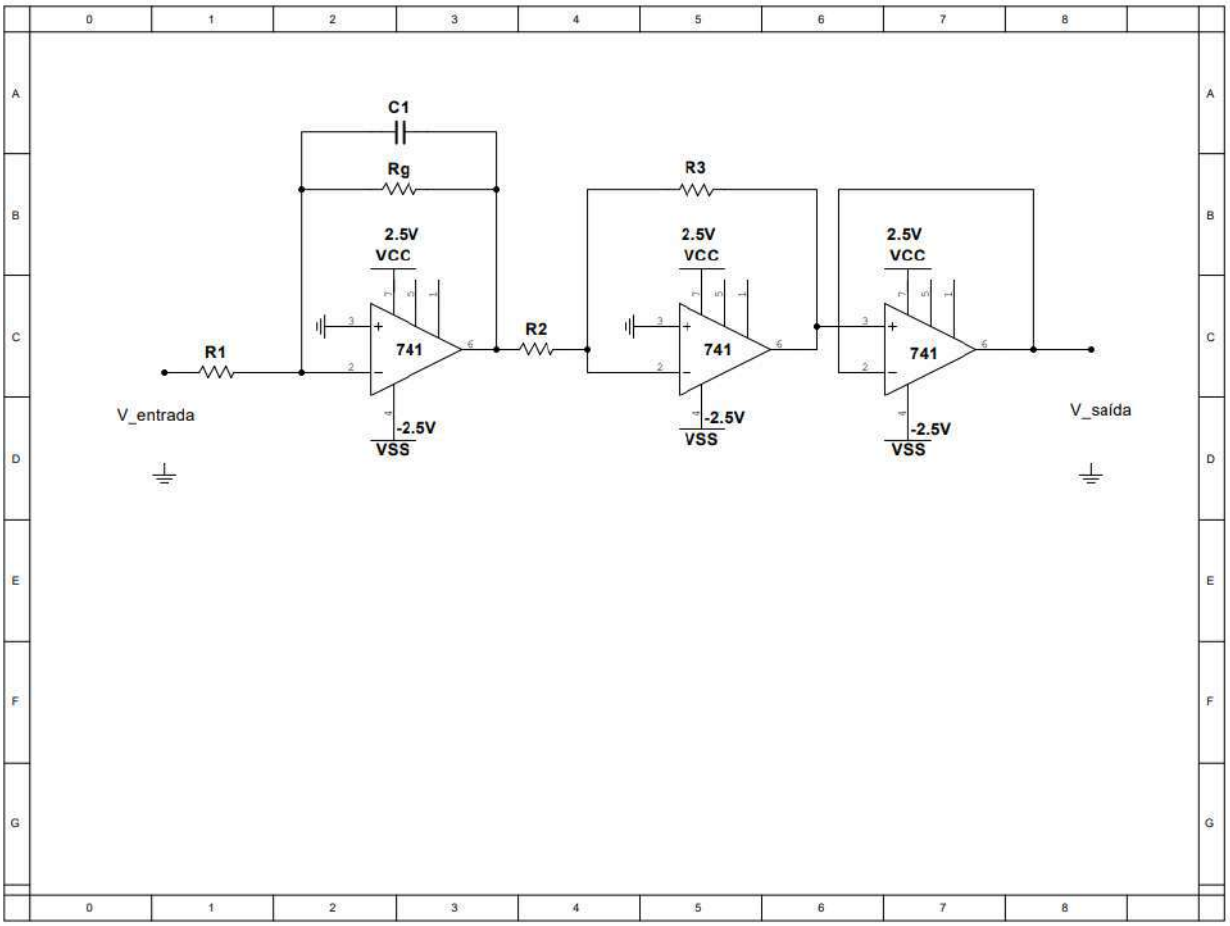

Figura A12. Circuito de amplificação montado no software de simulação com LM741.

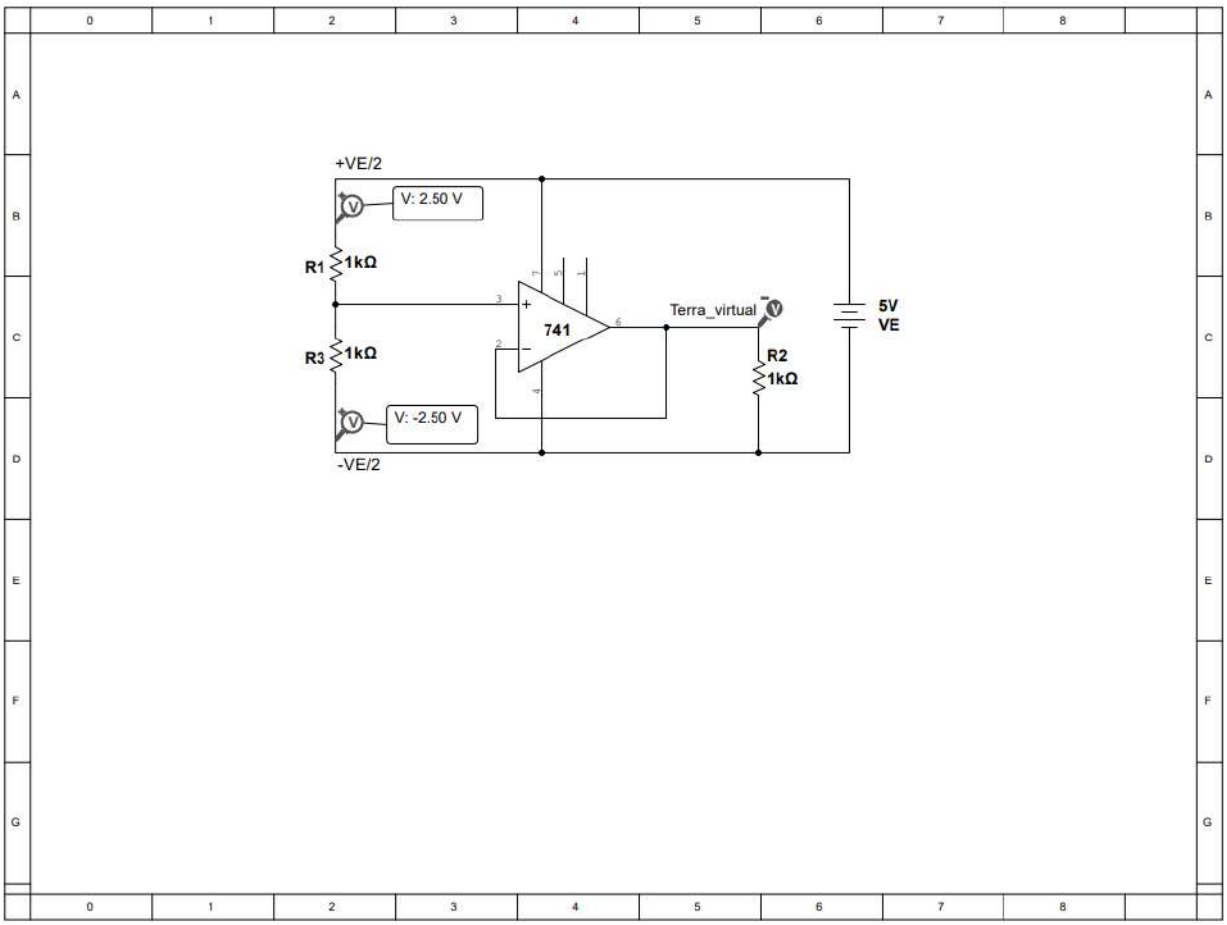

Figura A13. Circuito gerador de tensão simétrica montado no software de simulação.

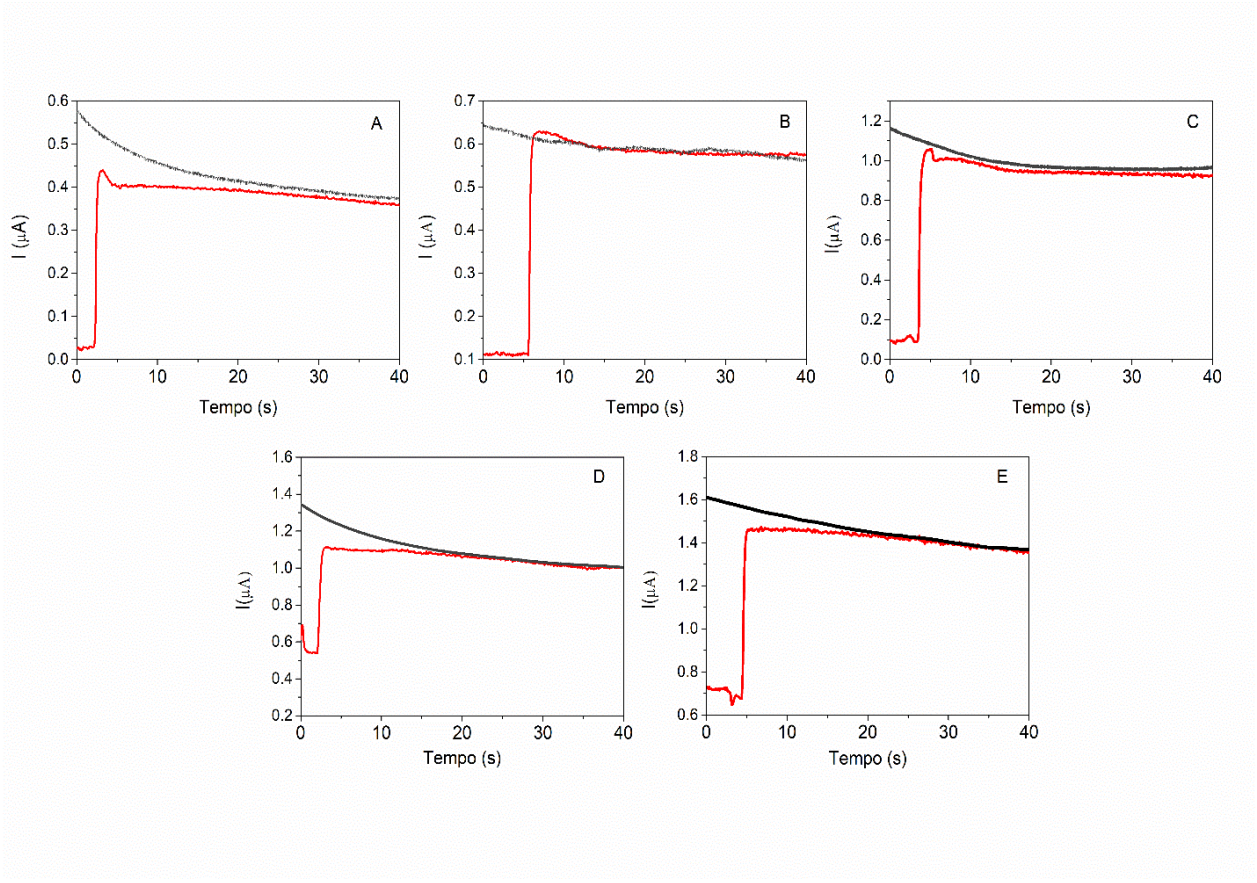

Figura A14. Cronoamperograma obtido para o sistema desenvolvido (curva vermelha) e para o potenciostato comercial (curva preta) nas concentrações de 1,0 mM (A), 2,0 mM (B), 3,0 mM (C), 4,0 mM (D) e 5,0 mM (E) da sonda redox ferri/ferrocianato, preparada em 0,1 M de KCl.

Tabela A4. Performance cronoamperométrica do dispositivo desenvolvido em relação ao comercial, em diferentes concentrações da sonda redox (t = 20 s), (n=3).

	Corrente de pico (μA)	Concentração				
		1,0 mM	2,0 mM	3,0 mM	4,0 mM	5,0 mM
Potenciostato comercial	Valor médio da corrente	0,39366	0,5856	0,939	1,06386	1.43523
Dispositivo desenvolvido	Valor médio da corrente	0,40997	0,59147	0,964	1,07529	1.4532
Desvio padrão		0,01153	0,00415	0,01698	0,00808	0.01271
Distinção (%)		3,978	0,9924	2,555	1,074	1,252

6) Participação em evento científico no período que abrange o relatório científico

[1] Beluomini, M.A., Stradiotto, N.R., Boldrin, M.V. Screen-Printed Electrode Modified with 3-D Nanoporous Nickel for the Determination of Narirutin in Wastewater from Citrus Industry. 239th ECS Meeting with the 18th International Meeting on Chemical Sensors (IMCS). Chicago-USA, Digital Meeting, 2021.
(https://iopscience.iop.org/article/10.1149/MA2021-01571542mtgabs/meta)

[2] Beluomini, M.A., Stradiotto, N.R., Boldrin, M.V. 3D-nanoporous nickel electrode for the determination of hesperidin in yellow water from citrus industry. II Fronteiras em Eletroquímica e Eletroanalítica: avanços realizados por jovens mulheres cientistas. Digital Meeting, 2021.

The Electrochemical Society
Advancing solid state & electrochemical science & technology

65 South Main Street, Building D
Pennington, New Jersey 08534-2839, USA
tel 1.609.737.1902
fax 1.609.737.2743

July 1, 2021

To Whom It May Concern:

This is to certify that Maísa Beluomini attended the 239th ECS Meeting with the 18th International Meeting on Chemical Sensors (IMCS), held virtually from May 30-June 3, 2021.

This also certifies that Maísa Beluomini presented the following paper titled: ***Screen-Printed Electrode Modified with 3-D Nanoporous Nickel for the Determination of Narirutin in Wastewater from Citrus Industry*** by: Maísa Beluomini (São Paulo State University), Nelson Ramos Stradiotto (São Paulo State University), Maria Valnice Boldrin Zanoni (São Paulo State University).

Sincerely,

Chris Jannuzzi
ECS Executive Director

IOPscience

Screen-Printed Electrode Modified with 3-D Nanoporous Nickel for the Determination of Narirutin in Wastewater from Citrus Industry

Maisa Beluomini[1], Nelson Ramos Stradiotto[1] and Maria Valnice Boldrin Zanoni[1]

ECS Meeting Abstracts, Volume MA2021-01, IMCS 04: Sensors for Agricultural and Environmental Applications

Citation Maisa Beluomini *et al* 2021 *Meet. Abstr.* **MA2021-01** 1542

[1] São Paulo State University

Maisa Beluomini https://orcid.org/0000-0003-3441-1572

Nelson Ramos Stradiotto https://orcid.org/0000-0002-1227-5242

Maria Valnice Boldrin Zanoni https://orcid.org/0000-0002-2296-1393

https://doi.org/10.1149/MA2021-01571542mtgabs

Abstract

Yellow Water (YW) is the term given to liquid residues produced from the washing of orange fruits, distilling activities of distilleries, and the production of essential oil from orange; the handling and disposal of these residues are a matter of great concern to orange industries worldwide. An average size orange plant produces about 100,000 liters of YW daily. This wastewater has a considerable amount of organic compounds with high polluting power. Citrus processing industries are commercially interested in recovering significant quantities of some usefully relevant compounds present in YW. Among the compounds that have high added value, citrus flavonoids show an important biological activities, highlighting the molecule narirutin - a flavanone glucoside, which has been shown to present interesting therapeutic properties against cancer, Alzheimer's disease, and more recently, effects against the coronavirus disease 2019 (COVID-19). So, this work reports for the first time the electrochemical determination of narirutin using three-dimensional nanostructured porous nickel with high surface area on screen-printed electrode (3DnpNi/SPE), since the literature reports only chromatographic methods for the detection and quantification of narirutin. The modified electrode was successfully developed by the dynamic hydrogen bubble template method. This method involves the evolution of hydrogen bubbles together with the metal deposition process. Thereby, these bubbles become a dynamic template for the electrochemical deposition. Compared to the non-modified SPE, the 3DnpNi/SPE presented better electrochemical performance in terms of the oxidation of narirutin. The 3DnpNi/SPE was characterized by scanning electron microscopy (SEM), proving the formation of nickel nanopores with homogeneous distribution on the electrode surface, with a diameter varying between 70 - 120 nm. The energy-dispersive X-ray spectroscopy (EDS) and X-ray photoelectron spectroscopy (XPS) showed the presence of nickel and nickel oxide in the nanostructure. The EIS technique was applied for the electrochemical characterization of the 3DnpNi/SPE. The electron-transfer resistance was analyzed using a solution of 5.0×10^{-3} mol L^{-1} $[Fe(CN)_6]^{3-/4-}$ in 0.1 mol L^{-1} KCl. The results obtained were discussed in terms of Rct (charge-transfer resistance) from the equivalent circuits. It was can observe the presence of a semicircle for the unmodified SPE with Rct of 2.3 KΩ. When the SPE was modified with nanoporous nickel, the electrochemical response appeared to be close to a straight line, and the R_{ct} value was notably lower, 39 Ω; this shows that the modification of the electrode facilitated the transfer of electrons between the redox probe and the electrode surface. The cyclic voltammetry (CV) results showed that the 3DnpNi/SPE exhibited a peak current 3.3 times greater than that of bare SPE. The oxidation process involved 1 electron and 1 proton in a single irreversible step, with the formation of phenoxyl radical, which was adsorbed on the electrode surface due to the irreversible reaction (dimerization), to form dimer products. The quantification of narirutin was conducted by differential pulse voltammetry (DPV), which showed a wide concentration range (1.0×10^{-7} – 1.0×10^{-5} mol L^{-1}), with low detection limit (3.9×10^{-8} mol L^{-1}), and excellent sensitivity (0.31 A L mol^{-1}). The good electrochemical performance of the proposed electrode was attributed to the high density of the nanostructured porous nickel on the SPE. The inter-electrode repeatability (n=5) was investigated by CV using the concentration of 5.0×10^{-6} mol L^{-1} of narirutin in 0.1 mol L^{-1} citrate buffer solution (pH 4.0). The average oxidation current obtained was 2.2 µA, with RSD of 5.9 %. In addition, the 3DnpNi/SPE was stored for 10 days in contact with air at room temperature (25 °C). The current response relative to narirutin detection was found to be 94.2 % of its initial peak current value. These results show that the 3DnpNi/SPE has good repeatability and long-term stability. The standard addition method was adopted for determining the concentration of narirutin in the sample. The sample was spiked with known concentrations of standard narirutin in the range of 2.0×10^{-6} mol L^{-1} to 6.0×10^{-6} mol L^{-1}. A linear relationship was observed between the current peak and the added concentration of narirutin. The regression equation was as follows: $y = 0.56\ x + 2.3\times10^{-6}$ ($R = 0.999$). From the standard addition curve, and based on the extrapolation of the straight line and the sample dilution (20-fold), the concentrations of narirutin found in the yellow water sample was $(8.3 \pm 0.39)\times10^{-5}$ mol L^{-1} (n=3). To determine the analytical accuracy of the proposed method, recovery experiments were performed in standard solutions. The recovery rates obtained ranged from 97.1% to 100.9%, with RSD lower than 7.0 %. The concentration of narirutin in the YW sample was also determined by HPLC and the concentration value obtained was $(8.6 \pm 0.25)\times10^{-5}$ mol L^{-1}. Thereby, the RSD obtained between the two techniques was 0.16 %. These results demonstrate a good agreement between the proposed method and the comparative method (HPLC); essentially, this points to the reliability of the method proposed in this work. Thus, the findings of the present study show that the proposed 3DnpNi/SPE-based electroanalytical method can certainly be used for the determination of narirutin in yellow water.

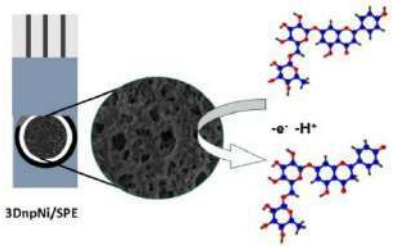

Figure 1

Export citation and abstract BibTeX RIS

◂ **Previous** article in issue

Next article in issue ▸

UNIVERSIDADE FEDERAL DO RIO DE JANEIRO

PRÓ-REITORIA DE EXTENSÃO

CERTIFICADO

Certificamos que Maisa Azevedo Beluomini concluiu o curso de extensão "II Fronteiras em Eletroquímica e Eletroanalítica: avanços realizados por jovens mulheres cientistas", realizado no período de 11 de fevereiro de 2021 a 12 de fevereiro de 2021, com carga horária de 16 horas, coordenado por MAIARA OLIVEIRA SALLES e registrado nesta Pró-reitoria.

Rio de Janeiro, 25 de junho de 2021

Ivana Bentes Oliveira
Pró-reitora de extensão

A autenticidade deste certificado pode ser confirmada através do seguinte endereço: https://sgod.ufrj.br/verificar, digitando-se o seguinte código: 9KLR74 .

7) Lista das publicações resultantes no período a que se refere o relatório científico.

[1] Beluomini, M. A., Stradiotto, N.R. Zanoni M. V. B. Simultaneous detection of hesperidin and narirutin in residual water using nanoporous platinum electrosynthesized by alloying-dealloying mechanis. Journal of Electroanalytical Chemistry. JELECHEM-D-21-01066. 2021.

[2] Beluomini, M. A., Stradiotto, N.R. Zanoni M. V. B. Electrosynthesis of three-dimensional nanoporous nickel on screen-printed electrode used for the determination of narirutin in citrus wastewater. Food Chemistry, v. 353, p. 129427, 2021. https://doi.org/10.1016/j.foodchem.2021.129427

[3] Garcia, M, B., Beluomini, M. A., Zanoni M.V.B. Using an Electrochemical MIP sensor for Selective Determination of 1-Naphthol in Oilfield Produced Water. Electroanalysis, v.33, p.1-11 2021. https://doi.org/10.1002/elan.202060545.

[4] Da Silva, J. L., Buffon, E., Beluomini, M. A., Pradela-Filho, L.A., Gouveia, D. A.A., Santos, A. L., Takeuchi, R. M., Stradiotto, N.R. Non-enzymatic lactose molecularly imprinted sensor based on disposable graphite paper electrode. Analytica Chimica Acta, p. 53-64, 2021. https://doi.org/10.1016/j.aca.2020.11.030.

8) Para as publicações listadas no item 7, inclua cópias das primeiras páginas,

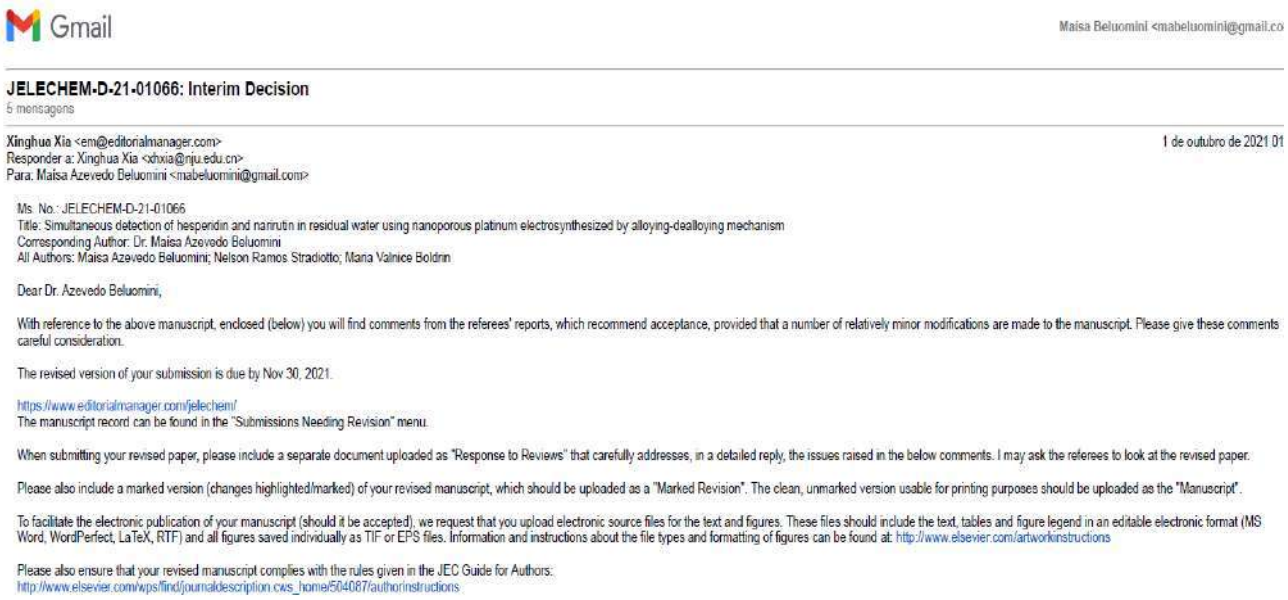

Gmail

Maisa Beluomini <mabeluomini@gmail.co

JELECHEM-D-21-01066: Interim Decision

5 mensagens

Xinghua Xia <em@editorialmanager.com> 1 de outubro de 2021 01
Responder a: Xinghua Xia <xhxia@nju.edu.cn>
Para: Maisa Azevedo Beluomini <mabeluomini@gmail.com>

Ms. No.: JELECHEM-D-21-01066
Title: Simultaneous detection of hesperidin and narirutin in residual water using nanoporous platinum electrosynthesized by alloying-dealloying mechanism
Corresponding Author: Dr. Maisa Azevedo Beluomini
All Authors: Maisa Azevedo Beluomini; Nelson Ramos Stradiotto; Maria Valnice Boldrin

Dear Dr. Azevedo Beluomini,

With reference to the above manuscript, enclosed (below) you will find comments from the referees' reports, which recommend acceptance, provided that a number of relatively minor modifications are made to the manuscript. Please give these comments careful consideration.

The revised version of your submission is due by Nov 30, 2021.

https://www.editorialmanager.com/jelechem/
The manuscript record can be found in the "Submissions Needing Revision" menu.

When submitting your revised paper, please include a separate document uploaded as "Response to Reviews" that carefully addresses, in a detailed reply, the issues raised in the below comments. I may ask the referees to look at the revised paper.

Please also include a marked version (changes highlighted/marked) of your revised manuscript, which should be uploaded as a "Marked Revision". The clean, unmarked version usable for printing purposes should be uploaded as the "Manuscript".

To facilitate the electronic publication of your manuscript (should it be accepted), we request that you upload electronic source files for the text and figures. These files should include the text, tables and figure legend in an editable electronic format (MS Word, WordPerfect, LaTeX, RTF) and all figures saved individually as TIF or EPS files. Information and instructions about the file types and formatting of figures can be found at: http://www.elsevier.com/artworkinstructions

Please also ensure that your revised manuscript complies with the rules given in the JEC Guide for Authors:
http://www.elsevier.com/wps/find/journaldescription.cws_home/504087/authorinstructions

Obs.: Artigo anexado na sequência (página 41), pois foi recentemente aceito e até o momento da submissão deste relatório ainda não consta disponível online por meio do DOI.

Food Chemistry 353 (2021) 129427

Contents lists available at ScienceDirect

Food Chemistry

journal homepage: www.elsevier.com/locate/foodchem

Electrosynthesis of three-dimensional nanoporous nickel on screen-printed electrode used for the determination of narirutin in citrus wastewater

Maísa Azevedo Beluomini [a,*], Nelson Ramos Stradiotto [a,b], Maria Valnice Boldrin [a]

[a] Analytical Chemistry Department, Institute of Chemistry, São Paulo State University (UNESP), 55 Prof. Francisco Degni St., Araraquara 14800-060, São Paulo State, Brazil

[b] Bioenergy Research Institute (IPBEN), São Paulo State University (UNESP), 55 Prof. Francisco Degni St., Araraquara 14800-060, São Paulo State, Brazil

ARTICLE INFO

Keywords:
Nanostructure
Differential pulse voltammetry
Electrochemical detection
Narirutin
Yellow water

Chemical compounds studied in this article:
Narirutin (PubChem CID: 442431)
Naringenin (PubChem CID: 932)
Hesperidin (PubChem CID: 10621)
D(+)-Glucose (PubChem CID: 107526)
D-fructose (PubChem CID: 5984)
Nickel chloride hexahydrate (PubChem CID: 11791229)

ABSTRACT

In this study, an electrochemical sensor was designed for the detection of narirutin using three-dimensional nanostructured porous nickel on screen-printed electrode (3DnpNi/SPE). The modified electrode was successfully synthesized by the dynamic hydrogen bubble template method. The 3DnpNi/SPE was characterized by spectroscopic, microscopic, and electrochemical methods. The results showed that the 3DnpNi/SPE presents good electrocatalytic activity for the oxidation of narirutin. The quantification of narirutin was conducted by differential pulse voltammetry, which showed a wide concentration range ($1.0 \times 10^{-7} - 1.0 \times 10^{-5}$ mol L^{-1}), with low detection limit (3.9×10^{-8} mol L^{-1}), and excellent sensitivity (0.31 A L mol^{-1}). The proposed electrode was applied toward the determination of narirutin in yellow water sample from the citrus industry, where it presented a good degree of accuracy. The 3DnpNi/SPE showed repeatability, long-term stability, and selectivity. The results obtained showed agreement with those obtained by HPLC/DAD method.

Chemical compounds studied in this article.

1. Introduction

The orange industry is one of the major industries in the world due to the high consumption of orange, orange juice and its derivatives. Currently, the annual orange production in the world is estimated to be approximately 70 thousand tons, with Brazil being the largest producer, followed by the United States, India, and China. In the orange industry, approximately 70% of the orange produced is transformed into juice, oil, marmalade, and other products, while a significant portion of the remaining 30% ends up as solid and liquid wastes (Calabrò et al., 2016). It is estimated that the citrus industry produces nearly 40 million tons of waste annually (Peerzada & Chidambaram, 2020). Among these residues, the huge amount of yellow water (term given to liquid residues produced from the washing of orange fruits, distilling activities, and the production of essential oil) has become a matter of great concern to the orange industries and other stakeholders involved. An average size plant produces about 100 m^3 of yellow water daily (Di Mauro, Fallico, Passerini, & Maccarone, 2000). Due to the high concentration of organic matter, this waste becomes a highly polluting agent. Citrus processing industries are commercially interested in recovering significant quantities of some useful relevant compounds in the wastes which are found to have high added value (Gómez-Mejía, Rosales-Conrado, León-González, & Madrid, 2019). One of the relevant compounds which deserve mentioning is citrus flavonoids; these molecules are a major class of secondary metabolites which has been extensively studied. (Sharma, Mahato, Cho, & Lee, 2017). Among these flavonoids includes narirutin (naringenin-7-O-rutinoside) - a flavanone glucoside, which has been shown to present interesting agricultural and therapeutic properties in studies related to the maintenance of the quality of food products by decreasing the accumulation of mycotoxins in crops (Pok et al., 2020), Alzheimer's disease therapy (Chakraborty & Basu, 2017), and the reduction of airway inflammation in mice (Funaguchi et al., 2007). In addition, several studies have shown that flavonoids have therapeutic effects against the coronavirus disease 2019 (COVID-19). The studies have demonstrated that flavonoids can bind with high affinity to the receptor angiotensin-converting enzyme 2 (ACE2) in the respiratory tract, causing a conformational change that inhibits the entry of coronaviruses in the human body (Ngwa et al., 2020; Tutunchi, Naeini,

* Corresponding author.
E-mail address: maisa.beluomini@unesp.br (M.A. Beluomini).

https://doi.org/10.1016/j.foodchem.2021.129427

Full Paper Wiley Online Library ELECTROANALYSIS

DOI: 10.1002/elan.202060545

Using an Electrochemical MIP Sensor for Selective Determination of 1-Naphthol in Oilfield Produced Water

Mariana Bartilotti,*[a, b] Maísa Azevedo Beluomini,*[a, b] and Maria Valnice Boldrin Zanoni[a, b]

Abstract: A molecularly imprinted polymer (MIP) sensor was successfully constructed on glassy carbon electrode for the determination of 1-naphthol (1-Nph). The sensor was constructed by electropolymerization on bare GCE in the presence of the target molecule. The recognition of 1-Nph was conducted indirectly using $[Fe(CN)_6]^{3-/4-}$ as redox probe. The MIP sensor presented wide linear working range and limit of detection of 1.5×10^{-9} mol L^{-1}. The MIP sensor was applied for the determination of 1-Nph in oilfield produced water. The results obtained showed good selectivity and sensitivity of the proposed sensor in terms of 1-Nph quantification.

Keywords: 1-Naphthol electroanalysis · electrochemical molecularly imprinted polymer · oilfield produced water · electrochemical sensor · naphthol detection

1 Introduction

The petroleum industry is regarded one of the ten largest sources of toxic wastes emission in the environment [1]. Oil extraction is one of the major activities that contribute to the emission of toxic waste into the environment through the generation of contaminated wastewater which is a by-product of the process. The oil extraction process uses water injection in the process in order to maintain enough pressure and to aid the flow of liquid and gases from the ground to the surface of the oilfield. The wastewater produced in this process is referred to as oilfield produced water (OPW). The content of OPW is regulated by environmental legislations and guidelines established by environmental agencies and regulatory bodies at both national and international levels due to the hazardous substances it contains which pose health and environmental risks [2].

The complex OPW matrix consists of a mixture of substances which include aromatic compounds, salts, gases, metals, oils, and grease [3,4]. More specifically, OPW contains BTEX (Benzene, Toluene, Etilbenzene and Xylenes); phenols; and polycyclic aromatic hydrocarbons (PAHs), which include anthracene, fluoranthene, and naphthalene [4]. The high degree of toxicity of the aromatic compounds can be attributed to some factors such as genotoxicity [5], mutagenicity [6], and bioaccumulation [5].

Studies published in the literature have investigated the toxicity of naphthalene, and the results show that the harmful effects caused by this compound in mammalian organisms are mainly due to its metabolic products; these products, which include 1-naphthol (1-Nph) and naphthoquinones, have been found to exhibit cytotoxicity [7–9]. In addition, 1-Nph is one of the main compounds derived from the degradation of naphthalene under UV-Vis in aqueous medium with dissolved oxygen [8]; this compound is quite prevalent in the marine environment.

The legal resolution on the Registration, Evaluation, Authorisation, and Restriction of Chemicals (REACH, n° 1907/2006) states that 1-Nph is harmful if swallowed or in contact with the skin, since it may cause serious eye damage, as well as respiratory irritation. So, the determination of 1-Nph, which is regarded an aqua-toxic emerging pollutant [10–14] in environmental effluents, is of extreme importance, particularly when one thinks of routinely discharged water that is heavily contaminated by PAHs.

The analytical methods employed for the quantification of 1-Nph concentration in real and synthetic samples are mainly carried out using gas chromatography with mass spectrometer [15]; high performance liquid chromatography coupled to a UV detector [16,17], or by fluorescence detection [18]. Although electrochemical techniques applied toward the detection of analytes have presented fast and reliable results with high sensitivity and selectivity, very few studies reported in the literature have employed these techniques for the determination of 1-Nph [19–25].

Most of the electroanalytical methods employed for the determination of 1-Nph are based on solid electrodes which have been strategically modified to improve the

[a] M. Bartilotti, M. A. Beluomini, M. V. Boldrin Zanoni
National Institute of Alternative Technologies for Detection, Toxicological Evaluation and Removal of Micropollutants and Radioactive Substances (INCT-DATREM), São Paulo State University (UNESP), 55 Prof. Francisco Degni St., Araraquara 14800-060, São Paulo State, Brazil
[b] M. Bartilotti, M. A. Beluomini, M. V. Boldrin Zanoni
Analytical Chemistry Department, Institute of Chemistry, São Paulo State University (UNESP), 55 Prof. Francisco Degni St., Araraquara 14800-060, São Paulo State, Brazil
E-mail: mariana.garcia@unesp.br
maisa.beluomini@unesp.br

Supporting information for this article is available on the WWW under https://doi.org/10.1002/elan.202060545

Analytica Chimica Acta 1143 (2021) 53–64

Contents lists available at ScienceDirect

Analytica Chimica Acta

journal homepage: www.elsevier.com/locate/aca

Non-enzymatic lactose molecularly imprinted sensor based on disposable graphite paper electrode

José Luiz da Silva [a,*], Edervaldo Buffon [a], Maísa Azevedo Beluomini [a], Lauro Antonio Pradela-Filho [b], Diele Aparecida Gouveia Araújo [b], André Luiz Santos [b], Regina Massako Takeuchi [b], Nelson Ramos Stradiotto [a,c]

[a] Analytical Chemistry Department, Institute of Chemistry, São Paulo State University (UNESP), 55 Prof. Francisco Degni St., Araraquara, 14800-060, São Paulo State, Brazil
[b] Institute of Exact and Natural Sciences of Pontal, Federal University of Uberlandia, 1600 20 St, Ituiutaba, 38304-402, Minas Gerais State, Brazil
[c] Bioenergy Research Institute (IPBEN), São Paulo State University (UNESP), 55 Prof. Francisco Degni St., Araraquara, 14800-060, São Paulo State, Brazil

HIGHLIGHTS

- A disposable paper-based non-enzymatic voltammetric sensor used for lactose detection.
- A novel electrosynthesized MIP modified disposable paper sensor for lactose detection.
- Lactose was selectively recognized by the MIP used as synthetic receptor.
- The proposed MIP paper-based sensor exhibited good reproducibility and robustness.
- The MIP sensor presented excellent performance for lactose determination in milk samples.

GRAPHICAL ABSTRACT

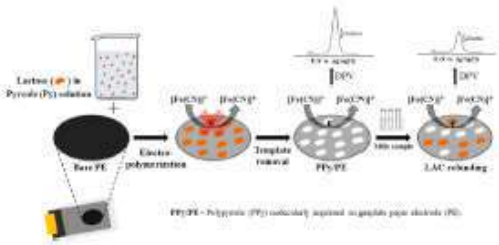

ARTICLE INFO

Article history:
Received 24 August 2020
Received in revised form
13 November 2020
Accepted 23 November 2020
Available online 24 November 2020

Keywords:
Paper-based electrode
Molecularly imprinted polymers
Electropolymerization
Experimental design
Non-enzymatic electroanalysis
Lactose sensing

ABSTRACT

Lactose (LAC) is a disaccharide - major sugar, present in milk and dairy products. LAC content is an important indicator of milk quality and abnormalities in food industries, as well as in human and animal health. The present study reports the development of an innovative imprinted voltammetric sensor for sensitive detection of LAC. The sensor was constructed using electropolymerized pyrrole (Py) molecularly imprinted polymer (MIP) on graphite paper electrode (PE). The MIP film was constructed through the electrosynthesis of polypyrrole (PPy) in the presence of LAC (template molecule) on PE (PPy/PE). To optimize the detection conditions, several factors affecting the PPy/PE sensor performance were assessed by multivariate methods (Plackett–Burman design and central composite design). Under optimized conditions, the proposed analytical method was applied for LAC detection in whole and LAC-free milks, where it demonstrated high sensitivity and selectivity, with two dynamic linear ranges of concentration (1.0–10 nmol L^{-1} and 25–125 nmol L^{-1}) and a detection limit of 0.88 nmol L^{-1}. The MIP sensor showed selective molecular recognition for LAC in the presence of structurally related molecules. The proposed PPy/PE sensor exhibited good stability, as well as excellent reproducibility and repeatability. Based on the results obtained, the PPy/PE is found to be highly promising for sensitive detection of LAC.

* Corresponding author.
E-mail addresses: jose.l.silva@unesp.br, silva_jluiz@yahoo.com.br (J.L. da Silva).

https://doi.org/10.1016/j.aca.2020.11.030
0003-2670/

ARTIGO ACEITO - JELECHEM-D-21-01066.

Simultaneous detection of hesperidin and naririutin in residual water using nanoporous platinum electrosynthesized by alloying-dealloying mechanism

Maisa Azevedo Beluomini[1*], *Nelson Ramos Stradiotto*[1, 2], *Maria Valnice Boldrin*[1]

[1] Department of Analytical, Physical-Chemical and Inorganic Chemistry, Institute of Chemistry, São Paulo State University (UNESP), 14800-060, Araraquara, São Paulo State, Brazil.

[2] Bioenergy Research Institute (IPBEN), São Paulo State University (UNESP), 14800-060 Araraquara, São Paulo, Brazil.

*Corresponding Author: mabeluomini@gmail.com

ORCID: http://orcid.org/0000-0003-3441-1572

ABSTRACT

This paper reports the versatile preparation of three-dimensional nanostructured porous platinum (3DnpPt) directly on the surface of a screen-printed electrode via a simple electrochemical method and its application for the simultaneous voltammetric determination of hesperidin (HES) and narirutin (NAR) in residual water from the citrus industry. The surface morphology of the electrode was characterized by field-emission scanning electron microscopy (FEG-SEM), electron diffraction X-ray (EDX), X-ray photoelectron spectroscopy (XPS), and by the electrochemical impedance spectroscopic (EIS) technique. The results obtained from the voltammetric studies conducted showed that the sensor has good electrocatalytic activity and selectivity for HES and NAR oxidation. The linear scanning voltammetry (LSV) technique employed yielded linear ranges of 10 μmol L^{-1} to 0.4 mmol L^{-1} and 10 μmol L^{-1} to 0.5 mmol L^{-1}, with detection limits of 6.61 μmol L^{-1} and 0.21 μmol L^{-1}, and amperometric sensitivity of 0.52 A L mol^{-1} and 0.79 A L mol^{-1} for HES and NAR, respectively. The proposed 3DnpPt-SPE sensor also exhibited good repeatability and high selectivity, as well as long-term stability. The sensor was successfully applied in residual water sample for the simultaneous quantification of HES and NAR where good recovery rates were obtained.

KEYWORDS: Flavonoids; Nanoporous; Platinum; Screen-printed electrode; Electroanalysis.

Introduction

Yellow Water (YW) is the term given to the residual water produced by the orange industry and from the activities related to the distillation of orange juice and the production of essential oil. On average, an industrial plant used for the production of orange juice produces about 100,000 liters of YW daily [1]. The proper disposal of this massive amount of residue is one of the major concerns of citrus industries worldwide; this is largely due to the high polluting power of the compounds found in the residue. Citrus processing industries are commercially interested in recovering significant quantities of high value-adding compounds found in citrus fruits and in developing innovative products that are environmentally friendly [2]. Over the past few years, studies published in the literature have proposed alternatives to the re-utilization of yellow water; among these alternatives include the application of yellow water in bio-refineries, energy production (bioethanol and biogas) and in the extraction of compounds of interest, creating new job opportunities and economic benefits for all the stakeholders involved [3].

One of the most relevant classes of compounds present in yellow water is flavonoids; these compounds are highly potential agro-industrial organic substances. Flavonoids consist of an important group of polyphenolic compounds that is extensively distributed in the plant kingdom and which presents a great structural diversity in terms of biological activity. As shown in Scheme 1, hesperidin (3′,5,7-trihydroxy-4′-methoxy-flavanone-7-rhamnoglucoside) and narirutin (5,7,4'-trihidroxi-flavanona-7-β-rutinosideo) belong to the class of flavanones, which is among the extensive classes of flavonoids. Previous studies published in the literature have shown that hesperidin and narirutin - represented in the present study by the initials HES and NAR, have a wide range of good properties. HES and NAR have been found to have anticarcinogenic, antihypertensive, antiviral, antioxidant, antidiabetic, anti-obesity, hepatoprotective, and anti-inflammatory effects [4–6]; furthermore, the compounds have been found to have beneficial effects when applied in the therapy for the treatment of Alzheimer's disease [7]. In addition, the use of HES and NAR has sparked considerable interest among

researchers due to their strong antiviral activity against a wide range of viruses including the Herpes Simplex Virus (HSV-1 and HSV-2), the Human Immunodeficiency Virus (HIV), the Hepatitis C Virus, the Adenoviruses and Poliovirus type 2 (PV2), and, more recently, the Severe Acute Respiratory Syndrome Coronavirus 2 (SARS-CoV-2) [8–10].

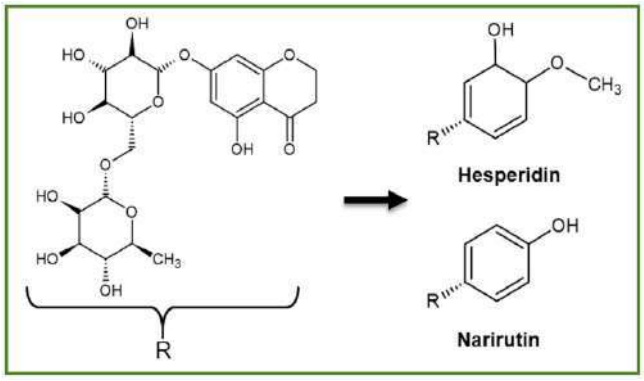

Scheme 1. Structural illustration of hesperidin and narirutin.

Considering the good chemical properties of HES and NAR, a wide range of analytical methods have been proposed in the literature for the determination of HES and NAR in different matrices including pharmaceutical formulations, biological fluids, citrus fruit peels and pulp, and juice, to name a few. The most widely applied methods for the determination of HES and NAR have included mainly chromatographic techniques[11–15]. Although these techniques offer high sensitivity, good selectivity, and low detection limits, they often require expensive and sophisticated instrumentation, long time of analysis, sample preparation, use of organic chemical solvents, and highly-trained personnel. These requirements have become obstacles to the wider application of chromatographic techniques.

Given the aforementioned requirements involving the use of chromatographic techniques, the use of electroanalytical techniques has sparked considerable interest among researchers over the past few years due to the fact that these methods involve relatively faster analysis time, apart from being relatively simpler and easier to perform; in addition, electroanalytical sensors can

also be used in miniaturized form with high degree of portability. However, one needs to point out that most of the electrochemical techniques reported in the literature have been based on mercury electrodes, unmodified carbon electrodes or carbon paste, and have mainly been confined to exploring the adsorptive property of HES; these techniques have also included an additional step (pre-concentration step) in the detection analysis where the molecule of interest is pre-concentrated on the electrode surface, and this has led to an increase in the time (duration) of analysis [16–19]. Also, a very limited number of studies in the literature have employed modified electrodes for HES determination [16,20–25]; to date, only one study has been reported for the electrochemical determination of NAR [22]. To the best of our knowledge, no study has been published in the literature regarding the simultaneous voltammetric determination of HES and NAR.

Thus, the objective of this study is to develop a voltammetric detection method that is sensitive, selective, portable, and easy to perform, as well as highly efficient for the simultaneous determination of HES and NAR. The proposed sensor was constructed using screen printed electrodes (SPEs). SPEs have become a suitable alternative material for the construction of substrates used in electroanalytical experiments; these electrodes have been found to eliminate the problems related to the use of conventional electrochemical cells with three electrodes and they do not require cleaning procedures once the electrodes are disposable after analysis. In addition, considering that the tools used for operating the SPEs are mostly portable and they require only a compact battery, this makes field analysis possible and easy to perform [26].

The modification of the surfaces of SPEs with nanomaterials including nanoparticles, carbon-based nanomaterials, magnetic nanoparticles, quantum dots, and nanoporous metals, offers outstanding advantages. Nanoporous (np) metals have a spongy morphology, and this provides them with notable surface area, larger active sites and lower density [27]. Additionally, building a three-dimensional nanoporous structure (3Dnp) can further improve the

electrochemical properties of an electrode, facilitating the diffusion process involving the electrode and the solution of interest, reducing pore clogging, and increasing the sensitivity of the sensor [28].

One of the metallic materials used for the nano-modification of electrodes is platinum; this material possesses high catalytic activity, large specific surface area, and good chemical stability [29]. Although platinum can be expensive to use, the construction of nanostructures using electrochemical techniques allows platinum to be reduced directly on the electrode in a single step and through the application of small amounts of analyte solution. Some nanoporous Pt-based sensors reported in the literature have been used for the non-enzymatic determination of glucose [30,31] and the selective sensing of hydrogen ions [32], glutamate [33], hydrogen [34], and hydrogen peroxide [35]. To the best of our knowledge, no studies published in the literature have combined the advantages of SPEs with those of three-dimensional nanostructured porous platinum (3DnpPt) to develop a sensitive and selective electrochemical sensor for the simultaneous determination of HES and NAR.

Bearing that in mind, this work sought to develop a 3DnpPt/SPE-based sensor for the simultaneous voltammetric determination of HES and NAR in yellow water. The nanoporous Pt was electrosynthesized directly on the surface of the SPE by cyclic voltammetry (CV); this facilitated the transfer of electrons during the oxidation of HES and NAR. The electrochemical method was developed by linear scanning voltammetry (LSV), and the results obtained showed that the proposed sensor has high sensitivity and good selectivity; furthermore, the method involves the application of low volume of solution and rapid analysis time. To prove the efficiency of the proposed method, the sensor was applied toward the analysis of real samples, and the results obtained were compared with those of the high-performance liquid chromatography-diode-array detector (HPLC-DAD) method.

2. Experimental

2.1.Reagents and apparatus

Hesperidin ($C_{28}H_{34}O_{15}$) ≥ 80%, Narirutin ≥ 98 % were obtained from Sigma – Aldrich Hexachloroplatinic acid hydrate (H_2PtCl_6), Sulphuric acid (H_2SO_4), potassium ferricyanide 99% ($K_3[Fe(CN)_6]$), potassium chloride 99 % (KCl), were purchased from Synth. Cyclic voltammetry, linear voltammetry and amperometry analyses were performed in a potentiostat Autolab PGSTAT30, with the aid of the Nova 2.0 software. The screen-printed electrodes (SPEs) were acquired from DropSens (DRP - C11L), which consisted of a carbon working surface (4.0 mm diameter), silver/silver chloride reference electrode, and carbon used as counter electrode.

Electrochemical impedance spectroscopic (EIS) experiments were conducted for the SPE and the npPt-SPE using a solution containing 5.0 mmol L^{-1} $Fe(CN)_6^{3-/4-}$ redox couple at the potential of 0.20 V and in the frequency range of 0.10 Hz to 100 kHz. The surface morphology of the modified sensor was characterized by field-emission scanning electron microscopy (FEG-SEM) using the microscope Jeol, model JSM 7500F), operated at 2 kV, coupled to an energy-dispersive X-ray spectroscopy (EDS) detector. The X-ray photoelectron spectroscopy analysis (XPS) was performed in a commercial spectrometer (UNI-SPECS UHV). The pressure inside the analyzer was maintained at 5.0×10^{-7} Pa using the Al Kα line (hν=1253.6 eV) with analyzer pass energy of 10 eV. The inelastic background spectra of C s, O1s, and Pt4f at electron core-level were subtracted using the Shirley's method. The composition (at. %) of the near surface region was determined using an accuracy of ± 5 % from the ratio of the relative peak areas corrected by Scofield's sensitivity factors of the corresponding elements. The spectra were deconvoluted using a Voigtian function, with Gaussian (70 %) and Lorentzian (30 %) combinations. The width at half maximum (FWHM) varied between 1.2 and 2.1 eV, and the accuracy of the peak positions was ± 0.1 eV.

2.2. Construction of the 3DnpPt-SPE

First, the SPE was activated via the application of several voltammetry cycles using 0.5 mol L^{-1} H_2SO_4 solution, with potential range of − 0.20 V to 1.2 V and scan rate of 100 mVs^{-1}, until a stable voltammogram was obtained. Nanoporous platinum was constructed using platinum-copper alloy in a solution containing 1.0 mmol L^{-1} H_2PtCl_4, 1.0 mmol $L^{-1}CuSO_4$, and 0.5 mol L^{-1} H_2SO_4. The electrodeposition process was conducted based on the application of 15 voltammetric cycles in the potential range of 1.4 V to − 0.40 V and at scan rate of 100 mVs^{-1}. During the application of the successive voltammetric cycles, the electrochemical deposition of the platinum-copper alloy was followed by the electrochemical dealloying of copper to obtain a nanoporous electrode with a high surface area.

2.3. Determination of the surface roughness of the nanoporous platinum electrode

The roughness of the dealloyed nanoporous platinum was evaluated by cyclic voltammetry (CV) using 0.5 mol L^{-1} H_2SO_4, with potential range of − 0.40 to 1.4 V and scan rate of 100 mV s^{-1}. The charge (μC) associated with the platinum oxide reduction peak area was divided by the conversion factor of 420 μC cm^{-2} [36], and the value of the real electrochemical area was obtained. The real electrochemical area was divided by the geometric area of the SPE (0.126 cm^2); this gave us the surface roughness factor (R*f*). The analysis of the surface roughness of the electrode enabled us to choose the best conditions for the formation of the nanoporous platinum.

2.4. Analytical measurements

The HES and NAR solutions were prepared in 50 % (*v/v*) acetonitrile: sulfuric acid solution (0.1 mol L^{-1}) and heated at 45 °C in an ultrasound bath for 20 min. The solutions were stored in dark bottles at 5°C until use. The electrochemical analysis was performed by cyclic voltammetry (CV) in the potential range of 0.0 - 1.0 V and at scan rate of 50 mV s^{-1}. The

analytical curve was obtained from the application of linear sweep voltammetry (LSV) in the potential range of 0.0 to 0.85 V and at scan rate of 50 mV s^{-1}.

2.5. Sample preparation

The yellow water (YW) sample was acquired from an orange industry in the city of Matão, São Paulo, Brazil. The sample was centrifuged at 3000 rpm for 15 min to remove any solid particles. The supernatants were filtered using filters with 0.47 and 0.22 μm filter; the fluids were then kept frozen until use. The sample was diluted 2.5 times in 0.1 mol L^{-1} H_2SO_4, and the sample solution was used for the simultaneous determination of HES and NAR. The concentrations of each compound (HES and NAR) in the YW sample were determined by the standard addition method. The recovery experiment was performed with the addition of known concentrations of the standard molecule of each compound in the sample. The measurements were performed three times.

2.6. Chromatographic analysis

For comparison purposes, the contents of HES and NAR in the yellow water sample was examined by the HPLC-DAD technique; this analysis was performed in order to compare the results obtained from the application of the proposed technique with those of the HPLC-DAD technique. The chromatographic analysis was performed using Shimadzu UV-1800 spectrophotometer based on a technique similar to the one described by Barfi et al., [37]. Chromatographic separations were performed using a Kinetex® 5u C18 100 Å, with column of 150 × 4.6 mm, temperature of 35˚C, and flow rate of 1 ml min^{-1}. The wavelength was kept at 280 nm. The separation of the four main flavonoids found in the sample (hesperdin, naringin, narirutin and naringenin) was performed by gradient elution, using water (eluent A) and acetonitrile containing 0.1% formic acid (eluent B). The conditions of the gradient elution were

as follows: 0 - 0.01 min, 80 % A – 20 % B; 0.01 - 10 min, 50 % A – 50 % B. Prior to being injected into the system, the mobile phase was filtered with 0.45 and 0.22 µm membrane filters and degassed in an ultrasound bath. The injected volume applied was 50 µL. Figure S1 shows the chromatograms obtained for the standard molecules and Figure S2 shows the chromatogram obtained for the yellow water sample. The analytical curves for HES and NAR can be found in Figure S3 and the data related to the chromatographic analysis are presented in Table S1, with the amount of concentration found for HES and NAR in the sample. For additional information on how the chromatographic analyses were carried out, please consult the supplementary material.

3. Results and discussion

3.1. Formation and characterization of the nanoporous platinum on the SPE

The formation of nanopores through the difference in chemical potential between the chemical elements of the alloy only occurs due to the selective corrosion of the less noble component of the alloy. The dealloying process was conducted via the electrodeposition of the Pt-Cu alloy on the surface of the SPE using successive CVs in a solution containing 1.0×10^{-3} mol L^{-1} H_2PtCl_6 and 1.0×10^{-3} mol L^{-1} $CuSO_4$ in 0.5 mol L^{-1} H_2SO_4, under the potential range of 1.2 to -0.60 V and at scan rate of 100 mV s^{-1}. For each cycle, a Pt-Cu film was electrodeposited on the SPE during the cathodic scan. When the voltammetric cycle was reversed, in the direction of the anodic scan, Cu was dissolved from the alloy, leading to the formation of nanoporous Pt.

The CVs presented in Figure 1A show the response of the SPE in a solution containing $CuSO_4$ (black curve), H_2PtCl_6 (blue curve), and $CuSO_4$ + H_2PtCl_6 (red curve). With regard to the curve related to Cu, one can observe the presence of two peaks; one peak at approximately -0.18 V, corresponding to Cu oxidation, and the other one at approximately -0.40 V, where Cu

reduction occurs. The curves related to Pt display peaks in the region between -0.10 and 0.10 V, which are attributed to hydrogen adsorption and desorption [35]. Pt oxidation occurs (Pt-OH) at potentials greater than 0.30 V and oxide reduction occurs in the cathodic scan (~ 0.20 V). The cyclic voltammetry in Figure 1B shows the presence of a reduction peak in the cathodic scan (Pa), which is attributed to the co-deposition of the Pt-Cu alloy on the SPE. The peak observed in the anodic scan (Pb) is attributed to dealloying or dissolution of the Cu - the less noble metal of the Pt-Cu alloy. During each CV, a layer of Pt-Cu alloy was electrodeposited during the cathodic scan and copper was dissolved from the alloy during the anodic scan. This resulted in the formation of the nanoporous platinum structure on the SPE. It should be noted that the number of voltammetric cycles applied is related to the growth, shape and structure of the nanopores, and these factors directly affect the surface roughness. Thus, the influence of the number of cycles on the formation of the 3DnpPt-SPE was studied in the cycle range of 5 - 25. After electrodeposition, the electrodes were subjected to successive CVs in 0.5 mol L^{-1} H_2SO_4 using the potential range of −0.40 to 1.4 V and scan rate of 100 mV s^{-1}, until the current was stabilized. The charge (μC) associated with the area of the platinum oxide reduction peak (Figure 1C) was divided by a conversion factor of 420 μC cm^{-2}. The value obtained (electrochemical area) was divided by the geometric area, and this yielded the surface roughness factor (R*f*). The R*f* calculation procedure is applied when the metal investigated has a well-defined region in the CV related to the formation and reduction of its oxide monolayer, as is the case of Pt. Thus, this factor is considered a good indicator of surface roughness. The R*f* obtained varied from 7, for the electrode subjected to 8 voltammetric cycles, to 24, for the electrode subjected to 15 voltammetric cycles (Figure 1D). There was an increase in the surface roughness of the electrode up to 15 voltammetric cycles. After that, a decrease in Rf was observed; the decline in R*f* may be attributed to the formation of a thicker layer, which may have affected the dealloying of the copper and caused a reduction in the surface roughness. Thus, considering that the application of

15 voltammetric cycles for the construction of the 3DnpPt-SPE resulted in a larger surface area, this number of cycles was chosen for the analysis of the flavonoids.

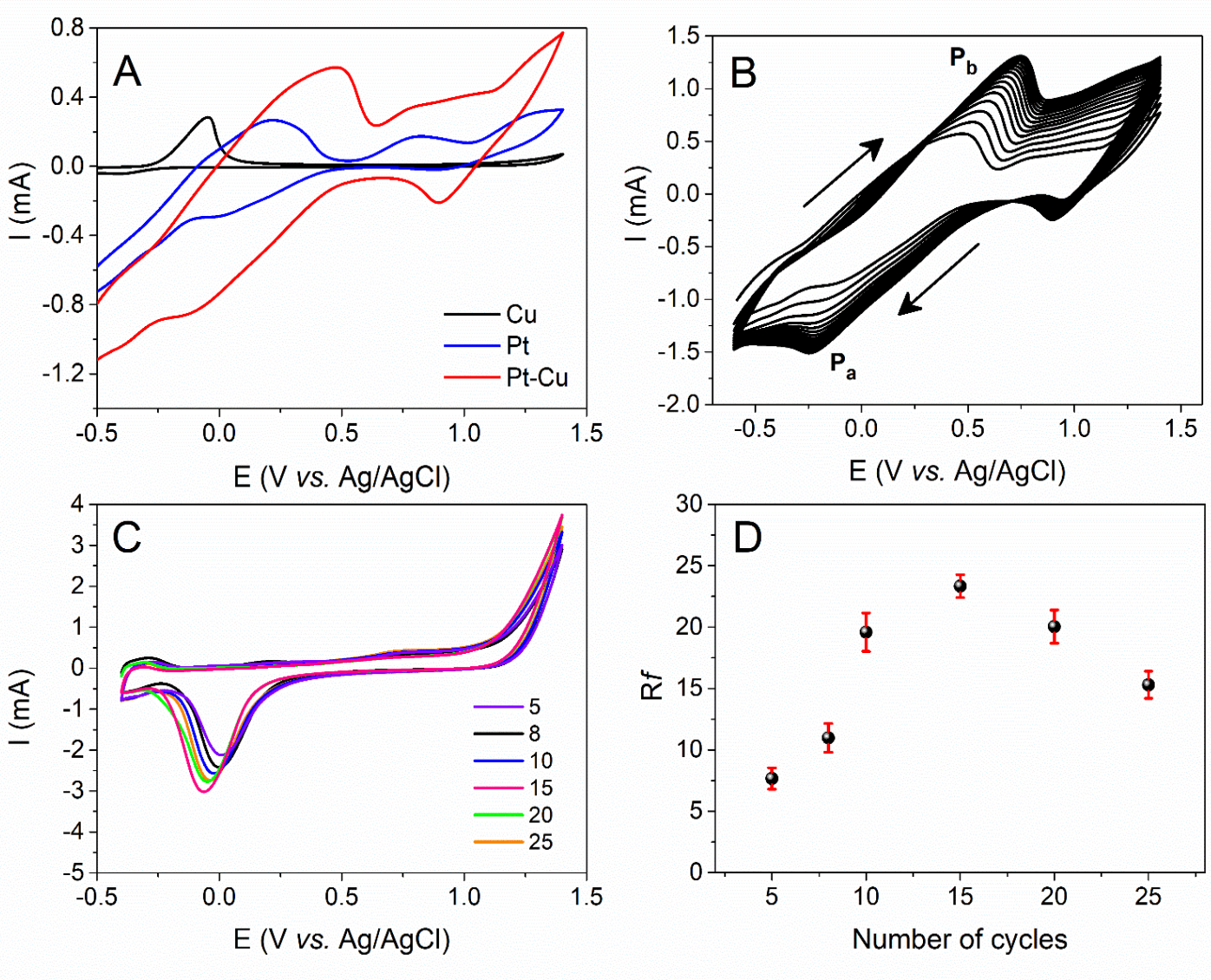

Figure 1. (A) CVs for Cu, Pt and Pt-Cu alloy in 0.5 mol L^{-1} H_2SO_4, at scan rate (υ) = 50 mV s^{-1}. (B) Successive CVs during the electrodeposition of Pt-Cu on the SPE. (C) CVs of 3DnpPt-SPE in 0.5 mol L^{-1} H_2SO_4, at scan rate of 100 mV s^{-1}. (D) Plot of surface roughness factor, R*f,* of the modified electrode in relation to the number of voltammetric cycles applied for the Pt-Cu alloy.

The surface morphology of the 3DnpPt-SPE was analyzed by scanning electron microscopy (SEM). Figures 2A and 2B show the surface morphology of the nanoporous Pt with 1 µm and 100 nm of magnification; looking at the figures, one will notice the presence of

clusters of Pt nanoparticles which were electrodeposited on the SPE. The spaces between the nanometer clusters of Pt may be related to the Cu ions which were dissolved from the structure, leading to the formation of gaps in the structure. Figure 2C shows the graph related to the respective EDS, which confirms the presence of large amounts of Pt compared to Cu (which remained in small quantity in the structure).

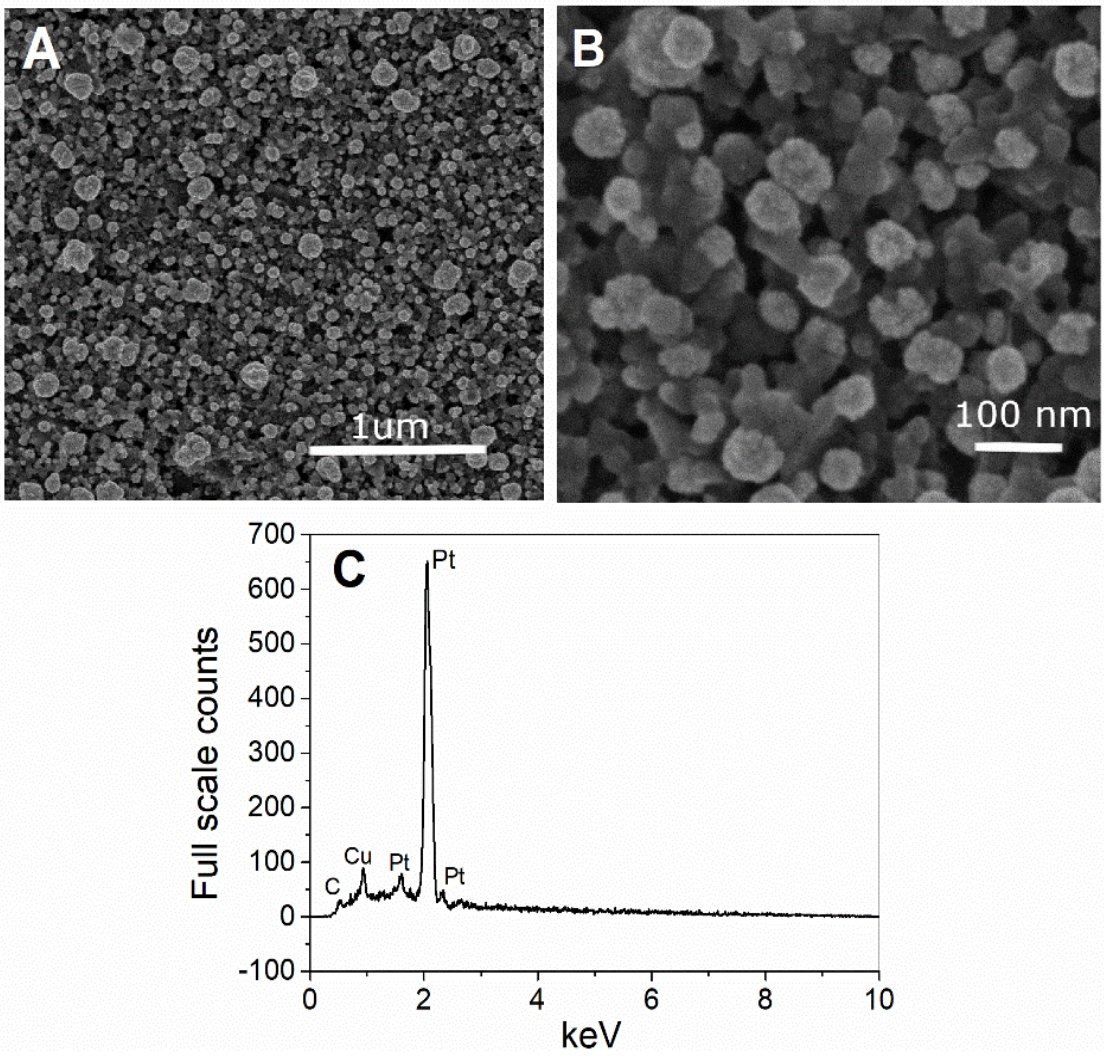

Figure 2. SEM images obtained for the 3DnpPt-SPE with 50 000 x (A) and 100 000 x (B) of magnification, in (C) respective EDS related to image A.

To gain a better understanding of the Pt deposition process, XPS analyses were carried out on SPE modified with 3DnpPt, as shown in Figure 3. The high-resolution C1s spectrum were

deconvoluted into five components; these corresponded to carbon atoms in different functional groups with binding energies of 285.4 (C-H), 286.3 (C-O), 287.9 (C=O), and 289.0 (O-C=O) eV. The oxygen spectra were monitored by the O1s signal; these spectra were deconvoluted into four components which corresponded to oxygen atoms in different functional groups with binding energies of 531.4 (C=O and -OH), 532.3 (CO), 533.6 (O-C=O), and 530.7 (O-Pt) eV. The XPS spectra of Pt, the peaks related to Pt4f7/2 and Pt4f5/2 electrons, can be found at 71.2 and 74.3 eV, respectively; this shows that Pt on the SPE surface has zero valence [36]. $Pt(OH)_2$4f7/2 and $Pt(OH)_2$4f5/2 groups can be observed at 72.3 and 75.7 eV, respectively, and the signals at 73.7 and 77.1 eV are linked to the $PtO_2$4f7/2 and $PtO_2$4f5/2 groups.

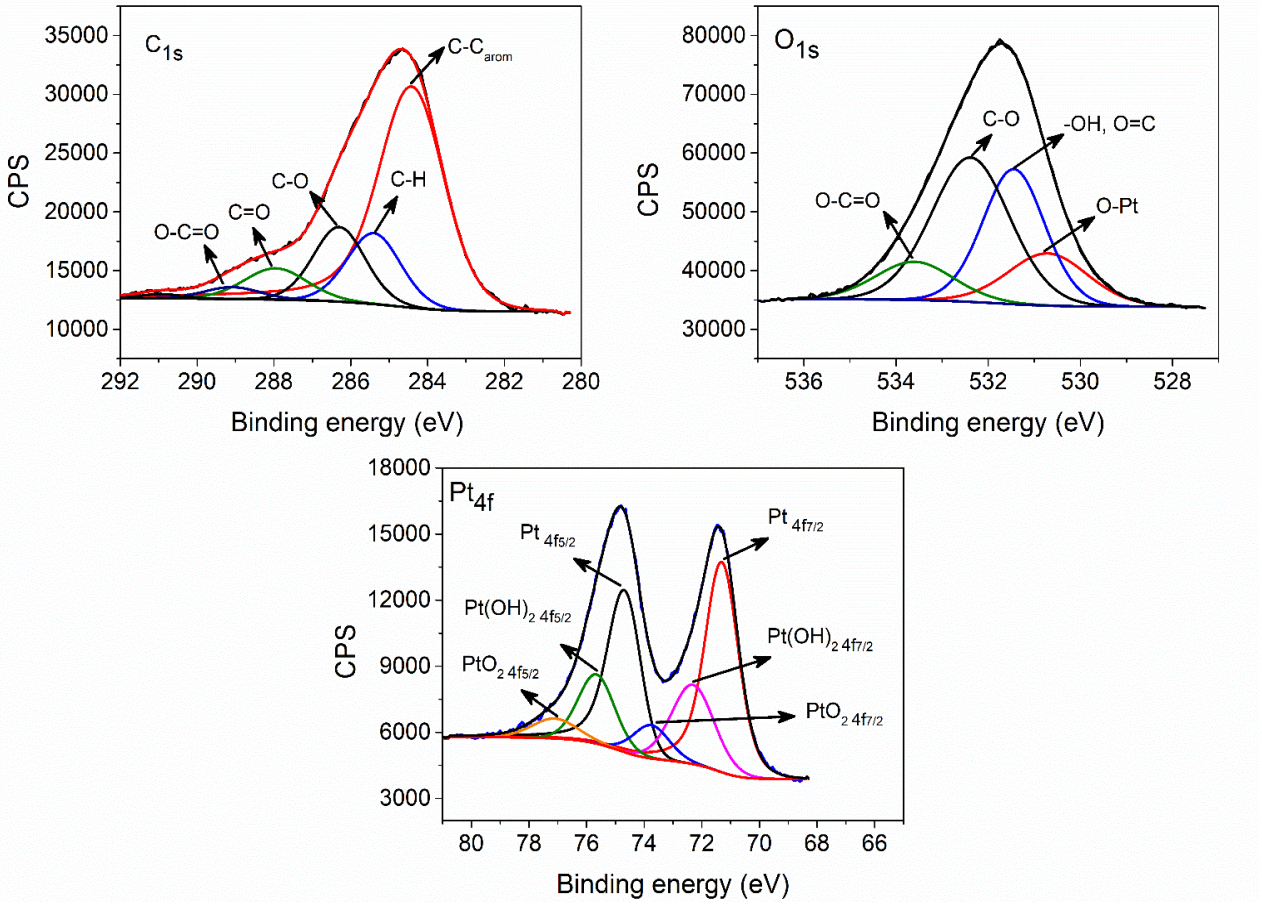

Figure 3. Deconvoluted C1s, O1s, Pt 4f XPS spectra of the 3DnpPt-SPE.

To study the electrochemical characteristics of the proposed sensor, EIS measurements were performed in the frequency range of 0.10 Hz to 100 kHz using a solution containing 5.0

mmol L^{-1} $[Fe(CN)_6]^{3-/4-}$ in 0.10 mol L^{-1} KCl as the electrochemical probe to monitor the electron transfer resistance at the 3DnpPt-SPE interface. $[Fe(CN)_6]^{3-/4-}$ was used as redox probe for the conduct of this analysis because it is an inner-sphere redox probe and the electron transfer can be affected by surface interactions and electronic factors. The equivalent Randles circuit was used to fit the data obtained by the Nyquist diagram and it is presented in the top-left inset of the Figure 4. In this circuit R_i stands for the solution resistance, C_{dl} being the constant phase element which is related to the double-layer capacitance, R_{ct} representing the charge-transfer resistance and the diffusion related process is represented by a Warburg (W). As can be observed in Figure 4, the Nyquist graph for the SPE (curve a) shows a semi-circle with R_{ct} of 2.4 kΩ. After modifying the surface of the SPE with the 3DnpPt (curve b), the R_{ct} decreased approximately 3.6 times, reaching the value of 663 Ω. These results show that the nanoporous platinum acted as an excellent mediator in the electron transfer process.

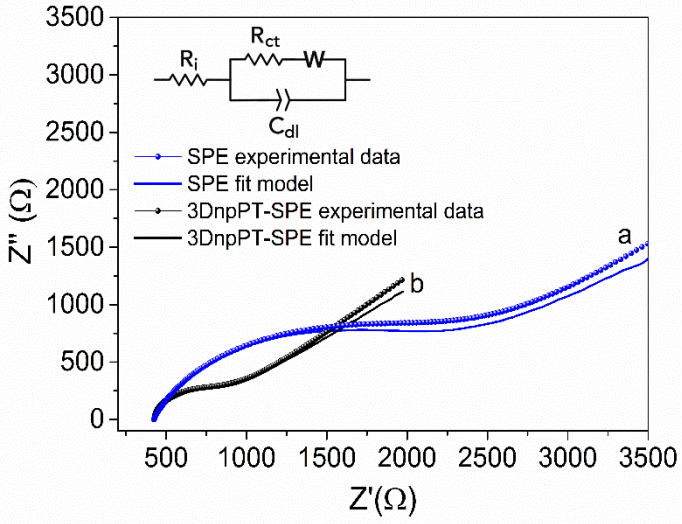

Figure 4. Nyquist plot obtained for (a) SPE (b) 3DnpPt-SPE applied in 5.0 mmol L^{-1} Fe $(CN)_6^{3-/4-}$ in 0.1 mol L^{-1} KCl in the frequency range of 0.1 Hz - 100 kHz; the curved line is a fit to the data, using the equivalent circuit, shown above the plot.

3.2. Electrochemical response of HES and NAR

The molecules of HES and NAR can be found to be structurally similar, and these molecules are characterized by the presence of two benzene rings which are linked by a pyran ring, as can be seen in Scheme 1. The binding of the electroactive hydroxyl group to these benzene rings makes the HES and NAR molecules bioactive, and this allows the molecules to be detected via the application of electrochemical techniques.

The electrochemical behavior of 0.2 mmol L^{-1} of HES, 0.2 mmol L^{-1} of NAR, and 0.2 mmol L^{-1} of both HES and NAR in 0.1 mol L^{-1} H_2SO_4 was analyzed by CV on the unmodified SPE and the 3DnpPt-SPE. Looking at the first scan of the oxidative region in Figure 5A, one will observe the presence of a peak at 0.46 V (P_1). When one looks at the reverse scan region, one notices the presence of a reductive wave at 0.22 V (P_2). In the second scan, one notices the presence of a new peak (P_3) in the oxidative region of 0.25 V with a decrease in the intensity of P_1. Based on this observation, it is reasonable to say that P_1 (system I) is an irreversible anodic peak and P_2/P_3 (system II) is a redox pair derived from the oxidation product of P_1.These findings are similar to those observed by Sims et al.,[23] and Manasa et al., [24] who pointed out that the oxidation of HES on carbon electrodes occurs according to the ECirrevE mechanism. The first peak observed on the SPE is typically characteristic of the irreversible electrochemical oxidation of the guaiacol unit of the HES molecule, with the formation of the almost reversible o-benzoquinone/catechol pair. The modification of the SPE with 3DnpPt led to an increase in the intensity of the currents but without the displacement of the peaks. The P_1 current increased about 2.5 times, while the currents of P_2 and P_3 increased 2.0 and 1.4 times, respectively; these results can be attributed to the greater surface area of the nanoporous Pt structure. Figure 5B shows the CV obtained for NAR on the SPE and 3DnpPt-SPE. One will observe the presence of an anodic peak at the potential of 0.72 V. The analysis of the reverse scan did not show the presence of any peaks, and this implies that the oxidation process of narirutin is irreversible; this result is in good agreement with the data previously reported in the literature [22]. A

comparative analysis of the SPE and the 3DnpPt-SPE showed that the latter exhibited a peak current 2.2 times higher than the former; this confirms that the greater porosity of the surface resulted in the electrocatalytic activity of NAR. Figure 5C shows the CVs obtained for a solution containing both HES and NAR applied on the SPE and the 3DnpPt-SPE. A comparison of the individual voltammetric response of HES and NAR with that of the blended solution containing HES and NAR showed that they exhibited similar electrochemical behavior; in other words, the individual response of HES and NAR was similar to that of the blended solution of HER and NAR. These results show that the 3DnpPt-SPE can be used for the simultaneous determination of HES and NAR with better sensitivity than the SPE. The sensor proposed in this work (3DnpPt-SPE) is the first sensing device reported in the literature for the simultaneous determination of HES and NAR.

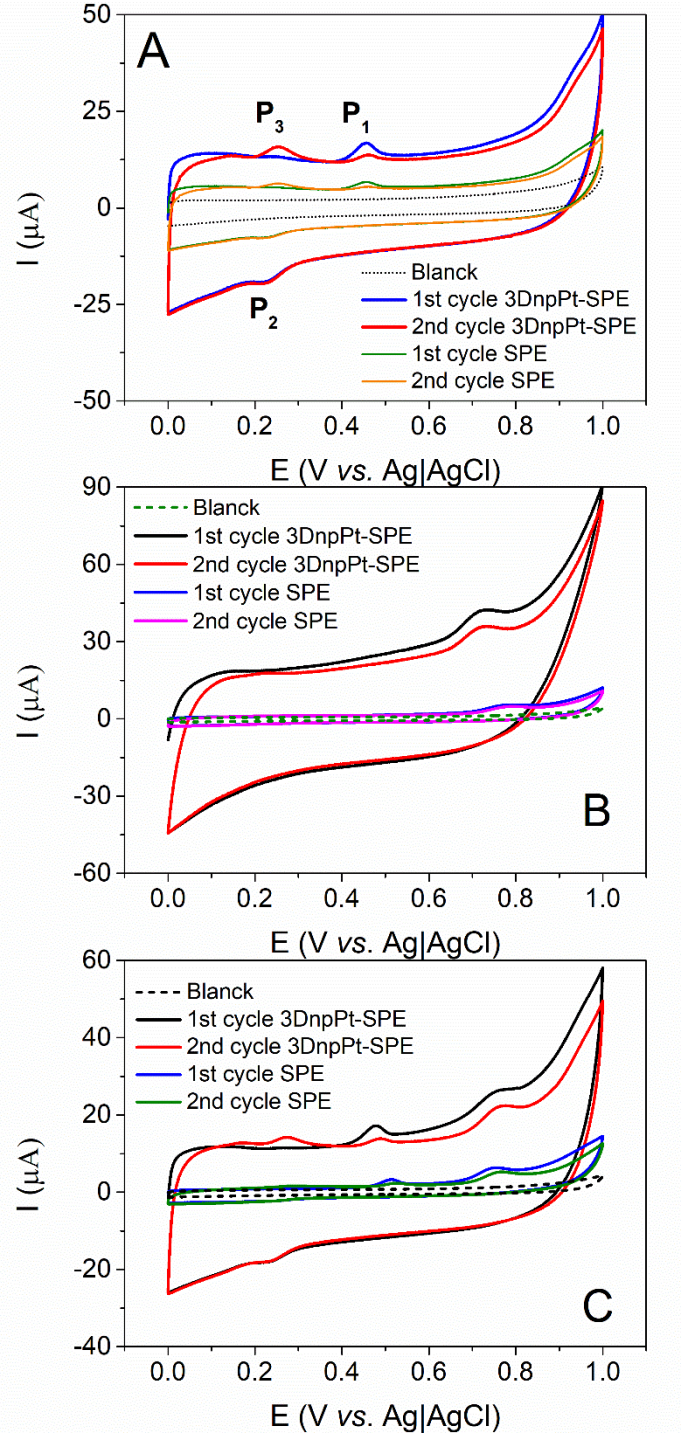

Figure 5. CVs obtained for 0.2 mmol L^{-1} (A) HES, (B) NAR, and (C) HES and NAR applied in 0.1 mol L^{-1} H_2SO_4, analyzed on SPE and 3DnpPt-SPE.

3.3. Effect of scan rate

The effect of scan rate on the electrochemical behavior of HES and NAR was also studied by cyclic voltammetry using 0.2 mmol L^{-1} of a mixture of HES and NAR in 0.1 mol L^{-1}

H_2SO_4. Figure S4 shows the CVs obtained at different scan rates ranging between 10 and 250 mVs^{-1}. Looking at the CVs, one will observe that both molecules exhibited a shift in oxidation peak potential to more positive potentials when the scan rate was increased; this points to the kinetic limitation of the electrochemical reaction [38]. Also, the plotting of the peak height (I) *vs*. scan rate (ν) (Figure S5) showed the existence of a linear relationship between them; this shows that that the process is adsorption-controlled. These results are in line with the results reported by a number of studies published in the literature involving the use of the nanoporous Pt-based electrodes [22,23,39]. A further point worth mentioning is that nanoporous Pt electrodes have previously demonstrated their ability to increase kinetically slow heterogeneous faradaic reactions [28,40]. Thus, since HES and NAR do not exhibit electrode reactions that are fast enough to be controlled by diffusion, the 3DnpPt-SPE sensor plays an important role in the determination of these molecules.

3.4. Simultaneous determination of hesperidin and narirutin

To demonstrate the applicability of the 3DnpPt-SPE for the determination of HES and NAR, initially, each of the two analytes was determined by keeping the concentration of one of them constant in a solution containing 0.1 mol L^{-1} H_2SO_4 using the LSV technique. Thus, for the construction of the analytical curve for HES, the concentration of NAR was kept constant at the concentration of 50 μmol L^{-1}. Figure 6A shows that the P_3 oxidation current for HES exhibited the best voltammetric profile and linearity as the compound concentration was increased and even in conditions in which NAR concentration was fixed (in which the peak oxidation current remained fairly constant). Since the P_3 was formed after the generation of P_1, as discussed in section 3.2, the peak current shown in Figure 6A corresponded to the previously added concentration. In essence, the P_3 current increased linearly with an increase in concentration in the range of 10 μmol L^{-1} to 0.4mmol L^{-1} (R = 0.9989). The corresponding linear regression

equation was $I_{HES3}(\mu A) = 19082.40\ C_{hes3} + 0.52$ (R = 0.9977) (Figure 6A') and the relative standard deviation (RSD) value obtained for the slope was 3.9 %. The limit of detection (LOD) was 6.61µmol L^{-1}, and the analytical sensitivity (As) was 0.52 A L mol^{-1} (n = 3). Likewise, the peak current of NAR increased linearly with an increase in concentration in the range of 10 µmol L^{-1} to 0.5 mmol L^{-1}(Figure 6B), and even in the presence of 50 µmol L^{-1} HES. The linear regression equation was $I_{NAR}(\mu A) = 18143.30\ C_{NAR} + 0.79$ (R = 0.9977) (see Figure 6B'), and the relative standard deviation (RSD) value obtained for the slope was 6.1 %. The LOD obtained was 0.21 µmol L^{-1} and the As was 0.79 A L mol^{-1} (n = 3).

The simultaneous detection analysis was performed using HES and NAR concentrations ranging between 20 µmol L^{-1} to 0.4 mmol L^{-1}, as can be observed in Figure 6C. The results obtained showed that a simultaneous increase in the concentration of HES and NAR led to a linear increase in the oxidation peak currents for P_{HES3} and P_{NAR}. The linear regression equation and RSD obtained for HES and NAR were as follows: $I_{HES3}(\mu A) = 14245.80\ C_{HESP3} + 0.87$ (R= 0.9979), with RSD of 7.6 % for the slope; and $I_{NAR}(\mu A) = 34433.90\ C_{NAR} + 0.06$ (R=0.9989), with RSD of 6.3 % for the slope (see Figure 6C'). It is worth noting that when these results were compared with the ones obtained from the individual determination of HES and NAR, the slopes were found to be of the same magnitude, with RSD of 14.5 % for HES and 20.3 % for NAR. These results show that the oxidation of HES on the 3DnpPt-SPE did not interfere in the quantification of NAR or *vice versa*. Thus, one can say that the detection processes are independent, and one can use the proposed sensor to simultaneously determine HES and NAR without experiencing any interferences; in addition, the sensor is also found to have good sensitivity.

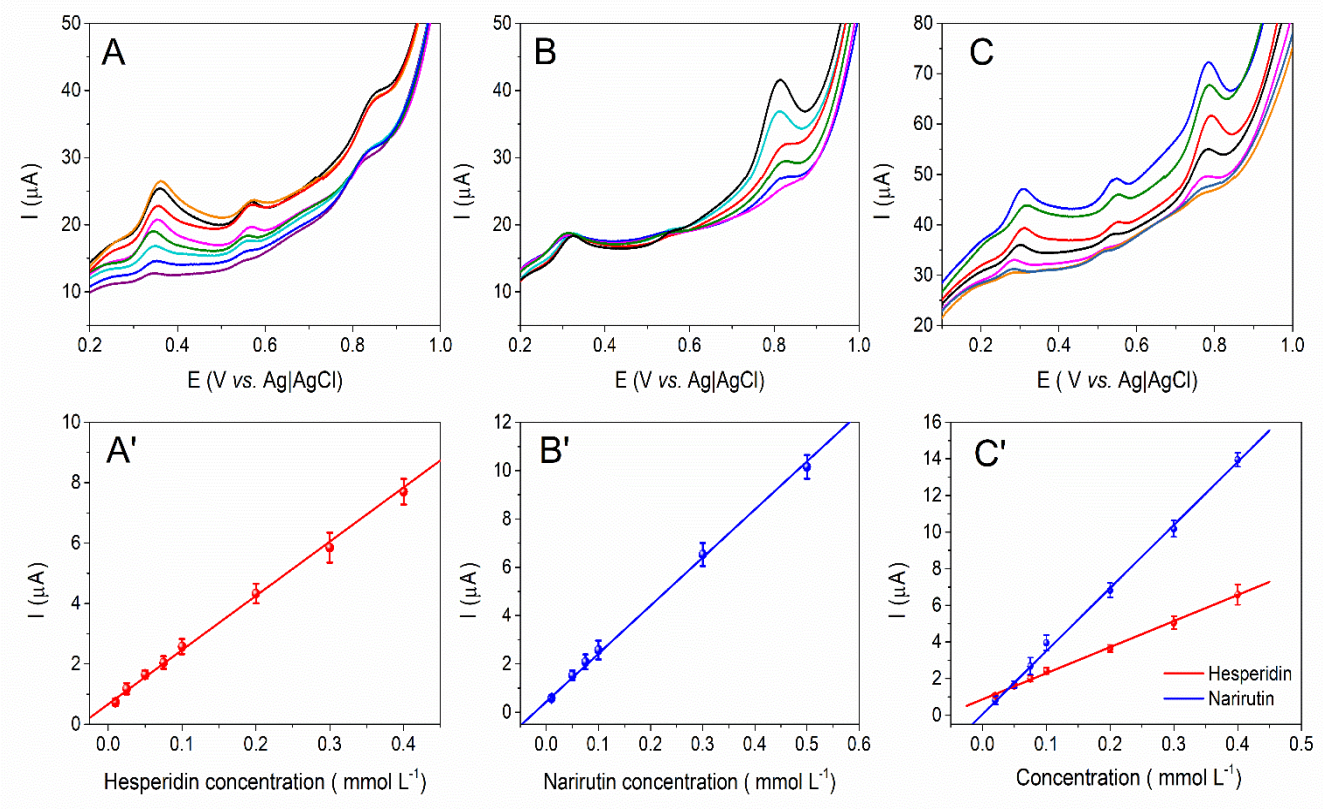

Figure 6. Linear sweep voltammetry obtained for 3DnpPt-SPE applied in 0.1 mol L^{-1} H_2SO_4 (A) in the presence of 50 µmol L^{-1} of NAR and different concentrations of HES (10 µmol L^{-1} to 0.4 mmol L^{-1}). (B) In the presence of 50 µmol L^{-1} of HES and different concentrations of NAR (ranging from 10 µmol L^{-1} to 0.5 mmol L^{-1}). (C) In different concentrations of HES and NAR (ranging from 20 µmol L^{-1} to 0.4 mmol L^{-1}). A', B' and C' shows the calibration plots of the peak currents vs. concentrations of HES, NAR, and solution containing a mixture of HES and NAR, respectively.

Taking into account the electrochemical technique, linear range and detection limits for HES and NAR, the results obtained from the comparative assessment of the analytical performance of 3DnpPt-SPE and other previously reported electrodes are shown in Table 1. One will notice that although Gao et al., [20] Sun et al., [21] Zhupanovaat et al., [25] and Manasa et al., [18] have reported good results, they employed far more steps to construct their proposed electrodes. Also, in some studies, the energy applied for the oxidation of HES was much higher: 0.65 V [18]; 0.91 V [17]; and 1.21 V [20]. Another interesting study that deserves mentioning is the one conducted by Temerk et al., [19] in this study, the authors employed hanging drop mercury electrode (HDME) for the reduction of HES using square wave cathodic adsorptive

voltammetry (SW-CASV). However, this type of electrode (HDME) is no longer used due to its high degree of toxicity. In addition, most of the analytical methods reported in the literature use the AdSV and CASV technique [17,19,23] or the DPV approach with pre-concentration of the solutions of interest [17]; these techniques require the application of an accumulation time, which, consequently, increases the analysis time. The aforementioned disadvantages of the previously reported techniques make our proposed technique comparably better. The LSV technique employed in this present study is fast and simple; the approach leads to the construction of a portable, practical, and viable detection platform. In addition, our proposed sensor is suitable and highly efficient for the simultaneous determination of HES and NAR. To date, there have been no reports in the literature regarding the development and application of a sensing platform capable of simultaneously determining HES and NAR. Another important point to consider is that in sample solutions such as orange juice, citrus fruit residues, and pharmaceutical formulations, the amount of HES and NAR found in these solutions was in the order of μM to mM; this shows that one does not need to employ analytical methods with very low values of LOD when one seeks to determine these molecules. In short, the outstanding advantages of the proposed 3DnpPt-SPE are as follows: i) ease of electrode preparation - involving a single, quick electrochemical step; ii) the sensor is capable of conducting simultaneous detection – this demonstrates the versatility of the device; ii) the technique involves a simple detection mechanism; iv) the sensor provides sensitive and selective analytical response; and v) the technique involves the use of low volume of solution (50 μL).

Table 1. Comparative analysis of merit figures obtained for the 3DnpPt-SPE-based method and other electroanalytical methods previously reported in the literature used for the determination of HES and NAR.

Electrode	Techinique	Analyte	Linear range (µM)	LOD (nM)	Ref.
3DnpPt-SPE	LSV	HES	10 – 400	6610	This work
		NAR	10 – 500	210	
AuNPs/rGO/GCE	AMP	HES	0.05–8.0	8.2	[20]
Mesoporous SiO_2-modified CPE	DPV	HES	0.5 – 25	250	[16]
MIP/AuNPs/UAC@GCE	DPV	HES	0.08–30.0	45	[21]
BDD	SW-AdSV	HES	4.1–120.0	120.0	[17]
3DnpNi/SPE	DPV	NAR	0.1 – 10	39	[22]
ePGE	DPV	HES	0.5 –10	200	[18]
MWCNT-BPPGE	SW-AdSV	HES	0.02–0.4	7.3	[23]
			0.4–30.0		
	CV-AdSV		0.5–15.0	610.0	
			15.0–40.0		
HMDE	SW-CASV	HES	0.019–0.654	7.54	[19]
nGp-Bg/MCPE	DPV	HES	0.1–7.0	50.0	[24]
			7.0–100.0		
Polyaluminon/f-SWCNT/GCE	DPV	HES	0.10–0.25	29.0	[25]

Abbreviations: AMP: Amperometry; DPV: Differential Pulse Voltammetry; SW-AdSV: Square-Wave Adsorptive Stripping Voltammetric; CV-AdSV: Cyclic voltammetric adsorptive voltammetry; SWCASV: Square wave cathodic adsorptive voltammetry; AuNPs/rGO/GCE: gold nanoparticles, reduced graphene oxide and modified glassy carbon electrode; CPE: carbon paste electrode; MIP/AuNPs/UAC@GCE: molecularly imprinted gold ultrafine activated carbon on glassy carbon electrode; BDD: Boron doped diamond; 3DnpNi/SPE: three-dimensional nanostructured porous nickel on screen-printed electrode; ePGE: pencil graphite electrode; MWCNT-BPPGE: Multiwalled carbon nanotube-Basal-Plane Pyrolytic graphite electrode; HMDE: hanging mercury dropping electrode; nGp-Bg/MCPE: nano-Graphene-platelets and π-e- of cationic Brilliant green on modified carbon paste electrode; Polyaluminon/f-SWCNT/GCE: polyaluminon/functionalized-single-walled carbon nanotubes/GCE.

3.5. Repeatability and stability

The stability of the 3DnpPt-SPE was evaluated by LSV using a solution containing 0.1 mmol L^{-1} HES and NAR in 0.1 mol L^{-1} H_2SO_4 for 7 days; one measurement was performed each day (when not in use, the electrode was stored at room temperature). At the end of the 7-day analysis period, the current still retained 82.1 % of its initial value for HES (P_3) and 89.8 % for NAR; this shows that the proposed electrode has good stability. To evaluate the inter-electrode repeatability, three electrodes were independently prepared under the same conditions; the electrodes were used to detect 0.1 mmol L^{-1} of HES and NAR, as shown in Figure S6 (n = 3). The average oxidation current values obtained for peak P_3 corresponding to HES and NAR were 2.4 µA and 4.3 µA, with RSD of 2.3 % and 5.7 %, respectively. These results show that the proposed 3DnpPt-SPE has satisfactory repeatability and long-term stability.

3.6. Selectivity

To study the selectivity of 3DnpPt-SPE, the voltammetric responses were analyzed in the presence of other species such as fructose, glucose, arabinose, naringenin, and ascorbic acid in the concentration of 0.1 mmol L^{-1}. The current signals obtained by LSV were compared in the absence and presence of these molecules.

For a molecule to be considered an interferent in the analysis, the change in current should not be ≤ ± 5.0 % (tolerance limit) of the current response of HES and NAR. Based on the results obtained from the LSV experiments (see Figure S7), the analysis of 0.2 mmol L^{-1} mixture of HES and NAR in the presence of the same amount of fructose (Figure S7A), glucose (Figure S7B) and arabinose (Figure S7C) showed that these molecules played no interfering role in the recognition of HES and NAR. When naringenin was added, an increase of 292.6 % was observed in the P_1 current of HES (Figure S7D). The P_2 and P_3 peaks exhibited a current increase of 1.2 % and 4.9 %, respectively. In the presence of ascorbic acid, the peak current related to P_1 recorded a marked decrease of 66.9 %; the P_2 and P_3 peak currents did not record any significant changes – the peak currents exhibited a current oscillation of 2.19% and 4.9 %, respectively. The results obtained suggest that the proposed sensor has good selectivity when applied toward the simultaneous determination of HES and NAR using peaks P_2 and P_3; these peaks showed the best linearity during the study of the analytical performance of the sensor.

3.7. Real sample analysis

In order to evaluate the analytical applicability of the proposed method, a sample of yellow water collected from the orange industry was used to investigate the applicability of the proposed 3DnpPt-SPE-based method for the simultaneous determination of HES and NAR. Prior to performing the analysis, the sample was diluted 2.5 times with 0.1 mol L^{-1} H_2SO_4. The LSV technique and the standard addition method were used for the conduct of the analysis. The sample was spiked with known concentrations of standard HES and NAR in the range of 0.075 to 0.2 mmol L^{-1}. Using the standard addition curve and the extrapolation of the straight line approach (Figure S8) (taking into account the dilution of the sample), the concentrations of HES and NAR found in the yellow water sample were $17.4 \pm 0.11 \times 10^{-5}$ mol L^{-1} and 81.8 ± 0.99 µmol L^{-1} (n = 3), respectively. As shown in Table 2, the recovery percentages obtained ranged

from 98.2 % to 102.0 %, and from 95.0 % to 103.8 % for HES and NAR, respectively. These results demonstrate that the 3DnpPt-SPE presents an excellent degree of accuracy in real sample analysis.

Student's *t-test* and *F-test* were used to conduct a comparative statistical analysis of the mean values obtained for the concentrations of HES and NAR present in the sample by the HPLC method and by the method proposed in this work. The results obtained in this analysis (see Table 3), with 95 % confidence level, showed that the calculated values related to *F* and *t-test* were lower than the critical values; in other words, there was no significant statistical difference between the methods. Based on these findings, one can conclude that the proposed 3DnpPt-SPE based method is highly reliable for the analysis of HES and NAR in a sample of yellow water; the method yields results that are similar to the HPLC method.

Table 2. Determination of HES and NAR in yellow water samples (n=3).

Analyte	Added (mmol L^{-1})	Found (mmol L^{-1})	Recovery (%)	RSD (%)
HES	0.075	0.065 ± 0.006	87.1	0.86
	0.10	0.091 ± 0.024	90.5	2.65
	0.20	0.208 ± 0.014	104.0	0.68
NAR	0.075	0.068 ± 0.003	90.7	0.42
	0.10	0.091 ± 0.17	91.7	1.85
	0.20	0.207 ± 0.007	103.2	0.34

Table 3. Values obtained from the comparative statistical analysis (using student-*t* and *F*) of the HPLC/DAD method and the proposed LSV method used for the determination of HES and NAR in yellow water samples (n = 3).

Analyte	Method	Mean (10^{-5} mol L^{-1})	Variance	*F-test*		*t-test*	
				Calculated	[a]Critical	Calculated	[b]Critical
HES	HPLC	17.6	0.00013	0.89	19.0	0.22	4.3
	LSV	17.4	0.0056				
NAR	HPLC	8.55	0.061	0.99	19.0	0.039	4.3
	LSV	8.54	0.28				

[a]$F_{critical}$: reported F value from *F-test* table with 95 % confidence level and 2/2 degrees of freedom.
[b]$t_{critical}$: reported t value from Student *t-test* table with 95 % confidence level.

4. Conclusion

The present work reported the development of 3DnpPt-SPE, based on a direct, fast, and fully efficient electrochemical method, and its successful application for the electrooxidation of HES and NAR. Compared to the unmodified SPE, the modified SPE electrode improved the electron transfer efficiency and the electrocatalytic activity of both HES and NAR. Being the first electrochemical sensor used for the simultaneous determination of HES and NAR, the sensor developed in this study exhibited excellent analytical performance, a wide linear range of work, excellent selectivity, high amperometric sensitivity, and long-term stability. The proposed 3DnpPt-SPE-based electrochemical method required the application of only 50 μL of the sample to determine the presence of HES and NAR in it in a relatively faster, simpler, and reliable way comparable to the HPLC method. The excellent properties of the 3DnpPt-SPE sensor make the device suitable for use as a sensing platform for the determination of HES and NAR, with potential application in residual water from the citrus industry.

Author Information

Corresponding Author: **Maísa Azevedo Beluomini** - Department of Analytical, Physical-Chemical, and Inorganic Chemistry, Institute of Chemistry, São Paulo State University

(UNESP), 55 Prof. Francisco Degni St., Araraquara 14800-060, São Paulo State, Brazil.; ORCID: http://orcid.org/0000-0003-3441-1572 ; e-mail: maisa.beluomini@unesp.br

Co-Authors: Nelson Ramos Stradiotto - Department of Analytical, Physical-Chemical, and Inorganic Chemistry and Bioenergy Research Institute (IPBEN), São Paulo State University (UNESP), 55 Prof. Francisco Degni St., Araraquara 14800-060, São Paulo State, Brazil. ORCID: http://orcid.org/0000-0002-1227-5242.

Maria Valnice Boldrin - Department of Analytical, Physical-Chemical, and Inorganic Chemistry, Institute of Chemistry, São Paulo State University (UNESP), 55 Prof. Francisco Degni St., Araraquara 14800-060, São Paulo State, Brazil. ORCID: https://orcid.org/0000-0002-2296-1393.

Declaration of conflicts interest

The authors declare to have no conflicts of interest.

Author Contributions

All the authors have given their approval for the submission of the final version of the manuscript.

Acknowledgments

M.A. Beluomini is particularly grateful to the São Paulo Research Foundation (FAPESP) for the post-doctoral scholarship granted her in support of her research (grant 2018/12131-6). The authors are also grateful to FAPESP for the financial support granted in the course of this research (grants 2014/50945-4 and 2017/22401-8).

Appendix A. Supplementary material

The following are the Supplementary data to this article:

REFERENCES

[1] A. Di Mauro, B. Fallico, A. Passerini, E. Maccarone, Waste Water from Citrus Processing as a Source of Hesperidin by Concentration on Styrene−Divinylbenzene Resin, J. Agric. Food Chem. 48 (2000) 2291–2295. doi:10.1021/jf990992w.

[2] E. Gómez-Mejía, N. Rosales-Conrado, M.E. León-González, Y. Madrid, Citrus peels waste as a source of value-added compounds: Extraction and quantification of bioactive polyphenols, Food Chem. 295 (2019) 289–299. doi:10.1016/j.foodchem.2019.05.136.

[3] F. Battista, G. Remelli, S. Zanzoni, D. Bolzonella, Valorization of Residual Orange Peels: Limonene Recovery, Volatile Fatty Acids, and Biogas Production, ACS Sustain. Chem. Eng. 8 (2020) 6834–6843. doi:10.1021/acssuschemeng.0c01735.

[4] C.-S. Seo, H.-K. Shin, Simultaneous Determination of 12 Marker Components in Yeonkyopaedok-san Using HPLC–PDA and LC–MS/MS, Appl. Sci. 10 (2020) 1713. doi:10.3390/app10051713.

[5] N. Funaguchi, Y. Ohno, B.L.B. La, T. Asai, H. Yuhgetsu, M. Sawada, G. Takemura, S. Minatoguchi, T. Fujiwara, H. Fujiwara, Narirutin inhibits airway inflammation in an allergic mouse model, Clin. Exp. Pharmacol. Physiol. 34 (2007) 766–770. doi:10.1111/j.1440-1681.2007.04636.x.

[6] C. Manach, C. Morand, A. Gil-Izquierdo, C. Bouteloup-Demange, C. Rémésy, Bioavailability in humans of the flavanones hesperidin and narirutin after the ingestion of two dose of orange juice, Eur. J. Clin. Nutr. 57 (2003) 235–242. doi:10.1038/sj.ejcn.1601547.

[7] S. Chakraborty, S. Basu, Multi-functional activities of citrus flavonoid narirutin in Alzheimer's disease therapeutics: An integrated screening approach and in vitro validation, Int. J. Biol. Macromol. 103 (2017) 733–743. doi:10.1016/j.ijbiomac.2017.05.110.

[8] P. Bellavite, A. Donzelli, Hesperidin and SARS-CoV-2: New light on the healthy function of citrus fruits, Antioxidants. 9 (2020) 1–18. doi:10.3390/antiox9080742.

[9] W. Ngwa, R. Kumar, D. Thompson, W. Lyerly, R. Moore, T.-E. Reid, H. Lowe, N. Toyang, Potential of Flavonoid-Inspired Phytomedicines against COVID-19, Molecules. 25 (2020) 2707. doi:10.3390/molecules25112707.

[10] P. Pandey, F. Khan, A. Kumar Rana, Y. Srivastava, S. Kumar Jha, N. Kumar Jha, A Drug Repurposing Approach Towards Elucidating the Potential of Flavonoids as COVID-19 Spike Protein Inhibitors, 11 (2021) 8482–8501. doi:10.33263/BRIAC111.84828501.

[11] X.J. Zhao, D. Chen, P.A. Kilmartin, B.N. Jiao, Simultaneous Determination of Phenolics and Polymethoxylated Flavones in Citrus Fruits by Ultra-High Performance Liquid Chromatography Coupled with Triple-Quadrupole Mass Spectrometry (UHPLC-QqQ-MS), Anal. Lett. 52 (2019) 1926–1938. doi:10.1080/00032719.2019.1584628.

[12] B. Barfi, A. Asghari, M. Rajabi, A. Barfi, I. Saeidi, Simplified miniaturized ultrasound-assisted matrix solid phase dispersion extraction and high performance liquid chromatographic determination of seven flavonoids in citrus fruit juice and human fluid samples: Hesperetin and naringenin as biomarkers, J. Chromatogr. A. 1311 (2013) 30–40. doi:10.1016/j.chroma.2013.08.078.

[13] C.S. Seo, H.K. Shin, Quality assessment of traditional herbal formula, Hyeonggaeyeongyo-tang through simultaneous determination of twenty marker components by HPLC–PDA and LC–MS/MS, Saudi Pharm. J. 28 (2020) 427–439. doi:10.1016/j.jsps.2020.02.003.

[14] H.E. Cho, S.Y. Ahn, S.C. Kim, M.H. Woo, J.-T. Hong, D.C. Moon, Determination of Flavonoid Glycosides, Polymethoxyflavones, and Coumarins in Herbal Drugs of *Citrus* and *Poncirus* Fruits by High Performance Liquid Chromatography–Electrospray Ionization/Tandem Mass Spectrometry, Anal. Lett. 47 (2014) 1299–1323.

doi:10.1080/00032719.2013.871548.

[15] K. Sutthanut, B. Sripanidkulchai, C. Yenjai, M. Jay, Simultaneous identification and quantitation of 11 flavonoid constituents in Kaempferia parviflora by gas chromatography, J. Chromatogr. A. 1143 (2007) 227–233. doi:10.1016/j.chroma.2007.01.033.

[16] D. Sun, F. Wang, K. Wu, J. Chen, Y. Zhou, Electrochemical determination of hesperidin using mesoporous SiO2 modified electrode, Microchim. Acta. 167 (2009) 35–39. doi:10.1007/s00604-009-0200-0.

[17] A. Yiğit, Y. Yardım, Z. Şentürk, Square-Wave Adsorptive Stripping Voltammetric Determination of Hesperidin Using a Boron-Doped Diamond Electrode, J. Anal. Chem. 75 (2020) 653–661. doi:10.1134/S1061934820050184.

[18] S. Šafranko, A. Stanković, A. Asserghine, M. Jakovljević, S. Hajra, S. Nundy, M. Medvidović-Kosanović, S. Jokić, Electroactivated Disposable Pencil Graphite Electrode – New, Cost-effective, and Sensitive Electrochemical Detection of Bioflavonoid Hesperidin, Electroanalysis. (2020) elan.202060511. doi:10.1002/elan.202060511.

[19] Y.M. Temerk, M.S. Ibrahim, M. Kotb, Square-wave cathodic adsorptive stripping voltammetric determination of 3-hydroxyflavone, Morin and Hesperidin in bulk form and biological fluids in absence and presence of Cu(II), J. Braz. Chem. Soc. 22 (2011) 2056–2064. doi:10.1590/S0103-50532011001100006.

[20] Y. Gao, X. Wu, H. Wang, W. Lu, M. Guo, Highly sensitive detection of hesperidin using AuNPs/rGO modified glassy carbon electrode, Analyst. 143 (2018) 297–303. doi:10.1039/C7AN01706E.

[21] B. Sun, X. Hou, D. Li, Y. Gou, F. Hu, W. Li, X. Shi, Electrochemical Sensing and High Selective Detection of Hesperidin with Molecularly Imprinted Polymer Based on Ultrafine Activated Carbon, J. Electrochem. Soc. 166 (2019) B1644–B1652. doi:10.1149/2.1141915jes.

[22] M.A. Beluomini, N.R. Stradiotto, M.V. Boldrin, Electrosynthesis of three-dimensional nanoporous nickel on screen-printed electrode used for the determination of narirutin in citrus wastewater, Food Chem. (2021) 129427. doi:10.1016/j.foodchem.2021.129427.

[23] M.J. Sims, Q. Li, R.T. Kachoosangi, G.G. Wildgoose, R.G. Compton, Using multiwalled carbon nanotube modified electrodes for the adsorptive striping voltammetric determination of hesperidin, Electrochim. Acta. 54 (2009) 5030–5034. doi:10.1016/j.electacta.2008.10.056.

[24] G. Manasa, R.J. Mascarenhas, A.K. Bhakta, Z. Mekhalif, Nano-graphene-platelet/Brilliant-green composite coated carbon paste electrode interface for electrocatalytic oxidation of flavanone Hesperidin, Microchem. J. 160 (2021) 105768. doi:10.1016/j.microc.2020.105768.

[25] A. Zhupanova, E. Guss, G. Ziyatdinova, H. Budnikov, Simultaneous Voltammetric Determination of Flavanones Using an Electrode Based on Functionalized Single-Walled Carbon Nanotubes and Polyaluminon, Anal. Lett. 53 (2020) 2170–2189. doi:10.1080/00032719.2020.1732402.

[26] R. Güell, G. Aragay, C. Fontàs, E. Anticó, A. Merkoçi, Sensitive and stable monitoring of lead and cadmium in seawater using screen-printed electrode and electrochemical stripping analysis, Anal. Chim. Acta. 627 (2008) 219–224. doi:10.1016/j.aca.2008.08.017.

[27] T. Juarez, J. Biener, J. Weissmüller, A.M. Hodge, Nanoporous Metals with Structural Hierarchy: A Review, Adv. Eng. Mater. 19 (2017) 1700389. doi:10.1002/adem.201700389.

[28] S. Park, Y.J. Song, J.H. Han, H. Boo, T.D. Chung, Structural and electrochemical features of 3D nanoporous platinum electrodes, Electrochim. Acta. 55 (2010) 2029–2035. doi:10.1016/j.electacta.2009.11.026.

[29] J. Agrisuelas, M.I. González-Sánchez, E. Valero, Hydrogen peroxide sensor based on in

situ grown Pt nanoparticles from waste screen-printed electrodes, Sensors Actuators, B Chem. 249 (2017) 499–505. doi:10.1016/j.snb.2017.04.136.

[30] A. Weremfo, S.T.C. Fong, A. Khan, D.B. Hibbert, C. Zhao, Electrochemically roughened nanoporous platinum electrodes for non-enzymatic glucose sensors, Electrochim. Acta. 231 (2017) 20–26. doi:10.1016/j.electacta.2017.02.018.

[31] Y.-J. Lee, D.-J. Park, J.-Y. Park, Y. Kim, Fabrication and Optimization of a Nanoporous Platinum Electrode and a Non-enzymatic Glucose Micro-sensor on Silicon, Sensors. 8 (2008) 6154–6164. doi:10.3390/s8106154.

[32] S. Park, H. Boo, Y. Kim, J.H. Han, H.C. Kim, T.D. Chung, pH-Sensitive solid-state electrode based on electrodeposited nanoporous platinum, Anal. Chem. 77 (2005) 7695–7701. doi:10.1021/ac050968j.

[33] J.H. Han, H. Boo, S. Park, T.D. Chung, Electrochemical oxidation of hydrogen peroxide at nanoporous platinum electrodes and the application to glutamate microsensor, Electrochim. Acta. 52 (2006) 1788–1791. doi:10.1016/j.electacta.2005.12.060.

[34] A. Abburi, N. Abrams, W.J. Yeh, Synthesis of nanoporous platinum thin films and application as hydrogen sensor, J. Porous Mater. 19 (2012) 543–549. doi:10.1007/s10934-011-9503-8.

[35] C. Xu, F. Sun, H. Gao, J. Wang, Nanoporous platinum-cobalt alloy for electrochemical sensing for ethanol, hydrogen peroxide, and glucose, Anal. Chim. Acta. 780 (2013) 20–27. doi:10.1016/j.aca.2013.03.068.

[36] S. Trasatti, O.A. Petrii, Real surface area measurements in electrochemistry, J. Electroanal. Chem. 327 (1992) 353–376. doi:10.1016/0022-0728(92)80162-W.

[37] B. Barfi, A. Asghari, M. Rajabi, A. Barfi, I. Saeidi, Simplified miniaturized ultrasound-assisted matrix solid phase dispersion extraction and high performance liquid chromatographic determination of seven flavonoids in citrus fruit juice and human fluid

samples: Hesperetin and naringenin as biomarkers, J. Chromatogr. A. 1311 (2013) 30–40. doi:10.1016/j.chroma.2013.08.078.

[38] A.J. Bard, L.R. Faulkner, L.R.F. Allen J. Bard, Electrochemical methods: fundamentals and applications, 2nd ed., Wiley Global Education, New York, 2001. doi:10.1016/B978-0-12-381373-2.00056-9.

[39] D. Obendorf, E. Reichart, Determination of hesperidin by catholic stripping voltammetry in orange juice and helopyrin, a phytopharmaceutical preparation, Electroanalysis. 7 (1995) 1075–1081. doi:10.1002/elan.1140071115.

[40] S.A.G. Evans, J.M. Elliott, L.M. Andrews, P.N. Bartlett, P.J. Doyle, G. Denuault, Detection of hydrogen peroxide at mesoporous platinum microelectrodes, Anal. Chem. 74 (2002) 1322–1326. doi:10.1021/ac011052p.

Supporting Information

Simultaneous detection of hesperidin and narirutin in residual water using nanoporous platinum electrosynthesized by alloying-dealloying mechanism

Maisa Azevedo Beluomini[1*], *Nelson Ramos Stradiotto*[2], *M. Valnice Boldrin*[1]

[1]Department of Analytical, Physical-Chemical and Inorganic Chemistry, Institute of Chemistry, São Paulo State University (UNESP), 14800-060, Araraquara, São Paulo State, Brazil.

[2]Bioenergy Research Institute, São Paulo State University (UNESP), 14800-060 Araraquara, São Paulo, Brazil

*Corresponding author: maisa.beluomini@unesp.br

Chromatographic study

The glycosidic flavanones most abundant in the residues of the Brazilian citrus industry are hesperdin, naringin, narirutin and naringenin [2,3]. Thus, the analytical standards for each of these molecules were prepared from a stock solution of 0.01 mol L^{-1} and diluted in ethanol to the concentration of 5.0×10^{-5} mol L^{-1}, and an aliquot of 5.0 μL was injected for gradient elution. The chromatogram is shown in Figure S1. The retention times for narirutin, hesperidin, naringin and naringenin were 4.63; 5.05; 5.47 and 10.92 min, respectively. The chromatographic identification of the flavonoids in the YW sample was performed by comparing the retention times of each molecule. Thus, 5.0 μL of the filtered sample was injected directly into the system and the chromatogram is shown in Figure S2. Only the peaks of (1) narirutin and (2) hesperidin were observed. With this, an analytical curve in the range of 5.0×10^{-6} mol L^{-1} to 1.0×10^{-4} mol L^{-1} (Figure S3) was constructed to obtain the concentration of these flavonoids in the sample. Through the peak areas obtained, the amount of narirutin and hesperidin was determined as shown in Table S2. The value found was $(8.5 \pm 0.2) \times 10^{-5}$ mol L^{-1} of narirutin and $1.7 \pm 0.1 \times 10^{-4}$ mol L^{-1} of hesperidin. With that, the development of electrodes modified with platinum nanopores (3DnpNi/SPE) to analyze the simultaneous determination of narirutin and hesperidin was carried out.

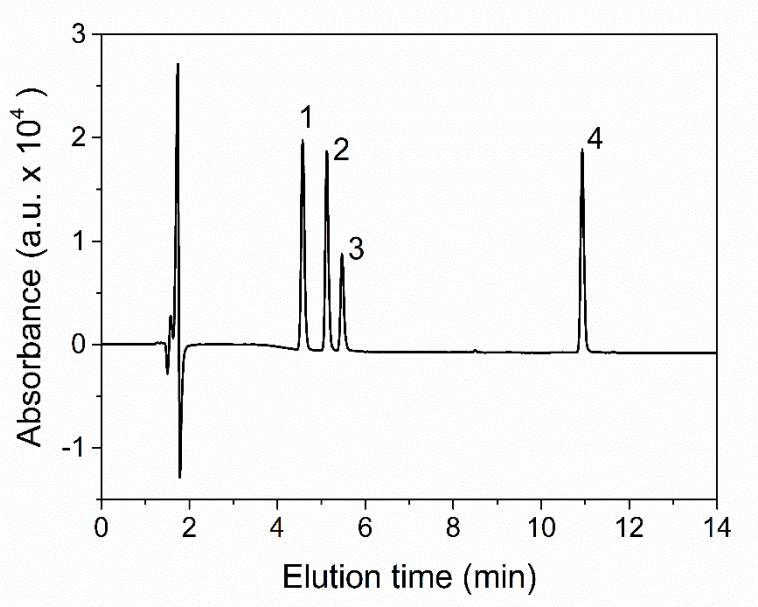

Figure S1. Chromatographic separation of 5.0×10^{-5} mol L^{-1} of (1) narirutin, (2) hesperidin, (3) naringin and (4) naringenin standard

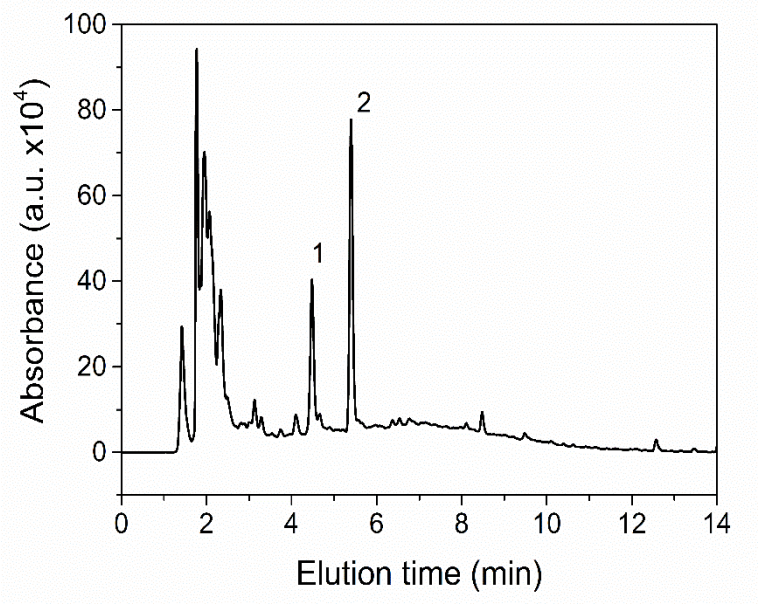

Figure S2. Chromatogram of the yellow water sample. In (1) the characteristic retention time of narirutin and (2) hesperidin

.

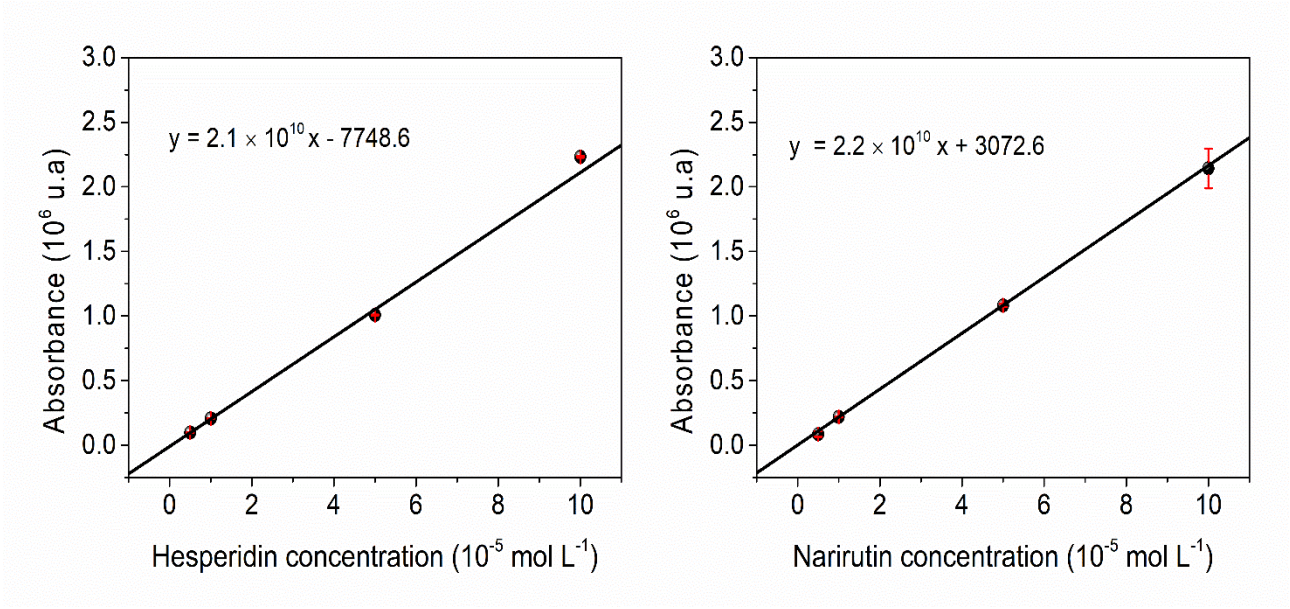

Figure S3. Analytical curve for HPLC analysis obtained in the range of 5.0 µmol L^{-1} – 0.1 mmol L^{-1} for (A) HES and (B) NAR.

Tabela S1. Chromatographic determination of NAR and HES in yellow water samples, (n = 3).

Flavonoid	Peak area	Amount found (10^{-5} mol L^{-1})
Narirutin		
1	1910512	8.8
2	1832054	8.4
3	1808043	8.3
Hesperidin		
1	3698884	17.4
2	3731592	17.6
3	3722160	17.6

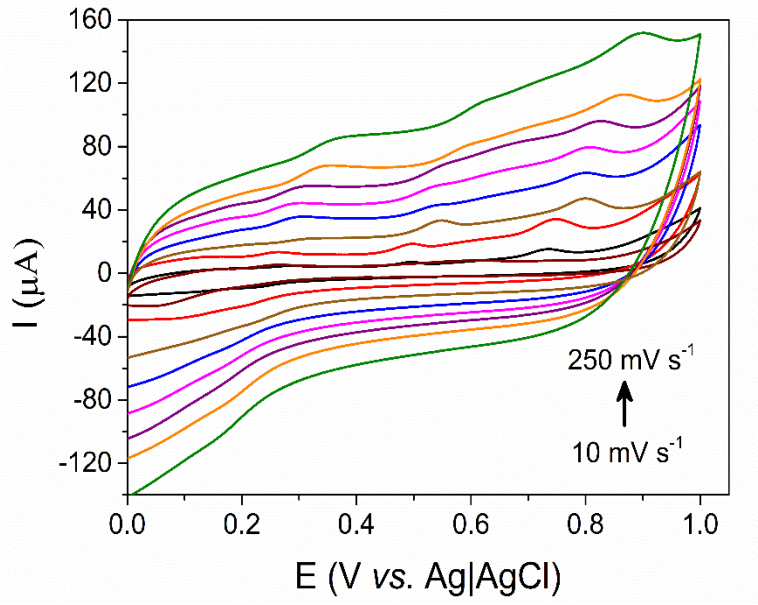

Figure S4. Cyclic voltammograms of the 3DnpPt-SPE with different scan rate (10 – 250 mV s^{-1} and in 0.1 mmol L^{-1} of HES and NAR (0.1 mol L^{-1} H_2SO_4).

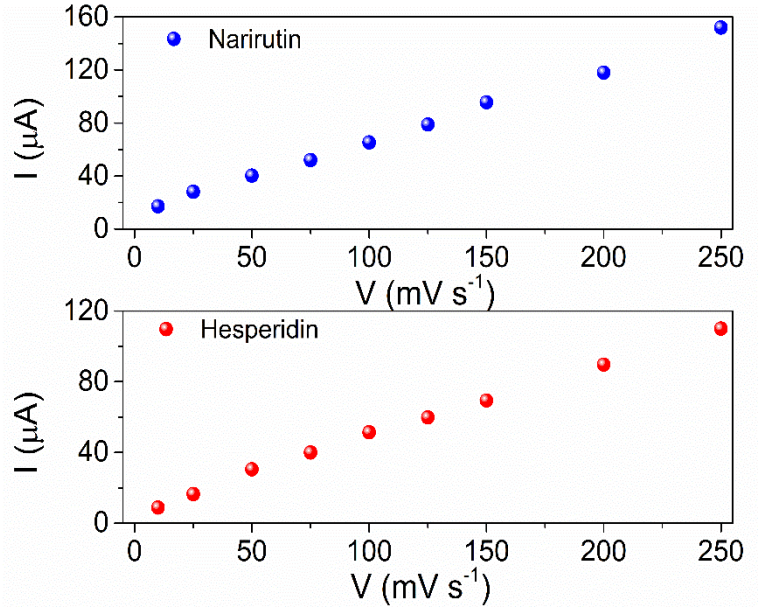

Figure S5. Plots of oxidation peak currents of narirutin and hesperidin vs. the scan rates.

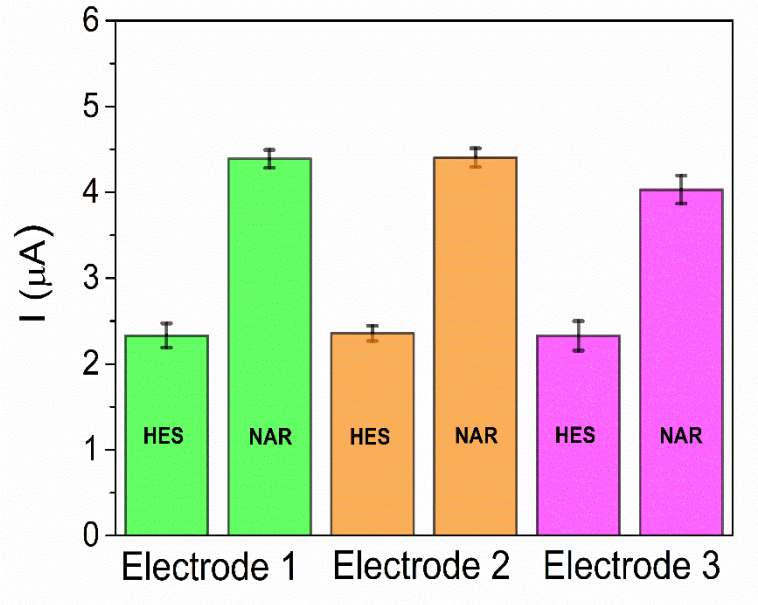

Figure S6. Inter-electrode repeatability for HES and NAR (n=3).

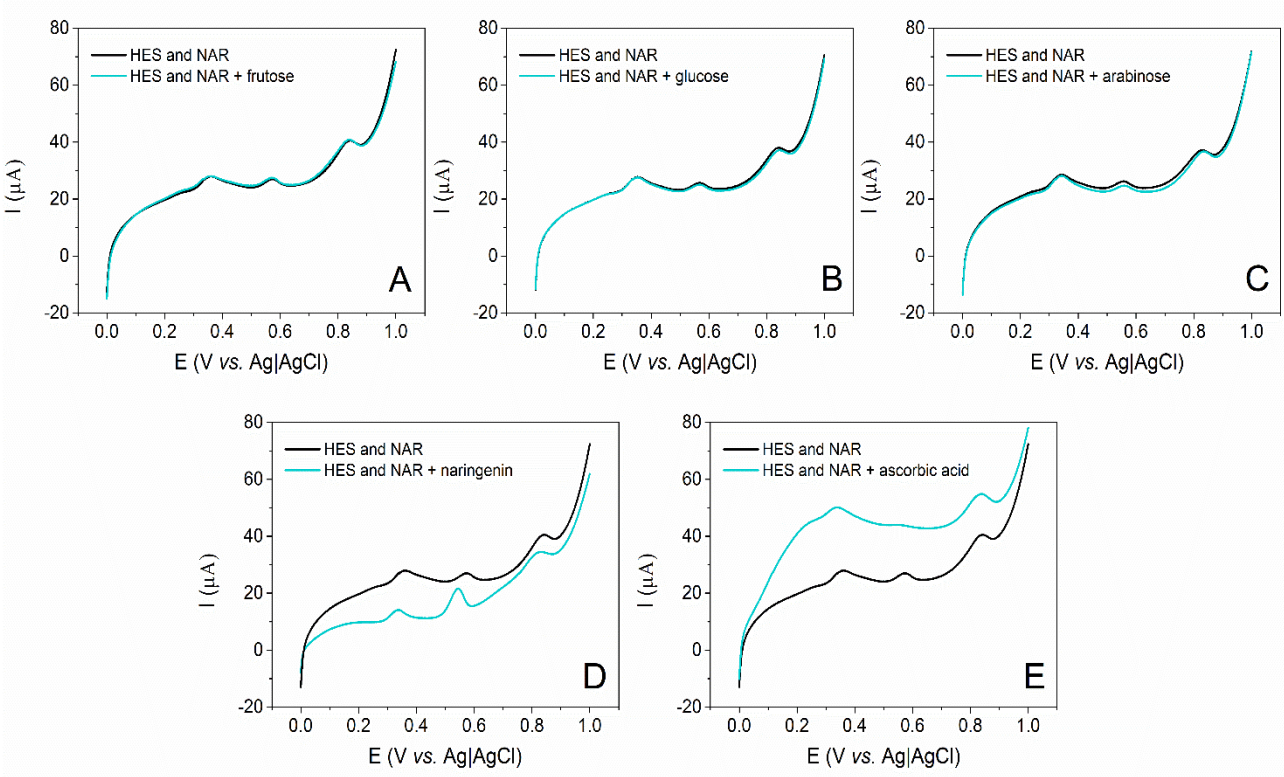

Figure S7. Selectivity studies in the presence of (A) frutose, (B) glucose, (C) arabinose, (D) naringenin, (E) ascorbic acid.

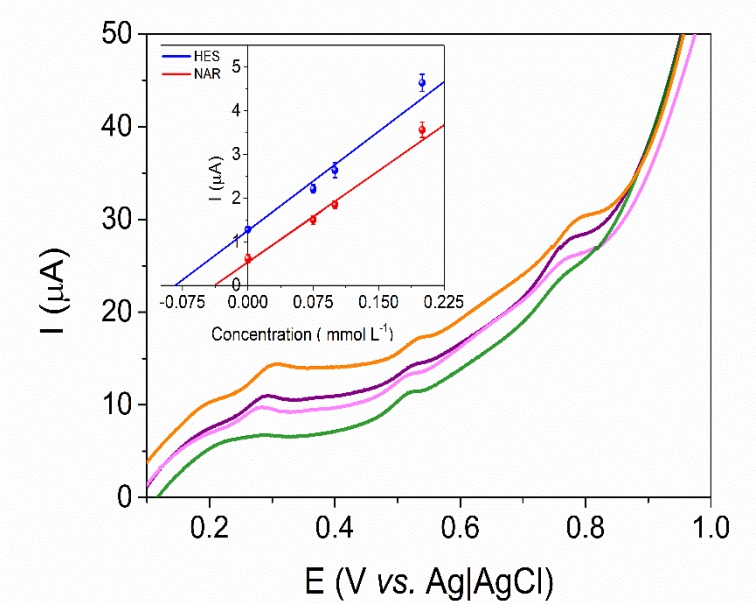

Figure S8. LSV for the determination of HES and NAR. Insert: Linear relationship between a current peak plotted against the added concentration of HES and NAR from 0.075 to 0.2 mmol L^{-1}.

9) Lista dos trabalhos preparados ou submetidos (e ainda não aceitos, pois os aceitos devem estar listados no item 7) para publicação, acompanhada de cópias destes trabalhos.

[1] Modenes-Junior, M.A., Beluomini, M.A., Stradiotto N.R. Voltammetric Determination of Sulfur in Biodiesel Microemulsion Using a Silver Solid Amalgam Electrode. Energy&Fuel, 2021. Manuscript ID: ef-2021-03518v.

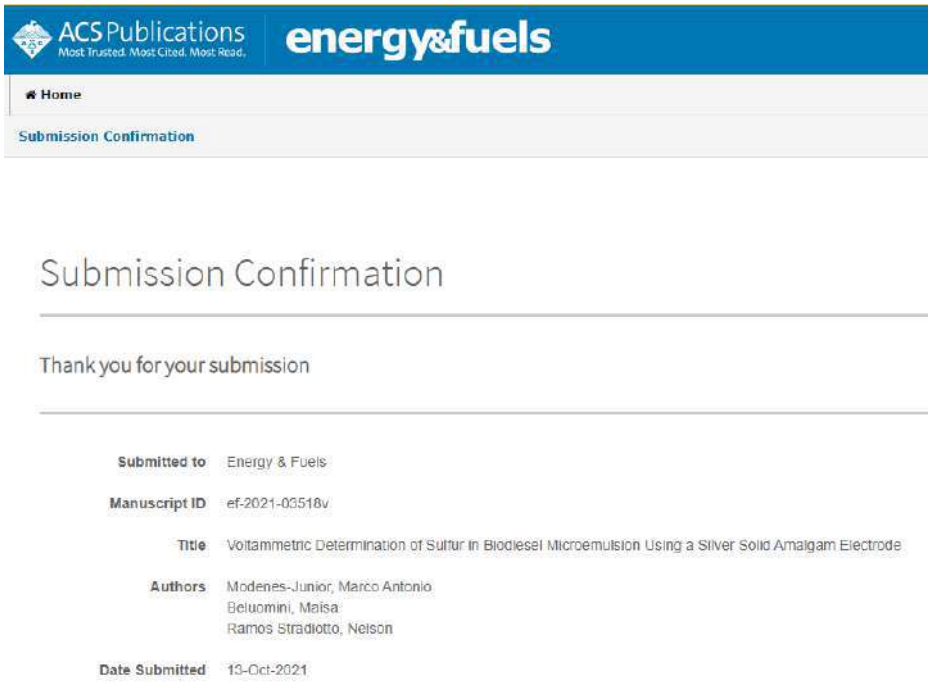

ACS Publications
Most Trusted. Most Cited. Most Read.

energy&fuels

Home

Submission Confirmation

Submission Confirmation

Thank you for your submission

Submitted to	Energy & Fuels
Manuscript ID	ef-2021-03518v
Title	Voltammetric Determination of Sulfur in Biodiesel Microemulsion Using a Silver Solid Amalgam Electrode
Authors	Modenes-Junior, Marco Antonio Beluomini, Maisa Ramos Stradiotto, Nelson
Date Submitted	18-Oct-2021

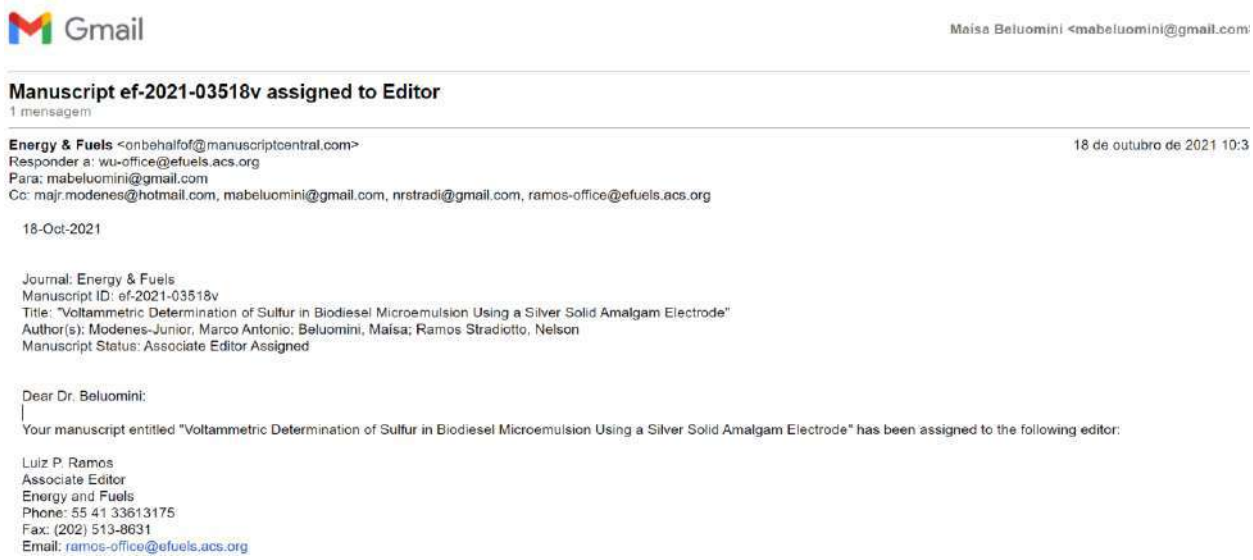

Gmail — Maisa Beluomini <mabeluomini@gmail.com>

Manuscript ef-2021-03518v assigned to Editor
1 mensagem

Energy & Fuels <onbehalfof@manuscriptcentral.com> — 18 de outubro de 2021 10:3
Responder a: wu-office@efuels.acs.org
Para: mabeluomini@gmail.com
Cc: majr.modenes@hotmail.com, mabeluomini@gmail.com, nrstradi@gmail.com, ramos-office@efuels.acs.org

18-Oct-2021

Journal: Energy & Fuels
Manuscript ID: ef-2021-03518v
Title: "Voltammetric Determination of Sulfur in Biodiesel Microemulsion Using a Silver Solid Amalgam Electrode"
Author(s): Modenes-Junior, Marco Antonio; Beluomini, Maisa; Ramos Stradiotto, Nelson
Manuscript Status: Associate Editor Assigned

Dear Dr. Beluomini:

Your manuscript entitled "Voltammetric Determination of Sulfur in Biodiesel Microemulsion Using a Silver Solid Amalgam Electrode" has been assigned to the following editor:

Luiz P. Ramos
Associate Editor
Energy and Fuels
Phone: 55 41 33613175
Fax: (202) 513-8631
Email: ramos-office@efuels.acs.org

Voltammetric determination of sulfur in biodiesel microemulsion using a silver solid amalgam electrode

Marco Antonio Modenes Junior[a], Maísa Azevedo Beluomini[a], Nelson Ramos Stradiotto[a,b],

[a] Department of Analytical, Physical-Chemical and Inorganic Chemistry, Institute of Chemistry, São Paulo State University (UNESP), 14800-060, Araraquara, São Paulo State, Brazil.

[b]Bioenergy Research Institute, São Paulo State University (UNESP), 14800-060 Araraquara, São Paulo, Brazil

* Corresponding author: maisa.beluomini@unesp.br

Graphical Abstract

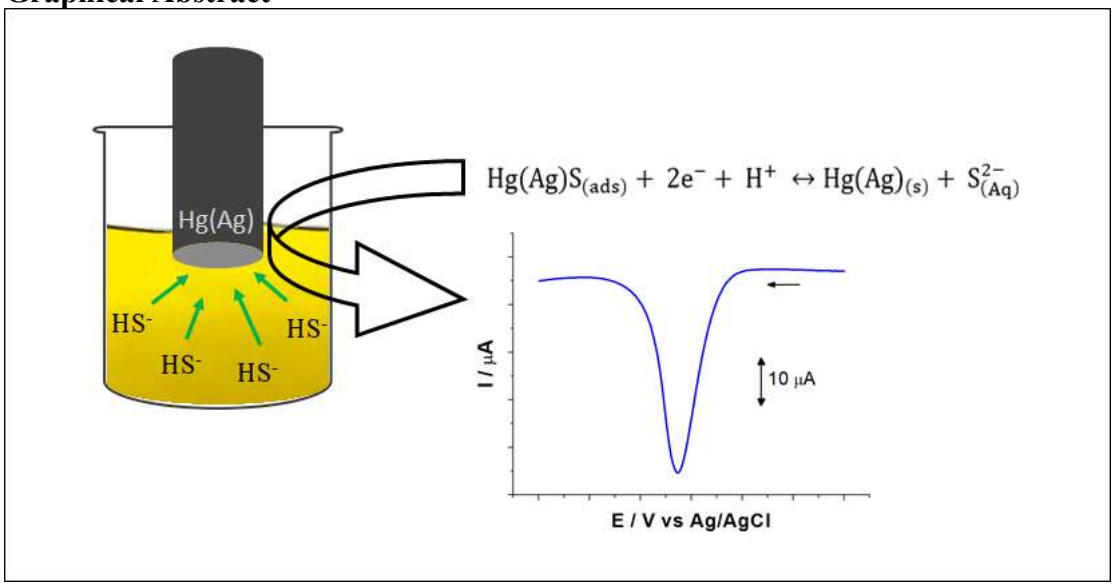

Abstract

The monitoring of sulfur in biodiesel is of fundamental importance, because even in low concentration, it can harm the operation of the engine parts and increase emission toxic gases and particulate material. Hence, a simple, rapid and sensitive adsorptive stripping voltammetry (AdSV) method, based on silver solid amalgam electrode (AgSAE) was developed for the determination of sulfur in biodiesel. The novel electrochemical method was evaluated through the techniques of linear sweep adsorptive stripping voltammetry (LSAdSV), square wave adsorptive stripping voltammetry (SWAdSV) and differential pulse adsorptive stripping voltammetry (DPAdSV), in NH_3/NH_4^+ buffer solution (pH 9.0), containing Na_2SO_3. Under optimal condition, the method was applied in biodiesel microemulsion samples. For this, a ternary phase diagram was constructed, employing three components: biodiesel/propan-1-ol/buffer solution. The microemulsion that showed better response was in the concentration of 25 % NH_3/NH_4^+ buffer (pH 9.0), 5.0 % biodiesel and 70 % propan-1-ol. The method reached a detection limit in the order of 10^{-7} mol L^{-1} of sulfur, and the recovery values between 80 % and 116 %. The methodology was applied in the determination of sulfur in biodiesel, and the amount in the samples was found to be below the value stipulated by the regulatory agencies. The method can be a promising alternative for determining sulfur in the microemulsion of biodiesel, being able to give a fast response on its quality of these biofuel.

1. Introduction

Among the various renewable biofuels developed so far, biodiesel is one of the most promising due to its environmentally friendly properties, as it comes from renewable sources and has low toxicity. Biodiesel is composed of alkyl esters of long-chain fatty acids, obtained through the process of transesterification of triglycerides or esterification of free fatty acids with short-chain alcohol in the presence of a base, acid or enzymatic catalyst [1].

To ensure the quality of biodiesel, some parameters are stipulated with the aim of imposing limits on its composition. The presence of some contaminants can decrease engine performance and increase emissions of toxic gases during combustion. The quality of biodiesel can vary according to the molecular structures of the constituent esters, or the contaminants present in the raw material, which can be formed during production and storage. Contaminants from the raw material can be phosphorus, sulfur, calcium and magnesium, and depending on the efficiency of the biodiesel production process, they can be present in greater or lesser amounts. The presence of these substances can decrease engine performance and increase emissions of toxic gases during combustion of this biofuel [2]. Among the various parameters to assess the quality of biodiesel, the one that determines the amount of sulfur is extremely important. The presence of this contaminant, even in low amounts, it can harm the operation of catalytic converters, increase emission toxic gases and particulate materials, causing corrosion problems of internal parts of the engine as well as causing damage to flora and fauna [3]. In view of the damage caused by sulfur, stricter standards for its biodiesel content were established, for example, the sulfur concentration must be below 15 and 10 ppm in the United States (ASTM D6751) and Europe (EN 14214), respectively [4]. In Brazil, the maximum permitted sulfur limit in biodiesel is 10 ppm, according to technical specification no. 3/2014 of resolution no. 45 of the National Petroleum Agency (ANP) [5].

Most of the methods found in the literature for analyzing sulfur are based on X-ray fluorescence (XRF) [6–8], Inductively coupled plasma optical emission spectrometry (ICP-OES) [3,9], and Inductively coupled plasma quadrupole mass spectrometry (ICP-QMS) [10–12]. Although these methods are sensitive and have a good detection limit, they require a long time of analysis, time-consuming sample preparation, and high volume of reagents and organic solvents, and high cost of equipment. On the other hand, electrochemical sensors can be an interesting alternative for the analysis of sulfur in biodiesel, since there are a large number of hanging mercury drop electrode (HMDE) applications for the determination of sulfur and its compounds in different matrices [13–17]. However, only one method was found in the literature that uses electrochemical techniques to quantify sulfur in biodiesel samples. Viégas, et al [18], developed a voltammetric method using the square-wave cathodic adsorptive stripping voltammetry (SW-AdCSV) and glassy carbon electrode modified with mercury film. Although the authors achieved low detection limits (3.29×10^{-10} mol L^{-1}), it was necessary to perform a pretreatment to solubilize the biodiesel sample using tetramethylammonium hydroxide (TMAH) at 90°C. However, TMAH has high toxicity and its dermal exposure can be fatal [19,20].

The direct analysis of compounds present in biodiesel becomes difficult due to its viscous and complex nature. On the other hand, a microemulsions (ME) present an interesting alternative to pre-treat biodiesel samples, since ME is a thermodynamically stable and isotropically translucent system, composed of water, oil and surfactant, and, in some cases, an alcohol [21,22]. In addition, ME is characterized by the formation of a solution microenvironment apparently homogeneous, but microscopically nanoheterogeneous, capable of solubilizing a large number of hydrophilic and lipophilic compounds and it is usually formed through the construction of a ternary phase diagram [21]. Thus, it is not necessary to use organic solvents or strong bases as a diluent, since the micro emulsified biodiesel starts to have a micellar structure that resembles that of an aqueous solution [23]. It is possible to find in the literature several works that show the feasibility

of using ME in the analysis of metals in biodiesel [22–25], but no study was reported for the electrochemical analysis of sulfur in this medium.

Therefore, the main goal of this work was to develop a voltammetric technique of analysis of sulfur in ME of biodiesel using a silver solid amalgam electrode (AgSAE). AgSAE was chosen in this work due to its ability to form complexes with sulfur-containing compounds (through semi-valent bonds) even in open circuit conditions, making it possible to use adsorptive stripping voltammetry [26]. In addition, the use of AgSAE makes it easy to renew the electrode surface, reduces adsorption of reaction products and is considered ecologically correct as the mercury released in each analysis is practically insignificant [27]. Additionally, the electrochemical method was evaluated through the techniques of linear sweep adsorptive stripping voltammetry (LSAdSV), square wave adsorptive stripping voltammetry (SWAdSV) and differential pulse adsorptive stripping voltammetry (DPAdSV), in which it proved to be efficient in the determination of sulfur traces in biodiesel on the AgSAE, with good sensitivity and low detection limit and can be an alternative procedure for the analysis of this element.

2. Experimental

2.1. Chemicals and samples

Propan-1-ol (purity 99.5 %), potassium chloride (purity 99 %), sodium hydroxide (≥ 97 %), ammonium nitrate (anhydrous), Ag powder (with granulometry between 5 to 9 μm ≥ 99.9 % trace metals basis), analytical grade liquid mercury (≥ 99.9 %) and sodium sulfide nonahydrate (≥ 98 %) were purchased from Sigma–Aldrich. Boric acid (P.A 100 %), phosphoric acid (85 %), glacial acetic acid (100 %), were purchased from Synth. The Britton-Robinson buffer (BR buffer) solution was prepared by solubilizing 2.47 g of boric acid in 100 ml of water. The solution was transferred to a 1000 ml volumetric flask and 2.74 ml of phosphoric acid and 2.30 ml of acetic acid, were added. The volume was completed, and the pH was adjusted using 1.0 mol L^{-1} NaOH solution. For the preparation of the ammonia and ammonium (NH_3/NH_4^+) buffer solution, 4.0 g of

NH_4NO_3 was dissolved in 50 ml of water. Then, the solution was transferred to a 500 ml volumetric flask and 2.92 ml of ammonium hydroxide concentration was added. The volumetric flask was filled with water and the pH of the final solution was 9.0, calculated using the Henderson - Hasselbalch equation [28]. A standard stock solution of sulfide (0.1 mol L^{-1}) was prepared through the solubilization of sodium sulfide nonahydrate (in water and stored at 4.0 °C.) All solutions were prepared using deionized water with resistivity not less than 18.2 MΩcm^{-1}. All the experiments were carried out at room temperature (25 ± 1.0 °C). When necessary, oxygen was removed from the solutions by bubbling N_2.

The voltammetric measurements were performed with a PGSTAT30 driven by General Purpose Electrochemical System (GPES) software. For the measurements, a conventional electrochemical cell with a three-electrode was used, being the Ag/AgCl (in saturated KCl solution) the reference electrode, platinum wire (Ø 1 mm) as the auxiliary electrode, and silver solid amalgam as the working electrode. Before each experiment, the solutions were reaerated by bubbling nitrogen for 15 min. For the development of the experiments, a stock solution of H_2S was prepared using $Na_2S{\cdot}9H_2O$ dissolved in BR buffer solution (pH 9.0).

2.2. Preparation of the silver solid amalgam electrode

The solid silver amalgam electrode was prepared from a mixture of powdered metallic silver with liquid mercury in the proportion of 30/70 (Ag/Hg; *m/m*). This concentration was chosen based on previous studies that demonstrated the formation of a simple phase (Ag_2Hg_3), without excess mercury or silver oxide [29]. Mechanical amalgamation was performed in a mortar and agate pistil until complete homogenization of the elements. The paste was inserted into a glass capillary tube with 2.7 mm diameter. After 20 min, the paste amalgam was solidified, and the electrical contact was provided using a copper wire fixed using silver glue. After that, the AgSAE was mechanical polishing using 1500 grit size sandpaper, followed by electrochemical pre-treated

to remove any impurities adsorbed on the AgSAE surface. This pre-treatment was performed applying the potential of 2.2 V for 300 cycles in 0.2 mol L^{-1} KCl. Subsequently, the electrode was subjected to multiple cyclic voltammetry (CV) in the potential range of 0 to -2.2 V (*vs*. Ag/AgCl) during 100 cycles (υ = 200 mV s^{-1}) in the same solution of 0.2 mol L^{-1} KCl (Fig. S1). This procedure was repeated after successive measurements (usually after 8 h of use) or when the electrode remained unused for more than 1 h.

2.3. Studies of the parameters of the adsorptive stripping voltammetry

The optimized parameters of the adsorptive stripping voltammetry technique (AdSV) were; accumulation potential (E_{acc}) in the range of – 0.5 V to – 4.0 V and the accumulation time (t_{acc}) in the range of 20 to 180 s. In the redissolution step, the linear scanning module was used.

For the optimization of the linear sweep-adsorptive stripping voltammetry (LSAdSV), the parameters studied were the variation of the scan rate in a range of 20 to 100 mVs^{-1} and the pH of the electrolyte. These experiments were carried out in an NH_3/NH_4^+ buffer solution (pH 9.0), containing 1.0×10^{-6} mol L^{-1} of Na_2SO_3.

The optimized parameters of the square-wave adsorptive stripping voltammetric (SWAdSV) were frequency (*f*), potential increase (ΔES), and pulse amplitude (ESW). The peak resolution was evaluated according to the relation to the maximum value of the peak current and the maximum selectivity (half-peak width, $w_{1/2}$). The studies were carried out in NH_3/NH_4^+ buffer solution (pH 9.0) containing 2.8×10^{-7} mol L^{-1} of Na_2SO_3.

2.4. Preparation of biodiesel microemulsions

The biodiesel microemulsions were prepared from homogeneous ternary mixture of three components, NH_3/NH_4^+ buffer solution (pH 9.0) as the aqueous phase, biodiesel as oil phase and

propan-1-ol as consolute. Propan-1-ol was chosen because of its high solubility in water and oil, being suitable for use in the composition of microemulsions. [21].

A ternary phase diagram was constructed by varying the reagents in order to obtain different microemulsion compositions. For this, the biodiesel was mixed with the aqueous phase under constant agitation. After that, propan-1-ol was slowly added until complete homogenization of the solution. The electrochemical behavior of the sulfide ions in different compositions of microemulsions was evaluated in terms of peak cathodic current (I_{pc}), peak cathodic potential (E_{pc}) and peak width at half height ($w_{1/2}$). Thus, the microemulsion that presented the best conditions was used in the development and application of the electroanalytical methodology.

2.5. Analytical measurements

The development of the methodology was based on the variation of the current with the concentration of sulfide, using the SWAdSV in aqueous medium and in biodiesel microemulsions. From the analytical curve data, the figures of merit including limit of detection (LOD), limit of quantification (LOQ) and amperometric sensitivity (As), were evaluated. LOD and LOQ were calculated using the equation LOD = 3.3SD/S and LOQ = 10SD/S, where SD is the standard deviation obtained from three measurements of the blank signal, and S is the analytical sensitivity obtained by the slope of the calibration curve.

2.6. Sample preparation

Four samples of different Brazilian biodiesel were used for the determination of sulfur. Two samples of soy biodiesel supplied by industries in the region of Curitiba and Araraquara. Biodiesel samples made from tucuma and murumuru fruits, obtained through the ethanolic transesterification method and synthesized by the laboratories of the University of São Paulo

(USP) in the city of Ribeirão Preto. The samples were prepared following the best conditions obtained according to the item 2.4.

For the sulfide determination, the standard addition method was used. For this, known amounts of the analyte were added in the sample. Recovery rates were determined by adding a defined concentration of sulfide to the samples in order to determine the efficiency of the methodology.

3. Results and discussion

3.1. Electrochemical characterization of the solid amalgam electrodes

The pH of the support electrolyte (buffer solution) is an important parameter considering that the distribution of sulfur species in solution depending on the pH value. The pH variation can modify the speciation of free sulfide ion (in which it relates the balance between H_2S and HS^-), in which it can affect the reactions at the surface of the working electrode. Thus, it becomes essential for the development of the method to analyze the influence of the pH of the solution. From the values found in the literature for pKa's of sulfide, in neutral medium the formation of the species H_2S and HS^- occurs. In alkaline medium (~pH 8.0), sulfur species are found in the HS^- form, while in higher values of pH the S^{2-} species predominates [30].

Therefore, to obtain a good analytical signal in terms of peak cathodic current, the pH optimization of the solution was evaluated in the range from 7 to 10 using BR buffer solution containing 4.9×10^{-6} mol L^{-1} of Na_2SO_3. The pH values were adjusted using 1.0 mol L^{-1} NaOH, and the technique used for this study was LSAdSV. The Fig. 1A shows the voltammograms recorded for the electrochemical reduction of the sulfide ions at four different pH values.

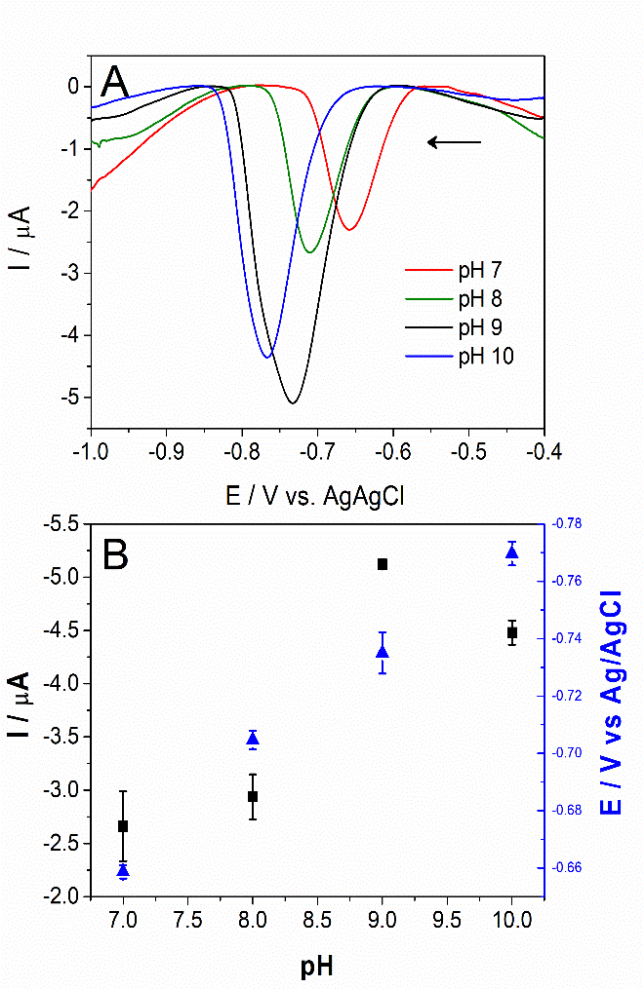

Fig. 1. (A) LSAdSV for 4.9×10^{-6} mol L^{-1} of Na_2SO_3 in BR buffer solution in the pH range of 7 to 10. (B) Behavior of peak cathodic current and cathodic peak potential as a function of pH. Conditions: t_{acc} = 120 s; υ = 50 mVs^{-1}.

Analyzing Fig. 1A, it is possible to observe a shift of the peak potential towards more negative values as the pH values increase. In the Fig. 1B, the peak cathodic current reached its maximum value at pH 9.0. Besides that, from the linear fit of the E_p *versus* pH plot yielded $\delta E_p/\delta$pH equal to − 38.9 mV, in accordance with that reported by Redinha et al., [31]. In fact, for pH > 7 the predominance in solution are sulfide ions (HS^-), and only one proton is involved in the reduction process of the $Hg(Ag)S_{(ads)}$ [32]. The Equation 1 and 2 describe the reaction mechanism suggested for this system on the AgSAE surface.

$Hg(Ag)_{(s)} + HS^-_{(aq)} \leftrightarrow Hg(Ag)S_{(ads)} + 2e^- + H^+$ (1)

$Hg(Ag)S_{(ads)} + 2e^- + H^+ \leftrightarrow Hg(Ag)_{(s)} + S^{2-}_{(aq)}$ (2)

Based on the aforementioned equations and in some works reported in the literature [14,33], it was observed that the use of a buffer solution that maintains the pH in 9.0, presents better sensitivity for electrochemical reduction of sulfur species.

3.2 Adsorptive stripping voltammetry

3.2.1 Effect of accumulation potential and preconcentration time

In adsorptive stripping voltammetry is an interesting electrochemical method for sulfide ions determination due to its effective preconcentration process, and the measurement process can be performed in two steps. The first step involves the accumulation time, in which the analyte is spontaneously adsorbed or through of the application of the potential on the working electrode. The second step refers to stripping, where the analyte accumulated is removed, accompanied by the recording of a voltammogram.

Due to the extremely low solubility product of mercury sulfide ($K_{sp} = 4.0 \times 10^{-54}$) and silver sulfide ($K_{sp} = 8.0 \times 10^{-51}$), this reaction is favorable for the formation of a precipitate [34]. The voltammetric technique based on the electroactivity that sulfur must consider the initial adsorption of sulfur on the electrode surface (which occurs relatively quickly). Thus, the maximum time required for the saturation of the surface of the AgSAE electrode to occur was studied by making a relationship between the sulfide cathodic peak current and the accumulation time (t_{acc}). The experiments were carried out with a buffer solution NH_3/NH_4^+ (pH 9.0), containing 1.0×10^{-6} mol L^{-1} of sodium sulfide. Noting that during the t_{acc} there was no application of potential, in order to investigate the spontaneous adsorption of sulfur on the electrode. The detection technique used in this study was linear sweep voltammetry (LSV). Analyzing Fig. S2, it is possible to observe that

when leaving the electrode in contact with the solution for 80 s, an exponential increase in the cathodic peak current due to the increase in the t_{acc} is observed. The maximum peak current was approximately -1.6 μA. For a longer t_{acc}, no current gain was observed. Therefore, the t_{acc} used in the experiments was 120 s, in order to guarantee the complete adsorption of the analyte on the AgSAE surface.

After contact for 120 s between the electrode and the solution, the E_{acc} was analyzed in the potential of -0.05, -0.1, -0.2, -0.3 and -0.4 mV, in a buffer solution NH_3/NH_4^+ (pH 9.0), containing 5.0×10^{-6} mol L^{-1} sodium sulfide. The results are shown in Fig. S3. Although some works in the literature mention the use of an accumulation potential to improve the sensitivity in the determination of sulfur compounds [31,35,36], the results obtained in this work show that there is no significant increase current when E_{acc} is supplied to the system. Through the results obtained, the adsorptive stripping voltammetry (AdSV) was chosen to continue the studies, without application of E_{acc}, since the preconcentration of the analyte occurred spontaneously by the capacity of adsorption of sulfide ions on the AgSAE surface.

3.3 Voltammetry techniques for sulfide ion determination

The optimization of experimental parameters for linear sweep adsorptive stripping voltammetry (LSAdSV), square wave adsorptive stripping voltammetry (SWAdSV) and differential pulse adsorptive stripping voltammetry (DPAdSV) were investigated, in order to choose the best technique to determine sulfide ions on the AgSAE.

3.3.1 Linear sweep adsorptive stripping voltammetry

For the LSAdSV, the studied parameter was the scan rate in the range from 20 to 100 mVs^{-1}. The adsorptive stripping voltammograms were recorded using a buffer solution NH_3/NH_4^+ (pH 9.0) containing 1.0×10^{-6} mol L^{-1} of sodium sulfide. The t_{acc} was 120 s before each measurement.

Fig. S4A shows the linear sweep voltammograms for this study. In Fig. S4B, it is possible to observe a linear relationship between the peak cathodic current of sulfide ions and the scan rate (R = 0.997), which indicates that the species involved in the redox reaction adsorbs on the electrode surface [37]. The scan rate adopted to proceed with the experiments was 50 mVs^{-1}.

To evaluate the analytical performance in the determination of sulfide ions on the AgSAE using LSAdSV, the analytical curve was constructed. For this, the additions of sodium sulfide were examined over the potential range from –0.4 V to –1.0 V, scan rate of 50 mVs^{-1}. Before each measurement a t_{acc} of 120 s was applied. The response obtained in the concentration range of 1.1 × 10^{-6} mol L^{-1} to 1.6 ×10^{-5} mol L^{-1} of sodium sulfide, with peak with good resolution near −0.75 V, is shown in Fig. 2, and the linear relationship between the variation in peak current and the concentration is shown in the insert. The linear regression equation and correlation coefficient obtained were I(A) = 6.7 – 5.6 ×10^{-6} C_S^{2-} , R = 0.998, respectively. The values obtained for LOD, LOQ, and AS were 1.0 × 10^{-6} mol L^{-1}, 3.4 × 10^{-6} mol L^{-1}, and 5.6 µA L mol^{-1} (n = 3), respectively.

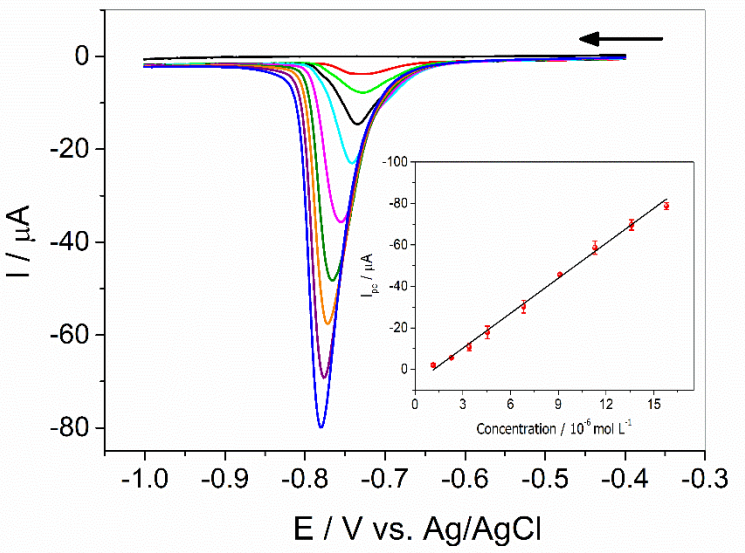

Fig. 2. LSAdSV in solution containing sodium sulfide and buffer solution NH_3/NH_4^+ (pH 9.0) in the concentration range from 1.1 × 10^{-6} mol L^{-1} - 1.6 ×10^{-5} mol L^{-1} on the AgSAE. Insert: Plot of peak current *versus* sulfide ions concentration.

3.3.2 Square wave adsorptive stripping voltammetry

SWAdSV was also used to evaluate the analytical performance of the sensor in sulfide determination. However, firstly, the parameters for applying the SWV technique, such as frequency (*f*), scan increment (ΔE_s) and pulse amplitude (E_{sw}), were optimized for exerting influence on the SWV response. The optimization of the parameters was studied using a buffer solution NH_3/NH_4^+ (pH 9.0) containing 2.5×10^{-7} mol L^{-1} of sodium sulfide, noting that before each measurement a t_{acc} of 120 s was applied. During the optimization process, one of the investigated parameters was varied while the others were kept fixe. The results obtained by the study are shown in Fig S5. The first parameter studied was the frequency, in the range of 10 to 100 Hz, keeping constant ΔE_S at 2 mV and E_{SW} at 50 mV. The peak cathodic current is significantly influenced by the increase in the square root of frequency and a linear dependence has been observed, characterizing an adsorptive system [38].There was no great variation in the peak width at half height ($w_{1/2}$) as a function of the square root of the frequency (as we can see in the Fig. S5A), therefore a frequency of 60 Hz was chosen to proceed with the studies. Then, the influence of the ΔE_S on the intensity of the peak cathodic current was evaluated. Fig. S5B shows the variation of ΔE_S in the range from 2.0 to 10 mV for the electrochemical reduction of the sulfide. An exponential increase in the peak cathodic current was observed in the studied range. However, proportionally, there was an increase in the $w_{1/2}$, interfering with peak resolution. Thus, the potential increment equal to 6.0 mV was chosen as the ideal to proceed with the experiments. The last parameter studied was the E_{SW} in the range from10 to 100 mV, as show the Fig. S5C. As can be seen, the peak cathodic current increased up to 50 mV. There were no considerable variations in the $w_{1/2}$. Therefore, the E_{SW} value of 50 mV was used because it has higher peak current and good resolution.

The linear relation between the analytical signal and sulfide ions concentration under optimized experimental conditions was evaluated. For this, successive additions of a 1.2×10^{-4} mol L^{-1} sodium sulfide stock solution prepared in NH_3/NH_4^+ (pH 9.0) were applied in the potential range of -0.4 to -1.0 V. Before each measured a t_{acc} of 120 s was applied. The voltammograms are shown in the Fig. 3 and the analytical curve, in the insert. The curve was linear in the range from 7.4×10^{-8} mol L^{-1} – 8.6×10^{-7} mol L^{-1} of sulfide ions. The linear regression equation was I(A) = 3.1 – 9.1 $\times 10^7$ C_S^{2-}, resulting in a correlation coefficient of 0.995. The LOD and LOQ were found to be 6.3×10^{-8} mol L^{-1} and 2.1×10^{-7} mol L^{-1}, respectively. The amperometric sensitivity was 9.1×10^7 µA L mol^{-1}.

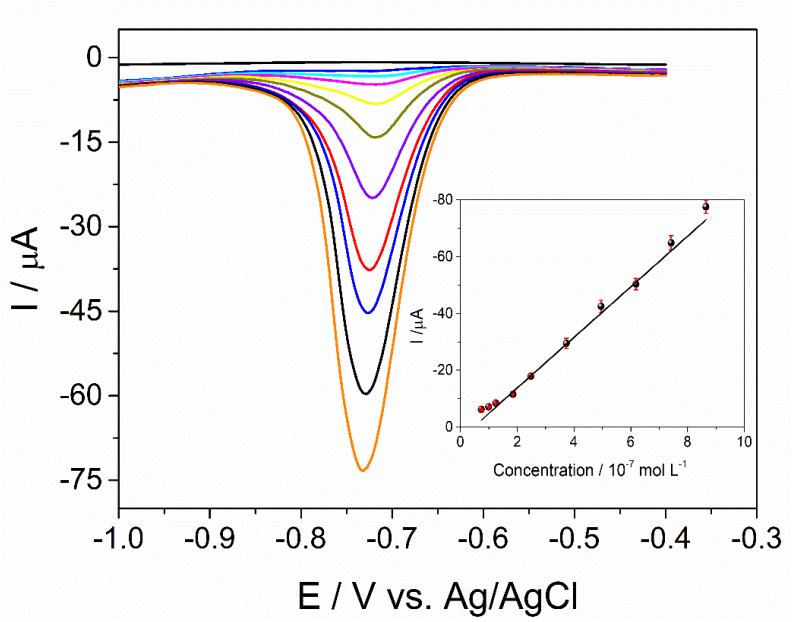

Fig. 3. SWAdSV at different sulfide ion concentrations from 7.4×10^{-8} to 8.6×10^{-7} mol L^{-1}. Insert: corresponding analytical curve.

3.3.3 Differential pulse adsorptive stripping voltammetry

The differential pulse voltammetric (DPV) parameters, such as pulse time (t_s), scan rate (υ) and pulse amplitude (E_{sw}), were optimized to find the best experimental setup for the quantification

sulfide ions. The experiments were carried out in electrolyte buffer solution NH_3/NH_4^+ (pH 9.0) containing 8.6×10^{-7} mol L^{-1} of sodium sulfide. Before each measurement an accumulation step of 120 s was performed. The t_p was analyzed in the range from 5.0 to 100 ms is shown in Fig. S6A. An exponential decrease in the peak cathodic current was observed with the increase in the pulse duration time, a characteristic behavior of the differential pulse voltammetry technique. Based on these results, t_p = 5.0 ms was chosen because it showed a higher peak of cathodic current. The second optimized parameter was the scan rate in the range from 2.5 to 15 mVs^{-1}, as can be seen in Fig. S6B. With the increase in υ, a small decrease in the peak cathodic current was observed. Although the scan rate of 2.5 and 4.0 mVs^{-1} present a higher current, υ of 10 mVs^{-1} was chosen due to the shorter analysis time, considering that there is no significant loss of signal. The pulse amplitude was analyzed in the range from 10 to 100 mV, as seen in Fig S6C. An exponential increase in the peak current of sulfide ions was observed at the pulse amplitude of 50 mV, this being the value used in further experiments.

After evaluating the parameters, a linear relation between the analytical signal and the concentration of sulfide ions was analyzed as show the Fig. 4. Successive additions of sulfide ions were carried out in the range from 4.9×10^{-7} to 1.7×10^{-6} mol L^{-1}, with good resolution peak near −0.67 V, sulphur characteristics. Before each measurement a t_{acc} of 120 s was applied.

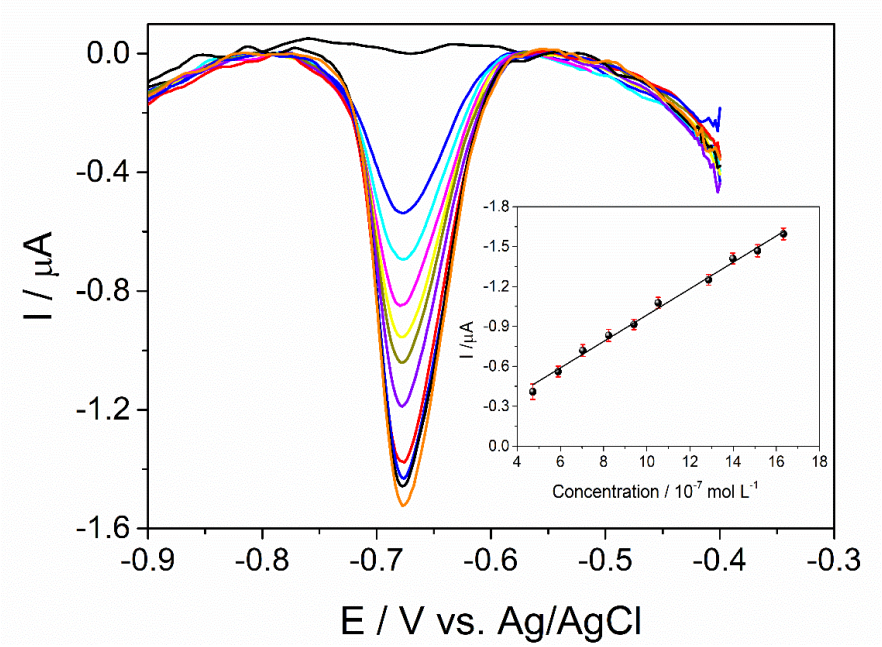

Fig. 4. DPAdSV at different sulfide ion concentrations from 4.9×10^{-7} to 1.7×10^{-6} mol L^{-1}. Insert: the corresponding analytical curve.

The analytical curve was found to be linear over the range 4.9×10^{-7} mol L^{-1} to 1.7×10^{-6} mol L^{-1}. The linear regression equation was $I(A) = -5.9 - 9.3 \times 10^{8} C_{S2}$ with a correlation coefficient of 0.995 (n = 3). The LOD and LOQ values were found to be 9.3×10^{-8} mol L^{-1} and 3.0×10^{-7} mol L^{-1}, respectively. The AS was 9.3×10^{8} µA L mol^{-1}. Table 1 summarizes the analytical parameters obtained for each technique studied.

Table 1. Analytical parameters for the LSAdSV, SWAdSV e DPAdSV technique in the determination of sulfide on the AgSAE.

Technique	Linear Range µmol L^{-1}	LOD µmol L^{-1}	LOQ µmol L^{-1}	SA µA L mol^{-1}	R
LSAdSV	1.1 – 0.16	1.0	3.4	5.6	0.998
SWAdSV	0.074 – 0.86	0.063	0.21	9.1	0.995

DPAdSV	0.49 – 1.7	0.093	0.30	9.3	0.995

3.4 Gibbs-Rozemboon Ternary Phase Diagram

To perform the application of the electroanalytical method on biodiesel samples, the best composition for the formation of microemulsion (ME) was studied. The use of ME contributed to the fuel analysis due to the increase in electrical conductivity due to the presence of electrolytes and decrease in the resistivity of the medium [21]. Furthermore, the use of ME provides a more orderly solution microenvironment capable of solubilizing most hydrophilic and lipophilic compounds. For the formation of ME, three components are essential: water, hydrophobic organic liquid and a third component capable of stabilizing the mixture, reducing the interfacial tension between the two liquids and improving the solubility and the contact surface between them. To better understand the proportion that the three ME components must present to solubilize the biodiesel sample, the construction of a ternary phase diagram is the ideal tool. Thus, it is possible to characterize the domain of the regions where the ME are formed and choose the most appropriate composition for the application of the method.

For the construction of the ternary phase diagram, several ME compositions were prepared in order to explore a vast inner region of the equilateral triangle. Biodiesel MEs were prepared by mixing a NH_3/NH_4^+ buffer solution (pH 9.0), biodiesel and propan-1-ol. Propan-1-ol is often used as a consolute (or cosurfactant) as it is a short-chain alcohol with a low molecular weight. The composition of MEs is indicated in % *v/v*. The black dots inside the equilateral triangle (Fig. 5) indicate the region where the mixture of the mentioned components form a homogeneous and translucent system, while the red dots indicate the formation of emulsions. Unlike ME, emulsions have limited stability with separation of immiscible components over time.

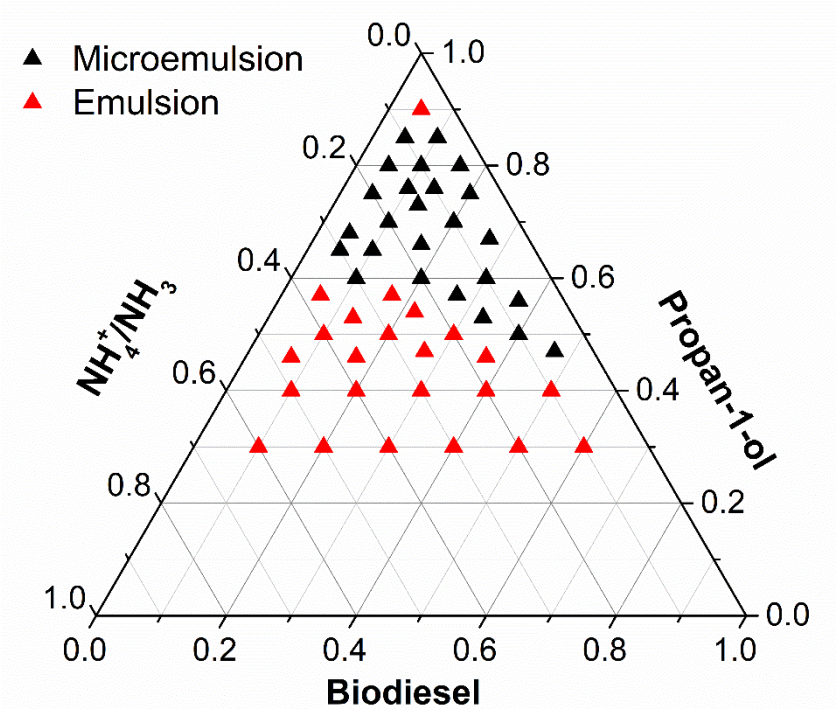

Fig. 5. Gibbs-Rozemboon ternary phase diagram for the aqueous NH_3/NH_4^+ buffer solution (pH 9.0)/propan-1-ol/biodiesel (% *v/v/v*) at 25 °C,

To evaluate the electrochemical behavior of sulfur in MEs, ten compositions were chosen in the ternary diagram of Gibbs-Rozemboon. The studied compositions of NH_3/NH_4^+ buffer solution (pH 9.0)/biodiesel/propan-1-ol were: 10/5/85, 10/5/85, 10/10/80, 15/5/80, 25/5/70, 20/10/70, 10/20/70, 20/20/60, 10/30/60 and 10/25/65 *v/v/v*. As previously mentioned, the pH control of the reaction medium is fundamental for the sulfur analysis. Thus, before each voltammetric measurement, the pH of the ME was checked.

To each microemulsion studied, a concentration of 2.5×10^{-6} mol L^{-1} sulfide ions was added. The voltammetric techniques employed in the study were LSAdSV, SWAdSV and DPAdSV. Voltammetric parameters such as peak cathodic current (I_{pc}), peak cathodic potential (E_{pc}) and peak width at half height ($w_{1/2}$) were evaluated. Among the ten MEs analyzed, only four showed significant voltammetric response, these MEs in the compositions of 5/15/80, 5/25/70,

10/30/60 and 10/25/65 *v/v/v* (*NH_3/NH_4^+* buffer solution/biodiesel/propan-1-ol). The voltammograms obtained are shown in Fig. S7. Table 2 summarizes the voltammetric parameters analyzed for each technique shown in Fig. S7. Based on these data, the composition used for the development of the electroanalytical methodology was 25/05/70% *v/v/v*, due to its stability during the analysis and intense cathodic peak current.

Table 2. Influence of microemulsion compositions on the I_{pc}, E_{pc} e $W_{1/2}$ for the LSAdSV, SWAdSV and DPAdSV techniques.

ME % (*v/v*/v)	LSAdSV			SWAdSV			DPAdSV		
	I_{pc} (μA)	E_{pc} (V)	$w_{1/2}$ (mV)	I_{pc} (μA)	E_{pc} (V)	$w_{1/2}$ (mV)	I_{pc} (μA)	E_{pc} (V)	$w_{1/2}$ (mV)
15/5/80	-2.23	-0.90	101	-0.20	-0.62	115	-1.13	-0.81	105
25/5/70	-3.23	-0.78	65	-7.56	-0.82	85	-3.12	-0.73	79
30/10/60	-3.05	-0.78	75	-7.15	-0.79	81	-2.25	-0.71	71
25/10/65	-2.26	-0.77	67	-5.91	-0.82	81	-2.03	-0.73	71

3.5 Development of electroanalytical methodology

Under the optimized conditions of ME formation, the analytical methodology was developed. The analytical performance of the AgSAE in the determination of sulfide ions was discussed in terms of linear range, amperometric sensitivity, detection and quantification limit. All studies carried out for the validation of the method were carried out in the composition 25/5/70 % *v/v/v* NH_3/NH_4^+ buffer solution/biodiesel/propan-1-ol. Fig. 6A. B and C shows the voltammograms for LSAdSV, SWAdSV, DPAdSV with the respective analytical curve. The linear regression equation obtained for LSAdSV was $I(A) = -0.56\ [S] + 9.0 \times 10^{-6}$, for SWAdSV was $I(A) = -2.7\ [S] + 4.4 \times 10^{-9}$ and for DPAdSV was $I(A) = -0.44\ [S] - 1.7 \times 10^{-8}$.

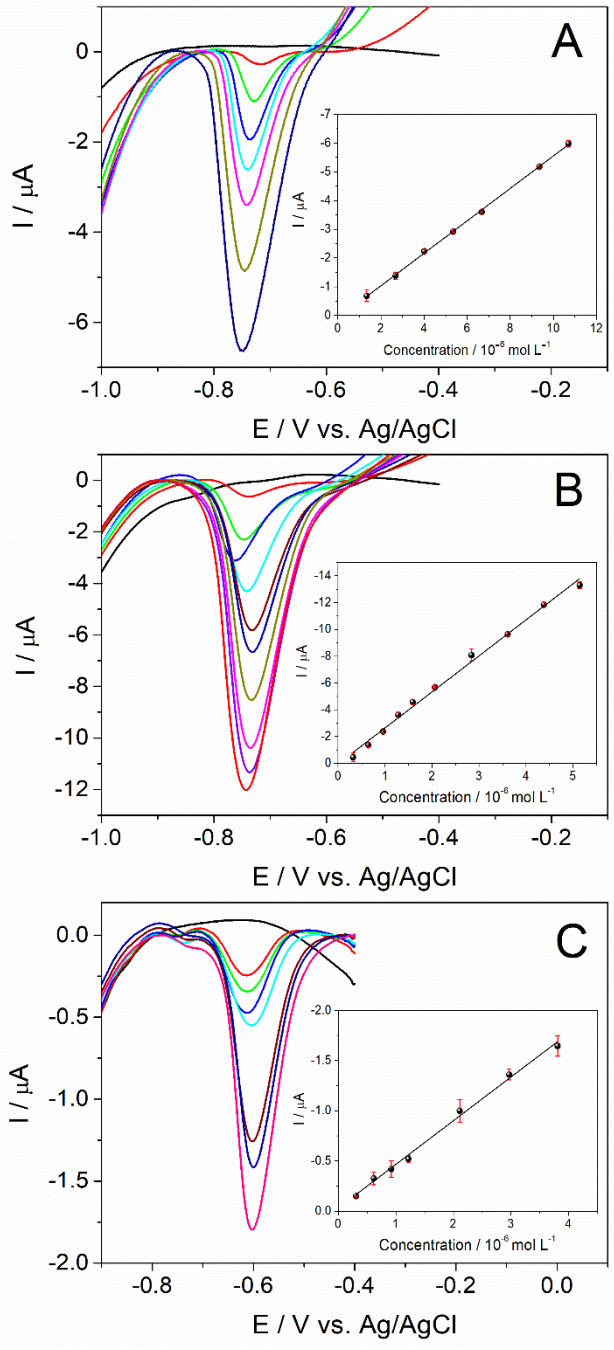

Fig. 6. (A) LSAdSV (B) SWAdSVand (C) DPAdSV for different concentrations of sulfur in the ME (25/5/70 % *v/v/v* of NH_3/NH_4^+ buffer solution (pH 9.0)/biodiesel/propan-1-ol). Insert: respective analytical curves.

Table 3 shows the figures of merit obtained in the development of the electroanalytical methodology for the LSAdSV, SWAdSV and DPAdSV techniques in biodiesel ME. Despite being a complex reaction medium, the detection limits obtained were in the order of 10^{-7} mol L^{-1}, being the smallest LOD obtained for the LSAdSV technique (0.26 µmol L^{-1} or 9.5 $\times 10^{-3}$ mg kg^{-1}). Although the LOD is smaller than the method described in the literature [18], in this work it was not necessary to use solvents dangerous to health to solubilize the biodiesel samples. In addition, the LOD found is suitable for determining the sulfur present in the biodiesel, since the LOD obtained is about 5 000 times smaller than the maximum tolerated limit of the element in the sample. Therefore, the AgSAE is a viable alternative for the determination of small amounts of sulfur in biodiesel.

Table 3. Figures of merit for determination of sulfur on the AgSAE in biodiesel samples (n = 3).

Technique	Linear Range	LOD	LOQ	SA	R
	µmol L^{-1}	µmol L^{-1}	µmol L^{-1}	µA L mol^{-1}	
LSAdSV	1.3 - 10	0.26	0.88	5.6×10^7	0.999
SWAdSV	0.31 - 5.1	0.97	0.21	2.7×10^8	0.997
DPAdSV	0.31 - 3.8	0.29	0.96	4.4×10^7	0.995

3.6 Accuracy

To determine the analytical accuracy, the recovery efficiencies of the proposed method was measured. For this, three different concentrations of sulfide was spiked in the soy biodiesel ME sample (see table 4). The values of recovery were from 80 to 116 %. These results show that the method presents an excellent degree of accuracy, since the recovery efficiencies were between 70 to 130% [39], indicating that the method offers good precision and accuracy.

Table 4. Recoveries of sulfur in biodiesel AgSAE in different voltammetric techniques (n = 3).

Technique	Add concentration (µmol L^{-1})	Found concentration (µmol L^{-1})	Spiked (%)
LSAdSV	1.6	1.9	116
	6.2	6.4	104
	10	10	103
SWAdSV	1.2	0.96	80
	3.5	3.2	93
	4.1	3.8	94
DPAdSV	0.56	0.57	109
	1.5	1.5	103
	3.2	3.3	102

3.7 Determination of Sulfur in biodiesel samples

The developed voltammetric method using AgSAE was used for determining the sulfur content in four different biodiesel ME samples. Two of these samples was provided from companies that use soy biodiesel, and two other samples was synthesized in the laboratory using the oilseeds tucumã and murumuru. The determination of sulfur in this biodiesel samples was carried out through the standard addition method, in order to minimize to the maximum the matrix interferences. The voltammetric techniques used were LSAdSV. SWAdSV and DPAdSV and the samples were spiked with known concentrations of the standards from 1.6 - 10, 1.2- 4.1, 0.56 - 3.2 µmol L^{-1}, respectively for each technique. A linear relationship was observed when peak current was plotted against the added concentration of sulfur. By extrapolation of the line the concentrations found in biodiesel samples were shown in the tables 4, 5 and 6. The sulfur

concentration was given in *m/m* units as indicated in the standards, and the accuracy of the determination was indicated in terms of coefficient of variation (CV).

Table 4. Determination of sulfur in biodiesel using LSAdSV

Sample	$C_{S^{2-}}$ (mg kg^{-1})	CV (%)
Murumuru	0.2	2.0
Tucumã	0.2	8.5
Soy 1	*	*
Soy 2	*	*

* undetectable

Table 5. Determination of sulfur in biodiesel using SWAdSV.

Sample	$C_{S^{2-}}$ (mg kg^{-1})	CV (%)
Murumuru	0.1	0.9
Tucumã	0.1	3.2
Soy 1	0.3	0.5
Soy 2	*	*

*undetectable

Table 6. Determination of sulfur in biodiesel using DPAdSV.

Sample	$C_{S^{2-}}$ (mg kg^{-1})	CV (%)
Murumuru	0.2	38.0
Tucumã	0.1	21.4
Soy 1	0.9	17.8

Soy 2	*	*

* undetectable

Analyzing the data obtained from the tables, it is possible to observe that in no sample analyzed the sulfur content was above the maximum limit of 50 mg kg^{-1} established by the ANP. The DPAdSV technique presented high CV values, impairing the accuracy of the method since the adequate CV for a trace analysis is up to 20 %. On the other hand, the LSAdSV and SWAdSV techniques proved to be efficient in the determination of sulfur traces in biodiesel, with a good CV, which means the value of the average concentration varies very little around the true value and could be an alternative procedure for the analysis of this element.

Conclusion

The proposed voltammetric method based on AgSAE, provides a rapid and sensitive determination of sulfur, which allowed to quantify the element in different samples of biodiesel microemulsion. The use of the biodiesel microemulsion proved to be promising since it is a simple and fast way to prepare the sample, obtained by mixing three components, eliminating traditional methods of extraction, acid digestion, and solubilization by organic solvents. The best ratio for microemulsion formation to be applied in the development of the electroanalytical methodology and in the sample determination was 25% NH_3/NH_4^+ (pH 9.0), 5.0 % biodiesel, and 70 % propan-1-ol. Furthermore, the LSAdSV, SWAdSV and DPAdSV techniques were evaluated for the construction of the method, with LSAdSV being the one that reached the lowest detection limit (9.5×10^{-3} mg kg^{-1}). The results obtained confirm that method is attractive when compared to current sulfur analysis methods in biodiesel recommended by fuel regulatory agencies. Through the developed methodology, it was possible to determine sulfur concentrations in different samples of biodiesel, which makes this an alternative method, and it may in the future be incorporated into biofuel quality control analyses.

Declaration of conflicts interest

The authors declare no conflicts of interest.

Acknowledgments

The authors gratefully acknowledge the financial support provided by São Paulo Research Foundation (FAPESP) grants no. 2018/12131-6, 2014/50945-4, 2017/22401-8 and 2011/05633-6.

References

[1] G. Dwivedi, S. Jain, M.P. Sharma, Impact analysis of biodiesel on engine performance—A review, Renew. Sustain. Energy Rev. 15 (2011) 4633–4641. doi:10.1016/J.RSER.2011.07.089.

[2] D. Singh, D. Sharma, S.L. Soni, S. Sharma, D. Kumari, Chemical compositions, properties, and standards for different generation biodiesels: A review, Fuel. 253 (2019) 60–71. doi:10.1016/J.FUEL.2019.04.174.

[3] C.G. Young, R.S. Amais, D. Schiavo, E.E. Garcia, J.A. Nóbrega, B.T. Jones, Determination of sulfur in biodiesel microemulsions using the summation of the intensities of multiple emission lines, Talanta. 84 (2011) 995–999. doi:10.1016/j.talanta.2011.01.008.

[4] Q. Xie, L. Cai, F. Xia, X. Liang, Z. Wu, Y. Liu, X. Li, M. Lu, Y. Nie, J. Ji, High vacuum distillation for low-sulfur biodiesel production: From laboratory to large scale, J. Clean. Prod. 223 (2019) 379–385. doi:10.1016/J.JCLEPRO.2019.03.160.

[5] I.P. Lôbo, S.L.C. Ferreira, R.S. da Cruz, Biodiesel: parâmetros de qualidade e métodos analíticos, Quim. Nova. 32 (2009) 1596–1608. doi:10.1590/S0100-40422009000600044.

[6] J. Christopher, M.B. Patel, S. Ahmed, B. Basu, Determination of sulphur in trace levels in petroleum products by wavelength-dispersive X-ray fluorescence spectroscopy, Fuel. 80 (2001) 1975–1979. doi:10.1016/S0016-2361(00)00213-1.

[7] Lydia R. Barker, W. Robert Kelly, William F. Guthrie, Determination of Sulfur in Biodiesel and Petroleum Diesel by X-ray Fluorescence (XRF) Using the Gravimetric Standard Addition Method−II †, Energy and Fuels. 22 (2008) 2488–2490. doi:10.1021/EF800165J.

[8] S. Sani, M.U. Kaisan, D.M. Kulla, A.I. Obi, A. Jibrin, B. Ashok, Determination of physico chemical properties of biodiesel from Citrullus lanatus seeds oil and diesel blends, Ind. Crops Prod. 122 (2018) 702–708. doi:10.1016/J.INDCROP.2018.06.002.

[9] W.P. de Oliveira Filho, D.L.G. Borges, T.D. Saint'Pierre, M. Dupim, F. Vale, B. Marques, F.R. Medeiros, Assessment of the equivalence and correlation between total sulfur determination methods in biodiesel: An use of isotope dilution inductively coupled plasma mass spectrometry, Fuel. 202 (2017) 227–232. doi:10.1016/J.FUEL.2017.03.097.

[10] G.L. Donati, R.S. Amais, J.A. Nóbrega, Interference standard and oxide ion detection as strategies to determine phosphorus and sulfur in fuel samples by inductively coupled plasma quadrupole mass spectrometry, J. Anal. At. Spectrom. 27 (2012) 1274–1279.

doi:10.1039/C2JA30038A.
[11] R.S. Amais, C.D.B. Amaral, L.L. Fialho, D. Schiavo, J.A. Nóbrega, Determination of P, S and Si in biodiesel, diesel and lubricating oil using ICP-MS/MS, Anal. Methods. 6 (2014) 4516–4520. doi:10.1039/C4AY00279B.
[12] R.S. Amais, G.L. Donati, J.A. Nóbrega, Interference Standard Applied to Sulfur Determination in Biodiesel Microemulsions by ICP-QMS, 23 (2012) 797–803.
[13] T.F. Rozan, S.M. Theberge, G. Luther, Quantifying elemental sulfur (S0), bisulfide (HS-) and polysulfides (S(x)2-) using a voltammetric method, Anal. Chim. Acta. 415 (2000) 175–184. doi:10.1016/S0003-2670(00)00844-8.
[14] M. Antonietta Baldo, S. Daniele, C. Bragato, G.A. Mazzocchin, Voltammetric investigation on sulfide ions in aqueous solutions with mercury-coated platinum microelectrodes, Anal. Chim. Acta. 464 (2002) 217–227. doi:10.1016/S0003-2670(02)00490-7.
[15] D.M. Serafim, N.R. Stradiotto, Determination of sulfur compounds in gasoline using mercury film electrode by square wave voltammetry, Fuel. 87 (2008) 1007–1013. doi:10.1016/J.FUEL.2007.07.012.
[16] Deqian Huang, Bolei Xu, Jie Tang, Jian Luo, Luhong Chen, Lili Yang, Zhengbiao Yang, Shuping Bi, Indirect determination of sulfide ions in water samples at trace level by anodic stripping voltammetry using mercury film electrode, Anal. Methods. 2 (2010) 154–158. doi:10.1039/B9AY00183B.
[17] D.R. Fernandes, P.F. de Aguiar, J.L. Miranda, E. D'Elia, Electrochemical determination of elemental sulfur in Brazilian naphtha: method and validation, J. Appl. Electrochem. 2009 3910. 39 (2009) 1655–1663. doi:10.1007/S10800-009-9855-9.
[18] H.D.C. Viégas, J.M.S. Almeida, C.A. Lacerda, J.B. Silva, A.L.B. Marques, E.P. Marques, A rapid and sensitive voltammetric determination of sulphur in biodiesel in samples no treated and treated with TMAH, Fuel. 202 (2017) 464–469. doi:10.1016/J.FUEL.2017.04.048.
[19] C.-H. Lee, C.-L. Wang, H.-F. Lin, C.-Y. Chai, M.-Y. Hong, C.-K. Ho, Toxicity of tetramethylammonium hydroxide: Review of two fatal cases of dermal exposure and development of an animal model:, Http://Dx.Doi.Org/10.1177/0748233710391990. 27 (2011) 497–503. doi:10.1177/0748233710391990.
[20] L. CH, W. CL, L. HF, C. CY, H. MY, H. CK, Toxicity of tetramethylammonium hydroxide: review of two fatal cases of dermal exposure and development of an animal model, Toxicol. Ind. Health. 27 (2011) 497–503. doi:10.1177/0748233710391990.
[21] L.F.P.P.L.F.P.P. Moreira, M.A.M.A. Beluomini, J.C.J.C. de Souza, N.R.N.R. Stradiotto, Study of the Electrochemical Behavior of Biodiesel Microemulsion, Electroanalysis. 29 (2017) 1941–1949. doi:10.1002/elan.201700174.
[22] A. de Jesus, M.M. Silva, M.G.R. Vale, The use of microemulsion for determination of sodium and potassium in biodiesel by flame atomic absorption spectrometry, Talanta. 74 (2008) 1378–1384. doi:10.1016/j.talanta.2007.09.010.
[23] G.F.S. dos Santos, R. de Q. Ferreira, Determination of Pb(II) and Cu(II) in microemulsified biodiesel using boron-doped diamond electrode, Microchem. J. 156 (2020) 104849. doi:10.1016/j.microc.2020.104849.
[24] G.C. Sedenho, L.L. Paim, N.R. Stradiotto, Simple and direct potentiometric determination of potassium ions in biodiesel microemulsions at a glassy carbon electrode modified with nickel(II) hexacyanoferrate nanoparticles, Anal. Methods. 5 (2013) 4145–4151. doi:10.1039/c3ay40774h.
[25] L.C. Martiniano, V.R. Abrantes, S.Y. Neto, E.P. Marques, T.C.O.O. Fonseca, L.L. Paim, A.G. Souza, N.R. Stradiotto, R.Q. Aucélio, G.H.R.R. Cavalcante, A.L.B.B. Marques, Direct simultaneous determination of Pb(II) and Cu(II) in biodiesel by anodic stripping

voltammetry at a mercury-film electrode using microemulsions, Fuel. 103 (2013) 1164–1167. doi:10.1016/j.fuel.2012.07.002.
[26] V. Hrdlička, M. Choińska, B. Ruiz Redondo, J. Barek, T. Navrátil, Determination of heavy metal poisoning antidote 2,3-dimercapto-1-propanesulfonic acid using silver solid amalgam electrode, Electrochim. Acta. 354 (2020) 136623. doi:10.1016/J.ELECTACTA.2020.136623.
[27] C.C.G. Silva, L.M. Silva, B.C. e Silva, S.S. Garrido, M.V. Boldrin, D. De Souza, Cathodic stripping voltammetric determination of β-cyfluthrin, a pyrethroid insecticide, using polished silver solid amalgam electrode, J. Solid State Electrochem. 2020 248. 24 (2020) 1819–1826. doi:10.1007/S10008-020-04538-W.
[28] G. Völgyi, E. Baka, K.J. Box, J.E.A. Comer, K. Takács-Novák, Study of pH-dependent solubility of organic bases. Revisit of Henderson-Hasselbalch relationship, Anal. Chim. Acta. 673 (2010) 40–46. doi:10.1016/j.aca.2010.05.022.
[29] A.N.D.S. Dantas, D. De Souza, J.E.S. De Lima, P. De Lima-Neto, A.N. Correia, Voltammetric determination of ketoconazole using a polished silver solid amalgam electrode, Electrochim. Acta. 55 (2010) 9083–9089. doi:10.1016/j.electacta.2010.08.026.
[30] Y. Kuang, S. Chen, Y. Long, Highly sensitive and selective determination of hydrogen sulfide by resonance light scattering technique based on silver nanoparticles, Anal. Bioanal. Chem. 409 (2017) 4001–4008. doi:10.1007/s00216-017-0343-5.
[31] J.S. Redinha, C. Paliteiro, J.L.C. Pereira, Determination of sulfide by square-wave polarography, Anal. Chim. Acta. 351 (1997) 115–125. doi:10.1016/S0003-2670(97)00333-4.
[32] L. Contreira-Pereira, M. Yücel, D. Omanovic, J.P. Brulport, N. Le Bris, Compact autonomous voltammetric sensor for sulfide monitoring in deep sea vent habitats, Deep. Res. Part I Oceanogr. Res. Pap. 80 (2013) 47–57. doi:10.1016/j.dsr.2013.05.014.
[33] K.J. Umiker, M.J. Morra, I. Francis Cheng, Aqueous sulfur species determination using differential pulse polarography, Microchem. J. 73 (2002) 287–297. doi:10.1016/S0026-265X(02)00097-8.
[34] A.I. Vogel, A Textbook of Quantitative Inorganic Analysis, 4th ed., London, 1978.
[35] L.M. Aleixo, S. Rath, O.E.S. Godinho, A.U. Ivaska, Determination of total sulphur in ethanol by reduction using Raney nickel and detection by cathodic stripping voltammetry, Analyst. 113 (1988) 1427–1429. doi:10.1039/AN9881301427.
[36] R. Piech, B. Baś, W.W. Kubiak, B. Paczosa-Bator, Fast cathodic stripping voltammetric determination of elemental sulfur in petroleum fuels using renewable mercury film silver based electrode, Fuel. 97 (2012) 876–878. doi:10.1016/J.FUEL.2012.01.079.
[37] A.J. Bard, L.R. Faulkner, Electochemical Method: Fundamentlas and Applications, 2nd ed., Wiley, 2000.
[38] D. de Souza, S.A.S. Machado, L.A. Avaca, Square wave voltammetry. Part I: Theoretical aspects, Quim. Nova. 26 (2003) 81–89. doi:10.1590/S0100-40422003000100015.
[39] GUIDELINES ON PERFORMANCE CRITERIA FOR METHODS OF ANALYSIS FOR THE DETERMINATION OF PESTICIDE RESIDUES IN FOOD AND FEED, (n.d.).

Instituto de Química
Departamento de Química Analítica

Relatório Científico de Pós-Doutorado

Sensores eletroquímicos baseados em eletrodos impressos modificados com nanoporos metálicos e monitorados por rede sem fio para determinação de flavonóides nos resíduos da indústria cítrica

Processo FAPESP n° 2018/12131-6

Período: 19 de outubro de 2021 - 31 de janeiro de 2024

Maísa Azevedo Beluomini
Pós-doutoranda

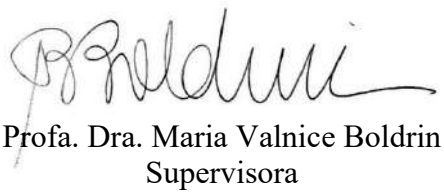

Profa. Dra. Maria Valnice Boldrin
Supervisora

Araraquara,
Fevereiro de 2024.

Sumário

1. Resumo do projeto proposto

A água residual da indústria cítrica é considerada um agente de alto poder poluente devido a sua rica composição orgânica. Por outro lado, o controle de modo rápido e eficiente destes compostos nos processos industriais é de alta relevância para a avaliação do reaproveitamento da biomassa, para fins mais econômicos, estratégicos e ambientalmente amigáveis. Neste contexto, os sensores eletroquímicos baseados em eletrodos impressos podem ser uma alternativa com respostas confiáveis, rápidas, de fácil manuseio e de baixo custo, pois permitem o desenvolvimento de métodos mais robustos, com elevado desempenho, portabilidade e superfícies livres de contaminantes. Assim, este projeto tem como objetivo desenvolver sensores eletroquímicos baseados em eletrodos impressos modificados com materiais metálicos nanoporosos para determinação dos flavonóides hesperidina, narirutina, sinensitina e naringenina. A oxidação destes analitos sobre os sensores de elevada condutividade elétrica e atividade eletrocatalítica proporcionará alta sensibilidade e seletividade na detecção desses flavonóides em resíduos da indústria cítrica. Além disso, pretende-se combinar a portabilidade desses sensores com a comunicação sem fio, através do desenvolvimento de plataformas que permitirá coletar, processar e enviar os dados via wi-fi para um smartphone/laptop, visando a aplicação em campo e em tempo real, através de dispositivos inteligentes, com baixo consumo de energia e robustos.

2. Realizações no período

Uma extensa revisão bibliográfica foi realizada sobre a construção de dispositivos eletroquímicos portáteis e com envio de sinal a distância. Durante este período finalizamos a colaboração com o Prof. Dr. Eduardo Paciência Godoy, do Instituto de Ciências e Tecnologia da UNESP campus Sorocaba, que nos auxiliou no desenvolvimento de um sistema de comunicação sem fio entre o sinal fornecido pelos eletrodos na oxidação/redução dos flavonoides e um software. Os testes realizados no circuito desenvolvido apresentaram resultados satisfatórios, e a placa de aquisição ESP32 para transmissão dos dados sem fio foi utilizada. A construção do circuito foi finalizada, utilizando a interface gráfica *LabView* da *National Instruments*. Neste software, foi possível visualizar em tempo real o sinal proveniente do eletrodo, devido a conexão entre a saída amplificada do circuito e a entrada analógica da placa de aquisição ligada a um

computador. No entanto, foi observado falta de estabilidade no sinal e tempo de resposta mais demorado em comparação ao potenciostato comercial da PalmSens3, utilizado na calibração. Assim, visando aprimorar o circuito desenvolvido, realizamos uma nova colaboração com o Parque Tecnológico de Ribeirão Preto (Supera), para alcançarmos os objetivos desse projeto. Com base nos dados apresentados no relatório anterior, aprimoramos o circuito, que antes ainda constava em *protoboard,* para um circuito próprio, mais robusto, menos instável e com capacidade de envio de dados via Wi-fi e Bluetooh. A comunicação de rede sem fio feita anteriormente era do tipo TCP/IP (Wi-fi), e tornando necessária a presença de um roteador ou *access point*. Essa comunicação, muitas vezes, não é eficaz em conectar longas distâncias, e muitas vezes a presença de uma simples parede pode deixar o sinal muito fraco, além de gastar mais energia. Além disso, qualquer instabilidade no roteador ou *access point,* irá dificultar a utilização do equipamento. Outras comunicações sem fio podem ser interessantes e, contornam esse problema se tiverem uma potência adequada, porque são do tipo ponto a ponto, não necessitando de um dispositivo intermediário. Assim, foi inserido no dispositivo os dois módulos de conexão, Wi-fi e Bluetooth. A fonte do dispositivo também foi aprimorada, sendo possível operar via bateria ou cabo. Para deixar o sistema de circuitos protegido e de fácil operação, foi realizada a impressão de um caixa em impressora 3D.

Durante este período também foi realizado o estágio de pesquisa no exterior, sob supervisão do Prof. Dr. Frank Marken na University of Bath, Reino Unido, como consta no relatório BEPE anexado em "outros documentos". Os resultados foram publicados na revista Electrochemistry Communications, intitulado: Polymer of intrinsic microporosity (PIM-1) enhances hydrogen peroxide production at Gii-Sens graphene foam electrodes - https://doi.org/10.1016/j.elecom.2022.107394. Além disso, obtivemos resultados promissores com os polímeros de microporosidade intrínseca (PIM-1) e continuamos nossa colaboração com o Professor Marken mesmo após a finalização do projeto BEPE. Devido ao extenso número de dados coletados neste período, estamos finalizando mais outro artigo que será submetido à ACS Applied Materials & Interfaces.

Ademais, durante o período desde relatório, a Dra. Maísa A. Beluomini também participou dos principais congressos da área, tendo a oportunidade de apresentar os trabalhos: 1) "*Simultaneous analysis of hesperidin and narirutin in wastewater from citrus industry using a screen-printed electrode modified with 3D-nanoporous platinum*" no 74th Annual Meeting of the International Society of Electrochemistry, em Lyon – France, 2023; 2) Electrochemical Investigation of Triphasic Oxygen Storage in Wet

Nanoparticulate Polymer of Intrinsic Microporosity (PIM-1), XXIV Simpósio Brasileiro de Eletroquímica e Eletroanalítica, Porto Alegre – RS, 2023. Também é importante destacar os trabalhos que foram apresentados em outros congressos e publicados através de colaborações e co-supervisões científicas realizadas pela pós-doutoranda, conforme detalhado nos itens 7 e 8 deste relatório

3. Resultados e Discussão

3.1. Construção do dispositivo tipo mini potenciostato sem fio.

A elaboração de um dispositivo mais robusto e com uma interface mais tecnológica foi realizada em parceria com o Parque Tecnológico SUPERA, de Ribeirão Preto. Foi desenvolvido um circuito que pudesse ser utilizado via bateria e fonte (porta USB de um computador), com menos ruído, resposta mais rápida, maior amplificação do sinal e envio por bluetooth e Wi-Fi. A seguir, será descrita as melhorias realizadas no circuito inicial.

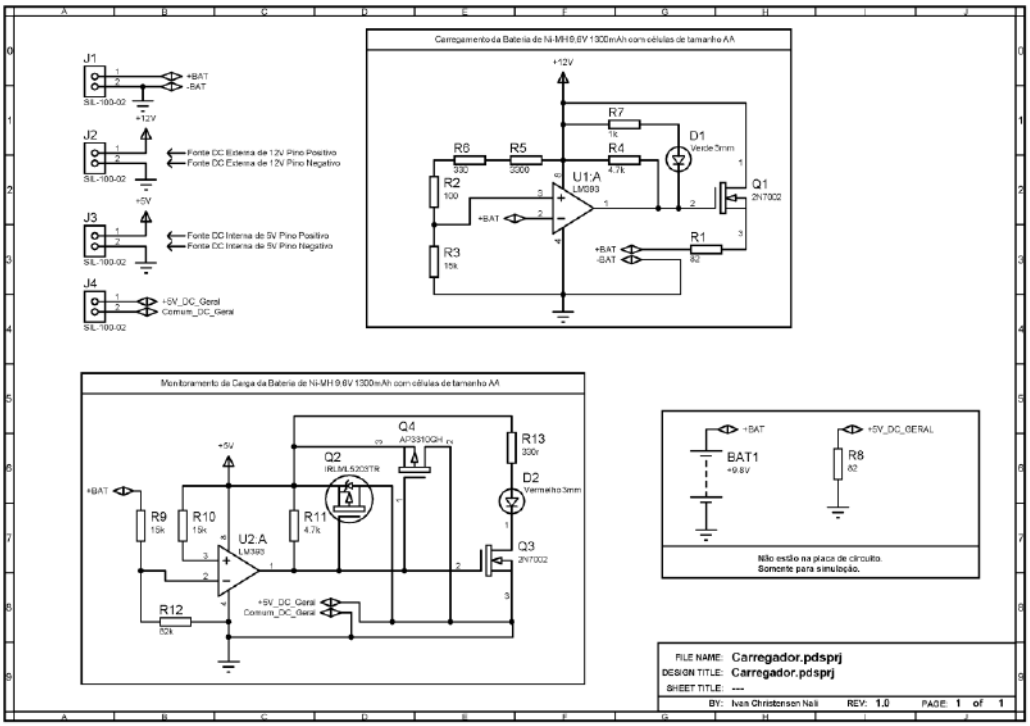

Figura 1. Circuito de carregamento e monitoramento da bateria que alimenta o dispositivo.

Na Figura 1 é apresentado o circuito de carregamento e monitoramento da bateria interna que alimenta o dispositivo de medição, o circuito de carregamento (U1:A) avalia a tensão elétrica da bateria em comparação com o valor da tensão elétrica da conexão para fonte de alimentação externa (J2). Caso a tensão da bateria esteja menor do que sua tensão padrão (9,6V), a passagem de corrente elétrica à bateria é permitida. Quando o carregamento da bateria se completa, a passagem de corrente elétrica de carregamento é interrompida e um emissor de luz LED (D1) é aceso para a indicação do final do carregamento.

O circuito de monitoramento (U2:A) funciona de forma semelhante ao de carregamento, possui a comparação de tensão elétrica com um valor de referência. Através desta comparação, quando a tensão elétrica da bateria diminui para o valor de 6V, um emissor de luz LED (D2) é acionado para a indicação de que a bateria deve ser carregada.

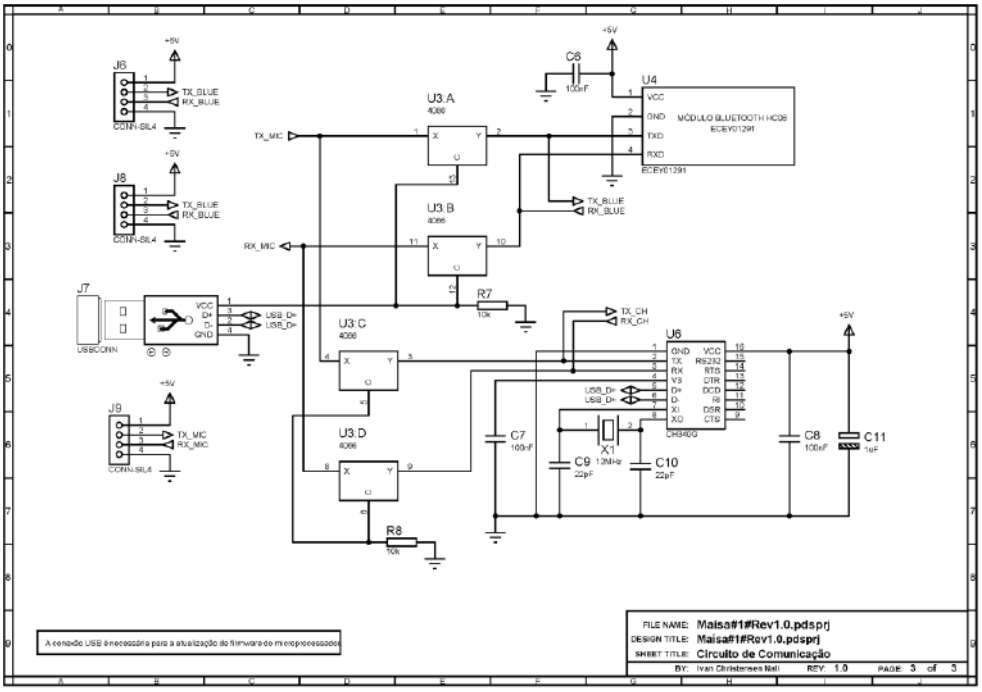

Figura 2. Circuito elétrico de comunicação.

A Figura 2 mostra o esquema elétrico do circuito de comunicação. Este circuito é composto por dois processadores, um com a função de possibilitar a conexão sem fio

(U4) e outro para a conexão através da porta USB de um computador (U6). Apesar do dispositivo de medição ser portátil, característica que foi possível através da incorporação do processador periférico de comunicação sem fio, todo o funcionamento do dispositivo de medição é realizado através de um processador principal que, para funcionar, precisa ser programado através de uma conexão cabeada. O processador principal do dispositivo de medição é o ATMEGA328P, este processador possui o periférico interno que é denominado porta serial para a programação de sua memória interna. A porta serial realiza a comunicação através de dois pinos, um de recepção e outro de transmissão. Os computadores continuam incorporando a comunicação serial em sua placa mãe, entretanto não a disponibilizam externamente como uma de suas saídas de conexão. Uma das alternativas mais utilizadas comercialmente é a incorporação de um processador periférico de conversão de padrões que consiga se conectar diretamente à conexão USB do computador. No caso do dispositivo de medição foi incorporado o processador periférico U6, que possibilita a conexão direta via USB fornecendo o padrão de comunicação serial para a gravação da memória interna do processador principal do dispositivo de medição.

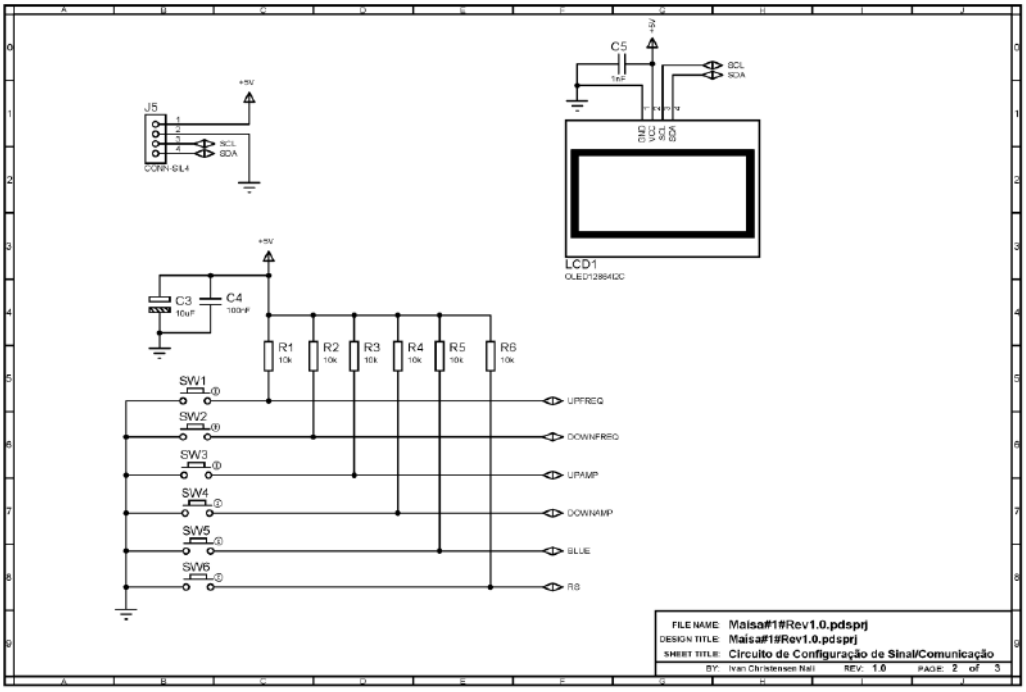

Figura 3. Componentes da interface de interação.

A Figura 3 contém os componentes da interface de interação do dispositivo de teste. Essa interação ocorre através da utilização de botões (SW1, SW2, SW3, SW4 e SW3) do tipo ação momentânea (o botão possui um dispositivo mecânico que faz com que seus contatos elétricos permaneçam abertos, somente sendo fechados durante a aplicação constante de pressão manual sobre os botões) e de um visor (LCD1) do tipo OLED com a área visível de 1,3 polegadas. O visor é do tipo monocromático (o fundo é na cor preta e os pontos visíveis, se acionados, apresentam cor branca). O visor exibe as informações de amplitude e frequência do sinal elétrico que será aplicado ao eletrodo de trabalho, e essas informações podem ser modificadas pelos botões (SW1, SW2, SW3 e SW4). Além dessas duas informações, o visor exibe o estado do circuito de comunicação, esse estado pode ser circuito ativado ou desativado, o qual pode ser alterado pelo botão SW5. O botão SW6 tem a função de interruptor da alimentação elétrica da bateria interna (bateria recarregável de Ni-MH de 9,6V 1300mAh de 8 células). O botão SW6 não é do tipo ação momentânea, isso significa que, após ser pressionado seus contatos permanecerão fechados mesmo que não haja mais a aplicação de pressão sobre o botão. Desta forma, para que os contatos sejam abertos novamente, outra pressão e soltura deve ser aplicada ao botão.

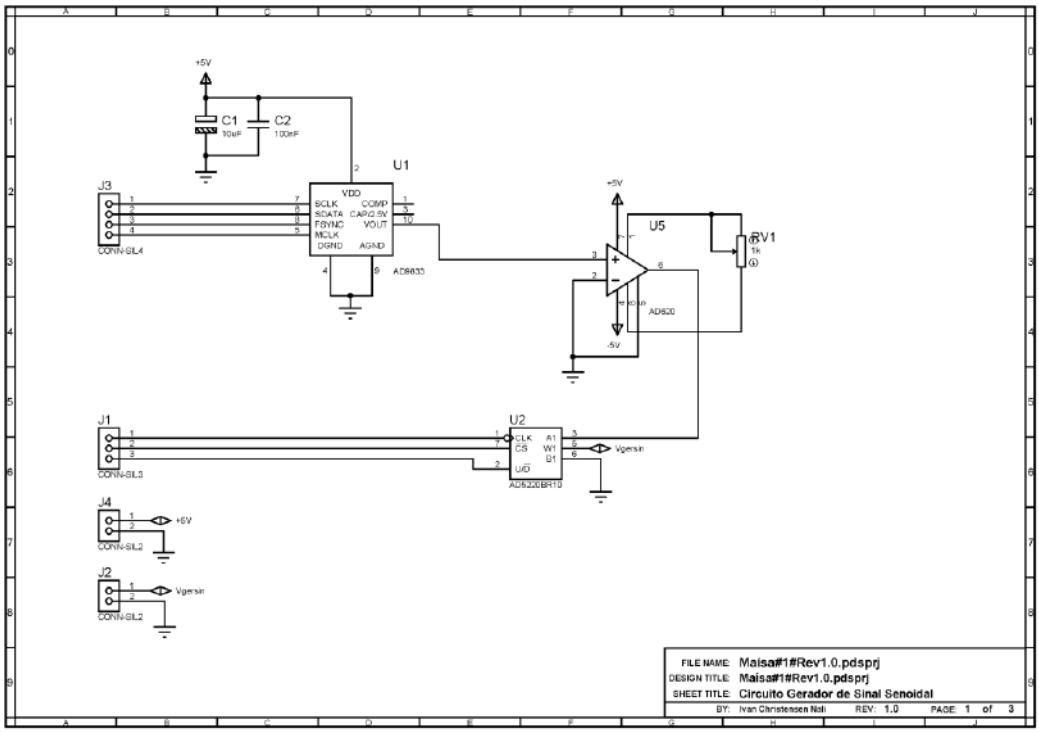

Figura 4. Circuito gerador de sinal senoidal.

A Figura 4 contém o circuito gerador de sinal senoidal que é composto por processador periférico do tipo Sintetizador Digital Direto (Direct Digital Synthesizer, sigla DDS - componente U1), um amplificador de sinal (U5) e um potenciômetro digital (U2). O DDS tem a função de geração do sinal elétrico senoidal de forma suavizada. A suavização é necessária para a eliminação dos degraus de variação de tensão elétrica dos geradores de sinal baseados somente em conversores Digital Analógico convencionais. Esses degraus na tensão elétrica do sinal senoidal ocasionam muitos ruídos na forma de onda, esses ruídos deformam o sinal elétrico e diminuem a faixa de resposta do sensor. O DDS permite a alteração da frequência do sinal elétrico quando comandado pelo processador principal do dispositivo de medição, para a alteração da amplitude foi utilizado um potenciômetro digital (U2). O processo de alteração do sinal elétrico que estará presente no eletrodo de trabalho basicamente ocorre da seguinte forma: o processador principal do dispositivo de medição realiza a interação com o circuito de configuração de sinal/comunicação e, em seguida, envia comandos ao DDS que modifica a frequência do sinal elétrico. Em seguida o processador principal envia comandos ao potenciômetro digital que altera a amplitude do sinal.

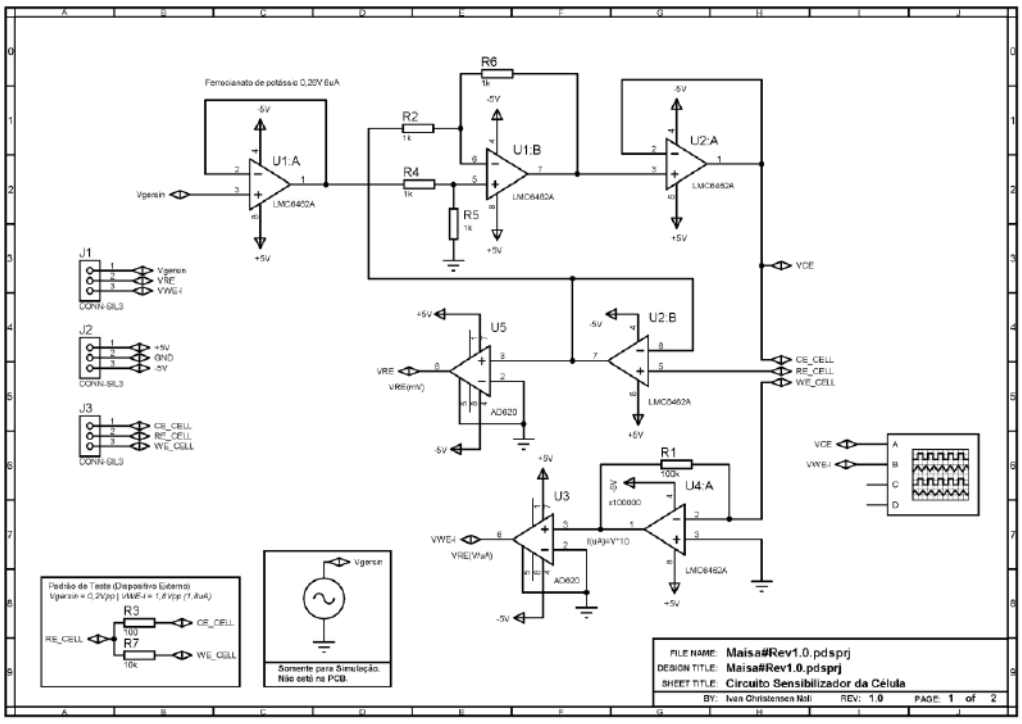

Figura 5. Esquema do circuito de sensibilização do eletrodo.

A Figura 5 possui o esquema elétrico do circuito de sensibilização da célula (eletrodos de trabalho, referência e contra). Este circuito tem as três funções necessárias para a avaliação do potencial químico da amostra em avaliação, essas funções são o fornecimento e o controle do fornecimento de uma tensão de alimentação para o eletrodo de trabalho (componentes U1:A, U1:B e U2:A), a leitura da tensão elétrica presente durante o processo de reação química da amostra perante a aplicação do potencial elétrico (U2:B e U5), e a leitura de corrente elétrica circulante durante o período de aplicação da tensão elétrica (U4:A e U3).

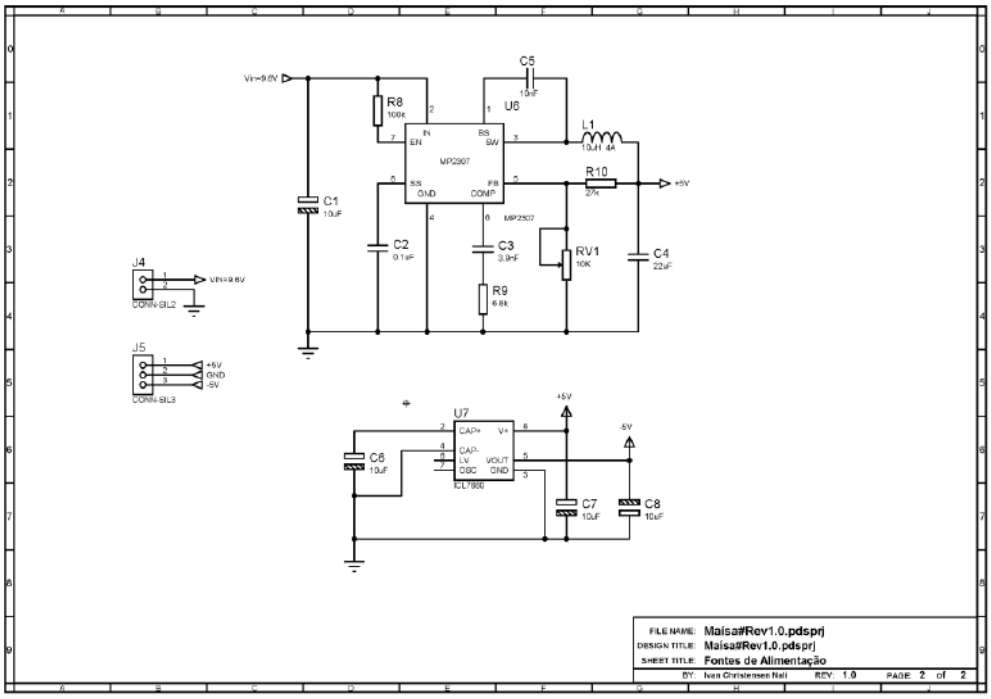

Figura 6. Esquema elétrico das fontes de alimentação do dispositivo.

A Figura 6 contém o esquema elétrico de duas fontes de alimentação do tipo conversor CC-CC (tanto a entrada quanto a saída funcionam com a presença de uma corrente elétrica do tipo contínua). A que está localizada na parte superior da imagem é uma fonte que pode receber em sua entrada uma tensão elétrica na faixa de 6 V a 24 V, seu circuito realiza uma regulação capaz de diminuir a tensão de entrada para uma saída constante de 5V. A capacidade de fornecimento de corrente elétrica dessa fonte é de 3 A. A parte inferior da imagem contém o esquema elétrico da segunda fonte, essa fonte não realiza diminuição de sua tensão elétrica de entrada, sua função é uma inversão de polaridade. Isso significa que a tensão elétrica que é fornecida em sua entrada

permanecerá a mesma em amplitude, mas o sentido da corrente elétrica circulante será invertido.

Após a otimização de todos os componentes do circuito, foi realizada a impressão, em impressora 3D, de um suporte para o encaixe do circuito, inserção do eletrodo e visor, como mostra a Figura 7.

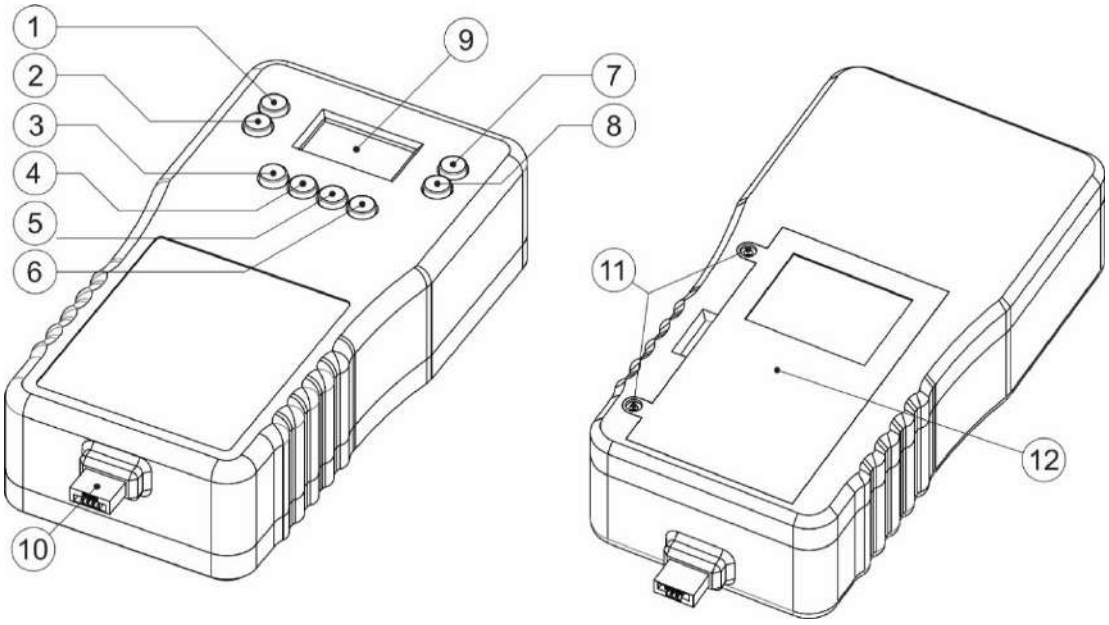

Figura 7. Descrição das partes do Equipamento.

Os números indicados na Figura 7, referem-se:

1 Botão para Ativação/Desativação da Comunicação sem fio.
2 Botão não utilizado (Reservado para incorporação de novas funções).
3 Botão para Aumento da Amplitude do Sinal Elétrico do Eletrodo de Trabalho.
4 Botão para Diminuição da Amplitude do Sinal Elétrico do Eletrodo de Trabalho.
5 Botão para Aumento da Frequência do Sinal Elétrico do Eletrodo de Trabalho.
6 Botão para Diminuição da Frequência do Sinal Elétrico do Eletrodo de Trabalho.
7 Botão para Ativar a Realização de uma amostragem de leituras de Tensão Elétrica no Eletrodo de Trabalho, e de Corrente Elétrica do Eletrodo de Trabalho.
8 Botão para Ligar/Desligar o Equipamento.

9 Visor para exibição das informações do Sinal Elétrico que será fornecido ao Eletrodo de Trabalho durante o período de realização da Amostragem

10 Conexão para Células de Leitura.

11 Parafusos para fixação da Tampa de Acesso que permite a Inserção/Retirada da Bateria Interna Recarregável.

12 Tampa de Acesso que permite a Inserção/Retirada da Bateria Interna Recarregável.

A seguir, são mostradas as imagens do (a) circuito antes de ser encaixado no suporte feito sob medida, (b) o circuito dentro do suporte, (c) onde é localizado a bateria, (d) o encaixe do eletrodo impresso, (e) as analisas de comunicação do dispositivo com o osciloscópio e (f) o dispositivo final.

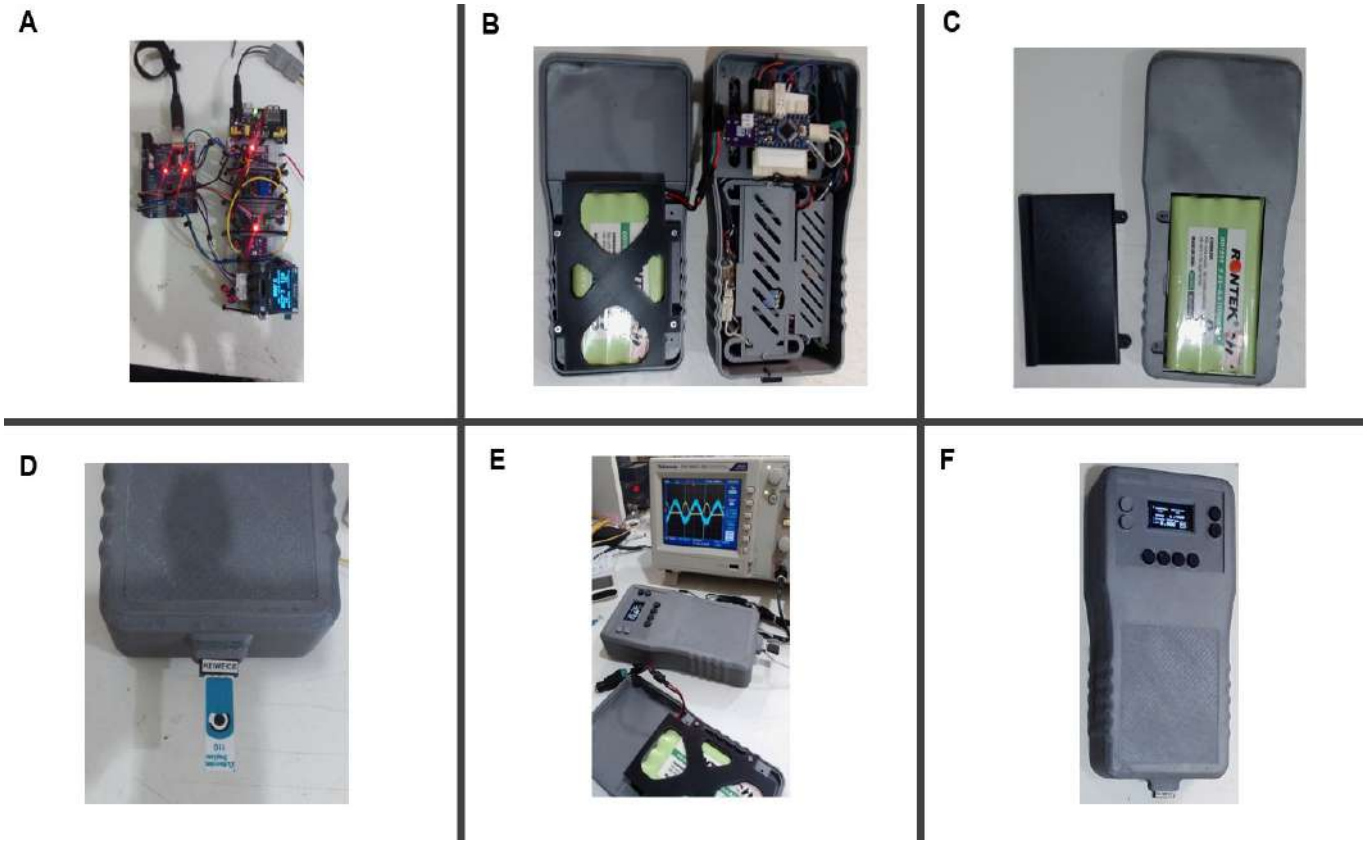

Figura 8. Fotografias de algumas etapas do desenvolvimento do dispositivo. A) Circuitos elétricos em fase de teste, B) adaptação para a caixa impressa, C) encaixe da bateria, D) local para inserção do eletrodo impresso, E) teste de sinal/ruído no osciloscópio, F) equipamento final.

A Figura 9 mostra um exemplo de cronoamperograma obtido com o dispositivo para 1,0 mM da sonda redox ferri/ferrocianato, preparada em 0,1 M de KCl, no qual mostrou ser mais rápido neste novo circuito e mais sensível. Outras técnicas eletroanalíticas também são possíveis de serem utilizadas e estão na finalização do protocolo. O dispositivo desenvolvido possui características únicas e inovadoras em relação às soluções existentes no mercado, justificando assim o potencial para patentear o dispositivo.

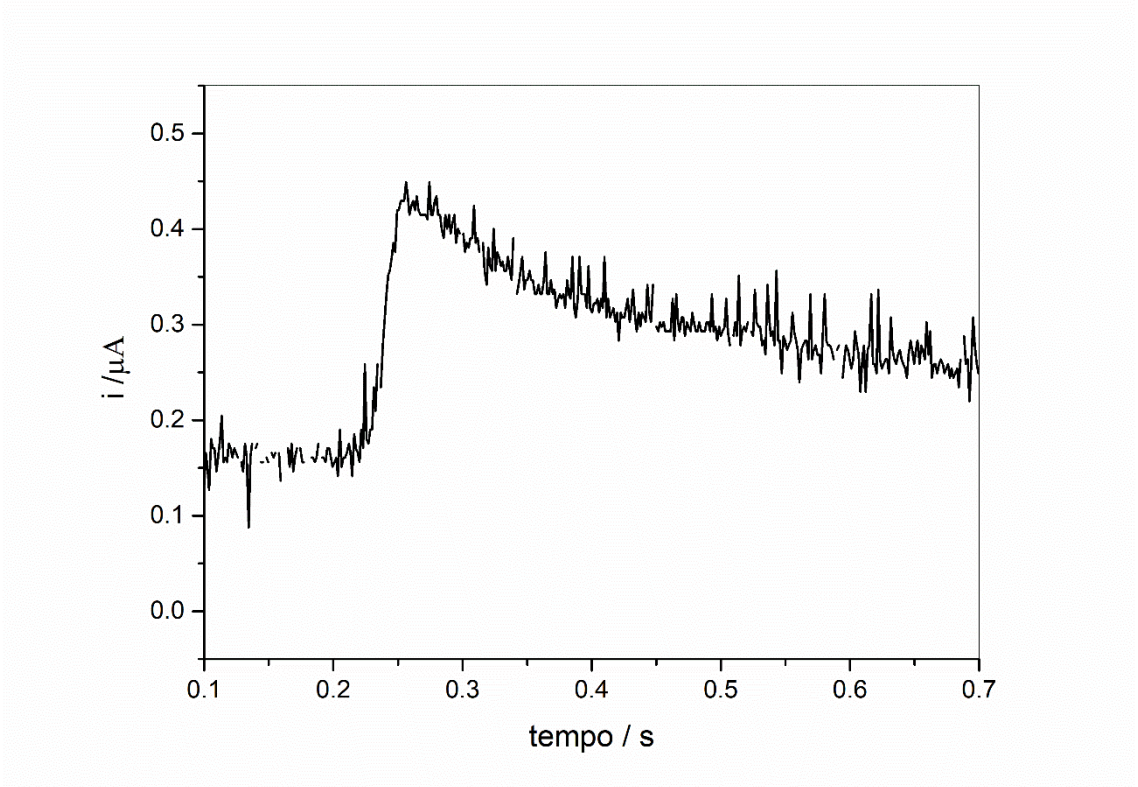

Figura 9. Cronoamperograma obtido para 1,0 mM da sonda redox ferri/ferrocianato, preparada em 0,1 M de KCl.

4. Conclusão

Neste relatório, apresentamos um novo dispositivo capaz de transmitir dados de forma wireless e Bluetooth para um laptop/smartphone, por meio do desenvolvimento de um circuito elétrico único e utilizando o software LabView para comunicação. Este dispositivo possibilita análises em campo e em tempo real, através do emprego de eletrodos impressos e os resultados obtidos demonstram um potencial significativo, o que nos leva a considerar o pedido de patente para esta inovação.

A parte aqui descrita está atualmente em fase de análise para um possível pedido de patente. Os dados anteriormente adquiridos estão sendo preparados para redação de um artigo, conforme detalhado no item 7.

5. Descrever como o Plano de Gestão de Dados está sendo seguido e eventuais modificações

Este item é aplicável somente para bolsas solicitadas a partir de 01/09/2020.

6) Participação em evento científico

6.1) Este trabalho foi apresentado por Maísa Azevedo Beluomini, em painel, no evento científico 74th Annual Meeting of The Internacional Society of Electrochemistry ocorrido de 3 – 8 de Setembro de 2023, na cidade de Lyon, na França.

74th Annual Meeting of the International Society of Electrochemistry

3-8 September 2023
Lyon, France

CERTIFICATE OF ATTENDANCE

This is to certify that **Maisa Azevedo Beluomini** participated with the **Poster** presentation entitled

Simultaneous analysis of hesperidin and narirutin in wastewater from citrus industry using a screen-printed electrode modified with 3D-nanoporous platinum.

(Co-Authors: Nelson Ramos Stradiotto, Maria Valnice Boldrin Zanoni)

in the 74th Annual Meeting of the International Society of Electrochemistry

Prof. Nadine Pébère — Prof Vincent Vivier

Co-Chairs, Organising Committee
74th Annual Meeting ISE 2023

74th Annual Meeting
of the International Society of Electrochemistry
3 - 8 September 2023, Lyon, France.

CERTIFICATE

This is to certify that **Maisa Azevedo Beluomini** has participated in the 74th Annual Meeting of the International Society of Electrochemistry held from 3 - 8 September 2023, Lyon, France.

Prof. Nadine Pébère
Co-Chair, Organizing Committee
74th Annual Meeting ISE 2023

Prof. Vincent Vivier
Co-Chair, Organizing Committee
74th Annual Meeting ISE 2023

6.2) Este trabalho foi apresentado por Maísa Azevedo Beluomini, oralmente, no evento científico XXIV Simpósio brasileiro de eletroquímica e eletroanalítica, ocorrido de 2 – 5 de outubro de 2023, na cidade de Porto Alegre, Brasil.

EXTENSÃO UNIVERSITÁRIA

UNIVATES

www.univates.br | 0800 7 07 08 09

CERTIFICADO

Certificamos que o trabalho intitulado *Electrochemical Investigation of Triphasic Oxygen Storage in Wet Nanoparticulate Polymer of Intrinsic Microporosity (PIM-1)*, de autoria de *Maísa Azevedo Beluomini, Nelson Ramos Stradiotto, Neil B. McKeown, Maria Valnice Boldrin Zanoni, Frank Marken*, foi apresentado por **Maísa Azevedo Beluomini** no **XXIV SIMPÓSIO BRASILEIRO DE ELETROQUÍMICA E ELETROANALÍTICA**, promovido pela Universidade do Vale do Taquari - Univates, por meio do Programa de Pós-Graduação em Ambiente e Desenvolvimento - PPGAD , no período de 02/10/2023 a 05/10/2023.

Lajeado, 23 de outubro de 2023

Evania Schneider
Reitora

6.3) Este trabalho foi apresentado por Ismael Carlos Braga Alves, oralmente, no evento científico VI workshop da Rede Bionorte & Semana do Quimico 2022, com tema “Avanços da Ciência & Tecnologia na Amazônia”, ocorrido de 20 – 23 de junho 2022, na cidade de Macapá, Brasil.

6.4) Este trabalho foi apresentado por Mateus Paula da Silva, na forma de paínel, no evento científico 45ª Reunião Anual da SBQ, ocorrido de 31 de maio a 3 de junho de 2022, cidade de Maceió, Brasil.

7) Lista das publicações resultantes da Bolsa no período a que se refere o Relatório Científico (inclusive as aceitas para publicação, informando em cada caso esta situação).

1. Braga, I.C.A; Dos Santos, J.R.; Marques, E.P.; Azevedo, L.; Beluomini, M.A.; Stradiotto, N.R.; Marques, A. Simultaneous determination of benzene, toluene and xylene (BTX) by Au nanoparticles (AuNP) anchored in reduced graphene oxide electrode. ELECTROANALYSIS, v. 1, p. 1, 2024.

2. Beluomini, M.A., Wang, Y.; Wang, L.; Carta, M.; Mckeown, N.B.; Wikeley, S.; James, T.D.; Lozano-sanchez, P.; Caffio, M.; Stadiotto, N.R Zanoni, M.V.B.; Marken, F. Polymer of intrinsic microporosity (PIM-1) enhances hydrogen peroxide production at Gii-Sens graphene foam electrodes. ELECTROCHEMISTRY COMMUNICATIONS, v. 1, p. 107394, 2023.

3.Braga, I.C.A; Dos Santos, J.R.; Marques, E.P.; Azevedo, L.; Beluomini, M.A.; Stradiotto, N.R.; Marques, A. Electrochemical sensor based on carbon nanotube decorated with manganese oxide nanoparticles for naphthalene determination. ANALYTICAL SCIENCES, v. 1, p. 1, 2023.

4. Da Silva, M.P.; Beluomini, M.A.; Freitas, C.; Brienzo, M.; STRADIOTTO, N.R. Electrochemical Detection of Xylobiose in Banana Biomass Using a 3D Porous Copper Oxide Foam Electrode Modified with a Molecularly Imprinted Poly-L-Arginine Film. JOURNAL OF FOOD COMPOSITION AND ANALYSIS, v. 1, p. 105658, 2023.

5.Modenos, M..; Beluomini, M. A.; Stradiotto, N. R. Voltammetric Determination of Sulfur in Biodiesel Microemulsion Using a Silver Solid Amalgam Electrode. Analytical Methods, v. 1, p. 50, 2022.

6.Mariano, T.; Beluomini, M.A.; Stradiotto, N.R. Molecularly Imprinted Polypyrrole on Glassy Carbon Electrode Modified with Reduced Graphene Oxide and Gold Nanoparticles for Isoamyl Alcohol Analysis in Fusel Oil. JOURNAL OF THE BRAZILIAN CHEMICAL SOCIETY, v. 1, p. 1-11, 2021.

8) Para as publicações listadas no item 7, inclua cópias das primeiras páginas.

Received: 23 August 2023 | Revised: 11 November 2023 | Accepted: 24 November 2023
DOI: 10.1002/elan.202300260

RESEARCH ARTICLE

ELECTROANALYSIS

Simultaneous determination of benzene, toluene and xylene (BTX) by Au nanoparticles (AuNP) anchored in reduced graphene oxide electrode

Ismael Carlos Braga Alves[1] | **José Ribamar Nascimento dos Santos**[1] | **Edmar Pereira Marques**[1] | **Lorena Carvalho Martiniano de Azevedo**[1] | **Maísa Azevedo Beluomini**[2] | **Nelson Ramos Stradiotto**[2] | **Aldaléa Lopes Brandes Marques**[1]

[1]NEPE (LPQA & LAPQAP), PPG-BIONORTE, Federal University of Maranhão (UFMA), São Luís, MA, Brazil

[2]Institute of Chemistry, São Paulo State University (UNESP), Araraquara, SP, Brazil

Correspondence
Ismael Carlos Braga Alves and Aldaléa Lopes Brandes Marques, NEPE (LPQA & LAPQAP), PPG-BIONORTE, Federal University of Maranhão (UFMA), São Luís, 65085-580 MA, Brazil.
Email: ismael.cba@ufma.br and aldalea.ufma@gmail.com

Funding information
CAPES-PROCAD AM, Grant/Award Number: SCBA: 88887.200615/2018-00]; CNPq, Grant/Award Number: 310664/2017-9; FAPEMA, Grant/Award Number: 01136/17; ANP, Grant/Award Number: 1.028/2021, 2.460/22; FAPESP, Grant/Award Number: 2018/12131-6, 2017/22401-8

Abstract

This work reports the development of an electrochemical sensor for the simultaneous determination of benzene, toluene and xylene (BTX). The sensor was prepared by coating the glassy carbon electrode (GCE) with reduced graphene oxide (RGO) film, decorated with gold nanoparticles (AuNP), by electrodeposition. Surface modification with AuNP/RGO-GCE favored the electron transfer process and increased the active area, providing greater sensitivity for the sensor. The AuNP/RGO-GCE sensor was characterized by cyclic voltammetry (CV), electrochemical impedance spectroscopy (EIS) and scanning electron microscope (SEM). Quantitative analyses of BTX were carried out using the differential pulse voltammetry (DPV) technique, after optimization of the parameters that influence the sensor performance. The sensor showed a linear response in the 30–240 μM concentration range, with a detection limit range of 1.8–2.2 μM, 2.2–2.7 μM, and 2.0–2.6 μM, and quantification limit range of 6.2–7.3 μM, 7.2–8.9 μM, and 6.6–8.8 μM, respectively for B, T and X. In addition to the satisfactory repeatability and stability, in the determination of BTX, the method still showed good selectivity even in the presence of molecules with similar chemical structure, such as: catechol, *p*-benzoquinone, resorcinol, ethanol, pyrene and in the presence of K^+, Mg^{2+} and Pb^{2+} ions. The device was successfully applied for the determination of the analytes (BTX) in water samples from fuel station separator boxes, where recovery rates close to 100% (97.8% to 103.1%) were obtained. The results obtained suggest that the AuNP/RGO-GCE sensor has strong potential for detecting BTX in wastewater discharge from industrial processes.

KEYWORDS
Au nanoparticles, BTX, electrochemical determination, reduced graphene oxide

Electrochemistry Communications 143 (2022) 107394

Contents lists available at ScienceDirect

Electrochemistry Communications

journal homepage: www.elsevier.com/locate/elecom

Polymer of intrinsic microporosity (PIM-1) enhances hydrogen peroxide production at Gii-Sens graphene foam electrodes

Maisa Azevedo Beluomini [a,b], Yu Wang [a,c], Lina Wang [a], Mariolino Carta [d], Neil B. McKeown [e], Simon M. Wikeley [a], Tony D. James [a,f], Pablo Lozano-Sanchez [g], Marco Caffio [g], Nelson Ramos Stradiotto [b], Maria Valnice Boldrin Zanoni [b], Frank Marken [a,*]

[a] Department of Chemistry, University of Bath, Claverton Down, Bath BA2 7AY, UK
[b] Institute of Chemistry, São Paulo State University (UNESP), 14800-060 Araraquara, São Paulo, Brasil
[c] School of Material Science and Engineering, Zhengzhou University, Henan 450001, China
[d] Department of Chemistry, Swansea University, College of Science, Grove Building, Singleton Park, Swansea SA2 8PP, UK
[e] EaStChem School of Chemistry, University of Edinburgh, Edinburgh EH9 3FJ, UK
[f] School of Chemistry and Chemical Engineering, Henan Normal University, Xinxiang 453007, China
[g] Integrated Graphene Ltd., Euro House, Wellgreen Place, Stirling FK8 2DJ, UK

ARTICLE INFO

Keywords:
Graphene
Hydrogen peroxide
Generator-collector voltammetry
Disinfection
Catalysis

ABSTRACT

3D-graphene foam electrodes (Gii-Sens) immersed in a phosphate buffer solution of pH 7 are shown to generate hydrogen peroxide at a significantly faster rate in the presence of a nanoparticulate polymer of intrinsic microporosity (PIM-1). The effect is demonstrated to be associated at least in part with oxygen binding into PIM-1 under triphasic conditions. The release of the oxygen at the electrode|solution interface quadruples H_2O_2 production. Generator–collector experiments are performed with a graphene foam disk generator and a platinum disk electrode collector to allow in situ detection of hydrogen peroxide and oxygen.

1. Introduction

Polymers of intrinsic microporosity (PIMs) are molecularly rigid and contorted structures which are unable to pack and are therefore able to form films of high microporosity [1] with a typical 1000 $m^2\ g^{-1}$ surface area and typical 1 nm pore size. PIMs have found applications primarily in gas phase separation and gas binding [2], but recently have also started to attract interest in electrochemistry [3]. Interfacial redox processes that have been investigated include the CO_2 reduction [4], formic acid oxidation [5], the $Fe(CN)_6^{3-/4-}$ system [6], bound quinones [7], and the oxygen reduction reaction [8]. For the oxygen reduction reaction, the onset for formation of hydrogen peroxide was noted to be shifted to positive potentials in the presence of PIM-1 (see molecular structure in Fig. 1), indicative of a locally higher oxygen activity under triphasic conditions (gas|liquid|polymer). Electrode processes involving redox-active gases dissolved in aqueous media have been shown to be beneficially affected by the presence of polymer of intrinsic microporosity coatings on electrodes, presumably via adsorption of gas into the wet microporous structure [9]. More generally, it has recently been highlighted by Erdosy et al. [10] that a wider range of materials with intrinsic microporosity physically increase the apparent solubility of poorly water-soluble gases like oxygen under triphasic conditions.

Hydrogen peroxide production is highly sensitive to the electrode material [11]. Graphene and graphene-oxide-related materials have been shown to be active in producing hydrogen peroxide cathodically [12] but the yield of H_2O_2 may vary, dependent on conditions, defects, or doping. On exfoliated and *N*-doped graphene surfaces, oxygen reduction to H_2O_2 (the 2-electron product) is observed only as an intermediate, and reduction to H_2O (the 4-electron product) is observed in particular in acidic media [13]. The reduction mechanism on graphene surfaces is complicated by the presence of oxygen binding defects and reactive sites. On pure graphene a prominent reduction peak has been reported, linked to O_2 binding into defects in the graphene surface [14]. Here, it is demonstrated that the formation of H_2O_2 on graphene foam can be enhanced by microporous polymer deposits on the electrode surface.

A graphene foam film electrode (Gii-Sens) with approximately 40 μm foam thickness is employed [15]. This film electrode represents a

* Corresponding author.
E-mail address: f.marken@bath.ac.uk (F. Marken).

https://doi.org/10.1016/j.elecom.2022.107394
Received 21 October 2022; Received in revised form 14 November 2022; Accepted 15 November 2022
Available online 17 November 2022

Analytical Sciences
https://doi.org/10.1007/s44211-023-00374-w

ORIGINAL PAPER

Electrochemical sensor based on carbon nanotube decorated with manganese oxide nanoparticles for naphthalene determination

Ismael Carlos Braga Alves[1] · José Ribamar Nascimento dos Santos[1] · Edmar Pereira Marques[1] · Janyeid Karla Castro Sousa[1] · Maísa Azevedo Beluomini[2] · Nelson Ramos Stradiotto[2] · Aldaléa Lopes Brandes Marques[1]

Received: 3 March 2023 / Accepted: 21 May 2023

Abstract
In this work, an electrochemical sensor was developed for the determination of naphthalene (NaP) in well water samples, based on a glass carbon electrode (GCE) modified as a nanocomposite of manganese oxides (MnO_x) and COOH-functionalized multi-walled carbon nanotubes (MWCNT). The synthesis of MnO_x nanoparticles was performed by the sol–gel method. The nanocomposite was obtained by mixing MnO_x and MWCNT with the aid of ultrasound, followed by stirring for 24 h. Surface modification facilitated the electron transfer process through the MnO_x/MWCNT/GCE composite, which was used as an electrochemical sensor. The sensor and its material were characterized by cyclic voltammetry (CV), transmission electron microscopy (TEM), scanning electron microscopy (SEM), energy-dispersive X-ray spectroscopy (EDS), X-ray diffraction (XRD) and Fourier transform infrared spectroscopy (FTIR). Important parameters influencing electrochemical sensor performance (pH, composite ratios) were investigated and optimized. The MnO_x/MWCNT/GCE sensor showed a wide linear range of 2.0–16.0 µM, a detection limit of 0.5 µM and a quantification limit of 1.8 µM, in addition to satisfactory repeatability (RSD of 7.8%) and stability (900 s) in the determination of NaP. The determination of NaP in a sample of water from a gas station well using the proposed sensor showed results with recovery between 98.1 and 103.3%. The results obtained suggest that the MnO_x/MWCNT/GCE electrode has great potential for application in the detection of NaP in well water.

Keywords Naphthalene · Nanocomposite · MnO_x · MWCNT · Electrochemical sensor

Introduction

Polycyclic aromatic hydrocarbons (PAHs) are formed by the incomplete combustion of carbon and hydrogen-containing substances such as crude oil, coal and wood tar [1]. Some PAHs fall into a group considered for human health hazardous [2–4], because they are potentially carcinogenic compounds and can cause intoxication when ingested, inhaled or in dermal contact with very high doses [5, 6].

✉ Ismael Carlos Braga Alves
ismael.cba@ufma.br

✉ Aldaléa Lopes Brandes Marques
aldalea.ufma@gmail.com

[1] NEEP (LPQA & LAPQAP), PPG-BIONORTE, Federal University of Maranhão (UFMA), São Luis, MA, Brazil

[2] Institute of Chemistry, São Paulo State University (UNESP), Araraquara, São Paulo, Brazil

Consequently, PAHs are monitored worldwide in various environmental matrices [7]. They can be found in different ecosystems, such as air, soil or water, caused mainly due to industrialization, urbanization, incomplete combustion of fossil fuels (coal, diesel and oil), and other organic materials [8].

These facts have aroused the interest of researchers in developing methodologies for their determination in the environment. Thus, groundwater is considered an interesting matrix for the determination of PAHs.

The Brazilian legislation in CONAMA resolution no. 460/2013 [9] establishes the value of 140 µg L^{-1} in groundwater. The United States Environmental Protection Agency (EPA) has established, among the different known PAHs, 16 of them as priority hazards. NaP (molecular formula $C_{10}H_8$, chemical structure shown in Fig. 1) is among these 16 PAHs, since 2000, after being considered one of the great problems in an environmental and occupational sense, due to its significant carcinogenic effects [10]. NaP is a constituent of

Published online: 03 June 2023

Journal of Food Composition and Analysis 124 (2023) 105658

Contents lists available at ScienceDirect

Journal of Food Composition and Analysis

journal homepage: www.elsevier.com/locate/jfca

Electrochemical detection of xylobiose in banana biomass using a 3D porous copper oxide foam electrode modified with a molecularly imprinted Poly-L-arginine film

Mateus Paula da Silva [a,c], Maísa Azevedo Beluomini [a,c,*,1], Carolina de Freitas [b], Michel Brienzo [b], Nelson Ramos Stradiotto [a,c]

[a] Institute of Chemistry, São Paulo State University (UNESP), Araraquara 14800-060, Brazil
[b] Institute for Research in Bioenergy (IPBEN), São Paulo State University (UNESP), Rio Claro 13500-230, Brazil
[c] Institute for Research in Bioenergy (IPBEN), São Paulo State University (UNESP), Araraquara 14800-060, Brazil

ARTICLE INFO

Keywords:
Banana pseudostem
Copper oxide foam
L-arginine
Molecularly imprinted polymer
Xylooligosaccharides
Xylan

ABSTRACT

Xylobiose (X2) presents numerous health benefits, including cancer prevention, and can be found in agro-industrial biomass, including bananas. Here, an electrochemical sensor based on molecularly imprinted poly-L-arginine film (MIP) and 3D porous copper oxide foam (3DnpCu) for the ultrasensitive detection of X2 is studied. The MIP/3DnpCu-GCE is prepared by dynamic hydrogen bubble template method, followed by electropolymerization of L-arginine in the presence of X2 as template, followed by electrochemical extraction, resulting in the formation of X2 recognition sites. The sensor was characterized using scanning electron microscopy, X-ray photoelectron spectroscopy, and electrochemical impedance spectroscopy. MIP/3DnpCu-GCE showed a wide linear response in the concentration range of 1.0×10^{-12} to 1.0×10^{-10} mol L^{-1}, limit of detection of 7.7×10^{-13} mol L^{-1} and sensibility of 1.4 μA $pmol^{-1}$ L. The sensor exhibited selective X2 recognition, long-term stability (maintaining 86% of its initial current over 8 days), while inter-electrode repeatability displayed an RSD of 2.4%. The applicability of the MIP/3DnpCu-GCE in real samples is demonstrated by successfully quantifying X2 concentration in banana biomass. Furthermore, the comparison between the data obtained using this method and those found by the HPLC method confirmed the accuracy of the sensor.

1. Introduction

Xylooligosaccharides (XOS) are oligomers of xylose linked by β(1→4)-glucosidic bonds. The degree of polymerization of XOS varies with the source of xylan and the production process, ranging from monomers to molecules containing up to 10 xylose units. Among the XOS, xylobiose (X2) has demonstrated heightened prebiotic effects, bestowing advantageous health benefits upon both humans and animals. X2 is thermally stable, have a low caloric value, exhibits antioxidant effects, enhances calcium absorption, prevents colon cancer, and has a low glycemic and insulinemic responses (Samanta et al., 2015). In this context, the food industry has been the largest user of XOS, accounting for 49.6%, followed by the pharmaceutical and beverage sectors at 25.4% and 23.2%, respectively (Ahmad, 2019). X2 can be obtained from hemicellulose-rich biomass, which is available in large quantities as agro-industrial and agricultural residues. This conversion can occur through chemical or enzymatic hydrolysis (Brienzo et al., 2010). Agro-industrial residues represent a substantial fraction of the available biomass and can be utilized for producing compost with enhanced value addition. The integration of this concept in the circular economy framework has gained considerable momentum, owing to its potential to generate positive environmental outcomes (Velvizhi et al., 2022).

Considering its biological importance and prevalence, the methods employed to detect and quantify X2 predominantly involve classical chromatographic techniques (Alyassin et al., 2020; Cürten et al., 2018; Fan et al., 2011; Li et al., 2016; Pu et al., 2016; Xu et al., 2013). Although these methods have been effectively utilized for X2 detection, they also present some non-negligible disadvantages, involving the utilization of environmentally unfriendly reagents and solvents, high cost of equipment for analysis and time-consuming sample preparation. For the

* Corresponding author at: Institute of Chemistry, São Paulo State University (UNESP), Araraquara 14800-060, Brazil.
E-mail address: maisa.beluomini@unesp.br (M.A. Beluomini).
[1] Orcid: 0000-0003-3441-1572

https://doi.org/10.1016/j.jfca.2023.105658
Received 19 July 2023; Received in revised form 23 August 2023; Accepted 30 August 2023
Available online 1 September 2023

Analytical Methods

ROYAL SOCIETY OF CHEMISTRY

PAPER

View Article Online
View Journal

Cite this: DOI: 10.1039/d2ay01263d

Voltammetric determination of sulfur in biodiesel microemulsion using a silver solid amalgam electrode†

Marco Antonio Modenes Junior,[a] Maísa Azevedo Beluomini[*a] and Nelson Ramos Stradiotto[ab]

Monitoring sulfur in biodiesel is of fundamental importance because even in low concentrations, it can harm the operation of the engine parts and increase the emission of toxic gases and particulate material. Hence, a simple, quick and sensitive adsorptive stripping voltammetry (AdSV) method based on a silver solid amalgam electrode (AgSAE) was developed to determine sulfur in biodiesel. The novel electrochemical method was evaluated through the linear sweep adsorptive stripping voltammetry (LSAdSV), square wave adsorptive stripping voltammetry (SWAdSV) and differential pulse adsorptive stripping voltammetry (DPAdSV) in a NH_3/NH_4^+ buffer solution (pH 9.0), containing Na_2SO_3. The method was applied in biodiesel microemulsion samples under optimal conditions. To this end, a ternary phase diagram was constructed, employing three components: biodiesel/propan-1-ol/buffer solution. The microemulsion with the best response was found to be 25% NH_3/NH_4^+ buffer (pH 9.0), 5.0% biodiesel and 70% propan-1-ol. The method reached a detection limit in the order of 10^{-7} mol L^{-1} of sulfur, and recovery values between 80% and 116%. The method was applied in the determination of sulfur in biodiesel, and the amount in the samples was found to be below the value stipulated by the regulatory agencies. The method can be a promising alternative for determining sulfur in the microemulsion of biodiesel, with the ability to provide a fast response regarding the quality of this biofuel.

Received 8th August 2022
Accepted 19th August 2022

DOI: 10.1039/d2ay01263d

rsc.li/methods

1. Introduction

Among the various renewable biofuels developed so far, biodiesel is one of the most promising due to its environmentally friendly properties, given that it comes from renewable sources and has low toxicity. Biodiesel is composed of alkyl esters of long-chain fatty acids, obtained through the process of transesterification of triglycerides or esterification of free fatty acids with short-chain alcohol in the presence of a base, acid or enzymatic catalyst.[1,2]

To ensure biodiesel quality, some parameters are stipulated in order to impose limits on its composition. The presence of some contaminants can decrease engine performance and increase the emission of toxic gases. Biodiesel quality can vary according to the molecular structure of the constituent esters, or the contaminants present in the raw material, which can be formed during production and storage. The contaminants from the raw material may include phosphorus, sulfur, calcium and magnesium, and depending on the efficiency of the biodiesel production process, they can be present in greater or lesser quantities. The presence of these substances can decrease engine performance and increase the emission of toxic gases during the combustion of this biofuel.[3] Among the various parameters assessing biodiesel quality, the one determining the amount of sulfur is extremely important. Even the presence of low levels of this contaminant can harm the operation of catalytic converters and increase the emission of toxic gases and particulate materials, causing corrosion problems to the internal parts of the engine and harm to flora and fauna.[4] In view of the damage caused by sulfur, stricter standards were established for its biodiesel content. For example, the sulfur concentration must be below 15 mg kg^{-1} and 10 mg kg^{-1} and in the United States (ASTM D6751) and Europe (EN 14214), respectively.[5] In Brazil, the maximum permitted sulfur limit in biodiesel is 10 mg kg^{-1}, according to technical specification no. 3/2014 of resolution no. 45 of the National Petroleum Agency (ANP).[6]

Most methods found in the literature for analyzing sulfur are based on X-ray fluorescence (XRF),[7–9] inductively coupled plasma optical emission spectrometry (ICP-OES),[4,10] and inductively coupled plasma quadrupole mass spectrometry (ICP-QMS).[11–13] Although these methods are sensitive and have a good detection limit, they require a long time of analysis, time-consuming sample preparation, a high volume of reagents and organic

[a]Institute of Chemistry, São Paulo State University (UNESP), Araraquara, 14800-060, São Paulo, Brazil. E-mail: mabeluomini@gmail.com
[b]Bioenergy Research Institute, São Paulo State University (UNESP), Araraquara, 14800-060, São Paulo, Brazil

† Electronic supplementary information (ESI) available. See https://doi.org/10.1039/d2ay01263d

https://dx.doi.org/10.21577/0103-5053.20200174
J. Braz. Chem. Soc., Vol. 32, No. 2, 240-259, 2021
Printed in Brazil - ©2021 Sociedade Brasileira de Química

Article

Molecularly Imprinted Polypyrrole on Glassy Carbon Electrode Modified with Reduced Graphene Oxide and Gold Nanoparticles for Isoamyl Alcohol Analysis in Fusel Oil

Thiago M. Mariano,[a] *Maísa A. Beluomini*[a] *and Nelson R. Stradiotto*[a,b]*

[a]*Instituto de Química, Universidade Estadual Paulista (Unesp), 14800-060 Araraquara-SP, Brazil*

[b]*Instituto de Pesquisa em Bioenergia, Universidade Estadual Paulista (Unesp), 14800-060 Araraquara-SP, Brazil*

A molecularly imprinted electrochemical sensor for determination of isoamyl alcohol was successfully constructed by modifying the glassy carbon electrode (GCE) with gold nanoparticles (AuNPs) and reduced graphene oxide (RGO). The modification of the GCE increased the electron transfer rate and the electrode surface area, which, consequently, made more room available for the formation of the molecularly imprinted polymer (MIP). The development of the MIP on the modified surface was carried out via electropolymerization of the pyrrole in acetate buffer solution in the presence of the target molecule. The MIP-AuNPs-RGO/GCE showed low limit of detection (8.4×10^{-8} mol L^{-1}), satisfactory quantification range, amperometric sensitivity of 1.1 A L mol^{-1}, excellent reproducibility and stability. Even when in the presence of analogous molecules, the sensor exhibited excellent selectivity. These results suggest that the proposed sensor is suitable for the detection of isoamyl alcohol in fusel oil samples.

Keywords: molecularly imprinted polypyrrole, reduced graphene oxide, gold nanoparticles, isoamyl alcohol, fusel oil

Introduction

The search for alternative fuels has become inevitable and urgent in the deeply seek to reduce the environmental impacts associated with the use of fossil fuels. In this sense, bioethanol plants and their byproducts have grown significantly in recent years as vital alternatives for lessening the use and even replacing fossil fuels and other harmful chemical substances employed as sources of energy.[1] Bioethanol has proved to be economically useful in addition to being renewable. These are relevant features that explain the fact that it is being internationally marketed to satisfy countries with limited biomass resources.

The production of bioethanol generates byproducts such as fusel oil, obtained after fermentation and distillation of biomass, composed mainly of higher alcohols containing three or more carbon atoms, including isoamyl alcohol, isobutanol, propanol, butanol, among others.[2,3] The fact that higher alcohols present in fusel oil are considered natural products provides these alcohols high commercial values. Since these alcohols are high octane and low in exhaust gas emissions, they occupy an important place among alternative fuels. The separation of these compounds is regarded essentially important, since the market value of fusel oil is directly related to the amount of higher alcohols, especially of isoamyl alcohol. In a commercial plant, for example in Brazil, the yield of the fusel oil may vary from 1 to 11 L *per* 1000 L of alcohol produced, depending on the fermentation and distillation conditions as well as on the amount of nitrogen.[4]

Chromatographic methods are the predominant mechanism employed when it comes to the determination of fusel oil constituents in the literature. Pérez *et al.*[5] quantified fusel oil constituents by gas chromatography for alcohols and esters, and liquid chromatography for carbonyl compounds using fusel oil samples from 3 different plants. The isoamyl (390 g L^{-1}), isobutyl (158 g L^{-1}), ethyl (28.4 g L^{-1}), methyl (16.6 g L^{-1}) and *n*-propyl (11.9 g L^{-1}) alcohols represent approximately 77% of the fusel oil composition. Neale[6] used high performance liquid chromatography to determine ethanol, isoamyl alcohol, isobutyl alcohol and L-propanol in alcoholic beverages.

*e-mail: nrstradi@gmail.com

9) Lista dos trabalhos preparados ou submetidos (e ainda não aceitos, pois os aceitos devem estar listados no item 7) para publicação, acompanhada de cópias destes trabalhos.

1) Beluomini, M.A. Stradiototto, N.R. Boldrin, M.V. Carta, M., McKeown, N.B., Marken, F. Electrochemical Investigation of Triphasic Oxygen Storage in Wet Nanoparticulate Polymer of Intrinsic Microporosity (PIM-1) on Platinum. In preparation.

2) Conceição, E. Buffon, E., Beluomini, M.A.,Falone, M.F., Batista. F.A., Contiero,J., Stradiotto, N.R. Electrochemical monitoring of poly(3-hydroxybutyrate) production from Burkholderia glumae MA13 using a molecularly imprinted polymer-reduced graphene oxide modified electrode. Submetido em Jan/2024. Analytica Chimica Acta.

Electrochemical Investigation of Triphasic Oxygen Storage in Wet Nanoparticulate Polymer of Intrinsic Microporosity (PIM-1) on Platinum

Maisa Azevedo Beluomini [1,2], Nelson Ramos Stradiotto [2], Maria Valnice Boldrin Zanoni [2], Mariolino Carta [3], Neil B. McKeown [4], and Frank Marken*[1]

[1] *Department of Chemistry, University of Bath, Claverton Down, Bath BA2 7AY, UK*

[2] *Institute of Chemistry, São Paulo State University (UNESP), 14800-060, Araraquara, São Paulo, Brazil*

[3] *Department of Chemistry, Swansea University, College of Science, Grove Building, Singleton Park, Swansea SA2 8PP, UK*

[4] *EaStCHEM School of Chemistry, University of Edinburgh, Joseph Black Building, David Brewster Road, Edinburgh, Scotland EH9 3JF, UK*

To be submitted to ACS Applied Materials and Interfaces

Proofs to F. Marken (F.Marken@bath.ac.uk)

Abstract

The triphasic interaction of gases with electrode surfaces immersed in aqueous electrolyte is crucial in many energy technologies (fuel cells, batteries). Some microporous materials modify this interaction via triphasic storage capacity for gases in aqueous environments. Here, a nanoparticulate polymer of intrinsic microporosity (PIM-1) in aqueous electrolyte is shown to store oxygen gas and thereby enhance electrochemical signals for oxygen reduction in aqueous media. Oxygen reduction current transient data at platinum disk electrodes suggest that the reactivity of ambient oxygen in aqueous electrolyte (typically

D_{oxygen} = 2.0 × 10^{-9} m^2s^{-1}; c_{oxygen} = 0.2 mM) is substantially modified ($D_{app,oxygen}$ = 10^{-13} m^2s^{-1}; $c_{app,oxygen}$ = 50 mM) with important implications for triphasic electrode processes. Potential applications in oxygen sensing are discussed.

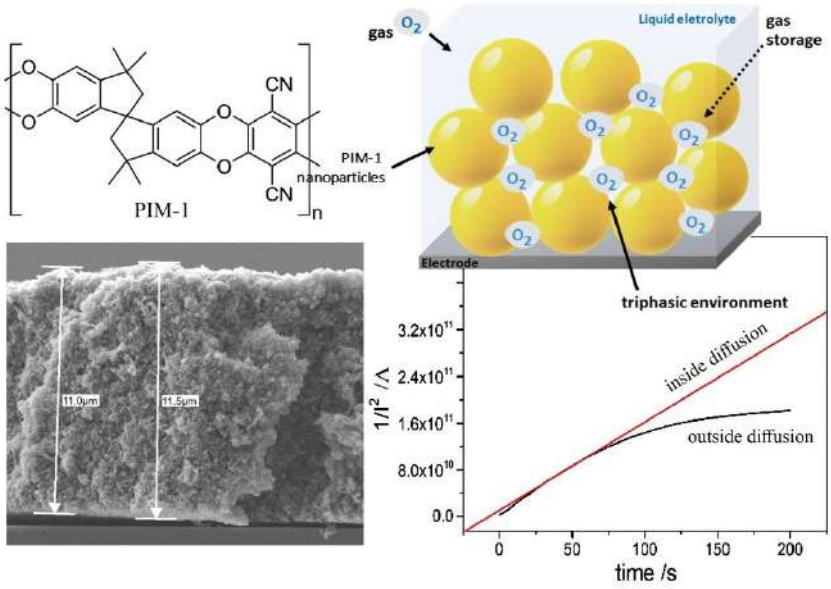

Graphical Abstract

Key words: triphasic gas storage; diffusion layer; energy storage; electrocatalysis; oxygen evolution

1. Introduction

The oxygen reduction reaction has been carefully studied in the context of sensing, hydrogen peroxide production, in battery technologies, in fuel cells, or in organic electrosynthesis . One particular challenge for this reduction reaction is linked to the relatively low solubility of oxygen in aqueous media (typically 0.2 mM in the presence of ambient oxygen). In order to enhance the reactivity/solubility of oxygen in aqueous media, either pressure can be applied or solubility enhancing additives can be added. In a recent report Erdosy *et al*. highlighted the ability of some microporous materials (MOFs, zeolites) to considerably enhance oxygen solubility in aqueous media. Similarly, we have shown that polymers of intrinsic microscopy (PIMs) and in particular PIM-1 (see molecular structure in Figure 1) provide a material for localised gas storage in aqueous media for example for hydrogen or for oxygen.

Polymers of intrinsic microporosity (PIMs) are molecularly rigid and contorted polymers with high specific surface area and selective permeability. Due to these properties, PIMs have been extensively studied for applications in separation membranes, catalysis, and gas storage. However, PIMs have found new applications also in wet (electrochemical) conditions either in aqueous media for sensing, in gas diffusion electrodes, or in organic solvents for example in batteries.

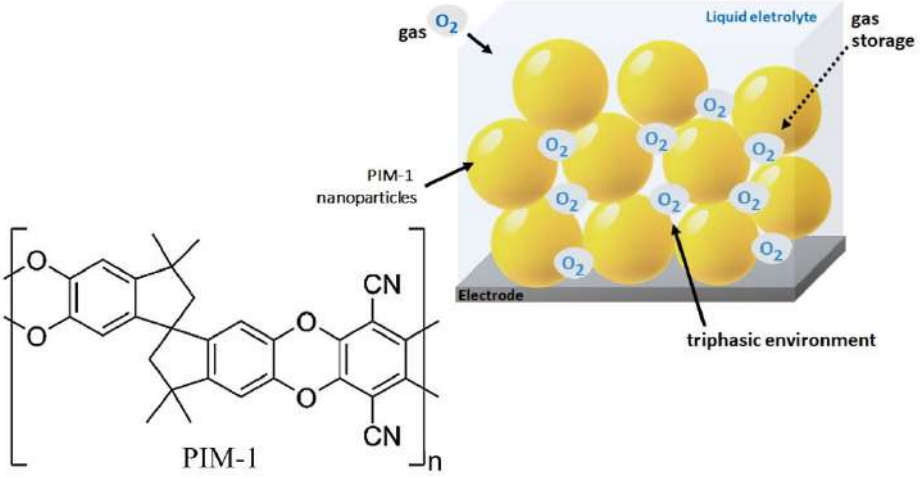

Figure 1. Illustration of PIM-1 nanoparticles packed at the electrode | solution interface creating a triphasic gas | liquid | solid environment.

Recently, studies have shown that PIM-1 nanoparticles are effective in multiphase electrodes and they can be utilized to store oxygen gas and enhance electrochemical

signals for oxygen reduction. These PIM-1 nanoparticles can act as a reservoir for oxygen, providing additional oxygen for the electrochemical reduction. However, the key parameters, the apparent concentration of oxygen ($c_{app,oxygen}$) and the apparent diffusion coefficient ($D_{app,oxygen}$) still need to be evaluated.

In this report, chronoamperometry transient data for oxygen reduction at platinum electrodes are obtained as a function of PIM-1 nanoparticle film thickness at the electrode surface. The current transients are shown to switch between internal diffusion within the PIM-1 nanoparticle film and external diffusion in the aqueous electrolyte. Combining data for different thicknesses allows both $c_{app,oxygen}$ and $D_{app,oxygen}$ within the PIM-1 nanoparticle films to be determined. It is demonstrated that PIM-1 can increase the local concentration of oxygen by two orders of magnitude. These results demonstrate that "gas storage" is possible directly at electrode surfaces and that traditional limits of solubility in aqueous are readily overcome in the design of new types of triphasic electrode processes.

2. **Experimental**

2.2 Reagents

Monobasic sodium phosphate (≥98.0 %), dibasic sodium phosphate (≥99.0 %), methanol and chloroform were obtained from Sigma-Aldrich and used without further purification. PIM-1 (2,3,5,6-Tetrafluorophthalonitrile-3,3,3′,3′-tetramethyl-1,1′-spirobisin dane-5,5′,6,6′-tetrol co-polymer, Sigma-Aldrich 918768, monomer molecular weight 460 g mol^{-1}) was synthesised using a method described in the literature. Argon and oxygen were purchased from BOC UK (Pureshield). Deionized and filtered water (18.2 MΩ cm at 20 ^{o}C) obtained from a Thermo Scientific water purification system, was used to prepare solutions. All experiments were conducted at a room temperature of 20 ± 2 °C. A 0.1 mol L^{-1} concentration of phosphate buffer solution pH 7 was used as a background electrolyte solution for all experiments.

2.2. Instrumentation

A potentiostat system (Autolab GPSTAT12, EcoChemie, The Netherlands) was employed with a Pt wire counter electrode and a KCl-saturated calomel reference. The working electrode was a platinum disk electrode (2 mm diameter). A conventional electrochemical cell was employed. The electrode modified with PIM-1 nanoparticles

was characterized using a scanning electron microscope (SEM, Hitachi SU3900) at an accelerating voltage of 5.0 kV.

2.3. Procedures

PIM-1 nanoparticles were synthesized with typically 50 nm diameter using an anti-solvent precipitation method, as reported previously [x]. Briefly, the PIM-1 polymer was dissolved in 2 mL of chloroform at a concentration of 1 mg mL-1. The solution was added dropwise into 20 mL of methanol under vigorous stirring during 12 h. The PIM-1 solution was centrifuged for 30 min at 5000 rpm followed by the removal of excess methanol. The PIM-1 nanoparticles were subsequently re-dispersed in methanol using an ultrasonication process. To prepare nanoparticulate films, a volume of 5 μL (4 mg mL^{-1}) of PIM-1 solution, equivalent to 20 μg PIM-1 (other quantities of PIM-1 used in this study were calculated proportionally), was droposited onto the platinum electrode to dry at room temperature.

2.4. Characterisation

Figure 2 shows a typical scanning electron microscopy (cross-sectional SEM) image of for a deposit of 600 μg of PIM-1 nanoparticles on a 25 mm^2 area (employing a silicon wafer substrate). A spongy microstructure is observed covering the surface with a thickness of approximately 12 μm. This value was employed to calibrate the thickness of films deposited onto the platinum disk electrode. Table 1 summarises the thicknesses of the nanoparticulate film for different amounts of PIM-1 deposited onto the electrode surface.

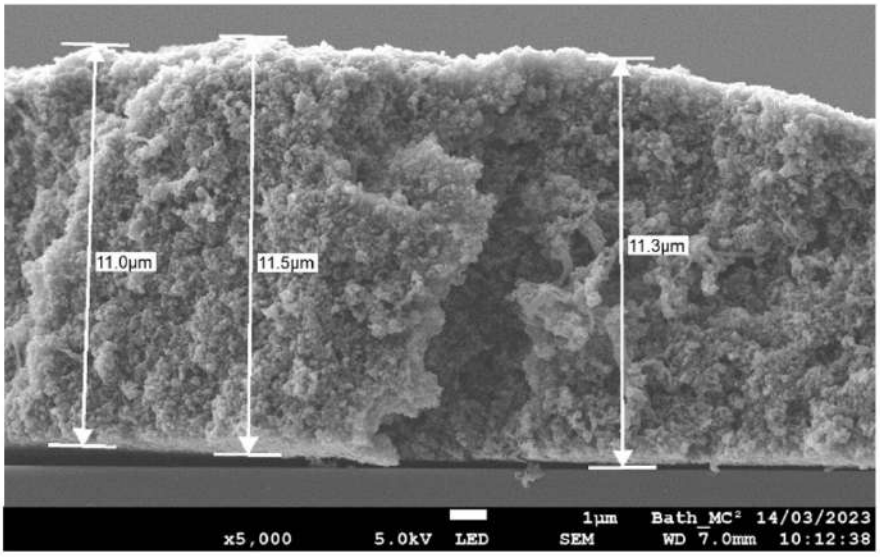

Figure 2. Scanning electron microscopy (SEM) of cross-sectional view of the silicon wafer coated with PIM-1 nanoparticles.

Table 1. Thickness variation of PIM-1 nanoparticles on Pt electrode (estimated from cross-sectional electron microscopy images).

PIM-1 weight of deposit / µg	Approximate thickness / µm
20	0.4
50	1
100	2
200	4
400	8
600	12

3. Results and Discussion

3.1. Detection of Oxygen Stored in Nanoparticulate PIM-1: Cyclic Voltammetry

In order to evaluate the ability of PIM-1 nanoparticles to store oxygen gas, different amounts of PIM-1 nanoparticles were deposited onto a 2 mm diameter Pt disk electrode. A solution containing 0.1 mol L^{-1} phosphate buffer pH 7 was employed in the voltammetric measurements. Cyclic voltammograms (50 mVs^{-1} scan rate) in Figure 3A show peaks for the oxygen reduction reaction at 0.0 V vs. Ag/AgCl. For the bare Pt electrode (curve in red) a peak current of -8 µA is observed. In the presence of varying amounts of PIM-1 nanoparticles on the Pt disk electrode the reduction current is

enhanced. With 600 µg PIM-1 nanoparticles the current triples. This increase in current can be assigned either to faster diffusion or (more likely) an increased concentration of oxygen locally at the electrode surface (or both).

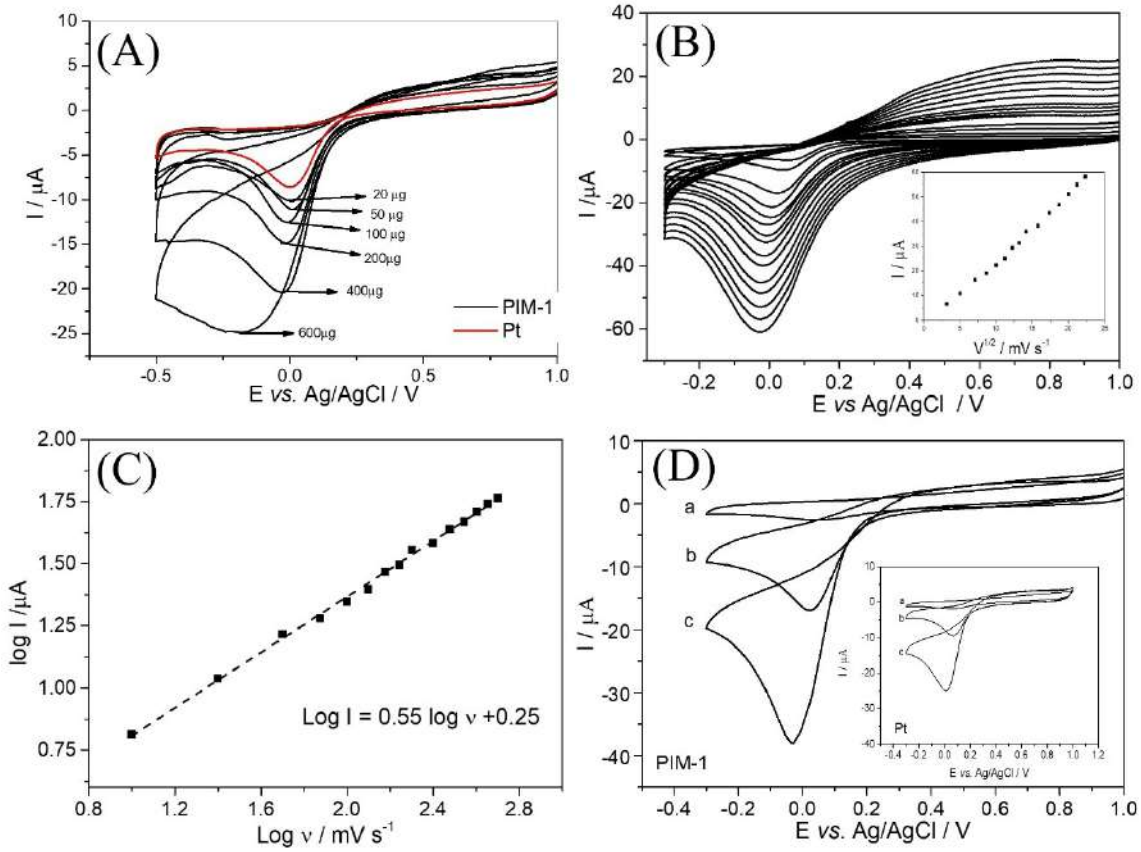

Figure 3. (A) Cyclic voltammograms (scan rate 50 mVs^{-1}) for a 2 mm diameter Pt electrode immersed in 0.1 mol L^{-1} phosphate buffer pH 7. Data are shown for the bare electrode (red) and for different amounts of PIM-1 nanoparticle deposits (20 – 600 µg). (B) Cyclic voltammograms (scan rates 10 – 500 mV s^{-1}) for 200 µg PIM-1 nanoparticles on a 2 mm diameter Pt disk. Insert: plot of peak currents of oxygen reduction versus square root of scan rate. (C) Double-logarithmic plot of the peak current for oxygen reduction versus the scan rate. (D) Cyclic voltammograms (scan rate 50 mV s^{-1}) for 200 µg PIM-1 nanoparticles on a 2 mm diameter Pt disk electrode in argon atmosphere (a), ambient air (b), and in pure oxygen atmosphere (c). Insert: the same conditions but for a bare Pt electrode.

Effect of scan rate on peaks. The influence of scan rate (υ) on the oxygen reduction peak currents for PIM-1 nanoparticles on Pt was investigated. The scan rate was varied from 10 to 500 mV s^{-1} (Figure 3B). The current peak at 0.0 V vs. Ag/AgCl corresponds to oxygen reduction in phosphate buffer solution pH 7. The peak currents increase with scan

rate, and the peak potentials shift towards more negative potentials. There is a linear relationship between the peak current versus square root of the scan rate (Figure 3C and D) indicative of a diffusion-controlled process. The equation for peak current versus scan rate can be expressed as log I (μA) = 0.55 log υ (mV s^{-1}) + 0.25 (R = 0.998) consistent with a diffusion process.

Effect of gas composition. Upon modifying the gas environment during the experiments (by 20 minutes gas purging with either oxygen or argon gas), significant (and anticipated) effects on the oxygen reduction reaction were observed. Figure 3D shows the data obtained from testing the PIM-1 nanoparticle coated Pt disk electrode. The oxygen reduction peak current is consistent with the oxygen content in the gas phase. The insert shows data for a bare Pt electrode for argon, ambient air, and for pure oxygen, revealing very similar changes in the reduction peak current linked to variations in oxygen concentration. Therefore, oxygen gas concentration equilibration occurs from the gas phase to the liquid phase and finally into the solid PIM-1 phase. The question arises whether the oxygen reduction peak current in the presence of PIM-1 nanoparticles is affected by changes in diffusion coefficient or by changes in concentration. Chronoamperometry experiments can be employed to answer this question.

3.2. Detection of Oxygen Stored in Nanoparticulate PIM-1: Chronoamperometry

Effect of the amount of PIM-1 deposit. Chronoamperometry data were recorded for 0, 20, 50, 100, 200, 400, and 600 μg PIM-1 nanoparticles deposited onto a 2 mm diameter Pt disk electrode immersed in 0.1 mol L^{-1} phosphate buffer (pH 7) with an applied potential of -0.2 V vs. Ag/AgCl within the oxygen reduction potential region (Figure 3). Figure 4A shows chronoamperometry transient data over 200 s for the reduction of ambient oxygen. The presence of the PIM-1 nanoparticles clearly substantially increases the reduction current and even after 200 s the higher current remains significant indicative of more oxygen reaching the electrode surface. 0. The ratio of transient currents is plotted in Figure 4D clearly showing the transition from inside to outside diffusion.

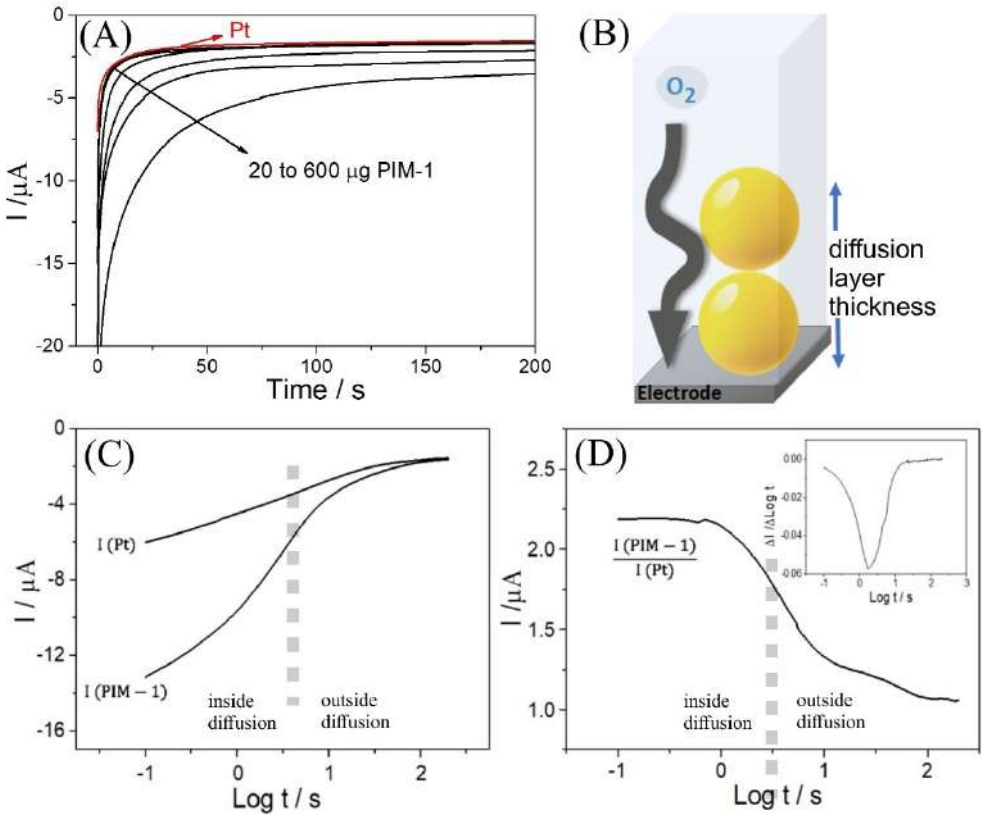

Figure 4. (A) Chronoamperometric response for a 2 mm diameter Pt disk electrode bare or coated with PIM-1 nanoparticles (20, 50, 100, 200, 400, and 600 µg PIM-1) immersed in 0.1 mol L^{-1} phosphate buffer pH 7 with applied potential -0.2 V vs. Ag/AgCl. (B) Illustration of oxygen diffusion through a layer of PIM-1 nanoparticles. (C) Oxygen reduction current transients versus logarithm of time for chronoamperometry at a bare Pt electrode and a PIM-1 nanoparticle covered Pt disk electrode (50 µg PIM-1). (D) Plot of the current ratio $I_{PIM\text{-}1|Pt}/I_{Pt}$ *vs.* Log *t*. Insert: first derivative to demonstrate the peak to identify the transition from inside diffusion to outside diffusion.

By plotting the current data versus logarithm of time, the diffusional transport first within the PIM-1 nanoparticle region and second within the external electrolyte phase can be seen more clearly (Figure 4C). When plotting the ratio of current in the presence and in the absence of PIM-1 (a dimensionless parameter), sigmoidally shaped plots are observed (Figure 4D) that step from a value of approximately 2.2 (for short time) to -1.0 (for longer time). The transition from diffusion inside to outside is not smooth due to porosity and heterogeneity in the polymer film, but a first derivative of the dimensionless parameter plot shows a clear peak indicating the point in time where the transition occurs. It is possible to evaluate the transition time for each PIM-1 film thickness and then evaluate the apparent diffusion coefficient based on Fickian diffusion (equation 1).

$$D_{app,oxygen} = \frac{\delta^2}{2t} \quad (1)$$

Table 2 summarises thickness, transition time, and $D_{app,oxygen}$ data. The diffusion coefficient for oxygen is decreased dramatically when compared to the diffusion coefficient in aqueous electrolyte. There is a three order of magnitude change/decrease and therefore diffusion of molecular oxygen in the PIM-1 nanoparticle film is extremely slow, comparable with diffusion in other types of polymers.

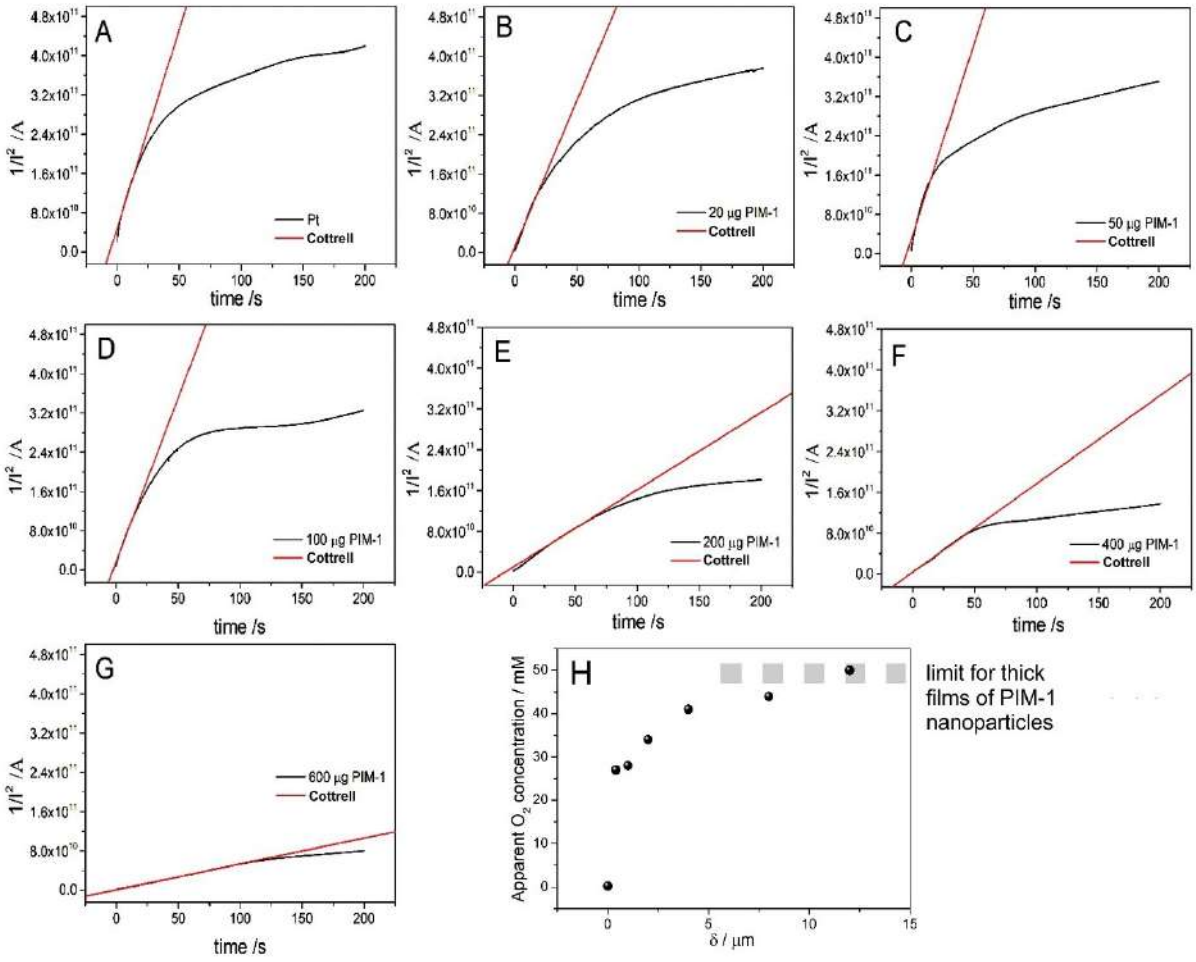

Figure 5. Cottrell plots ($1/I^2$ *versus* time) for of different amounts of PIM-1 nanoparticles on a 2 mm diameter Pt disk electrode (for (A) 0, (B) 20, (C) 50, (D) 100, (E) 200, (F) 400, and (G) 600 µg PIM-1) immersed in a solution containing 0.1 mol L^{-1} of phosphate buffer pH 7. Black line: experimental data; red line: fitting of Cottrell line. (H) Plot of the apparent oxygen concentration *versus* PIM-1 nanoparticle thickness limiting at approx. $c_{app,oxygen}$ = 50 mM.

Next, by means of chronoamperometry, the currents flowing through the PIM-1 modified electrode during the early stages of the transient are investigated. Cottrell plots ($1/I_2$ *versus* time) of the data (Figure 5) are fitted with the Cottrell line to match the early data

points (red line). The Cottrell equation (equation 2) is employed to describe planar diffusion to the electrode surface.

$$I = \frac{nFACD^{1/2}}{\pi^{1/2}t^{1/2}} \quad (2)$$

In this equation F is the Faraday constant (96485 C mol^{-1}), A is the geometric area of the electrode (0.0314 m^2), C is the concentration of the oxygen species, n is the number of electrons for each oxygen molecule diffusing to the surface ($n = 4$), and D is the diffusion coefficient in m^2s^{-1} (as evaluated based on the equation 1). The equation is transformed into equation 3 to show that the slope in the Cottrell plots in Figure 5 provide access to the apparent concentration of oxygen.

$$\frac{1}{I^2} = \frac{\pi}{n^2F^2A^2C^2D}\ t \quad (3)$$

Table 2 summarises the data. Figure 5H shows a plot of the apparent oxygen concentration in the PIM-1 film limiting at approx. 50 mM which is more than 2 orders of magnitude higher when compared to the concentration of oxygen in aqueous solution under ambient conditions. The PIM-1 nanoparticles are able to store high amounts of gas (oxygen) locally at the electrode surface and this can affect the mechanism and activity of oxygen at the electrode surface.

Table 2. Experimental data from chronoamperometry for oxygen reduction at Pt disk electrode with PIM-1 nanoparticle deposits immersed in ambient 0.1 M phosphate buffer pH 7.

Amount of PIM-1 / µg	**Transition time / s**	**Film thickness / µm**	$D_{app,oxygen}$ **/ m^2s^{-1}**	**Approx. Cottrell slope / $A^{-2}s^{-1}$**	**Apparent oxygen concentration $c_{app,oxygen}$ / mM**
0	0.0	0.0	2.0×10^{-9}	8.0×10^{9}	0.4*
20	0.5	0.4	1.9×10^{-13}	1.5×10^{10}	27
50	2	1	2.5×10^{-13}	6.6×10^{9}	28
100	4	2	5.0×10^{-13}	7.4×10^{9}	34
200	10	4	8.0×10^{-13}	1.6×10^{9}	41
400	21	8	1.6×10^{-12}	7.4×10^{8}	43
600	45	12	1.6×10^{-12}	5.1×10^{8}	50

*For the Pt electrode without PIM-1 addition an apparent oxygen concentration of 0.4 mM is obtained (considering $D_{oxygen} = 2.0 \times 10^{-9}$ $m^2 s^{-1}$)

Effect salt concentration (PIM-1). It is interesting to explore the effects of ionic strength (buffer concentration) on the triphasic gas storage capability of PIM-1 nanoparticles. Figure 6A shows cyclic voltammetry data for the reduction of ambient oxygen in 0.01, 0.10, 0.25, and 0.50 M phosphate buffer pH 7 at a PIM-1 nanoparticle coated Pt disk electrode (400 µg PIM-1). By analysing the data, it becomes evident that the PBS concentration exerts some influence on the heterogeneous oxygen kinetics, however the diffusivity of oxygen remained practically constant (Table 3). As the PBS concentration increased from 0.1 to 0.25 M and 0.5 M, the current exhibited a decrease, thereby signifying a reduction in the concentration of dissolved oxygen and, consequently, a lower gas capacity of PIM-1.

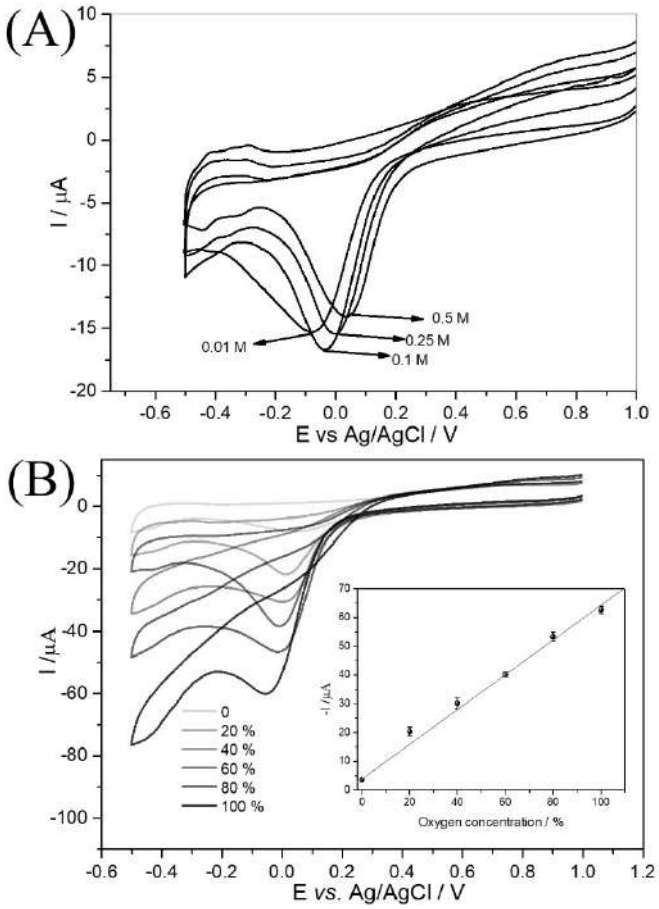

Figure 6. (A) Cyclic voltammograms (scan rate 50 mVs^{-1}) for the reduction of ambient oxygen in 0.01, 0.10, 0.25, and 0.50 M phosphate buffer pH 7 at a PIM-1 nanoparticle coated Pt disk electrode (400 µg PIM-1). (B) Cyclic voltammograms (scan rate 50 mVs^{-1}) of 400 µg PIM-1 deposited on a 2 mm diameter Pt disk electrode immersed in 0.1 mol L^{-1} of phosphate buffer pH 7 saturated with gas containing argon and oxygen. Insert: Calibration plot of the sensor for oxygen determination.

Table 3. Experimental results for a 400 µg PIM-1 nanoparticle deposit on a 2 mm diameter Pt disk electrode. Transients with a Pt Substrate in different concentration of sodium phosphate solution pH 7.

PBS / mol L^{-1}	**slope**	**D / m^2 s^{-1}**	**Time /s**	**O_2 / mM**
0.01	2.2×10^9	2.9×10^{-12}	11	19
0.1	7.4×10^8	1.6×10^{-12}	21	43
0.25	2.3×10^9	2.7×10^{-12}	12	19
0.5	6.0×10^9	3.2×10^{-12}	10	11

Some of these numbers are strange. - calculations have been redone.

3.3. Detection of Oxygen Stored in Nanoparticulate PIM-1: Sensor Electrodes

In order to demonstrate experimental detection of oxygen, the dissolved oxygen concentration in the 0.1 mol L^{-1} of phosphate buffer pH 7 was controlled by mixing oxygen and argon gas prior to purging the solution. Different ratios of oxygen to argon (flowing into the solution to equilibrate for approximately 20 min) were controlled accurately using gas mass-flow controllers (MFC, Platon). The flow rate of oxygen gas was controlled to give 20%, 40%, 50%, 80%, and 100% partial pressure. The laboratory temperature was maintained at 21 ˚C throughout all measurements. Figure 6B shows cyclic voltammograms for the reduction of oxygen at Pt disk electrode coated with 400 μg PIM-1. A clear oxygen reduction the peak was observed at -0.05 V vs. Ag/AgCl. The current increased with oxygen concentration and the peak potential shifted slightly with increasing oxygen concentration. A linear calibration plot demonstrates the fact that the PIM-1 enhanced reduction current signals are directly proportional to the partial pressure of oxygen in the gas phase. This can be interpreted in terms of both oxygen and argon binding into PIM-1 in the same ratio as given by the purging gas.

In terms of practical applications, the observation of enhanced oxygen reduction currents and significantly enhanced local concentrations of oxygen at the electrode surface may lead to benefits in electrochemical devices such as fuel cells, air-metal batteries, or oxygen sensors. By using PIM-1 nanoparticles to locally store oxygen can affect oxygen activity and reactivity at the electrode surface. Similar effects are anticipated for other types of gases.

4. Conclusions

The effect of PIM-1 nanoparticles at a platinum electrode immersed in aqueous 0.10 M phosphate buffer pH 7 has been quantified. Oxygen gas reduction at the electrode is enhanced due to triphasic gas storage in PIM-1. In the presence of PIM-1 nanoparticles (i) the apparent solubility of oxygen in the aqueous phase increases from 0.4 to 50 mM and (ii) the apparent diffusivity of oxygen decreases from 2.0×10^{-9} to 1.6×10^{-9} m^2 s^{-1}. Reactivity of oxygen gas at the electrode is considerably modified.

The effect of PIM materials on triphasic electrode processes has been reported previously for oxygen and for hydrogen gas. It is likely that the effect is general and potentially beneficial in other processes such as electrochemical nitrogen reduction or electrochemical carbon dioxide reduction. More generally, processes involving gas evolution such as hydrogen evolution and oxygen evolution are likely to be enhanced due to the "in situ storage" of gas close to the electrode surface. This phenomenon will allow gaseous products to be generated and stored similar to the case of battery energy storage but without the need for lithium and intercalation reactions. Further potential for application and for further structural evolution of PIM materials for specific applications is high.

Acknowledgements

M.A.B. is particularly grateful for the São Paulo Research Foundation (FAPESP) for a post-doctorate scholarship (grants 2020/01822-8 and 2014/50945-4). F.M. thanks EPSRC for support (EP/K004956/1).

Submetido: Analytica Chimica Acta

Electrochemical monitoring of poly(3-hydroxybutyrate) production from *Burkholderia glumae* MA13 using a molecularly imprinted polymer-reduced graphene oxide modified electrode.

Emanuela da Conceição[a,b], Edervaldo Buffon[a,b], Maísa Azevedo Beluomini[a,b*] Max Fabrício Falone [a,b], Fernanda Batista de Andrade[c,d], Jonas Contiero[c,d], Nelson Ramos Stradiotto[a,b]

[a] Institute of Chemistry, São Paulo State University (Unesp), 14800-060, Araraquara, São Paulo, Brazil.

[b] Institute for Research in Bioenergy (IPBEN), São Paulo State University (UNESP), Araraquara,14800-060, Brazil.

[c] Institute of Biosciences, São Paulo State University (Unesp), 13506-900, Rio Claro, São Paulo, Brazil.

[d] Institute for Research in Bioenergy (IPBEN), São Paulo State University (UNESP), Rio Claro, 13500-230, Brazil.

* Corresponding author: maisa.beluomini@unesp.br

ABSTRACT

The present study reports the development and application of an electrochemical sensor to detect poly(3-hydroxybutyrate) (P3HB) – a bioplastic derived from agro-industrial residues. To overcome the challenges of molecular imprinting of macromolecules such as P3HB, this study employed methanolysis reaction to break down the P3HB biopolymer chains into methyl 3-hydroxybutyrate (M3HB) monomers. Thereafter, M3HB were employed as the target molecules in the construction of molecularly imprinted sensors. The electrochemical device was then prepared by electropolymerizing a molecularly imprinted poly(3IAA) thin film on a glassy carbon electrode surface modified with reduced graphene oxide (GCE/rGO-MIP) in the presence of M3HB. Electrochemical impedance spectroscopy (EIS), cyclic voltammetry (CV), scanning electron microscopy with field emission gun (SEM-FEG), and Raman spectroscopy were employed to characterize the electrode surface. Under ideal conditions, the MIP sensor exhibited a wide linear working range of 0.1 – 10 nM and a detection limit of 0.3 pM (n = 3). The sensor showed good repeatability, selectivity, and stability over time. For the sensor application, the bioproduction of P3HB was carried out in a bioreactor containing the *Burkholderia glumae* MA13 strain and sugarcane byproducts as a supplementary carbon source. The analyses were validated through recovery assays, yielding recovery values between 102 % and 104 %. These results indicate that this MIP sensor can present advantages in the monitoring of P3HB during the bioconversion process.

Keywords: Molecularly imprinted sensor; graphene; methanolysis; bioplastics; biomass.

1. INTRODUCTION

The current concern about environmental issues resulting from the improper disposal of plastic materials has contributed to the development of research for the production of biodegradable plastics, also known as bioplastics [1,2]. Polyhydroxyalkanoates (PHAs) are promising polymers for replacing plastic materials from the petrochemical industry because they exhibit properties similar to those of various thermoplastics and are completely biodegradable when disposed of in diverse environmental conditions [3]. PHAs are fully degraded in the environment by microorganisms to water and carbon dioxide in the presence of oxygen, and to methane under anaerobic conditions [2]. In addition, PHAs have attracted increasing attention for their application as bioplastics due to their biodegradability, biocompatibility, and the ability to be produced from different renewable raw materials [3–5].

PHAs are aliphatic polyesters that, during their production process, accumulate intracellularly in several bacteria as an energy reserve when the culture medium has excess carbon and a limitation of certain nutrients, such as nitrogen, phosphorus, sulfur, oxygen and/or magnesium [2,6,7]. PHAs consist of monomers with varying numbers of carbon atoms in their molecular structure. Poly(3-hydroxybutyrate), or P3HB, is composed of monomers with four carbon atoms, and is the most common and widely studied PHA [6–8]. P3HB is a biopolymer that shares several properties with polypropylene (PP), a polymer obtained from the petrochemical industry. These properties include molecular weight, melting point, stiffness, and glass transition temperature [6]. Therefore, P3HB serves as a promising alternative to replace PP in various industrial applications, with the overarching goal of mitigating the environmental impacts associated with improper disposal of plastic materials.

The biosynthesis of P3HB occurs when there is an excess availability of suitable carbon sources and stress conditions related to other nutrients during cellular growth. With the aid of modern biotechnology tools, it is possible to convert agricultural waste, such as sugarcane byproducts, into P3HB. The biotransformation of agricultural residues is gaining prominence with the implementation of biorefineries. These facilities propose the coproduction of value-added products alongside biofuels, presenting a bioeconomy solution to support industrial bioproducts and waste materials. In this scenario, more than 80 bacterial strains are reported for the production of P3HB, with *Burkholderia glumae* MA13 being a promising gram-negative bacterium found in the Atlantic rain forest [5,7].

To evaluate the efficiency of the PHAs production process, various analytical techniques are employed. To conduct these analyses, the PHAs polymer chains are cleaved, and the precursor monomer is detected and quantified. The methodologies available to characterize the production of these biopolymers are based on techniques such as spectrophotometry, Fourier transform infrared spectroscopy, nuclear magnetic resonance spectroscopy, high-performance liquid chromatography, and gas chromatography coupled to mass spectroscopy [1]. However, these techniques require relatively expensive instrumental apparatus, long analysis times, laborious sample preparation, and complex operational procedures.

On the other hand, electroanalytical techniques offer several advantages compared to the aforementioned methods, such as low cost, ease of operation, fast analysis, portability, and simplicity. In the literature, some enzymatic electrochemical sensors have been used to determine the monomer 3-hydroxybutyrate (3HB) [9–15]. These enzymatic sensors are characterized by their low cost, fast analysis, and remarkable selectivity. Despite these advantages, these biosensors have some limitations, such as the potential

for enzymatic activity loss, poisoning of the electrode surface due to the adsorption of intermediates, and low stability depending on temperature and pH.

To develop a new method for detecting the amount of P3HB formed after the bioconversation process, a non-enzymatic sensor based on molecularly imprinted polymers (MIPs) was constructed. MIPs are synthetic polymers capable of selectively recognizing a specific molecule. In other words, these polymers have the ability to mimic interactions occurring at biological receptors, such as antigen-antibody and enzyme-substrate [16,17]. Generally, the synthesis of MIPs involves trapping a template molecule around a polymeric matrix that contains a functional monomer as a precursor. Following the polymerization process, the removal of the template molecules promotes the formation of cavities with sizes, shapes, and orientations complementary to the target molecule. Following the creation of these cavities, the MIPs can be used for the detection of analytes through molecular recognition processes [18,19].

Molecular imprinting technology has demonstrated excellent performance in imprinting low molecular weight molecules, such as sugars, steroids, amino acids and their derivatives, drugs, and pesticides, among others. However, a significant challenge has been the application of this technique to macromolecules, including proteins, polysaccharides, polymers and even cells [20,21]. To date, there are few works documented in the literature that report the imprinting of large chain molecules, such as P3HB. This is mainly due to the complexity and intrinsic instability of macromolecules, which sometimes result in molecular imprints with low selectivity and limited affinity. Furthermore, the larger size of the target molecule leads to diffusion limitation, as macromolecules cannot effectively penetrate the cavities imprinted in a bulky structure [22,23]. As a result, imprinting macromolecules represents a significant challenge that requires innovative approaches.

In this context, following the production of poly(3-hydroxybutyrate) (P3HB) using the Burkholderia glumae MA13 strain, the product underwent a methanolysis reaction to cleave the polymeric chains of P3HB. Subsequently, the cleaved methyl(R)-3-hydroxybutyrate monomer, M3HB, resulting from this cleavage, was employed as the target molecule in the construction of electrochemical devices. Among the several functional monomers available for the preparation of MIPs, 3-indoleacetic acid (3IAA) possesses some interesting characteristics for the electropolymerization method. 3IAA can be easily electropolymerized and has good mechanical stability, excellent electrical conductivity, and the ability to interact with different analytes via hydrogen interactions. Moreover, 3IAA is a biodegradable polymer, which aligns with the principles of green chemistry and environmental sustainability [24,25]. This makes it suitable for the development of a MIP-based non-enzymatic electrochemical device for monitoring P3HB production.

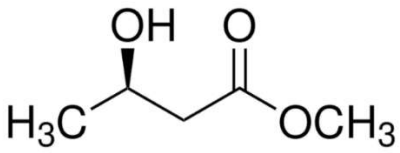

Fig. 1. Chemical structure of Methyl (R)-3-hydroxybutyrate

To enhance the sensitivity of MIP-based electrochemical devices, prior to immobilizing MIP films, the glassy carbon electrode (GCE) has been modified with nanostructured materials. Reduced graphene oxide (rGO) is a graphene-derived material obtained by reducing graphene oxide (GO) in a process that restores the sp^2 hybridizations of the graphene network. As a result of this process, rGO exhibits higher electrical conductivity compared to GO, in addition to having a high surface area and good chemical and mechanical stability [26–28]. Moreover, the modification of electrodes with rGO

increases the roughness of these devices, facilitating the adhesion of the MIP films to the electrode surfaces and expanding up to 15 times the number of cavities formed for the detection of the target molecules [29].

Bearing that in mind, this work report, for the first time, the application of methanolysis to cleave P3HB and form M3HB molecules capable of interacting with 3IAA, resulting in a selectively thin film on the electrode surface. Furthermore, this work reports the development of a selective analytical method to quantify a bioplastic formed from sugarcane waste. All the steps to develop the sensor were performed via electropolimerization, ensuring the control of the sensor thickness and the quality of the cavities. Characterization was conducted utilizing scanning electron microscopy (SEM), electrochemical impedance spectroscopy (EIS), and Raman spectroscopy. The GCE/rGO-MIP showed high selectivity, sensitivity, a low detection limit, reproducibility, and good stability. The sensor was successfully applied in the determination of M3HB using *Burkholderia glumae* MA13 for production of polyhydroxyalkanoate (PHA) from sugarcane byproducts.

2.EXPERIMENTAL

2.1 Reagents and apparatus

All reagents employed in this study were of analytical grade and included: graphene oxide (GO, 4.0 mg mL^{-1}, purity: > 95.0%), 3-indoleacetic acid (3IAA, purity: 98.0%), sodium sulfate (Na_2SO_4, purity: ≥ 99.0%), sucrose (purity: ≥ 99.5%), potassium ferricyanide ($K_3[Fe(CN)_6]$, purity: 99.0%), potassium chloride (KCl, purity: ≥ 99.0%), potassium phosphate bibasic (purity: ≥ 98.0%), citric acid (purity: ≥ 99.5%), glacial acetic acid (purity: ≥ 99.0%), sulfuric acid (purity: 95.0–98.0%), benzoic acid (purity: ≥ 99.5%), chloroform (purity: ≥ 99.9%), ethanol (purity: > 99.9%), methanol (purity: ≥ 99.9%),

methyl 3-hydroxybutyrate (M3HB, purity: ≥ 95%), methyl 3-hydroxyvalerate (M3HV, purity: ≥ 98%), methyl 3-hydroxyhexanoate (M3HH, purity: ≥ 98%), methyl 3-hydroxyoctanoate (M3HO, purity: > 98%), methyl 3-hydroxydecanoate (M3HD, purity: > 98%). All solutions were prepared using ultrapure water obtained from a Milli-Q system (18.2 MΩ cm^{-1}).

Electrochemical measurements were conducted with an AUTOLAB PGSTAT30 potentiostat/galvanostat (Metrohm – Herisau, Switzerland) controlled by NOVA 1.11 software. The setup of the conventional three-electrode electrochemical consisted of a glassy carbon electrode (GCE, Ø = 3.0 mm) modified with rGO and MIP film (GCE/rGO-MIP) as the working electrode, Ag/AgCl (3.0 M KCl) as reference electrode, and a platinum wire as the auxiliary electrode.

2.2 GCE/rGO-MIP electrode preparation

Initially, the GCE was mechanically polished using an alumina suspension with a particle size of 0.30 μm. After this polishing process, ultrapure water was used to wash the electrode and eliminate any alumina particles adsorbed on its surface. An aqueous suspension of 0.5 mg mL^{-1} graphene oxide in 0.1 M Na_2SO_4 was employed to modify the GCE. To this end, the potential of − 1.5 V was applied for 500 s for the electroreduction of the graphene oxide sheets directly on the electrode surface [26]. Then, the GCE was taken to an oven at 50 ºC for drying and obtaining the GCE/rGO electrode.

The synthesis of the MIP film on the surface of the GCE/rGO electrode was performed by electropolymerization. To this end, the electrode was immersed into a solution of citrate-phosphate buffer (CPB, 0.1 M, pH 5.0) containing 3.0 mM 3IAA and 17.5 mM M3HB. Electropolymerization was performed in a potential range of 0.0 to 1.3 V for three voltammetric cycles at 50 mV s^{-1}. After the electropolymerization step, the

M3HB molecule was removed from the poly(3IAA) polymer structure using a solvent mixture containing 90% ethanol and 10 % acetic acid (*v:v*) for 60 s. For comparison, a polymer film without M3HB molecules, denoted non-imprinted polymer (NIP), was electropolymerized onto the GCE/rGO surface using the same experimental conditions.

The electrochemical behavior of the proposed sensor during the molecular recognition process was investigated by cyclic voltammetry (CV) and electrochemical impedance spectroscopy (EIS) using 5.0 mM $K_3[Fe(CN)_6]$ in 0.5 M KCl solution as a redox probe. Furthermore, the GCE/rGO-MIP electrode was characterized microscopically using a field emission gun scanning electron microscope (FEG-SEM) from JEOL (model: SM 7500F). Raman spectroscopy measurements involved a spectrometer from HORIBA JOBIN YVON (model: LabRAM HR800), which was equipped with a He-Ne laser at 623 nm.

2.3 PHA production

Burkholderia glumae MA13 were isolated from the Atlantic rainforest in Ubatuba (São Paulo State, Brazil) and used as a bacterial strain for polyhydroxyalkanoate (PHA) production from sugarcane bagasse hydrolysis [5,7]. Lysogeny broth (LB), composed of 10 g/L tryptone, 5 g/L NaCl and 5 g/L yeast extract was employed for inoculum preparation and bacterial maintenance. This was carried out on Petri plates and in an ultra-low-temperature freezer at −80°C. The bacterial cultures were stored in cryovials, with a final glycerol concentration of 20% (v/v). Then, a 1:100 (*v:v*) pre-inoculum was performed in a mineral salts medium (MSM) as described by De Paula et al., [5]. Sugarcane bagasse hydrolysis follows the methodology based on the work of Beluomini et al., [30] The bagasse hydrolysate was added to MSM as PHA precursors. A concentration of 20 g L^{-1} sucrose was used as pure the carbon sources, with the addition

of sucrose as a carbon source at 37° C. The solid media were prepared by incorporating 20 g/L agar. The culture was kept under agitation at 200 rpm for high aeration and maximum growth of the bacteria. After 18 h of cultivation, the pre-inoculum was used for the fermentation process employing a 1:10 (*v:v*) inoculum. The fermentation step was performed in a 2.0 L capacity BioFlo®120 bioreactor (Eppendorf, USA) containing 1.0 L of supplemented MSM. The cultures were kept at 37°C with gentle agitation at 120 rpm for 96 h.

2.4 PHA analysis

After the fermentation process concluded, the centrifugation of the product was performed at 8,000 rpm for 20 minutes at 4°C, and the supernatant was discarded. The recovered biomass was lyophilized, and each 10 mg of cell lyophilized was subjected to methanolysis, carried out as follows: 2 ml of chloroform and 2 ml of methanol acidified with 15% sulfuric acid (85:15 *v/v*) were added to glass test tubes and maintained at 85°C for 4 hours. After the methanolysis reaction, the tubes were cooled to room temperature, and 2 mL of MilliQ H_2O were added and stirred for 30 seconds, followed by 3 hours of incubation to separate the organic and aqueous phases. Finally, after separation, the aqueous phase was discarded, and the organic phase containing the methyl esters was stored at –20°C for further analysis [31].

2.5 M3HB determination using the GCE/rGO-MIP electrode.

After the methanolysis reaction, which was performed to cleave the polymeric chains of P3HB, the resulting product (M3HB) was quantified using the GCE/rGO-MIP electrode. To this end, the organic phase was diluted by a factor of 1 ppm using CPB (0.1 M, pH 5.0). Differential pulse voltammetry (DPV) was the electrochemical technique

used during the measurements in a solution containing 5.0 mM $K_3[Fe(CN)_6]$ in 0.5 M KCl solution as a redox probe. DPV were conducted using a pulse height of 50 mV, a pulse width of 50 ms, and a pulse time of 0.5 s. The determination of M3HB was performed by the standard addition method, in which known concentrations of the analyte were added to the sample under analysis [32]. The results obtained were validated by recovery tests and compared with the GC-MS technique.

3. RESULTS AND DISCUSSION

3.1 Morphological Characterization of the GCE/rGO-MIP electrode

Fig. 2 displays the FEG-SEM images of the electrode surface after each modification step. In Fig. 2A, the GCE appears uniform and smooth prior to any modification. Fig. 2B illustrates the electrodeposition of RGO sheets onto the GCE, which clearly shows a homogeneous coverage and of roughened. This increased surface roughness enhances the adhesion of the MIP film during the electropolymerization process. Fig. 2C and 2D show the GCE/rGO-MIP and GCE/rGO-NIP following the electropolymerization process, respectively. It is possible to observe that the polymeric structure of poly(3IAA) has coated uniformly all RGO sheets, resulting in a less rough surface. Additionally, the poly(3IAA) film appears to have a thin thickness, as evidenced by the folds of some rGO sheets visible underneath the polymeric structure.

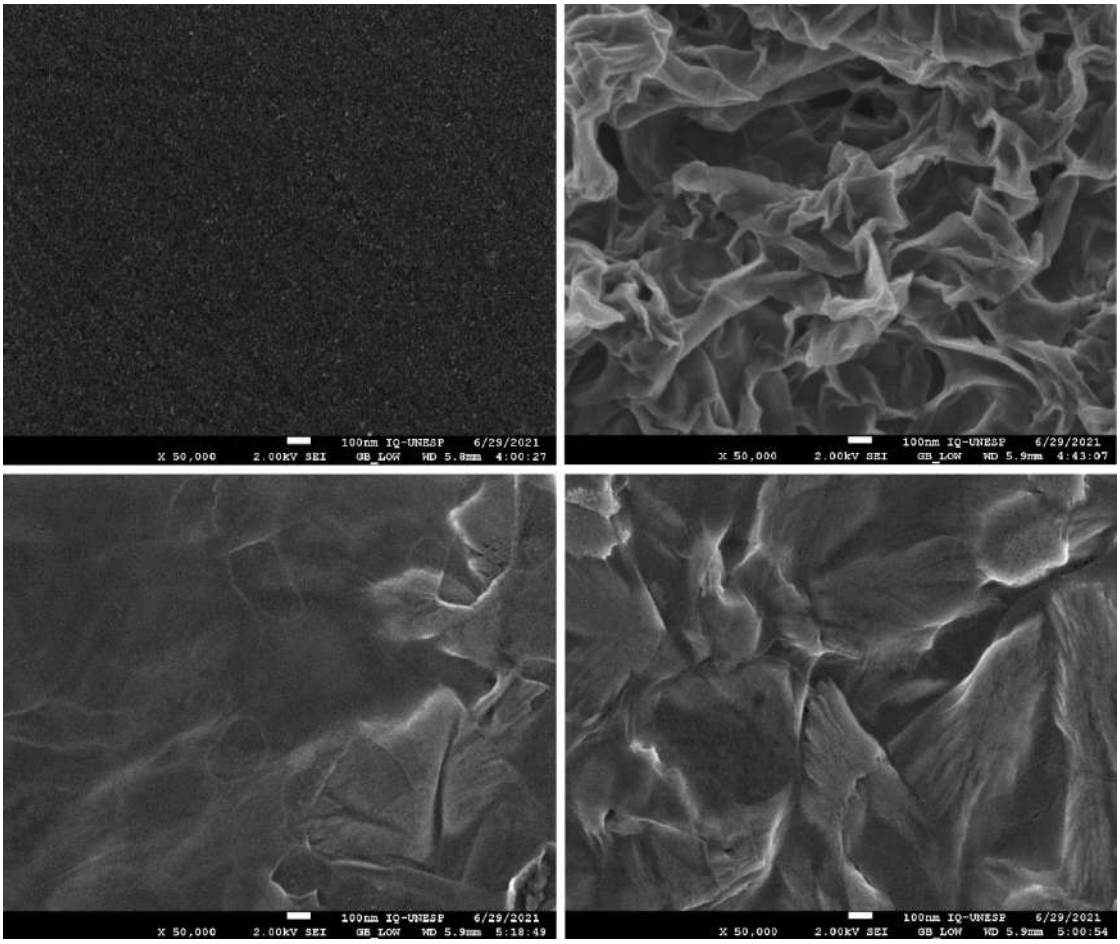

Fig. 2. FEG-SEM images for: (A) GCE, (B) GCE/rGO, (C) GCE/rGO-MIP and (D) GCE/rGO-NIP.

The GCE, GCE-rGO, GCE/rGO-MIP, and GCE/rGO-NIP electrodes were also characterized using Raman spectroscopy, a non-destructive technique employed in the analysis of materials based on carbon. In the spectra shown in Fig. 1S, two characteristic carbon bands can be observed: the D-band at 1350 cm^{-1}, indicates the presence of defects in carbon structures (rupture of C=C sp^2 domains), and the G-band at 1575 cm^{-1} is characteristic of in-plane vibrations associated with sp^2 carbon atoms [33].

In this investigation, following the electrode modification with rGO, there was a relatively higher intensity of the G band compared to the D band. This observation

suggested that the electrodeposition of rGO film led to an increased concentration of sp^2 carbon on the GCE. The ratio between the intensities of the D and G bands (I_D/I_G) serves as an indicator of the level of defects in the analyzed carbon material. In this study, the modification of the electrode with rGO resulted in a decrease in the ID/IG value from 2.25 to 1.35. This result was attributed to the reduced number of defects on the GCE, indicating a lower amount of structural defects in rGO compared to GCE [34].

However, after electropolymerization, the ID/IG value increased from 1.35 to 2.24 due to the amorphous nature of the poly(3IAA) film. This suggested that the incorporation of the polymer into the rGO structure resulted in a heightened presence of carbon defects on the electrode surface. Furthermore, it was observed that the intensities of the D and G bands were higher for the GCE/rGO-MIP and GCE/rGO-NIP compared to the GCE/RGO, indicating that the formation of the polymeric structure on the GCE/rGO contributed with the increase in carbon concentration on the surface of the electrode. In conjunction with the SEM-FEG, these findings confirm the effective modification of the GCE surface with both rGO and a polymeric poly(3IAA) film.

3.2 Electrochemical Characterization of the GCE/rGO-MIP

The GCE, GCE/rGO, GCE/rGO-MIP and GCE/rGO-NIP electrodes were electrochemically characterized by CV and EIS after each modification step. The characterization was performed using solution of $5.0\,mmol\,L^{-1}$ $[Fe(CN)_6]^{-3}$ in $0.5\,mol\,L^{-1}$ KCl as a redox probe. Fig. 3A shows the distinctive reversible electrochemical behavior of redox probe on the GCE (curve a). Following the modification of the GCE with rGO (curve b), an increase in the electrochemical probe current was observed. This increase is attributed to the electrodeposition of reduced

graphene sheets onto the GCE, promoting an increase in terms of the electroactive area of the electrode.

EIS measurements were conducted to study the modified electrode surface. The results was illustrated through Nyquist diagrams, characterized by a semicircular region in the high-frequency range and a linear region in the low-frequencies range. In these diagrams, the dimension of the semicircle directly correlates with the magnitude of the charge-transfer resistance (R_{ct}); the R_{ct} involves the construction of the theoretical electrical circuit that simulates the experimental data obtained. The Nyquist diagrams obtained through the electrode modification are shown in Fig. 3B, along with an equivalent circuit that aligns with the experimental data. The circuit equivalent is composed of the solution resistance (R_s), constant phase element (CPE), R_{ct}, and Warburg diffusion element (W). In the Fig. 3B, a clearly defined semicircle is observed for the GCE, with an associated R_{ct} value of 142 Ω (curve a). After modifying the electrode surface with rGO, a decrease in the size of the semicircle was observed, and a value of 76 Ω was obtained for R_{ct}, as shown in Fig. 3B, curva b. This observation suggests that the enhanced electroactive area of the electrode, as a consequence of graphene sheets electrodeposition, significantly improves the charge transfer at the interface between the electrode and solution.

The surface of the GCE/rGO was employed for the development of the MIP-based sensor. After the electropolymerization step in the presence (GCE/rGO-MIP) and absence (GCE/rGO-NIP) of M3HB, the modified electrode was also characterized. Figure 3C shows that, following electropolymerization, the GCE/rGO-MIP (Fig. 3C, curve a) and GCE/rGO-NIP (Fig. 3C, curve b) electrodes did not exhibit any redox peaks from the electrochemical probe. This suggests that a non-conductive poly(3-IAA) film covered the entire surface of the GCE/rGO, preventing any electronic transfer between the

electrochemical probe and the surface of this electrode. Following the removal of the M3HB template molecules from the GCE/rGO-MIP electrode using an ethanolic solution containing 10% acetic acid for 60 s, it was possible to observe the redox peak of the electrochemical probe (Fig. 3C, curve c). This behavior indicates the efficiency of the extraction process in eliminating the template molecules and, consequently, forming the imprinted cavities. As a result, the redox probe could reach the electrode surface through the formed cavities, facilitating the oxidation/reduction process on the GCE/rGO surface. In an opposite way, after the rebinding process using a 10 nmol L^{-1} M3HB solution (CPB; 0.1 M; pH 5.0) for 10 min, a notable decrease in the current intensities of the electrochemical probe was observed (Fig. 3C, curve d). This reduction in current intensity suggests that some imprinted cavities were occupied by M3HB molecules during the rebinding process, leading to a decrease in the number of cavities accessible for the electrochemical probe to access the electrode surface.

The EIS results acquired after electropolymerization corroborate the observations made in the CV studies. Fig. 3D shows a large semicircle for GCE/rGO-MIP (Fig. 3D, curve a) and GCE/rGO-NIP (Fig. 3D, curve e); the R_{ct} value of these electrode, were 86.4 kΩ and 95.0 kΩ, respectively. This notable increase in the R_{ct} parameter, in comparison with the non-electropolymerized electrode, was attributed to the non-conductive nature of the poly(3IAA) film. Remarkably, after the formation of imprinted cavities in the polymer matrix, a noteworthy decrease to 14.5 kΩ was observed in the R_{ct} value (Fig. 3D, curve c). This result indicates that the redox probe successfully permeated the polymeric structure through the cavities toward the GCE/rGO surface. It is worth noting, however, that after the rebinding process, there was an increase in the Rct value to 23.6 Ω (Fig. 3D, curve d). These data show the successful imprinting of M3HB molecules on the electrode

surface. Subsequently, after their removal, access cavities are formed for the electrochemical redox probe to generate the signal.

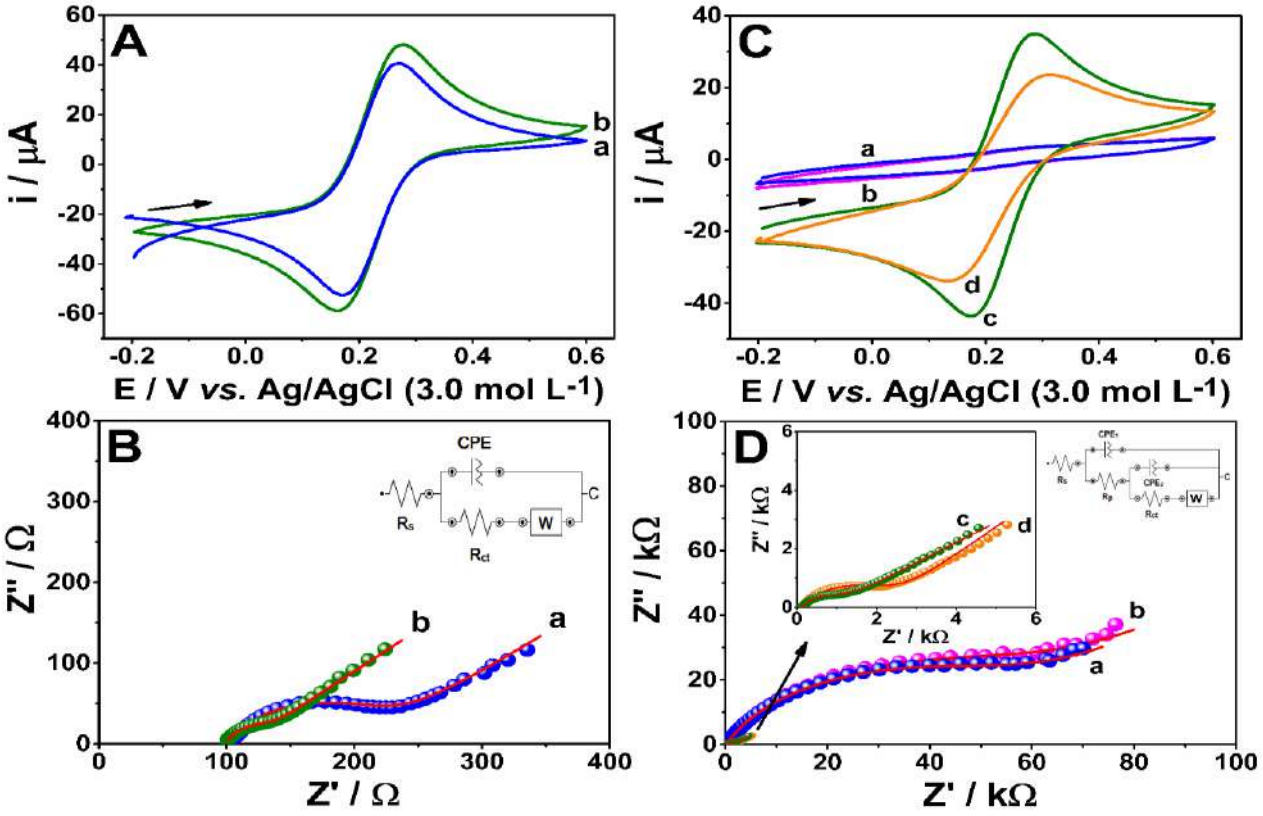

Fig. 3. (A) Cyclic voltammograms at 50 mV s^{-1} and (B) Nyquist diagrams obtained in a frequency range of 100 kHz to 10 mHz using a fixed potential of 0.23 V and a potential amplitude of 10 mV for: (curve a) GCE and GCE/rGO, (curve b). (C) CV and (D) EIS for GCE/rGO-MIP after electropolymerization (curve a) and GCE/rGO-NIP (curve b). After removing process of the template molecules from the poly(3IAA) structure (curve c) and after the rebinding process (curve d). All measurements were performed using 5.0×10^{-3} mol L^{-1} $K_3[Fe(CN)_6]$ in 0.50 mol L^{-1} KCl solution as a redox probe.

3.3 Electropolymerization process

During the construction of the MIP sensor, the electropolimerization process of poly(3IAA) on the GCE was studied by voltammetry, as shown in Fig. S2A. At 0.35V, a

small peak is observed, attributed to the electrooxidation of the monomer, resulting in the oxidation product cationic 3-methyleneindolenine carboxylic acid. This process involves $-2e^-$ and $-H^+$[24]. Additionally, another anodic peak is noted at 0.77 V, indicating the creation of a dimer from the cationic 3-methyleneindolenine carboxylic acid. In Fig. S2A, the diminishing current intensities signify the development of a low-conductivity poly(3IAA) film on the GCE/rGO, resulting in the obstruction of the electrode surface. Throughout the electropolymerization step, M3HB molecules are trapped within the polymeric structure owing to their interactions with 3IAA monomers. These interactions may take place between the hydroxyl and carboxyl groups of the M3HB and the NH_2 group presents in the 3IAA units. Additionally, M3HB molecules can also engage in H-interactions with the cationic indole molecules of the poly(3IAA) film [35]. These interactions play a crucial role in the creation of specific cavities on the electrode surface. The electropolymerization of 3IAA in the presence of M3HB is shown in the voltammogram of Fig. S2B. The voltammetric profile is nearly identical to that obtained in the absence of M3HB (Fig. S2A). This result suggests that the 3-HB molecule exhibits no electroactive behavior on the surface of the GCE/rGO electrode. Considering this, the performance of the electrochemical device proposed for M3HB detection was evaluated using the redox probe $K_3[Fe(CN)_6]$. For this, the signal was based on the change in its current intensity (Δi), calculated using the following equation: $\Delta i = i_0 - i_x$, where i_0 and i_x represent the current intensities before and after the rebinding process, respectively.

3.4 Optimization studies

The experimental variables associated with the preparation of the MIP film were found to directly impact the analytical performance of the resulting electrochemical device. In this regard, the main parameters influencing the electrosynthesis and

performance of the molecularly imprinted poly(3IAA) film were investigated. During these studies, the electrode response was monitored by DPV using 5.0 mM $K_3[Fe(CN)_6]$ in 0.5 M KCl solution as a redox probe. The results of the optimization studies are discussed in Section S3 of Appendix A.

In summary, under optimized conditions, the development of the MIP film on the GCE/rGO surface was carried out over a potential range of 0 to 1.3 for three voltammetric cycles at a scan rate of 50 mV s^{-1} using a CPB (0.1 M, pH 5.0) solution containing 3.0 mM 3IAA and 17.5 mM M3HB. Following electropolymerization, the template molecules were removed for 60 s using a solvent mixture containing 90% ethanol and 10% acetic acid (*v:v*). Subsequently, rebinding studies were performed using CPB (0.1 mol L^{-1}, pH 5.0) for 10 minutes, in solutions with varying concentrations of M3HB.

3.5 Analytical performance of the GCE/rGO-MIP electrode in M3HB analysis.

After optimizing the experimental conditions, analytical curves were constructed to assess the performance of the GCE/rGO-MIP and GCE/rGO-NIP electrodes in M3HB detection. Fig. 4A shows the voltammograms obtained after the rebinding steps using different M3HB concentrations. In this figure, a decrease in the peak current of the redox probe is observed in response to an increasing concentration M3HB. This behavior was attributed to the filling of the imprinted cavities with M3HB molecules, hindering the access of the electrochemical probe to the electrode surface for the electron transfer process [36,37]. Fig. 4B shows the calibration curves obtained for the GCE/rGO-MIP and GCE/rGO-NIP electrodes across a concentration range of 0.1 to 10 nM. In this figure, it is possible to observe that the GCE/rGO-NIP electrode exhibited lower current intensities compared to the GCE/rGO-MIP electrode. This difference was attributed to the absence of imprinted cavities in the NIP film, rendering it unsuitable for the detection of M3HB

molecules. Concerning the GCE/rGO-MIP electrode, the decrease in the current intensity of the electrochemical probe exhibited a direct proportionality to the increase in M3HB concentration across two linear ranges: 0.1 – 1.0 nM and 1 – 10 nM, with the corresponding linear regression equations: $\Delta i\ (A) = 3.4 \times 10^{4}\ (M) + 6.1 \times 10^{-5}$ (R^2 = 0.9910) and $\Delta i\ (A) = 2.2 \times 10^{3}\ (M) + 9.2 \times 10^{-5}$ (R^2 = 0.9963), respectively.

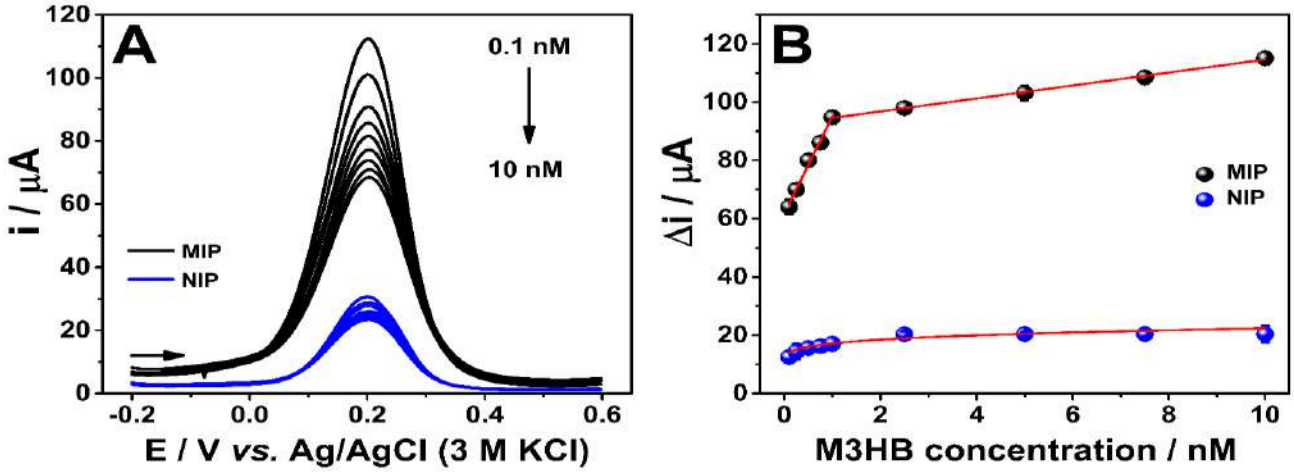

Fig. 4 (A) DPVs obtained for the GCE/rGO-MIP and GCE/rGO-NIP electrodes after the rebinding process for 10 min using solutions of CPB (0.1 M, pH 5.0) containing different M3HB concentrations. DPV measurements were performed using 5 mM $K_3[Fe(CN)_6]$ in 0.5 M KCl solution as a redox probe. (B) Calibration curves obtained for the GCE/rGO-MIP and GCE/rGO-NIP electrodes over a M3HB concentration range of 0.1 to 10 nM (n = 3).

The existence of two linear ranges in MIP sensors is frequently reported in the literature [18,29,38]. This observation is attributed to the mass transfer resistance that M3HB molecules need to overcome to access the cavities situated in the inner part of the MIP film. When the GCE/rGO-MIP electrode is employed for the molecular recognition process, the M3HB molecules selectively occupy the cavities situated on the surface of

the film. These surface cavities offer lower resistance to the rebinding process. As the M3HB concentration increases, the surface cavities get completely occupied, and the rebinding process initiates in the cavities situated in the innermost part of the film. However, these inner cavities are less susceptible to the rebinding process due to the mass transfer resistance. Consequently, a reduction in the angular coefficient of the calibration curve is observed once all the cavities are occupied by the M3HB molecules.

The limits of detection (LOD) and quantification (LOQ) of the GCE/rGO-MIP electrode were determined using the first concentration range (0.1 – 1 nM) and the subsequent equations: $\mathrm{LOD} = {}^{3\mathrm{SD}}/_{m}$ and $\mathrm{LOQ} = {}^{10\mathrm{SD}}/_{m}$. Here, SD represent the standard deviation, and *m* is the slope of the calibration curve (n = 3). The obtained values for *m*, LOD and LOQ were 3.4×10^4 A M^{-1}, 30 pM and 0.1 nM, respectively. The performance of the GEC/rGO-MIP electrode was compared to other analytical methods documented in the literature. As shown in Table 1, the electrode proposed in this work presented the lowest LOD compared to other methodologies found in the literature. Furthermore, it is noteworthy that the present work makes a significant and novel contribution to the literature regarding the electrochemical monitoring of P3HB production from *Burkholderia glumae MA13.*

Table 1. Analytical performance of the GCE/rGO-MIP and other analytical methods reported in the literature for the detection and quantification of 3HB.

Electrode	**Linear range (µM)**	**LOD (µM)**	**Detection method**	**sample**	**Ref.**
THI/rGO/SPCE	10 -400	1	amperometry	Human serum	[9]

Screen printed electrode mixed with Fc-OH and thionine	50 - 5000	16	amperometry	Human blood	[10]
Au-PCB/Ru/MXene-β-HBD-NAD^+-GA-BSA electrode	360 - 17900	45	amperometry	Human serum	[11]
3-HBDH/$[Ru(bpy)_3]^{2+}$ /GO/NAD^+/SPCE	200 - 2000	-	amperometry	Bovine serum	[12]
1,10-PD/NAD^+/$^{3-}$ HBDH/EPAD	100 - 6000	300	amperometry	spiked whole blood	[13]
GCE /SAF	10 - 60	2	DPV	whole blood	[14]
Mn_2O_3/SPCE	0 – 10000	500	CV	Artificial Urine	[15]
GCE/rGO-MIP	1×10^{-4} – 1×10^{-2}	3.0×10^{-5}	DPV	*Burkholderia glumae MA13*	This work

SPCE: Sreen-sprinted carbon electrode; rGO: reduced graphene oxide; THI: thionine; Au-PCB: Gold-printed circuit board; β-HBD: β-hydroxybutyrate dehydrogenase composite; BSA: bovine serum albumin; GA: glutaraldehyde; EPAD: electrochemical paper-based analytical device; 1,10-PD: 1,10-phenanthroline-5,6-diol; SAF: salicylate moiety linked to a reporter amino ferrocene.

To date, there are no existing MIP-based electrochemical sensors designed for the determination of P3H3 using M3HB as the template molecule. The majority of works reported in the literature that can be applied to determine P3HB are based on biosensors utilizing the enzyme 3-hydroxybutyrate dehydrogenase (3-HBDH). The focus of these biosensors was on determining ketoacidosis in blood or human serum. In general, these studies involved the use of catalysts such as the NAD^+/NADH system,

Ferrocenemethanol (Fc-OH) employed as the oxidant, and thionine as the electron transfer agent. However, these systems have drawbacks, including a significant overpotential for NADH oxidation and electrode passivation. Additionally, enzyme-based sensors exhibit significant disadvantages, including complex and multi-step procedures for enzyme immobilization, poor reproducibility, inadequate stability, and high costs. Furthermore, the performance of these sensors is limited by environmental conditions such as temperature, pH, and humidity [15,39]. In fact, the stability of biosensors is crucial for their practical application. Therefore, compared to existing sensors, the GCE/rGO-MIP has significant advantages for determining P3HB. These involve the use of 3IAA as a biodegradable monomer and the application of minimal solution volumes for electrochemical analyses, which is environmentally and economically favorable.

3.5 Selectivity of the GCE/rGO-MIP electrode for M3HB detection

When it comes to MIP-based devices, the selective identification of the target molecule by the molecularly imprinted film can be compromised by the presence of other compounds with similar structures in the sample under analysis. In this study, the performance of the MIP film for selective recognition of the M3HB molecule was evaluated using other methyl esters that can be produced during cleavage of PHA chains. These methyl esters included: methyl 3-hydroxyvalerate (M3HV), methyl 3-hydroxyhexanoate (M3HH), methyl 3-hydroxyoctanoate (M3HO) and methyl 3-hydroxydecanoate (M3HD). Fig. 5 shows that when compared to the GCE/rGO-MIP, the GCE/rGO-NIP electrode exhibited lower current intensities for all compounds under study, which were attributed to the absence of imprinted cavities in the NIP film.

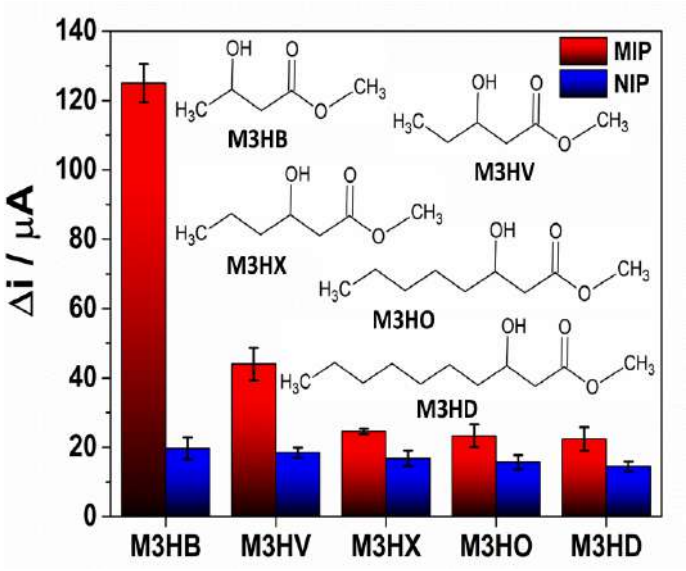

Fig. 5. Sensitivity of the GCE/rGO-MIP and GCE/rGO-NIP electrodes for the detection of M3HB, M3HV, M3HX, M3HO and M3HD (1 nM). The current intensity was monitored by DPV using 5 mM $K_3[Fe(CN)_6]$ in 0.5 M KCl solution as a redox probe (n = 3).

The response of the GCE/rGO-MIP electrode was inversely proportional to the size of the M3HB, M3HV, M3HX, M3HO and M3HD molecules (see Fig. 5), indicating that the M3HV, M3HX, M3HO and M3HD molecules have steric hindrance preventing them from entering the cavities formed for the M3HB molecules. This electrode presented a current intensity (Δi) of nearly 2.8, 5.1, 5.4 and 5.6 times higher for the detection of M3HB than for the M3HV, M3HX, M3HO and M3HD molecules, respectively. This current difference indicates that the GCE/rGO-MIP electrode is selective for the detection of the M3HB molecule in comparison to the other molecules employed in this study.

The selectivity of the GCE/rGO-MIP electrode for recognizing the P3HB molecule was also evaluated using the imprinting (α) and selectivity (β) factors. The α parameter allows the evaluate of the capacity of the imprinted cavities to interact with the target molecules [40]. As can be seen in Table 2, the value of α was 6.3 for P3HB and

less than 2.4 for the other compounds under study. This indicates that the cavities created in the poly(3IAA) structure preferentially recognize the M3HB molecule. Furthermore, the β values demonstrate that the imprinted cavities are selective for the recognition of this molecule. Essentially, the results obtained in this work reveal that the GCE/rGO-MIP electrode can be used for the selective analysis of the P3HB molecule.

Table 2: Selectivity parameters for the GCE/rGO-MIP and GCE/rGO-NIP sensors used for the detection of M3HB and some possibly interfering molecules.

	MIP (μA)*	**NIP (μA)***	**α****	**β*****
M3HB	125	19.7	6.3	*
M3HV	44	18.5	2.4	2.7
M3HX	24.6	16.8	1.5	4.3
M3HO	23.3	15.7	1.5	4.3
M3HD	22.4	14.5	1.5	4.1

*The replicates of the experiments were carried out with different sensors.

** α =Δi(GCE-MIP)/ Δi(GCE-NIP).

*** β = α (3-HB) / α (interferent).

3.6 Repeatability, reproducibility and stability of the GCE/rGO-MIP electrode

The analytical performance of the GCE/rGO-MIP was also evaluated in terms of repeatability through the detection of P3HB for 10 consecutive trials using the same electrode. To this end, after each detection step, the extraction procedure was performed to remove the M3HB molecules from the imprinted cavities and leave these sites available for the next rebinding process. After 10 consecutive measurements, the electrode under study exhibited a relative standard deviation (RSD) of 5.0%. The reproducibility of the GCE/rGO-MIP electrode was assessed during the detection of P3HB using 10 different electrodes, which were prepared separately following the procedure described in Section

2.2. The RSD value obtained during P3HB detection using 10 different electrodes was 4.3%.

The stability of the GCE/rGO-MIP electrode was studied during M3HB detection over time For this purpose, an electrode was prepared and stored in a dry place at room temperature. This device was used for the detection of P3HB for 15 days. After this period, the electrode showed a decrease in its current intensity of less than 10%. This decrease was attributed to the loss of the capability of the imprinted cavities to recognize the P3HB molecule over time. Essentially, the results obtained in these studies reveal that the GCE/rGO-MIP electrode exhibits a reproducible and stable performance for P3HB detection.

3.7 Quantification of P3HB from Burkholderia glumae MA13

The applicability of the GCE/rGO-MIP was assessed by determining P3HB, in a sample of polyhydroxyalkanoate (PHA) sample obtained from sugarcane wastes. The determination employed the addition method, involving the addition of known concentrations of the species of interest to a known volume of the sample. To achieve this, samples with incorporated standards were prepared in a range of 0.1 – 0.5 nM and utilized to generate voltammograms. The relationship between the amount of substance added to the sample and the respective peak currents was plotted, as illustrated in Fig. S8. The resulting curve yielded the following linear regression equation: $I\ (A) = 4.6\times10^{4}\ C_{M3HB}\ (M) + 7.2\times10^{-6}$ ($R^2 = 0.9997$).

The point where the straight line intersects the ordinate axis represents the voltammogram current of the substance being determined, without any addition of the standard. Extrapolating the straight line defines, on the abscissa axis, the concentration of the substance in the analyzed sample.

Table 3. Determination of M3HB in a PHA sample (n = 3).

Sample	Amount Added (10^{-10} mol L^{-1})	Amount Detected (10^{-10} mol L^{-1})	Recovery (%)	RSD (%)
PHA	-	1.7 ± 0.1	-	-
	1.0	2.8 ± 0.1	104	3.5
	2.5	4.3 ± 0.1	102	3.3
	5.0	7.0 ± 0.2	104	2.8

Taking the dilution factor into account, the concentration of P3HB determined in the sample under study was 0.2 nM, equivalent to 18 mg L^{-1}. These results were validated through recovery tests involving three different concentrations of P3HB. Table 3 shows that recovery values ranged from 102 to 104 %, with relative standard deviation values between 2.8 and 3.5%. These results suggested that the GCE/rGO-MIP electrode exhibits a high level of accuracy for the detection and quantification of P3HB.

4. CONCLUSIONS

This study demonstrated the application of an MIP sensor based on rGO and molecularly imprinted film of poly(3-IAA) for the detection and quantification of P3HB. The proposed electrode exhibited low limits of detection, high sensitivity, stable voltammetric responses, reproducible, as well as good selectivity for P3HB recognition. In addition, the recovery values found indicated that the proposed methodology achieved good precision for P3HB detection when applied to PHA samples obtained from sugar cane waste. These results suggest that the strategy to form M3HB as the target molecule for the recognition of P3HB was a versatile approach for the quantification of this

molecule. The concentration of P3HB found in the sample suggests that sugarcane waste can be utilized to produce bioplastics and reduce the environmental impacts caused by the improper disposal of plastics from the petrochemical industry.

Declaration of interests

The authors declare that they have no known competing financial interests or personal relationships that could have appeared to influence the work reported in this paper.

Author contributions

Emanuela Conceição: Methodology, Investigation, Formal analysis, Validation, **Edervaldo Buffon:** Methodology, Investigation, Formal analysis, Validation, Writing - Original Draft. **Maísa Azevedo Beluomini:** Methodology, Investigation, Validation, Writing - review & editing. **Max Fabrício Falone**: Methodology, Investigation. **Fernanda Batista de Andrade:** Investigation, Formal analysis. **Jonas Contiero**: Supervision, Resources, Funding acquisition. **Nelson Ramos Stradiotto**: Conceptualization, Resources, Supervision, Funding acquisition, Writing - review & editing.

Acknowledgements

The authors would like to thank the São Paulo Research Foundation (FAPESP; grants #2017/22401-8, #2018/12131-6, and #2019/13818-8), the National Council for Scientific and Technological Development (CNPq; grant #121298/2020-5) for the financial assistance provided to this work.

Appendix A. Supporting information

Supplementary data associated with this article can be found in the online version.

REFERENCES

[1] S. Godbole, Methods for identification, quantification and charaterization of Polyhydroxyalkanoates - A review, Res. J. Biotechnol. 9 (2014) 99–105.

[2] T.V.B. Figueiredo, M.I. Campos, L.S. Sousa, J.R. Da Silva, J.I. Druzian, Produção e caracterização de polihidroxialcanoatos obtidos por fermentação da glicerina bruta residual do biodiesel, Quim. Nova. 37 (2014) 1111–1117. doi:10.5935/0100-4042.20140183.

[3] G.Y.A. Tan, C.L. Chen, L. Li, L. Ge, L. Wang, I.M.N. Razaad, Y. Li, L. Zhao, Y. Mo, J.Y. Wang, Start a research on biopolymer polyhydroxyalkanoate (PHA): A review, Polymers (Basel). 6 (2014) 706–754. doi:10.3390/polym6030706.

[4] L.K.M. Quines, J.L. Ienczak, M. Schmidt, K. Zanfonato, M.I. Rodrigues, W. Schmidell, G.M.F. Aragão, Extraction of poly(3-hydroxybutyrate), produced by Cupriavidus necator, with propylene carbonate, Quim. Nova. 38 (2015) 214–220. doi:10.5935/0100-4042.20140297.

[5] C.B.C. de Paula, F.C. de Paula-Elias, M.N. Rodrigues, L.F. Coelho, N.M.L. de Oliveira, A.F. de Almeida, J. Contiero, Polyhydroxyalkanoate Synthesis by Burkholderia glumae into a Sustainable Sugarcane Biorefinery Concept, Front. Bioeng. Biotechnol. 8 (2021) 1–14. doi:10.3389/fbioe.2020.631284.

[6] F.C. de Paula, S. Kakazu, C.B.C. de Paula, J.G.C. Gomez, J. Contiero, Polyhydroxyalkanoate production from crude glycerol by newly isolated Pandoraea sp. Polyhydroxyalkanoate production from crude glycerol, J. King

Saud Univ. - Sci. 29 (2017) 166–173. doi:10.1016/j.jksus.2016.07.002.

[7] F. Coutinho de Paula, S. Kakazu, C. Bilia Chimello de Paula, A.F. de Almeida, J.G. Cabrera Gomez, J. Contiero, Burkholderia glumae MA13: A newly isolated bacterial strain suitable for polyhydroxyalkanoate production from crude glycerol, Biocatal. Agric. Biotechnol. 20 (2019) 101268. doi:10.1016/j.bcab.2019.101268.

[8] J. Yu, H. Natural, Chapter 23 . Microbial Production of Bioplastics from Renewable Resources, Elsevier B.V., 1960. doi:10.1016/B978-0-444-52114-9.50024-4.

[9] G. Martínez-García, E. Pérez-Julián, L. Agüí, N. Cabré, J. Joven, P. Yáñez-Sedeño, J.M. Pingarrón, An Electrochemical Enzyme Biosensor for 3-Hydroxybutyrate Detection Using Screen-Printed Electrodes Modified by Reduced Graphene Oxide and Thionine, Biosens. 2017, Vol. 7, Page 50. 7 (2017) 50. doi:10.3390/BIOS7040050.

[10] B. Feng, Y.-N. Liu, The Fabrication of Screen Printed Electrode Mixed Ferrocenemethanol and Thionin for β-hydroxybutyrate Biosensor, Int. J. Electrochem. Sci. 10 (2015) 947–955. www.electrochemsci.org (accessed November 27, 2023).

[11] A. Koyappayil, S.G. Chavan, M. Mohammadniaei, A. Go, S.Y. Hwang, M.H. Lee, β-Hydroxybutyrate dehydrogenase decorated MXene nanosheets for the amperometric determination of β-hydroxybutyrate, Microchim. Acta. 187 (2020) 1–7. doi:10.1007/S00604-020-04258-Y/FIGURES/4.

[12] M. Veerapandian, R. Hunter, S. Neethirajan, Ruthenium dye sensitized graphene oxide electrode for on-farm rapid detection of beta-hydroxybutyrate, Sensors Actuators B Chem. 228 (2016) 180–184. doi:10.1016/J.SNB.2016.01.028.

[13] C.C. Wang, J.W. Hennek, A. Ainla, A.A. Kumar, W.J. Lan, J. Im, B.S. Smith, M. Zhao, G.M. Whitesides, A Paper-Based Pop-up Electrochemical Device for Analysis of Beta-Hydroxybutyrate, Anal. Chem. 88 (2016) 6326–6333. doi:10.1021/ACS.ANALCHEM.6B00568/ASSET/IMAGES/LARGE/AC-2016-00568A_0003.JPEG.

[14] T.Y. Chen, V. Mani, S.T. Huang, P.C. Chang, C.H. Huang, N.M. Huang, Synthesis of robust electrochemical substrate and fabrication of immobilization free biosensors for rapid sensing of salicylate and β-hydroxybutyrate in whole blood, Anal. Chim. Acta. 990 (2017) 78–83. doi:10.1016/J.ACA.2017.08.051.

[15] A. Ngamaroonchote, K. Karn-orachai, Non-enzymatic Electrochemical Sensing of 3-Hydroxybutyric Acid by Incorporating Manganese Oxide Modified Electrode and Nitroprusside Electrolyte, J. Electrochem. Soc. 169 (2022) 097502. doi:10.1149/1945-7111/AC8BB0.

[16] T.M. Mariano, M.A. Beluomini, N.R. Stradiotto, Molecularly imprinted polypyrrole on glassy carbon electrode modified with reduced graphene oxide and gold nanoparticles for isoamyl alcohol analysis in fusel oil, J. Braz. Chem. Soc. 32 (2021) 249–259. doi:10.21577/0103-5053.20200174.

[17] M.P. da Silva, M.A. Beluomini, C. de Freitas, M. Brienzo, N.R. Stradiotto, Electrochemical Detection of Xylobiose in Banana Biomass Using a 3D Porous Copper Oxide Foam Electrode Modified with a Molecularly Imprinted Poly-L-Arginine Film, J. Food Compos. Anal. (2023) 105658. doi:10.1016/J.JFCA.2023.105658.

[18] E. Buffon, N.R. Stradiotto, Using a disposable platform based on reduced graphene oxide, iron nanoparticles and molecularly imprinted polymer for voltammetric determination of vanillic acid in fruit peels, Food Chem. 397 (2022) 133786. doi:10.1016/J.FOODCHEM.2022.133786.

[19] N. Leibl, K. Haupt, C. Gonzato, L. Duma, Molecularly imprinted polymers for chemical sensing: A tutorial review, Chemosensors. 9 (2021) 1–19. doi:10.3390/chemosensors9060123.

[20] L. Dery, D. Zelikovich, D. Mandler, Electrochemistry of molecular imprinting of large entities, Curr. Opin. Electrochem. 34 (2022) 100967. doi:10.1016/J.COELEC.2022.100967.

[21] M.A. Beluomini, J.L. da Silva, A.C. de Sá, E. Buffon, T.C. Pereira, N.R. Stradiotto, Electrochemical sensors based on molecularly imprinted polymer on nanostructured carbon materials: A review, J. Electroanal. Chem. 840 (2019) 343–366. doi:10.1016/j.jelechem.2019.04.005.

[22] S. Li, S. Cao, M.J. Whitcombe, S.A. Piletsky, Size matters: Challenges in imprinting macromolecules, Prog. Polym. Sci. 39 (2014) 145–163. doi:10.1016/J.PROGPOLYMSCI.2013.10.002.

[23] H.R. Culver, N.A. Peppas, Protein-Imprinted Polymers: The Shape of Things to Come?, Chem. Mater. 29 (2017) 5753–5761. doi:10.1021/ACS.CHEMMATER.7B01936/ASSET/IMAGES/CM-2017-019369_M005.GIF.

[24] E. Buffon, N.R. Stradiotto, Disposable p-coumaric acid sensor containing reduced graphene oxide, nickel nanoparticles and biodegradable molecularly imprinted polymer for fruit peel analysis, J. Food Compos. Anal. 118 (2023) 105186. doi:10.1016/J.JFCA.2023.105186.

[25] B.B. Prasad, I. Pandey, Electrochemically imprinted molecular recognition sites on multiwalled carbon-nanotubes / pencil graphite electrode surface for enantioselective detection of d - and l -aspartic acid, Electrochim. Acta. 88 (2013) 24–34. doi:10.1016/j.electacta.2012.10.095.

[26] L.F.P.P. Moreira, E. Buffon, A.C. de Sá, N.R. Stradiotto, Fructose determination in fruit juices using an electrosynthesized molecularly imprinted polymer on reduced graphene oxide modified electrode, Food Chem. 352 (2021) 129430. doi:10.1016/J.FOODCHEM.2021.129430.

[27] M.A. Beluomini, J.L. da Silva, A.C. de Sá, E. Buffon, T.C. Pereira, N.R. Stradiotto, Electrochemical sensors based on molecularly imprinted polymer on nanostructured carbon materials: A review, J. Electroanal. Chem. 840 (2019) 343–366. doi:10.1016/j.jelechem.2019.04.005.

[28] M. Rahman, J. Niu, X. Cui, C. Zhou, N. Tang, H. Jin, D. Cui, Electrochemical Biosensor Based on l -Arginine and rGO-AuNSs Deposited on the Electrode Combined with DNA Probes for Ultrasensitive Detection of the Gastric Cancer-Related PIK3CA Gene of ctDNA , ACS Appl. Bio Mater. 2022 (2022) 5103. doi:10.1021/ACSABM.2C00393/ASSET/IMAGES/LARGE/MT2C00393_0005.JPEG.

[29] M.A. Beluomini, N. Karimian, N.R. Stradiotto, P. Ugo, Tailor-made 3D-nanoelectrode ensembles modified with molecularly imprinted poly(o-phenylenediamine) for the sensitive detection of L-arabitol, Sensors Actuators, B Chem. 284 (2019). doi:10.1016/j.snb.2018.12.091.

[30] M.A. Beluomini, J. Luiz Da Silva, N.R. Stradiotto, Determination of uronic acids in sugarcane bagasse by anion-exchange chromatography using an electrode modified with copper nanoparticles, Anal. Methods. 7 (2015). doi:10.1039/c4ay03060e.

[31] G.N.M. Huijberts, H. van der Wal, C. Wilkinson, G. Eggink, Gas-chromatographic analysis of poly(3-hydroxyalkanoates) in bacteria, Biotechnol. Tech. 8 (1994) 187–192. doi:10.1007/BF00161588.

[32] K. Danzer, L.A. Currie, Guideline for calibration in analytical chemistry— Part

1. Fundamentals and single component calibration, Pure Appl. Chem. 70 (1998) 993–1014. doi:10.1351/pac199870040993.

[33] E. da Conceição, E. Buffon, N.R. Stradiotto, Lead signal enhancement in anodic stripping voltammetry using graphene oxide and pectin as electrode modifying agents for biofuel analysis, Fuel. 325 (2022) 124906. doi:10.1016/J.FUEL.2022.124906.

[34] L.F. Pompeu Prado Moreira, E. Buffon, N.R. Stradiotto, Electrochemical sensor based on reduced graphene oxide and molecularly imprinted poly(phenol) for D-xylose determination, Talanta. 208 (2020) 120379. doi:10.1016/j.talanta.2019.120379.

[35] T. Hu, G. Dryhurst, Electrochemical oxidation of indole-3-acetic acid: Mechanisms and products formed in acidic medium, J. Electroanal. Chem. 362 (1993) 237–248. doi:10.1016/0022-0728(93)80026-E.

[36] E. Buffon, N.R. Stradiotto, A molecularly imprinted polymer on reduced graphene oxide-gold nanoparticles modified screen-printed electrode for selective determination of ferulic acid in orange peels, Microchem. J. 167 (2021) 106339. doi:10.1016/J.MICROC.2021.106339.

[37] M. Bartilotti, M.A. Beluomini, M.V. Boldrin Zanoni, Using an Electrochemical MIP Sensor for Selective Determination of 1-Naphthol in Oilfield Produced Water, Electroanalysis. 33 (2021) 1346–1355. doi:10.1002/elan.202060545.

[38] M.F. Falone, E. Buffon, N.R. Stradiotto, Molecularly imprinted electrochemical sensor for monitoring mercaptan sulfur in aviation biofuel, Fuel. 307 (2022) 121783. doi:10.1016/j.fuel.2021.121783.

[39] M.A. Beluomini, N.R. Stradiotto, M.V. Boldrin, Electrosynthesis of three-dimensional nanoporous nickel on screen-printed electrode used for the determination of narirutin in citrus wastewater, Food Chem. 353 (2021) 129427. doi:10.1016/j.foodchem.2021.129427.

[40] E. Buffon, N. Ramos, Sensors and Actuators B : Chemical Electrochemical sensor based on molecularly imprinted poly (ortho-phenylenediamine) for determination of hexahydrofarnesol in aviation biokerosene, Sensors Actuators B. Chem. 287 (2019) 371–379. doi:10.1016/j.snb.2019.02.059.

10) Caso tenha realizado estágio BEPE, incluir cópia do relatório do estágio e a avaliação do supervisor no exterior.

A cópia do relatório BEPE e a avaliação do supervisor no exterior, consta anexado em "Outros documentos" no sistema.